

https://dspace.org/

Utilizing legacy seismics and non-seismic geophysical methods for deep mineral targeting and near-surface characterization: implications for mine development planning

Mutshafa, Ndamulelo

2023

University of the Witwatersrand, Johannesburg

https://hdl.handle.net/10539/41827

Mutshafa, Ndamulelo. (2023). Utilizing legacy seismics and non-seismic geophysical methods for deep mineral targeting and near-surface characterization: implications for mine development planning [PhD thesis, University of the Witwatersrand, Johannesburg]. WireDSpace.https://hdl.handle.net/10539/41827

Downloaded from a DSpace repository. https://dspace.org/

Utilizing legacy seismics and non-seismic geophysical methods for deep mineral targeting and near-surface characterization: implications for mine development planning

By

Ndamulelo Mutshafa

A thesis submitted in fulfillment of the requirements for the degree of

Doctor of Philosophy

In the

Faculty of Science,

School of Geosciences

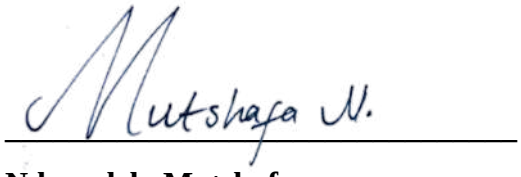
University of the Witwatersrand, Johannesburg



December 2023

DECLARATION

I declare that this thesis is my own, unaided work. It is being submitted for the Degree of Doctor of Philosophy at the University of the Witwatersrand, Johannesburg. It has not been submitted before for any degree or examination in any other University**.**



Ndamulelo Mutshafa
Student Number: 886156

Signed on the

14 day of December 2023 at University of the Witwatersrand.

ABSTRACT

This thesis demonstrates through several case studies how the reprocessing of legacy reflection seismic data using advanced algorithms can be of value to mineral exploration and mine development, especially in hard-rock environments. The thesis also showcases how the integration of seismic and non-seismic geophysical datasets can assist in delineating near-surface geological structures (e.g., boulders and fractures) for mine planning and designs.

Papers I and II demonstrate how the reprocessed legacy reflection seismic data have been used to delineate and image the world-class gold deposits such as the Black Reef (BLR) and Ventersdorp Contact Reef (VCR) of the Witwatersrand goldfields in South Africa. The two legacy reflection seismic profiles (Paper I) were acquired in 1988 for deep mineral exploration and mine planning over an area that is dominated by dolomitic outcrops that cause scattering of seismic energy at the near-surface, preventing energy propagation into the subsurface. Various migration approaches, namely, pre-stack time, pre-stack depth, and post-stack time migration were applied to test their capabilities in improving structural imaging. Reprocessing results from the pre-stack depth migration using the Kirchhoff algorithm provided the most improved subsurface images, especially the deeper targets due to its ability to honour complex lateral variations in the velocity field. In addition, Kirchhoff's pre-stack and post-stack time migration techniques improved the continuity of the near-surface reflections below the dolomitic rocks.

Paper II presents the results from the recovered and processed 25.3 km long legacy seismic survey that was acquired in 1983 by the Gold Division of Anglo-American as part of the Witwatersrand goldfields exploration program. The reprocessing of the data improved the imaging of the gold-bearing horizon termed Ventersdorp Contact Reef (VCR), which is situated at depths between ~2400 and ~4100 m below the ground surface near the South Deep mine in Fochville, South Africa. The pre-stack time and phase-shift migration approaches were tested during processing, and both revealed a dipping reflection associated with the gold-bearing horizon and major steeply dipping faults that crosscut and displace the deposit. The interpretation of the results was constrained using borehole logs and surface geology. This is encouraging and motivates the use of legacy seismic data in the exploration of deep-seated targets.

Papers III, IV and V present the results from the use of multi-geophysical methods (resistivity, magnetics, seismic, ground penetrating radar and multichannel analysis of surface waves) at Tharisa platinum mine to provide a comprehensive understanding of the subsurface

geology by accurately delineating and locating boulders, mapping fractures and groundwater aquifers to improve Platinum Group Elements (PGEs) mining efficiency and reduce risks. The results from these integrated geophysical methods were successful in complementing each other in terms of providing a clear picture of the near-surface geological structures to help the mine plan better for future operations.

ACKNOWLEDGEMENTS

I would like to thank my supervisor, Professor Musa Manzi, for allowing me the opportunity to be part of the Wits Seismic Research Centre of the School of Geosciences at the University of the Witwatersrand, Johannesburg. Thank you for your kind support, patient guidance, and encouragement, and for giving me a chance to grow academically and personally. I am grateful for allowing me to participate in workshops, conferences, and other social gatherings. I appreciate being part of the crew for fieldwork.

I would like to thank Ian James and Michael Westgate for the crash course in Globe Claritas seismic processing software. Thanks to Ian James for being there for me when I needed help with the computation of the first breaks travel time tomograms and reprocessing the reflection seismic data. I want to thank all my colleagues, especially the group I worked closely with; Sikelela, Kenneth, Mpofana, Nombuso, Marcus, Omphulusa, Salizwa, Nondumiso, and all those that I have forgotten.

Thank you to the geophysics academic staff: Profs Raymond Durrheim, Susan Webb, Gordon Cooper, and Dr. Stephanie Enslin for their guidance in scientific engagement and for being role models in the academic environment. I would also like to thank the School of Geosciences and the University of the Witwatersrand for allowing me to pursue my degree.

The donation of 2D legacy seismic data by Sibanye Stillwater and Anglo Gold Ashanti is acknowledged and greatly appreciated. I wish to acknowledge my co-authors for their collaboration on all the papers on which this thesis is based. I would like to thank Dr. Yolanda Davids for helping me with getting scholarships such as the Research Office Carnegie Bursary and the Kirsh Foundation during my PhD studies. The Council for Geoscience (CGS), Research Office Carnegie Bursary, and National Research Foundation are acknowledged for financial support.

I would like to thank my family for understanding and supporting me throughout my Ph.D. journey: Matodzi, Tshilidzi, Masindi, Lufuno, Livhuwani, Tsireledzo, Unarine, Mulweli, Adivhaho, Rendani, Thabelo, Ompha, Romu.

I would like to thank Vhugala, Lydia, Ndivhuho, Khathutshelo, Vivian, Vhutshilo, and Ntombizodwa.

I am very grateful to God Almighty for the good health and prosperity that was necessary to finish my studies.

CONTENTS

Declaration ii

Abstract ..... *iii*

Acknowledgements v

List of Figures vii

List of abbreviations xii

1. INTRODUCTION 1

1.1 Aims and objectives 3

1.2 Thesis structure 4

1.3 Authorship statement 5

2. GEOLOGICAL SETTINGS 8

2.1 Dominion Group 9

2.2 Witwatersrand Supergroup 11

2.3 Ventersdorp Supergroup 14

2.4 Transvaal Supergroup 16

2.5 Bushveld Complex 19

3. SEISMIC REFLECTION METHOD 23

3.1 Background 23

3.2 Seismic modeling 25

3.3 Acquisition 29

3.4 Processing 34

3.5 Interpretation 43

4. 3D SEISMIC IMAGING: ATTRIBUTE ANALYSIS 51

4.1 Picking horizons 54

4.2 Surface creation 56

4.3 Surface attributes 58

4.4 Fault mapping 60

4.5 Implications for mining 62

5. REFERENCES 63

6. SUMMARY OF SCIENTIFIC CONTRIBUTIONS 74

7. Paper I: Seismic imaging of the gold deposit and geological structures through reprocessing of legacy seismic profiles near Kloof–Driefontein Complex East Mine, South Africa 78

8. Paper II: Seismic imaging of deep-seated gold deposit and host rocks through reappraisal of legacy seismic data in the Fochville mining area, South Africa 113

9. Paper III: Integrated geophysical methods for boulder delineation to improve mining 145
10. Paper IV: Multi-geophysical methods for characterizing fractures in an open pit mine, western Bushveld Complex, South Africa 183
11. Paper V: Integration of ground geophysical methods to characterize near-surface groundwater aquifers within an active mine 224
12. DISCUSSION..... 264
13. CONCLUSION 268
14. APPENDIX 269

List of Figures

Figure 2.1: (a) Simplified geological map showing the local geology including the Transvaal Supergroup (TS), with an emphasis on its strata-bound igneous unit i.e., Hekpoort Formation, other TS formations, and Bushveld Complex (BC) in the Transvaal sub-basin (TB). (b) The Kaapvaal Craton boundaries and preserved extent of the TS are mainly distributed within the TB. RLS: Rustenburg Layered Suite (modified after Humbert et al., 2020). Study areas are shown by red dotted rectangle (Witwatersrand Basin) and blue rectangle (Bushveld Complex). 9

Figure 2.2: Generalized stratigraphic column of the Dominion Group with three formations (modified from SACS, 1980; Jackson, 1992)..... 11

Figure 2.3: Generalized stratigraphy of Central Rand and West Rand Groups of Witwatersrand Supergroup (SACS, 1980; Kositcin et al., 2003)..... 13

Figure 2.4: Generalized lithostratigraphy column of the Ventersdorp Supergroup (SACS, 1980; Armstrong et al., 1991; Van der Westhuizen et al., 1991). 16

Figure 2.5: Generalized lithostratigraphy column of the Transvaal Supergroup (SACS, 1980; Jahn et al., 1990; Eriksson et al., 1993)..... 17

Figure 2.6: Simplified chronostratigraphic column of the Bushveld Complex (after SACS, 1980; Jones, 2018). Red arrows schematically show the relative position of major ore-bearing layers. 22

Figure 3.1: An illustration of Body waves. (a) Primary wave motion; (b) Secondary or Shear wave motion (Anderson et al., 1998; Rogers, 2015). 24

Figure 3.2: An illustration of Surface waves. (a) Rayleigh wave motion; (b) Love wave motion (Rogers, 2015). 24

Figure 3.3: An illustration of Huygens' principle - the superposition of elementary waves (after Russer and Russer, 2015). 28

Figure 3.4: Illustration of an incident wave being reflected and transmitted at the boundary where the angle $\theta i = \theta r$ (angle of the incident wave is equal to the angle of the reflected wave) (modified from Dukhin and Goetz, 2010) Additionally, the angle θt is governed by the difference between v1 and v2 and a larger difference results in a 'flatter' transmitted wave.. 31

Figure 3.5: An illustration of the Fresnel zone (A – A') where Z_0 is the reflection depth, λ is the dominant frequency and S is the source (Yilmaz, 2001; Nanda, 2016). 33

Figure 3.6: Example of seismic reflection processing workflow used for profiles 1 and 2 presented in chapter 6 (Table 3.1; Mutshafa et al., 2022). 35

Figure 3.7: List of headers information from profile AC_05 (chapter 7). (a) Trace from raw legacy data, and (b) trace from legacy data after reassigning the x coordinates of the source and receiver and assigning their elevation..... 36

Figure 3.8: Quality control check of the geometry set-up. Example from the legacy profile in Paper II (chapter 7). 37

Figure 3.9: Seismic survey geometry. (a) Horizontal layer with multiple receivers (g) and single source (s), (b) Common midpoint (CMP) gather for a horizontal layer, (c) Dipping layer with a single source and multiple receiver/geophones, (d) Common midpoint gather for dipping layer. The seismic wave travels from the source (s) to the subsurface reflector and is reflected in the geophones/receivers (g) where it is recorded (Manzi, 2014)..... 38

Figure 3.10: A representation of the Normal Move-out correction principle. For a horizontal stratification, an averaged velocity termed 'root mean square' (V_{RMS}) is the correct velocity and not a linearly averaged velocity over depth or transit time, and the V_{RMS} is stacked (van der Kruk, 2005). 39

Figure 3.11: Examples of migration strategies (modified from Yilmaz, 2001). 40

Figure 3.12: Example of post-stack migration and pre-stack migration of the same section (after Longde et al., 2015). 43

Figure 3.13: A sketch of an autopicker's operation (after Dorn, 1998). 45

Figure 3.14: A complex seismic trace. The seismic time axis is t. The real part x (t) of the complex trace is the actual seismic trace; the imaginary part y (t) is a mathematical function calculated from the real trace by a Hilbert transform process (after Taner et al., 1979). 47

Figure 3.15: An illustration of the relationship between the seismic trace (x(t)) and the quadrature (y(t)) in Cartesian coordinates. The amplitude and phase attributes represent the point in polar coordinates, the seismic and quadrature traces represent the point in polar coordinates, while the seismic and quadrature traces represent the point in Cartesian coordinates. φi(t) is the cosine of the instantaneous phase and a(t) is the instantaneous amplitude attribute (after Sehoole, 2019). 48

Figure 4.1: The location of historical surveys over the West Rand and West Wits Line goldfields (after Manzi et al., 2012a). The survey of interest for this study is the 2003 Kloof-South Deep seismic survey. 52

Figure 4.2: Depth-converted seismic sections. (a) The legacy post-stack Kirchhoff time migrated (PostSTM) section. (b) The 2020 reprocessed section - pre-stack reverse time migrated (PreSTM) section. Note that 2020 PreSTM shows better resolution relative to the legacy PostSTM. Blue arrows indicate Black Reef, green arrows indicate Ventersdorp Contact Reef, while yellow arrows indicate fault zone..... 53

Figure 4.3: Three-dimensional visualization of Kloof-South Deep seismic survey and 2D seismic profile. The 3D seismic cube displays the inline (y-axis), crossline (x-axis), and depth slice (z-axis) sections. 54

Figure 4.4: Horizon picking on Ventersdorp Contact Reef (VCR). (a) 2D manual identification for VCR. (b) Combined confidence classification map to validate the interpretation of VCR. The red, green, and blue colors show high, intermediate, and low levels of confidence, respectively. 55

Figure 4.5: Horizon picking on Black Reef (BLR). (a) 3D auto-tracking interpretation of BLR. (b) Combined confidence classification map to validate the interpretation of BLR. The red, green, and blue colors show high, intermediate, and low levels of confidence, respectively. 56

Figure 4.6: Depth maps generated from the picked horizons. (a) VCR surface, and (b) BLR surface. The color bar is given in meters. The elevation depth ranges from 1500 to 2500 m. BLR: Black Reef, VCR: Ventersdorp Contact Reef. 57

Figure 4.7: Comparison between the depth map and influential data attribute. (a) VCR depth map, and (b) VCR influential data map, and (c) BLR depth map, (d) BLR influential

data map. The elevation depth ranges from 1500 to 2500 m. BLR: Black Reef, VCR: Ventersdorp Contact Reef. 58

Figure 4.8: The dip angle (a) and dip azimuth (b) attributes computed on the VCR surface highlighting faults features. A major feature is indicated by a white arrow in both attributes. VCR: Ventersdorp Contact Reef. 59

Figure 4.9: The dip angle (a) and dip azimuth (b) attribute computed on the BLR surface highlighting faults features. The map is dominated by dip azimuth values ranging from 180 to 360 degrees). BLR: Black Reef. 59

Figure 4.10: Edge detection attribute map showing high-resolution imaging of the faults on the VCR surface. The edge detection attribute color bar is given in %. Areas where the surface is faulted, appear red and orange, between 0 – 40 %. The horizon is faulted with known faults such as the West Rand Fault and Wrench Fault. VCR: Ventersdorp Contact Reef. 60

Figure 4.11: Edge detection attribute map showing high-resolution imaging of the faults on the BLR surface. The edge detection attribute color bar is given in %. Areas where the surface is faulted, appear red and orange, between 0 – 20 %. BLR: Black Reef. 61

Figure 4.12: Three-dimensional visualization of combined 3D VCR edge detection surface and modeled faults (color bar for edge detection attribute is given in%). These faults do not offset the BLR on seismic sections. BLR: Black Reef, VCR: Ventersdorp Contact Reef. 62

List of abbreviations

2D	Two dimensional
3D	Three dimensional
Au	Gold
BC	Bushveld Complex
BLR	Black Reef
CDP	Common depth point
CMP	Common midpoint
ERT	Electrical resistivity tomography
FD	Finite difference
FE	Finite element
Ga	Giga annum (Billion years ago)
km	Kilometres
KDC	Kloof-Driefontein Complex
Ma	Mega annum (Million years ago)
MASW	Multichannel analysis of surface waves
NMO	Normal move-out
PGEs	Platinum group elements
PostSTM	Post-stack time migration
PSMIG	Phase-shift migration
PreSDM	Pre-stack depth migration
PreSTM	Pre-stack time migration
RC	Reflection coefficient
RLS	Rustenburg Layered Suite
RMS	Root-mean-square
RTM	Reverse time migration
SRT	Seismic refraction tomography
TB	Transvaal sub-basin
TS	Transvaal Supergroup
TWT	Two way-travel-time
U	Uranium
VCR	Ventersdorp contact reef

1. INTRODUCTION

The mining industry has long relied on traditional mapping and drilling methods for exploration and mine planning. There is growing recognition that new deep exploration techniques must be employed if the mining industry is to maintain its long-term profitability (Milkereit et al., 1996; Salisbury et al., 1996). The reflection seismic method is a powerful geophysical technique that uses the reflection of seismic waves to obtain an image of the Earth's subsurface (Yilmaz, 2001; Manzi et al., 2012a). Reflected seismic waves bring very useful information about the rocks and geological structures in the subsurface (Ahmadi, 2015). The method has proven its capability in mineral exploration and mine planning (Gillot et al., 2005; Markovic et al., 2020). When compared to other geophysical methods, seismic methods provide better imaging of geologic structures hosting mineral deposits and can be used to delineate mineral deposits at depths greater than 1 km (Cheraghi et al., 2012; Koivisto et al., 2012; Malehmir et al., 2012a; Manzi et al., 2012b). This benefit led the hard-rock mining industry to take advantage of the method and seek solutions to their prospecting problems (Malehmir et al., 2012a; Manzi et al., 2012b). Reflection seismology found wide application for gold, platinum, and base metal exploration in the early 1980s in Southern Africa (Stevenson and Durrheim, 1997). Following several successful surveys, the technique became useful for mine planning and designs (Stevenson and Durrheim, 1997). Before this, reflection seismics was mainly used to explore oil and gas in soft sedimentary basins around the world (De Beer, 2016).

Modern data from new instruments are generally preferred by most geophysicists and mineral explorers today over so-called "legacy data" (Malehmir et al., 2019). The term "legacy data" refers to information that has been collected in the past but whose restoration would take a lot of effort and resources without a guarantee of success. These legacy data sets frequently suffer from poor documentation and incorrect coordinates. They are stored on devices that are difficult to access, such as tapes or printed versions/hard copies, or they may already be largely contaminated. In any case, legacy data are as yet significant, particularly if they are from brownfield or close mine investigation sites, and can be restored and improved (Malehmir et al., 2019; Manzi et al., 2019). The new information acquired from the legacy data may profit future mine planning operations by finding new ore deposits, giving a superior estimation of the resources and information that will assist with siting and sinking future shafts (Manzi et al., 2019). Legacy data have their advantages such as being less defiled by noise from mining exercises and frameworks; being acquired in places that presently may be unavailable; and

being cheaper to reprocess and reinterpret than to collect new data as data acquisition often makes up the bulk of a survey's cost.

It is advantageous to reprocess and interpret legacy data to improve the detection of steeply dipping structures and geological features beneath the conventional seismic resolution limits (i.e., a quarter of the dominant wavelength), which was impractical with the tools that were available when the data were first acquired and processed (Manzi et al., 2018; 2019). The deep mining industry in South Africa is particularly interested in the most recent seismic algorithms because the country is home to the largest hard rock seismic database in the world, which could benefit from new processing methods. These methods could be used on legacy seismic data to identify interesting areas, enhance structural resolution, and locate deeper ore deposits (Manzi et al., 2018). Legacy data occasionally lack or lose important information. Company mergers and frequent employee turnover may be to blame for this. For instance, crucial information like the precise location and coordinate systems are frequently left out of old data observer reports and header files of the raw data. Reprocessing is often difficult since very little information is available (Terracin and Manzi, 2017; von Ketelhodt et al., 2019).

Due to geological characteristics that result in discontinuities in the rock mass, rock slope stability is a problem that most open pit miners must deal with. Mining, engineering, and hydrogeological issues are brought on by open cracks in mine walls. Also, the presence of boulders in open pit mining is a concern because they constitute barriers that might reduce productivity in mining operations (Dan et al., 2016; Ofterdinger et al., 2019; Shao et al., 2020). It is typically difficult to locate boulders using traditional geological mapping techniques due to their irregular distribution and variability. To solve these problems, one needs to use multi-geophysical techniques that complement each other. Multi-geophysical methods are a set of techniques that involve the integration of different geophysical methods to provide a more comprehensive understanding of subsurface structures.

In this study, geophysical methods at the open pit Marikana mine of Tharisa (Pty) Ltd in the Western Bushveld Complex, are used to accurately characterize fractures, boulders and aquifers within the rock mass, which can improve platinum mining efficiency while reducing costs and mining risks. The geophysical techniques used are ground magnetics, electrical resistivity tomography, seismics, ground penetrating radar and multichannel analysis of surface seismic waves.

1.1 Aims and objectives

In this thesis, legacy seismic data from the Witwatersrand goldfields were reprocessed using new techniques to improve the imaging of deep-seated (> 1 km) gold-bearing horizons (locally termed reefs) and host rocks (Papers I and II). The aim was to test various latest migration techniques and compare their capabilities in terms of defining complex geological structures. The effort was made to improve the velocity model used for migrations. Other pre-stack processing steps (mainly statics correction) were carefully applied to the data to enhance the quality of the data, especially in the near-surface where the dolomitic outcrops were dominant. In Papers I and II, processing, modeling, and interpretation techniques were applied to the 2D reflection seismic data that cover mines from the West Rand goldfields such as the Kloof-Driefontein Complex (KDC) and South Deep gold mine in the Witwatersrand Basin.

Paper I: The reprocessing of legacy data in the geologically complex Witwatersrand Basin of South Africa has improved the imaging of gold-bearing reefs and faults using today's seismic processing algorithms. Two seismic profiles were reprocessed to image the gold deposits known as Black Reef (BLR) located between 0.5 km and 2 km depth, near the KDC East Mine in the West Rand goldfield. Paper II: A high-resolution reflection seismic profile was reprocessed using the post-stack Phase-shift migration (PSMIG) and Kirchhoff pre-stack time migration (PreSTM) techniques to image the Ventersdorp Contact Reef (VCR) located at depths between 2 km and 4 km below ground surface.

In Papers III, IV, and V, multi-geophysical methods are used to delineate boulders, and characterize fractures and near-surface groundwater aquifers at the Tharisa Marikana open pit mine in the western Bushveld Igneous Complex. New sets of geophysical data were acquired, processed and interpreted to characterize the near-surface geology of the open pit mine. The geophysical methods used for these surveys include seismic, magnetics, electrical resistivity tomography, ground penetrating radar and multichannel analysis of seismic surface waves. The integration of these geophysical methods complemented each other, e.g., they successfully delineated the boulders and mapped other geological features such as fractures in the pit area. By combining these techniques, mining companies can obtain a more accurate picture of the subsurface geology, which can be used to optimize mining operations and reduce costs (Paper III).

In Paper IV, multi-geophysical techniques proved useful in characterizing fractures within the rock mass. By characterizing these fractures, mining companies can better understand the structural integrity of the rock mass and identify potential areas of instability. The main aim of

that study was to delineate fractures that may be potential conduits for water migration into the pit (Tharisa mine).

In Paper V, ground geophysical methods such as seismic refraction tomography (SRT), multichannel analysis of surface waves (MASW) and electrical resistivity tomography (ERT) are used to map the weathered aquifers systems in open pit mine (Tharisa mine). The results indicate a low level of overburden protection, high hydraulic conductivity, high surface and groundwater mixing, and extensive and deep weathering. The water inflow in the mine pits is associated with mining at depths larger/below the weathered and crystalline rock aquifers.

1.2 Thesis structure

This thesis is structured to provide a comprehensive overview of the research undertaken. **Chapter 1** introduces the reflection seismic method in mineral exploration, the application of seismic reflection in gold, platinum, and other base metals and in the oil and gas industries. It reviews the legacy reflection seismic data and outlines their advantages and disadvantages. It also outlines the study's motivation and objectives.

Chapter 2 gives an overview of the geological settings in the Witwatersrand Basin and summarizes the generalized stratigraphy of the study area (Papers I and II). **Chapter 3** provides a detailed theoretical background of the seismic reflection technique. It gives an overview of seismic modeling, acquisition, processing and interpretation. Some of the acquisition parameters of 2D legacy seismic data from Paper I are summarized. The general processing steps given in Papers I and II are summarized and they include pre-processing and quality control; refraction statics correction; frequency filtering; deconvolution; velocity analysis and stacking; and migration. Interpretational aspects are also given here.

Chapter 4 provides 3D interpretation results by using attribute analysis**. Chapter 5** serves as a compilation of references utilized in **Chapters 1** through **4**, while **Chapter 6** offers a succinct summary of the scientific contributions made throughout the study. **Chapters 7** to **11** cover a collection of papers denoted as Papers I to V, which encompass published, under-review, or submitted works. Furthermore, **Chapter 12** engages in an in-depth discussion of the research, delving into its implications and a broader context. In **Chapter 13**, the culmination of the research is presented through conclusive findings.

The **Appendix** supplements the thesis by including peer-reviewed extended abstracts submitted to both international and local geophysical conferences and events, showcasing talks delivered throughout this Ph.D. program. This organizational framework offers a

comprehensive insight into the study's progression and outcomes.

1.3 Authorship statement

The project aims and objectives were set up by Musa S.D. Manzi (Supervisor). The supervisor was responsible for providing raw seismic datasets and assisted with reviewing the manuscripts. The candidate (Ndamulelo Mutshafa) co-authored several papers and presented the findings of the research to local and international conferences throughout the PhD journey. The candidate's contribution to each paper is summarized below. The candidate is the primary author of chapters 7 to 8; the seventh author of chapters 9 and 10; and a secondary author of chapter 11.

Chapter 7: ***Mutshafa, N.****, Manzi, M. S., Westgate, M., James, I., Brodic, B., Bourdeau, J. E., Durrheim, R.J., and Linzer, L. (2022). Seismic imaging of the gold deposit and geological structures through reprocessing of legacy seismic profiles near Kloof–Driefontein Complex East Mine, South Africa. Geophysical Prospecting. http://dx.doi.org/10.1111/1365-2478.13283*

The candidate was responsible for preparing the 2D legacy seismic data, processing, interpretation, and manuscript preparation. Other co-authors: I. James and M. Westgate assisted with processing and reviewing the manuscript. M.S.D. Manzi assisted with the interpretation and guidance while generating images. Others assisted with reviewing the manuscript.

Chapter 8: ***Mutshafa, N.****, Manzi, M. S., James, I. (Under review). Seismic imaging of deep-seated gold deposit and host rocks through reappraisal of legacy seismic data in the Fochville mining area, South Africa, Geophysical Prospecting*

The candidate was responsible for recovering the raw 2D legacy seismic data and process while assisted by I. James. I prepared the manuscript and generated images with assistance from M.S.D. Manzi. All authors reviewed the manuscript. The candidate interpreted the data with M.S.D. Manzi.

Chapter 9: *Gomo S., Rapetsoa M. K., Manzi M. S. D., Onyebueke E., Dildar J., Sihoyiya M.,* ***Mutshafa, N****., Harrison W., Bourdeau J E., Brovko, O., James I., Cooper G. R. J., Scheiber S., Durrheim R. J. (2023). Integrated geophysical methods for boulder delineation to improve mining. Geophysical Prospecting. https://doi.org/10.1111/1365-2478.13322*

I was involved in the design and acquisition of the data; seismic, electrical resistivity and ground penetrating radar (GPR). M.K. Rapetsoa and the candidate assisted with seismic geometry setup and first break picking. E. Onyebueke assisted with GPR data processing and interpretation. S. Gomo prepared the manuscript and generated images. O. Brovko assisted with magnetic 3D modeling, while I. James assisted with producing P-wave tomography inversions. Other authors assisted with reviewing the manuscript and acquisition.

Chapter 10: *Rapetsoa, M. K., Gomo, S., Manzi, M. S. D., James, I., Dildar, J., Sihoyiya, M.,* ***Mutshafa, N****.,* Durrheim, R.J., *Multi-geophysical methods for characterizing fractures in an open pit mine, western Bushveld Complex, South Africa, Geophysical prospecting.*

The candidate was involved in the design and acquisition of the data (seismic, electrical resistivity and magnetics) with M.K. Rapetsoa, S. Gomo, N. Mutshafa, M.S.D. Manzi. M.K. Rapetsoa prepared the manuscript and images under guidance of M.S.D. Manzi. Other authors assisted with reviewing the manuscript and were also part of acquisition.

Chapter 11: *Gomo, S.,* ***Mutshafa, N****., Manzi, S.D., Bourdeau, J. E., Brodic, B., James, I., Cooper, R.J., Durrheim, R. J. (Under review). Integration of ground geophysical methods to characterize near-surface groundwater aquifers within an active mine, Near Surface Geophysics.*

The candidate was involved in the acquisition of the data; seismic refraction tomography (SRT), multichannel analysis of surface waves (MASW), electrical resistivity tomography (ERT). The candidate, together with S. Gomo processed and interpreted the resistivity data. S. Gomo prepared the manuscript and generated images under the guidance of M.S.D. Manzi. B.

Brodic assisted with traveltime residuals plots, while I. James assisted with producing P-wave tomography inversions. M.S.D. Manzi, J.E. Bourdeau, B. Brodic, G.R.J. Cooper and R.J. Durrheim assisted with reviewing the manuscript.

2. GEOLOGICAL SETTINGS

The study areas are located in the Witwatersrand Basin and Bushveld Igneous Complex, which are both located within the Kaapvaal Craton in South Africa (Figure 2.1a). The Witwatersrand Basin is an approximately 7 km thick terrigenous sequence (Coward et al., 1995) and it is known to host the world's largest gold reserves. The basin hosts several gold mines with most mining taking place at depths between 1 km and 3.5 km depths below the surface. The Witwatersrand Basin is viewed as a part of the Kaapvaal Craton that formed during the later stages in the development of extensively mineralized segments of the Earth's crust (Robb and Meyer, 1995). The Bushveld Igneous Complex is the world's largest known layered igneous intrusion, and it hosts the world's largest Platinum Group Elements (PGEs) deposits and also major chrome and vanadium ore bodies. The complex was emplaced in the northern part of the Kaapvaal Craton at around 1.9 Ga (Kirk et al., 2002).

The Kaapvaal Craton (Figure 2.1b) is the ancient segment of continental crust that formed and stabilized between about 3.7 to 2.7 Ga by the emplacement of major granite batholiths in southern Africa (Robb and Meyer, 1995). The craton is a mixture of early Archaean granite-greenstone terranes and older tonalitic gneisses (3.6-3.7 Ga).

Subsequent growth of the Kaapvaal Craton was accompanied by continental magmatic activity, with the possibility of Cordilleran-style accretion of composite terranes along the margins of the proto-continent, and the deposition of appropriate sedimentary basins (Robb and Meyer, 1995; Kirk et al., 2002).

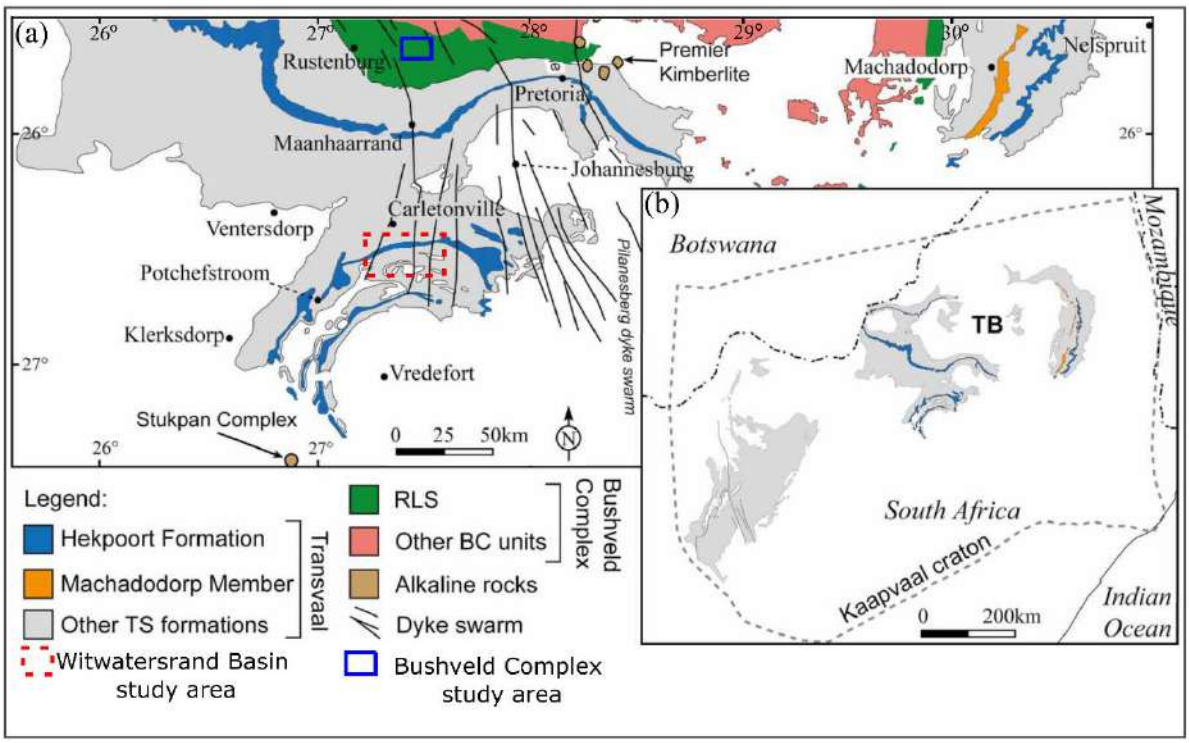


Figure 2.1: *(a) Simplified geological map showing the local geology including the Transvaal Supergroup (TS), with an emphasis on its strata-bound igneous unit i.e., Hekpoort Formation, other TS formations, and Bushveld Complex (BC) in the Transvaal sub-basin (TB). (b) The Kaapvaal Craton boundaries and preserved extent of the TS are mainly distributed within the TB. RLS: Rustenburg Layered Suite (modified after Humbert et al., 2020). Study areas are shown by red dotted rectangle (Witwatersrand Basin) and blue rectangle (Bushveld Complex).*

2.1 Dominion Group

The Dominion Group is a metamorphosed (greenschist to amphibolite grade) supra-crustal succession containing clastic metasediments and volcanic rocks of the late Archaean age which unconformably overlies granitoid basement and underlies the gold-bearing metasediments of the Witwatersrand Supergroup in northern South Africa (SACS, 1980; Jackson, 1992). The succession consists of basal clastic metasedimentary units with conglomerates containing placer gold (Au) and uranium (U) (Jackson, 1992) overlain by mafic lavas and capped by massive feldspar-pyric felsic volcanics, dated at 3074 Ma (Myers et al., 1990; Dankert and Hein, 2010). It has been estimated that the Dominion Group presently covers an area of approximately 15 000 km^2 (Tankard et al., 1982; Armstrong et al., 1991). The Dominion Group consists of three formations namely, Rhenosterspruit Formation, Rhenosterhoek Formation, and Syferfontein Formation (Armstrong et al., 1991; Jackson, 1992;

Figure 2.2). The lower Rhenosterspruit Formation comprises mainly basic to intermediate volcanics, while the upper Syferfontein Formation is dominated by quartz-feldspar porphyries (Armstrong et al., 1991).

Rhenosterspruit Formation

It consists of the basal clastic sedimentary unit of the Dominion Group that overlies the Archaean granitoid basement with an erosional nonconformity (SACS, 1980; Jackson, 1992) Watchorn (1980; 1981) which indicated that the Rhenosterspruit Formation consists of 0.02 to 0.12 km thick sequence of coarse arkose-rich quartzite, grits, conglomerate, schists, and interbedded volcanics. The base of the formation consists of two mineralized conglomerate units:

(1) The Lower Reef is described as a large-pebble conglomerate with clasts of rounded vein quartz and a coarse-grained sericite sandstone matrix, and

(2) The Upper Reef with a small-pebble conglomerate which is a thin but persistent horizon (Malan, 1959; Watchorn, 1980; Jackson, 1992).

The Lower Reef mineralization is mainly auriferous with only minor and sporadic uranium whereas the Upper Reef contains uranium mineralization with little gold, mostly confined to a very thin band with a concentration of heavy minerals at the top of the reef (Malan, 1959; Watchorn, 1980). Von Backstrom (1981) studied the nature of the uranium mineralization and gives the grades of Au and U content in different areas as well as the mining history of the Dominion reefs.

Rhenosterhoek Formation

This volcanic formation overlies the Rhenosterspruit Formation. It is composed mostly of mafic to intermediate, amygdaloidal lavas with a few interbeds of tuffs and felsic porphyry (Jackson, 1992). The formation consists of homogenous fine-grained, mostly aphyric lavas usually containing abundant amygdales filled with quartz, calcite, chlorite, clinozoisite, and pyrite (Jackson, 1992). Jackson (1992) showed that the petrography of the Rhenosterspruit Formation consists of greenschist facies mineralogy, variably altered by carbonatization and silicification, primary igneous textures of the lavas are locally well preserved, but they have been recrystallized. The metamorphic mineralogy of this formation comprises albite, chlorite, tremolite-actinolite, and carbonate with minor quartz, magnetite, and epidote or clinozoisite

(Bowen et al., 1986; Jackson, 1992).

Syferfontein Formation

The uppermost formation of the Dominion Group consists mainly of massive quartz-feldspar porphyry, with only local occurrences of breccia textures, amygdaloidal structures, and flow banding along with minor intercalations of mafic to intermediate lavas and tuffs (Jackson, 1992). Volcaniclastic metasedimentary units now converted to massive pyrophyllite ("Wonderstone") are a significant component of the upper Syferfontein Formation. These rocks are generally massive and very fine-grained (Nel et al., 1937; Jackson, 1992).

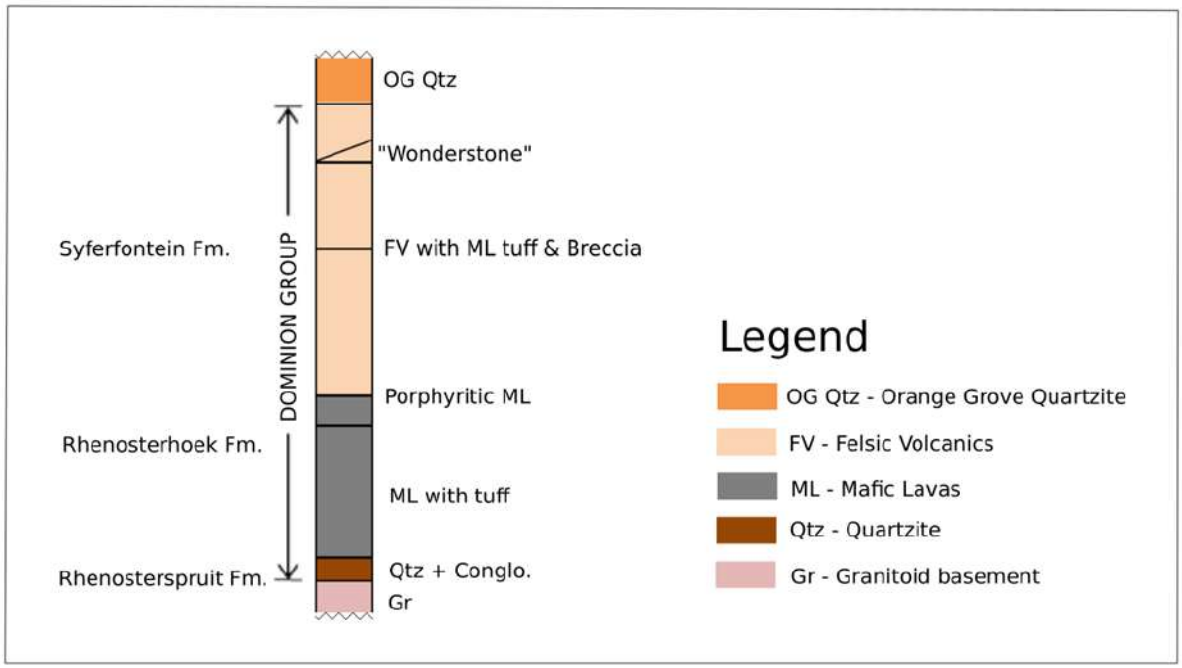


Figure 2.2: *Generalized stratigraphic column of the Dominion Group with three formations (modified from SACS, 1980; Jackson, 1992).*

2.2 Witwatersrand Supergroup

The Witwatersrand Supergroup (Figure 2.3) contains the world's largest known gold and uranium deposits (Barton et al., 1989; Myers et al., 1990; Armstrong et al., 1991; Kositcin et al., 2003). The supergroup is an approximately 7.5 km thick succession of siliciclastic metasedimentary rocks and it overlies a basement composed of mainly granitoid rocks with few greenstone remnants (Barton et al., 1989; Kositcin et al., 2003). The age of the Witwatersrand metasedimentary rocks is bracketed between that of basement granites and the Dominion Group that unconformably underlies the sequence and the age of the Ventersdorp

Supergroup lavas that unconformably overlie the succession (Kositcin et al., 2003).

The age of 3074 ± 6 Ma (Figure 2.1) is for underlying volcanic rocks from the upper Dominion Group and it provides a maximum age constraint for the onset of Witwatersrand Supergroup deposition (Armstrong et al., 1991; Kositcin et al., 2003). The minimum age of the Witwatersrand Supergroup is provided by the age of the overlying Ventersdorp flood basalts that have been dated at 2714 ± 8 Ma (Armstrong et al., 1991; Kositcin et al., 2003; Figure 2.1). The Witwatersrand Supergroup is divided into two groups, namely, the lower West Rand and upper Central Rand Groups. The West Rand Group is divided into the lower Hospital Hill, middle Government, and upper Jeppestown Subgroups (Armstrong et al., 1991; Kositcin et al., 2003). The Central Rand Group unconformably overlies the West Rand Group and is divided into lower Johannesburg and upper Turffontein Subgroups. Subgroups of the Central and West Rand Groups are divided into numerous formations (SACS, 1980; Figure 2.3).

	GROUP	SUBGROUP	FORMATION	LITHOLOGY
WITWATERSRAND SUPERGROUP	Central Rand	Turffontein	Mondeor	Quartzite, Bird Amygdaloid
			Elsburg	
			Gold Estates	
			Robinson	
		Johannesburg	Booysens	
			Krugersdorp	
			Luipaardsvlei	
			Randfontein	Quartzite and conglomerate
			Main	
			Blyvooruitzicht	
	West Rand	Jeppestown	Maraisburg	Quartzite, shale, and conglomerate
			Roodepoort	
			Crown	
			Babrosco	Amygdaloidal lava
			Rietkuil	
			Koesdoeslaagte	
		Government	Afrikander	Shales, quartzites, and conglomerate
			Elandslaagte	
			Palmietfontein	
			Tusschenin	
			Coronation	
			Promise	
		Hospital Hill	Bonanza	
			Brixton	
			Parktown	
			Orange Grove	

Figure 2.3: *Generalized stratigraphy of Central Rand and West Rand Groups of Witwatersrand Supergroup (SACS, 1980; Kositcin et al., 2003).*

West Rand Group

The West Rand Group is about 4.5 km thick and forms the lower portion of the Witwatersrand Supergroup, and it consists mainly of sandstones and shales with rare conglomerates (Barton et al., 1989; Myers et al., 1990). Texturally and mineralogically, the West Rand Group consists of super mature quartz arenites, such as the Orange Grove Quartzite (OG Qtz) Formation (Figures 2.2 and 2.3) that occur at the base of the succession. The sequence of events began with the deposition of the Hospital Hill Subgroup over an extensive area of the Kaapvaal Craton (Myers et al., 1990; Figure 2.3).

Central Rand Group

The Central Rand Group is about 3 km thick and contains mainly sandstones and conglomerates with subordinate shale horizons (Barton et al., 1989). Central Rand Group deposition is considered to have commenced after 2914 Ma (Armstrong et al., 1991; Robb and Meyer, 1995). The Central Rand Group has a minor component of volcanic intercalation called the Bird Amygdaloid (Armstrong et al., 1991). The group hosts more than 90% of all the economic gold-bearing horizons (reefs) mined in the Witwatersrand Basin.

2.3 Ventersdorp Supergroup

The Ventersdorp Supergroup comprises a substantial accumulation of volcanic and metasediments recorded on the Kaapvaal Craton (Armstrong et al., 1991; Van der Westhuizen et al., 1991; Figure 2.4). The development of the Ventersdorp Supergroup on the Kaapvaal Craton was initiated by the outflow of lava of komatiitic affinity during an epoch of crustal extension (Van der Westhuizen et al., 1991). The succession varies considerably in thickness, a maximum of 5.1 km of volcanic and up to 2.9 km of metasediments have been recorded in boreholes (Winter, 1976; Armstrong et al., 1991). The Ventersdorp Supergroup comprises three groups namely the lower Klipriviersberg Group, the middle Platberg Group, and the upper Pniel Group. The Klipriviersberg Group consists of mafic volcanic (Van der Westhuizen et al., 1991) whilst the middle Platberg Group is composed of metasediments deposited in grabens followed by a bimodal volcanic suite with intermixed metasediments and tuff towards the top. The uppermost Pniel Group overlies the Platberg Group with a marked unconformity and consists of an arenaceous unit, followed by a mafic to intermediate volcanic sequence (SACS, 1980; Van der Westhuizen et al., 1991). The Ventersdorp Contact Reef (VCR) occurs at the base of the Ventersdorp Supergroup and is auriferous where it lies unconformably on the

eroded and beveled beds of the Witwatersrand rocks (Rundle and Snelling, 1977; Manzi et al., 2014). The auriferous conglomeratic lithofacies of the Venterspost Formation referred to as the VCR dated at 2729 ± 19 Ma (discordant U-Pb SHRIMP ages) from igneous-detrital xenotime/zircon aggregate (Kositcin et al., 2003; Manzi et al., 2014). The VCR is one of the most extravagant ore horizons in the Witwatersrand Basin (Manzi et al., 2014).

Klipriviersberg Group

The Klipriviersberg Group is subdivided into six formations based on lithological criteria (Figure 2.4). The basal Klipriviersberg Group represents a flood basalt sequence covering an area of more than 30000 km^2 and is up to 2 km thick (Myers et al., 1990; Armstrong et al., 1991; Van der Westhuizen et al., 1991). The succession consists mainly of sub-aerially extruded lava flows. The lava flows are generally amygdaloidal, making the delineation of individual flows simple (Van der Westhuizen et al., 1991).

Platberg Group

The Platberg Group overlies the Klipriviersberg Group unconformably, and it is subdivided into four formations (Figure 2.4). It consists of a very heterogeneous group of rocks including chemical and clastic sediments as well as mafic and acid volcanic (Van der Westhuizen et al., 1991). The Kameeldoorns Formation at the base consists of immature sedimentary materials which were deposited in small grabens (Armstrong et al., 1991; Van der Westhuizen et al., 1991). The volcanic rocks of the Platberg Group comprise a mafic to a felsic bimodal assemblage of lava flows and pyroclastic extrusions which were deposited during graben development (SACS, 1980).

Pniel Group

The Pniel Group overlies the Platberg Group unconformably (SACS, 1980; Van der Westhuizen et al., 1991). The Pniel Group consists of the arenaceous Bothaville Formation at the base and the upper Allanridge Formation. The graywackes of the Bothaville are more mature than those of the Platberg Group (Van der Westhuizen et al., 1991). The Allanridge Formation consists of predominant green amygdaloidal basaltic lava (Winter, 1976; Van der Westhuizen et al., 1991). Allanridge lavas are recognized by their characteristic dark grey-green colour, their apparent freshness, their finely porphyritic texture, and large irregularly shaped white, pink and canmine amygdales in certain flows (Van der Westhuizen et al., 1991).

	GROUP	FORMATION	LITHOLOGY
VENTERSDORP SUPERGROUP	Pniel	Allanridge	Andesitic lava
		Bothaville	Sediments
	Platberg	Rietgat	Lava and Sediments
		Makwassie	
		Goedgenoeg	Quartz feldspar porphyry
		Kameeldoorns	Andesitic lava Sediments
	Klipriviersberg	Edenville	Amygdaloidal and porphyritic lavas with subordinate tuffs
		Loraine	
		Jeannette agglomerate	
		Orkney	Quartzite and conglomerate
		Alberton porphyry	
		Venterspost	

Figure 2.4: *Generalized lithostratigraphy column of the Ventersdorp Supergroup (SACS, 1980; Armstrong et al., 1991; Van der Westhuizen et al., 1991).*

2.4 Transvaal Supergroup

The Transvaal Supergroup comprises a 15 km thick sequence of relatively undeformed/un-metamorphosed clastic and chemical metasedimentary and volcanic rocks of 2550 -2050 Ma (Eriksson et al., 1993; Eriksson et al., 1995; Eriksson and Altermann, 1998).

The Transvaal Supergroup is divided into two groups namely Chuniespoort and Pretoria Groups (Moore et al., 2001; Figure 2.5). At the base of the Transvaal Supergroup, a conglomerate bed is present, the Black Reef Quartzite Formation, that contains minor gold mineralization. A minimum age of 2.642 ± 0.002 Ga is given for this horizon (Eriksson et al., 1995). After this, an approximately 3 km thick succession of argillaceous-arenaceous metasediments of the Pretoria Group was deposited between approximately 2.035 – 2.1 Ga (Walraven and Martini, 1995).

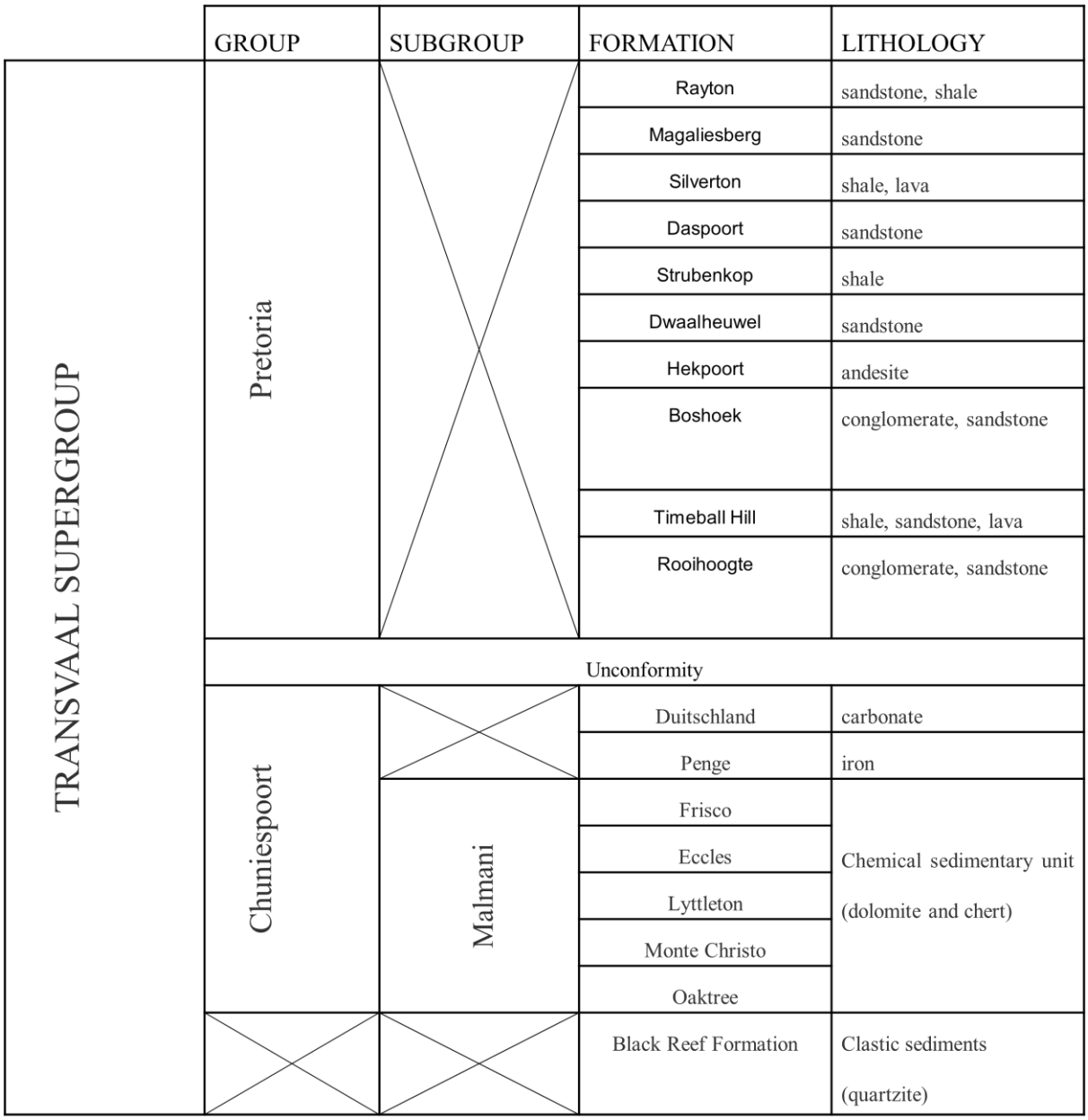


Figure 2.5: *Generalized lithostratigraphy column of the Transvaal Supergroup (SACS, 1980; Jahn et al., 1990; Eriksson et al., 1993).*

Chuniespoort Group

The group contains one of the earliest carbonate successions (limestone $CaCO_3$ and dolomite Ca-$MgCO_3$). The Chuniespoort Group contains more than 1 km thick of dolomite and the total thickness of the Group is up to 2 km. Dolomites and the subsidiary iron formations of the Chuniespoort Group (Walraven and Martini, 1995) were deposited at approximately 2.557 Ga (Jahn et al., 1990). This group only consists of one subgroup, namely, the Malmani Subgroup.

Malmani Subgroup

The Malmani carbonate succession of approximately 1.2 km thick is characterized by predominant dolomites, subordinate limestones, lesser cherts, and minor interbedded shales (Eriksson and Altermann, 1998). The Malmani Subgroup is subdivided into the lowermost Oaktree, and succeeding Monte Christo, Lyttelton, Eccles, and uppermost Frisco Formations. The geometry of the preserved carbonate succession in the Transvaal Supergroup indicates a sheet-like nature for the different formations (Eriksson et al., 1995). The upper dolomite formations in the south and southeast of the preserved Transvaal Supergroup have been removed by erosion; some of this erosion was probably coeval with the deposition of the post Duitschland Formation (Eriksson et al., 1995; Eriksson and Reczko, 1995; Eriksson and Altermann, 1998).

Penge and Duitschland Formations

The Penge Formation overlies the Malmani dolomite sequence gradationally (Eriksson et al., 1993). The Penge Formation is comprised predominantly of micro-to macro-banded iron formations with laterally persistent monomineralic or mixed mineral laminae of quartz, magnetite, hematite, stilpnomelane, riebeckite, minnesotaite, grunerite, and ferruginous carbonate minerals (Button, 1986; Eriksson et al., 1993). The Duitschland Formation contains diamictite, intermediate volcanic rocks, and carbonates, reaching a thickness of 1 km (Martini, 1979; Eriksson et al., 1993). The carbonaceous mudrocks, limestones, and dolomites, with subordinate conglomerates, diamictites, and lavas of the Duitschland Formation, which overlies the Penge Formation unconformably are interpreted as a final, shallow, regressive facies of the Malmani-Penge epeiric sea (Clendenin, 1989; Eriksson et al., 1993).

Pretoria Group

The Pretoria Group overlies the chemical sedimentary rocks of the Chuniespoort Group

unconformably; the unconformity is commonly both angular and Karstic (Button, 1973; Eriksson et al., 1993). The banded iron formation near the top of the chemical sedimentary succession is approximately 2430 Ma of age (Eriksson et al., 1995). The lithostratigraphy of the Pretoria Group comprises a predominant alternation of mud rocks and sandstones, with less critical volcanic horizons and subordinate diamictites and conglomerates (Eriksson et al., 1993). When paired with the alluvial fan and fault-controlled delta palaeo-environments estimated for many of the sandstone's strata, the volcanic solid component of the Pretoria Group raises the idea of fault-controlled or graben basins. (Eriksson et al., 1993; 1995).

The basal Rooihoogte Formation of the Pretoria Group comprises a lowermost chert breccia-reworked conglomerate member, overlain by mud-rocks and an uppermost arenaceous member (Button, 1973; Eriksson et al., 1993). The breccias are mostly *in situ* residual deposits overlying the palaeokarst landscape developed on the Malmani carbonate (Button, 1973). The Timeball Hill Formation consists of basal carbonaceous mud rocks, with micro-algal fossils (Eriksson et al., 1993). The Timeball Hill palaeoenvironment comprised a relatively deep basin, filled by fluvial-deltaic complexes. The diamictites within the upper Timeball Hill mud-rocks and the conglomerate/diamictites of the succeeding Boshoek Formation were correlated by Visser (1971). The diamictite immature sandstone-conglomerate lithologies correlated by Visser (1971), are interpreted as being glacial, glaciofluvial, and glaciomarine deposits. There are no reliable lower age constraints on the Pretoria Group, given that the only direct ages are Rb-Sr whole-rock measurements from the Hekpoort lavas and ‘Pretoria shales’ (2263 Ma) (Hamilton, 1977; Moore et al., 2001).

2.5 Bushveld Complex

The Bushveld Complex is world famous for its abundant deposits of platinum group elements (platinum, palladium, rhodium, osmium, iridium, and ruthenium), as well as other valuable minerals such as chromium, vanadium, and nickel. The PGE-rich layers, known as chromitite layers, are of economic interest. The Bushveld Complex (2.5 – 1.6 Ga) is a large igneous intrusion located in the northern part of the Kaapvaal Craton and occupies a total surface area of ~65 000 km^2 (Hunt, 2006; Cawthorn, 2015; Jones, 2018). The complex is composed of four limbs, namely, the northern, eastern, western and southern limbs (Hunt, 2006). The Bushveld Complex intruded at an unconformity between the Rooiberg Group volcanic rocks and the Transvaal metasediments. The complex consists of three major plutonic

suites (Figure 2.6) – the Rashoop granophyre suite; the Rustenburg layered suite; the Lebowa granite suite (SACS, 1980; Cawthorn and Webb, 2001; Cawthorn, 2015).

Rooiberg Group

The Rooiberg Group is a thick and extensive lava succession, comprising rare basaltic andesite, dacites, rhyolite and tuffs, covering at least 50 000 km^2 (Schweitzer et al., 1995). The Rooiberg group unconformably overlies the Transvaal Supergroup (Kinnaird, 2005; Lenhardt and Eriksson, 2012). The group is associated with four formations: The Dullstroom, Damwal, Kwaggasnek and Schrikkloof formations, with the Dullstroom Formation at the bottom and the Schrikkloof at the top (Kinnaird, 2005; Lenhardt and Eriksson, 2012). Deposition of the Transvaal Supergroup terminated with the eruption of large volumes of volcanic rocks of basaltic andesite to rhyolitic composition that makes up the Dullstroom Formation (Harmer and Farrow, 1995).

Rashoop Granophyre Suite

The Rashoop Granophyre Suite (2061.8 ± 5.5 Ma) occurs as an intrusive sheet into the Rooiberg rhyolites and the Transvaal Supergroup rocks. The granophyre-rhyolite magma is assumed to have formed due to partial melting of the lower crust, likely of granitic composition (Walraven, 1987; Hunt, 2006). Based on textural differences, the Rashoop Granophyre Suite is divided into three units: the Stavoren Granophyre, the Zwartbank pseudogranophyre, and the Rooikop Granite Porphyry (SACS, 1980). Granophyres do not have associated mineralization; however, they frequently operate as traps for mineralizing fluids from the underlying granites.

Rustenburg Layered Suite

Stratigraphically, the Rustenburg Layered Suite is divided into five zones. The Marginal Zone consists mainly of norite with some pyroxenite. The Lower Zone is ultramafic, dominated by pyroxenite, harzburgite, and dunite. The lower part of the Critical Zone is essentially pyroxenite, whereas the upper part is represented by cyclic layers of pyroxenite, norite and anorthosite. The Main Zone is predominantly norite and gabbro, with some layers of anorthosite and pyroxenite (SACS, 1980; Kinnaird, 2005; Hunt, 2006; Figure 2.6). The main units mined for platinum are the UG2 (Upper Group 2) chromitite layer and the Merensky Reef, which occur in the upper part of the Critical Zone in the eastern and western limbs of the complex.

Lebowa Granite Suite

The Lebowa Granite Suite is a 1.5 – 3.5 km thick sheet-like sill intruded between the Rooiberg Group and the Rashoop Granophyre Suite (Kinnaird, 2005) with an aerial extent of some 30 000 km^2. SACS (1980) classified the Lebowa Granite Suite into seven facies, with finer-grained variants breaking through or grading into porphyritic types. The Nebo Granite is predominant; the aplitic Lease Granite and the coarse-grained red Bobbejaankop Granite are widespread facies defined largely on colour and texture, whereas the coarse-grained porphyritic Verena Granite, the porphyritic Balmoral Leucogranite, the coarse-grained, locally porphyritic biotite-rich Makhutso Granite, and the medium-fine grained usually porphyritic Klipkloof Granite of the eastern Bushveld are geographically restricted facies (Wilson et al., 2000; Kinnaird, 2005). The granites of the Lebowa Suite are compositionally predominately alkali feldspar granites with iron-rich ferromagnesian minerals and silical contents (Skursch et al., 2022). The Nebo Granite is the main component of the Lebowa Granite Suite which forms the felsic part of the Bushveld Complex (Wilson et al., 2000; Skursch et al., 2022). The Nebo Granite was emplaced at 2054 ± 1.4 Ma (SACS, 1980).

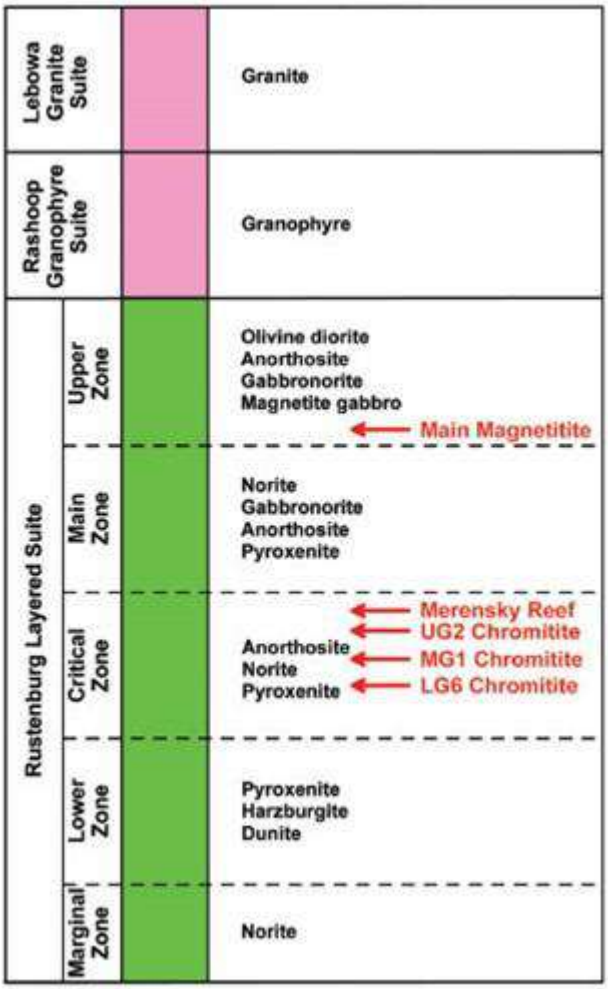


Figure 2.6: *Simplified chronostratigraphic column of the Bushveld Complex (after SACS, 1980; Jones, 2018). Red arrows schematically show the relative position of major ore-bearing layers.*

3. SEISMIC REFLECTION METHOD

3.1 Background

The reflection seismic method encompasses sending elastic waves into the subsurface using an energy source and subsequently, the energy that arrives back at the surface is recorded. The recorded energy is due to reflection, refraction, and diffraction at subsurface boundaries of the waves. These boundaries are interfaces between layers of the Earth that have different acoustic and elastic properties (van Veldhuizen, 2006). Seismic methods can be classified as active or passive. Active seismic method uses artificial sources to send the energy/signal into the Earth's subsurface, while passive seismic methods don't require an artificial source such as vibroseis but use the natural signal/energy. Active seismics is widely employed by the seismic exploration industry in its extensive and detailed studies of the subsurface. The primary aim of seismic exploration is to study geological features such as boundaries of geologic formation, oil and gas resources, and mineral deposits (Keydars et al., 2018). Seismic surveys can either be acquired in 2D or 3D. 2D seismic surveying is acquired with a single line of receivers and shot points. In 3D surveying, data is acquired with a large array of seismic receivers and an array of shot points. It is generally known that 3D seismic data are more expensive to acquire than 2D seismic data (Spitzer et al., 2001; Schmelzbach et al., 2007; Onyebueke et al., 2018).

The seismic method can be applied for both shallow subsurface investigation and for deep targeting of geological structures. In shallow subsurface exploration, seismic techniques are employed to examine the upper layers of the Earth's crust, typically within a depth range of a few meters to a few hundred meters. Onyebueke (2018) showed that shallow reflection seismics differ from the deep reflection seismics used in mineral exploration and hydrocarbons with respect to their energy sources, source-receiver geometries, and the number of receivers deployed. For example, the energy source for shallow reflection surveys includes weight drop systems and sledgehammers, while for deep reflection seismic surveys vibroseis and explosives are commonly used as energy sources. By deploying powerful seismic sources and sensitive receivers, researchers can map the intricate layering, fault systems, and subsurface rock properties associated with oil reservoirs, mineral deposits, and tectonic plate boundaries.

Types of seismic waves

Seismic waves are classified into two main groups, namely body waves, and surface waves. Body waves consist of two subgroups namely primary waves (P-waves), which are

faster than surface-waves and their motion is the same as that of a sound wave (Kearey et al., 2002; Rogers, 2015; Figure 3.1a), and another type of body wave is secondary or shear wave (S-wave), which is slower than P-waves. During propagation, S-waves shear the rock sideways at right angles to the direction of travel (Figure 3.1b). S-waves cannot propagate in the liquid parts of the Earth (Anderson et al., 1998; Rogers, 2015).

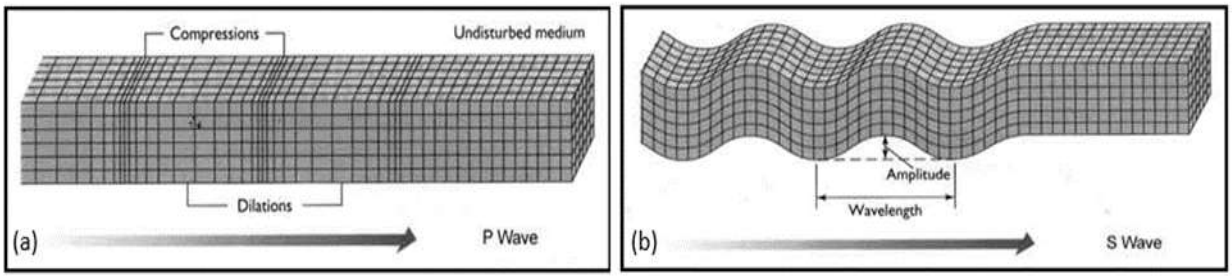


Figure 3.1: *An illustration of Body waves. (a) Primary wave motion; (b) Secondary or Shear wave motion (Anderson et al., 1998; Rogers, 2015).*

Surface waves are restricted to near-the-ground surface motion. Surface waves are divided into two subgroups: Rayleigh and Love waves (Kearey et al., 2002). Rayleigh waves move both vertically and horizontally more like rolling ocean waves in a vertical plane pointed in the direction in which the waves are traveling (Rogers, 2015; Figure 3.2a). The Love waves are essentially S-waves that have no vertical displacement, they move the ground from side to side in a horizontal plane but at right angles to the direction of propagation (Figure 3.2b). Surface waves travel more slowly than Body waves (P-waves and S-waves) (Kearey et al., 2002).

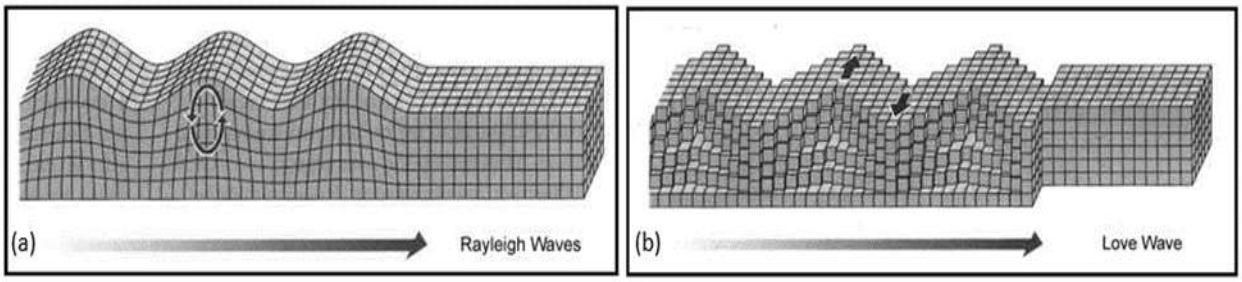


Figure 3.2: *An illustration of Surface waves. (a) Rayleigh wave motion; (b) Love wave motion (Rogers, 2015).*

Density and elasticity affect the velocity at which Primary waves (P-waves) and

Secondary or Shear waves (S-waves) travel. We can represent the velocity of P-waves and S-waves mathematically as follows:

$$V_P = \sqrt{\frac{K+\frac{4}{3}\mu}{\rho}} \quad (1)$$

and

$$V_S = \sqrt{\frac{\mu}{\rho}} \quad (2)$$

where V_P is the P-wave velocity, V_S is the S-wave velocity, K is the bulk modulus, ρ is the density of the rock, and μ is the shear (rigidity) modulus (Anderson et al., 1998; Kearey et al., 2002).

3.2 Seismic modeling

Seismic modeling is one of the foundations of geophysical data processing. Seismic modeling is a technique of simulation of a recorded seismic wavefield, seismic amplitudes, or seismic traveltimes (Yilmaz, 2001; Carcione et al., 2002). The goal is to anticipate the seismogram with a set of sensors that would record, given an expected subsurface structure. This technique is a significant tool for seismic interpretation and an essential part of seismic inversion algorithms. The evaluation and design of seismic surveys is another important application of seismic modeling. There are three main categories of seismic modeling, namely, (1) ray-tracing methods, (2) direct methods, and (3) integral-equation methods.

Ray tracing methods

Ray tracing or asymptotic methods are frequently used in seismic modeling and imaging. These approaches are approximate because they don't consider the entire wavefield. However, they may be the most effective numerical simulation methods (Gebrande, 1976). The increase in computer CPU time can be significant, particularly for large, three-dimensional models. According to these techniques, the wavefield is seen as an ensemble of specific events, each arriving at a specific time (traveltime) and having a specific amplitude. Asymptotic approaches have been extremely useful in seismic imaging based on the Born approximation for heterogeneous reference velocity models because of their effectiveness. The modeling and identification of individual events on seismic recordings is a significant use of these techniques

(Gebrande, 1976; Cerveny, 1987). Green's functions relate the source (seismic energy release) and the receiver (seismic sensor) to the observed wavefield.

Green's function describes a spherical wavefront that propagates at speed c_0. A first-time disruption of the medium at $t = 0$ and $x = x_s$, expanding in space as time passes, at time t, it arrives at the sphere $|x - x_s| = c_0 t$ (Carcione et al., 2002). The function

$$\varphi(x, x_s) = |x - x_s|/c_0 \tag{3}$$

measures the time needed for the disturbance to travel from source x_s to the point x and it's called the travel time function. The amplitude of the disturbance is given by:

$$A(x, x_s) = \frac{1}{4\pi|x - x_s|} \tag{4}$$

With Equations 3 and 4, we can rewrite the Green's function for a constant velocity medium as:

$$G(x, x_s, t) = A(x, x_s)\delta(t - \varphi(x, x_s)) \tag{5}$$

The temporal Fourier transform of the Green's function is denoted by $G(x, x_s, \omega)$, and for a constant velocity case is given by:

$$G(x, x_s, \omega) = A(x, x_s)e^{i\omega\varphi(x, x_s)} \tag{6}$$

The velocity typically changes with position x. This is mostly brought on by changes in geological formations or lithologies, but there are other causes as well, such as variations in pressure or fluid content of the rocks. It can be demonstrated that $G(x, x_s, \omega)$ continues to take the form of Equation 6, where $\varphi(x, x_s)$ and $A(x, x_s)$ are general traveltime and amplitude functions, respectively, in the limit $\omega \to \infty$ (thus the name asymptotic). In the heterogeneous situation, the wavefront is no longer spherical.

Direct methods

To solve the wave equation by direct methods, the geological model is approximated by a numerical mesh – the model is discretized in a finite number of points. These techniques are also known as grid methods and full-wave equation methods (Carcione et al., 2002). Direct methods have no constraints on material variation and can be quite accurate when a small enough grid is utilized. Furthermore, the technique can handle the implementation of various rheologies and is well-suited for the generation of snapshots, which can be useful in interpreting the results. The disadvantage of these generic methods is that they can be more expensive in terms of computer time than analytical and ray methods. The method is classified into five main aspects of the modeling, namely, (1) time integration, (2) calculation of spatial derivatives, (3) source implementation, (4) boundary conditions, and (5) absorbing boundaries.

The wave equation's numerical solution necessitates the discretization of the time variable using finite differences (FD). The fundamental idea behind FD techniques is to substitute partial derivatives with approximations based on Taylor series expansions of functions close to the point of interest. Forward and backward difference time derivative approximations (Smith et al., 1985; Carcione et al., 2002) result in explicit and implicit FD methods, respectively. In circumstances when the accuracy requirements are relatively low, finite differences are simple to program and efficient when compared to other techniques. In this regard, a second-order in-time and fourth-order in-space FD algorithms may be a reasonable choice. When staggered differential operators are utilized, pseudo-spectral approaches can be more expensive in some circumstances, but they ensure good accuracy and significantly lower background noise (Carcione et al., 2002). These operations are also appropriate when there are considerable fluctuations in Poisson's ratio in the model (for example, in a fluid-solid interface). In three dimensions, pseudo-spectral algorithms use the fewest grid points and can be the best option when computer capacity is restricted. The finite element (FE) approach is the best algorithm for modeling surface topography and curved interfaces. However, for large variations in the Poisson's ratio, FE methods may prove unstable (Carcione et al., 2002).

Integral-equation methods

Integral equation methods are based on wavefield integral representations. Green's function is used in these representations to account for wave propagation in the embedding medium. When compared to direct methods, these methods can be relatively efficient for

specific geometries (such as boreholes or other boundaries, media containing cracks, and inclusions of bounded extent). The reason for this efficiency is that the number of unknown functions to be determined is limited.

The integral-equation method can be formulated by first considering Huygens' principle which states that the wavefield originating from a light source such as a flame can be considered as a superposition of waves due to point sources located in the flame (Figure 3.3).



Figure 3.3: *An illustration of Huygens' principle - the superposition of elementary waves (after Russer and Russer, 2015).*

Mathematically, we consider the scalar wave equation for a homogeneous medium (i.e., with constant density and constant speed of sound $c = c_0$),

$$\left(\nabla \cdot \nabla - \frac{1}{c_0^2}\frac{\partial^2}{\partial t^2}\right) p = -q, \tag{7}$$

where ∇ is the gradient operator, p is the pressure, c is the compressional-wave velocity, $q = c_0^{-2} f$, and f is the body force.

The integral representation for this scalar wave equation is given by (Carcione et al., 2002):

$$p(x,t) = \int G(x, x_s, t - t')\, q(x_s, t') dx_s dt' \tag{8}$$

where x is the position vector. Since the velocity is constant, the Green's function G is given by:

$$G(x, x_s, t) = \frac{\delta(t-|x-x_s|/c_0)}{4\pi|x-x_s|} \quad (9)$$

The Green's function is the medium's response to a point source and satisfies the wave Equation (7) for a point source given by $q = \delta(x - x_s)\delta(t)$. If Equation 9 is substituted into Equation 8, the integral representation is obtained (Carcione et al., 2002):

$$p(x,t) = \int_D \frac{q(x_s,\ t-|x-x_s|/c_0)}{4\pi|x-x_s|} dx_s \quad (10)$$

where D is the region in space where the source term q is present. Equation 10 is the mathematical formulation of Huygens' principle illustrated in Figure 3.3. The integration is a summation over volumetric wave field densities, $q/4\pi|x - x_s|$.

3.3 Acquisition

In the seismic reflection method, the down-going wave field is generated by seismic sources (common seismic sources are sledgehammer, accelerated weight drop, and vibroseis) at the surface, and detectors (geophones) (van Veldhuizen, 2006) measure the upcoming wave fields. Typical parameters required are the minimum and maximum distance between source and receiver, and the spacing between neighboring sources and receivers. Parameters like these determine the range of depths and dips that can be imaged, and they influence the feasibility of velocity estimation and attenuation of multiple reflections. Some of the main seismic acquisition parameters are shown as an example in Table 3.1 for profiles OK-212 and OK-213, and they are presented in chapter 6.

Table 3.1: *Example of main seismic acquisition parameters (after Mutshafa et al., 2022) for profiles OK-212 and OK-213, which are presented in chapter 6.*

Survey parameters	Profile 1	Profile 2
Type of survey	2D	2D
Year	1988	1988
Profile length	16.9 km	15.7 km
Trend	S-N	N-S

Spread	2975–25–X–25–2975 (m)	2975–25–X–25–2975 (m)
Nominal fold	25	25
Average fold	37	38
Recording system		
Recording device	CS2502 SN368	CS2502 SN368
Sampling rate	4 ms	4 ms
Recording length	6 s	6 s
Sweep length	18 s	18 s
Sweep frequencies	8 – 62.5 Hz	8 – 62.5 Hz
Source information		
Source spacing	100 m	100 m
Source type	4 VIBS/8ws/vp	4 VIBS/8ws/vp
Receiver information		
Receiver spacing	50 m	50 m
Geophone type	10 Hz (SM4)	10 Hz (SM4)

Acoustic impedance and reflection coefficient

The seismic reflection method looks at an elastic wave reflected off the subsurface layers and gets information about the subsurface from the amplitude and shape of the wave (Burger, 1992). The seismic wave reaches the boundary between two layers with different acoustic impedance, then some waves get to be reflected on the surface where they are recorded. The acoustic impedance is given by:

$$Z = \rho v \tag{11}$$

Where, ρ is the density and v is the velocity (Kearey et al., 2002).

The ratio of the amplitude of a reflected wave to that of the incident wave is termed the Reflection coefficient (RC) (Sheriff, 2002; Zhang et al., 2015). The Reflection coefficient can be derived from the acoustic impedance, where the Reflection coefficient is given by:

$$RC = \frac{Z_2 - Z_1}{Z_2 + Z_1};\ -1 \leq R\ \leq +1 \tag{12}$$

where a negative value for RC indicates a phase change of 180° in the reflected ray, RC = 0 implies all the incident rays are transmitted (i.e. no contrast of acoustic impedance at the boundary), and RC = 1 implies the incident ray is reflected (Kearey et al., 2002; Figure 3.4).

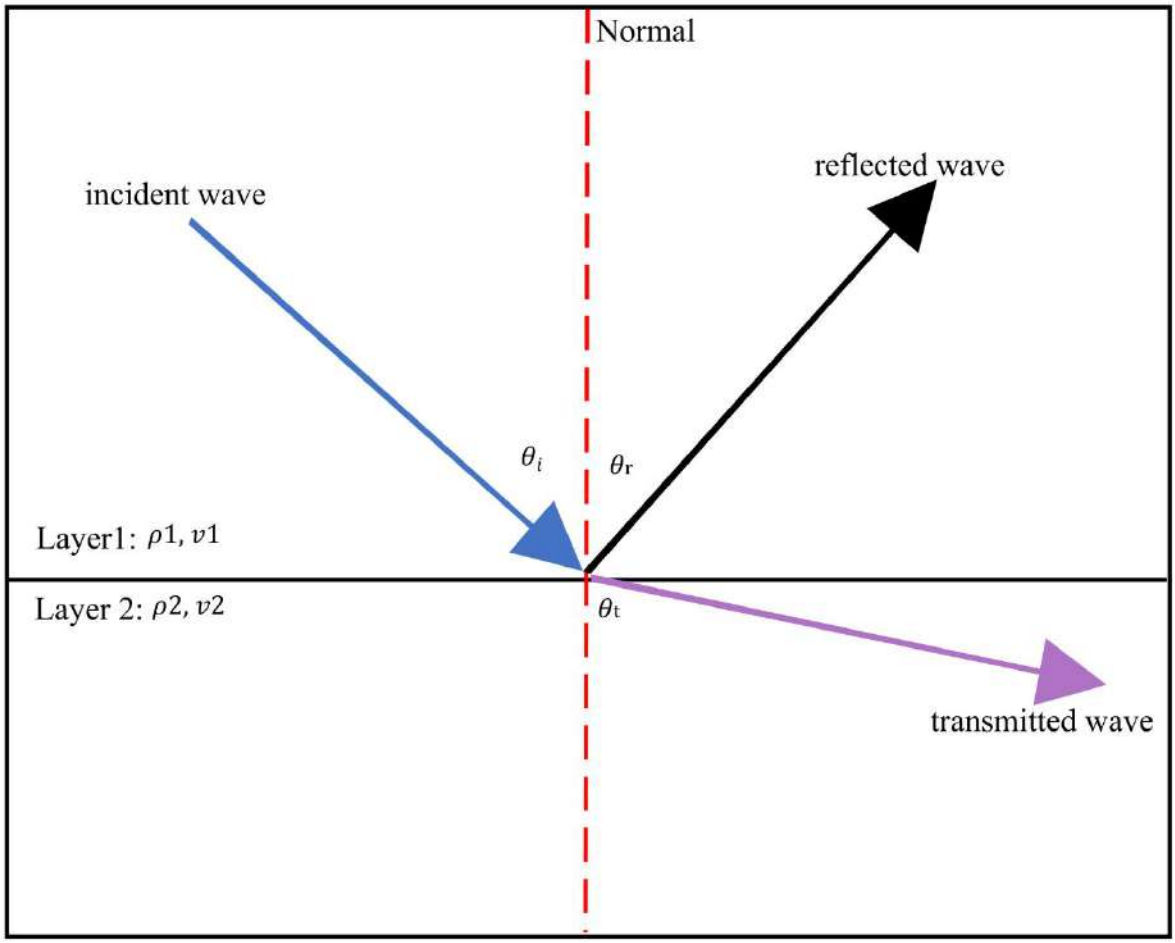


Figure 3.4: *Illustration of an incident wave being reflected and transmitted at the boundary where the angle θi = θr (angle of the incident wave is equal to the angle of the reflected wave) (modified from Dukhin and Goetz, 2010). Additionally, the angle θt is governed by the difference between v1 and v2 and a larger difference results in a 'flatter' transmitted wave.*

Bin size

A bin is a subdivision of a seismic survey. The area of the survey is divided into bins, which are commonly on the order of 25 m long and 25 m wide (Hardage, 1997). Traces are assigned to specific bins according to the midpoint between the source and the receiver reflection point. The bin size can be determined by developing a stratigraphic model of the target that is to be imaged and then using that model to define the narrowest feature that needs

to be seen. Once the minimum target is defined, stacking bins with lengths and widths that are approximately one-fourth of the minimum target width must be created if the target is to be recognized in a 3D data volume (Ebrom et al., 1995; Hardage, 1997). Ebrom et al (1995) showed that halving the bin size will quadruple the number of stacked traces (assuming square bins), so there is a considerable economic incentive to make the bins as large as possible.

Seismic resolution

The seismic resolution is the ability to distinguish two features or points from one another (Kallweit and Wood, 1982; Yilmaz, 2001). There are two types of seismic resolution namely, vertical and horizontal. Vertical resolution is the ability to differentiate between two closely separated layers at different depths while horizontal resolution recognizes two lateral displaced features on the single interface (Kallweit and Wood, 1982).

Aspects that control seismic resolution are velocity, frequency, and wavelength. Seismic waves that travel to great depth will result in a decrease in frequency and their velocity and wavelength will increase (Yilmaz, 2001; Rost and Thomas, 2009; Mondol, 2010). As the frequency decreases, the seismic resolution will also decrease. At great depths, low frequency waves and thus lower resolution prevails, whereas, at the shallow depths where high frequencies dominate high resolution is experienced and the attenuation in frequency is to a large extent controlled by the geology (Yilmaz, 2001; Chopra et al., 2006).

The Widess Model represents the relationship between the wavelength and bed thickness (Widess, 1973). The thickness of the bed model is resolvable where the wavelength is equal or greater than $\lambda/4$. If the bed's wavelength is thinner, there is no distinct reflection, and the vertical resolution is limited (Widess, 1973; Chopra et al., 2006). The resolution limit is the minimum separation distance that indicates that there is more than one interface (Sheriff, 2002). Widess (1973) proposed $\lambda/8$ as the resolution limit of the data with high signal-to-noise ratio, λ being the dominant wavelength in the data. In the presence of noise, this resolution is usually taken to be only $\lambda/4$. One of the methods to resolve thin beds is to increase the frequency during acquisition (e.g., using a broadband seismic source) and processing of the data since the wavelength depends on the velocity and frequency and is given by:

$$\lambda = \frac{v}{f} \tag{13}$$

where v is the velocity and f is the dominant frequency (Widess, 1973; Yilmaz, 2001; Chopra et al., 2006).

The horizontal resolution is much poorer when compared to the vertical resolution. The

poorer resolution is due to a focusing issue and as a result, energy does not return from the single reflection point as it creates a finite region of the point that influences the reflection (Chopra et al., 2006). This region that reflects the energy has a phase difference of one half-cycle and this energy creates constructive interference. This region is called a Fresnel zone (Figure 3.5) from which most of the energy of a reflection is returned but the arrival times differ by less than half a period from a first break. If the returned wavelength is larger than $\lambda/4$, the zone where the energy was reflected is also larger, and subsequently then the resolution is lower (Nanda, 2016). The Fresnel zone defines the horizontal resolution of the seismic signal at a certain depth and the Fresnel zone must be wider than $\lambda/4$ to be detected.

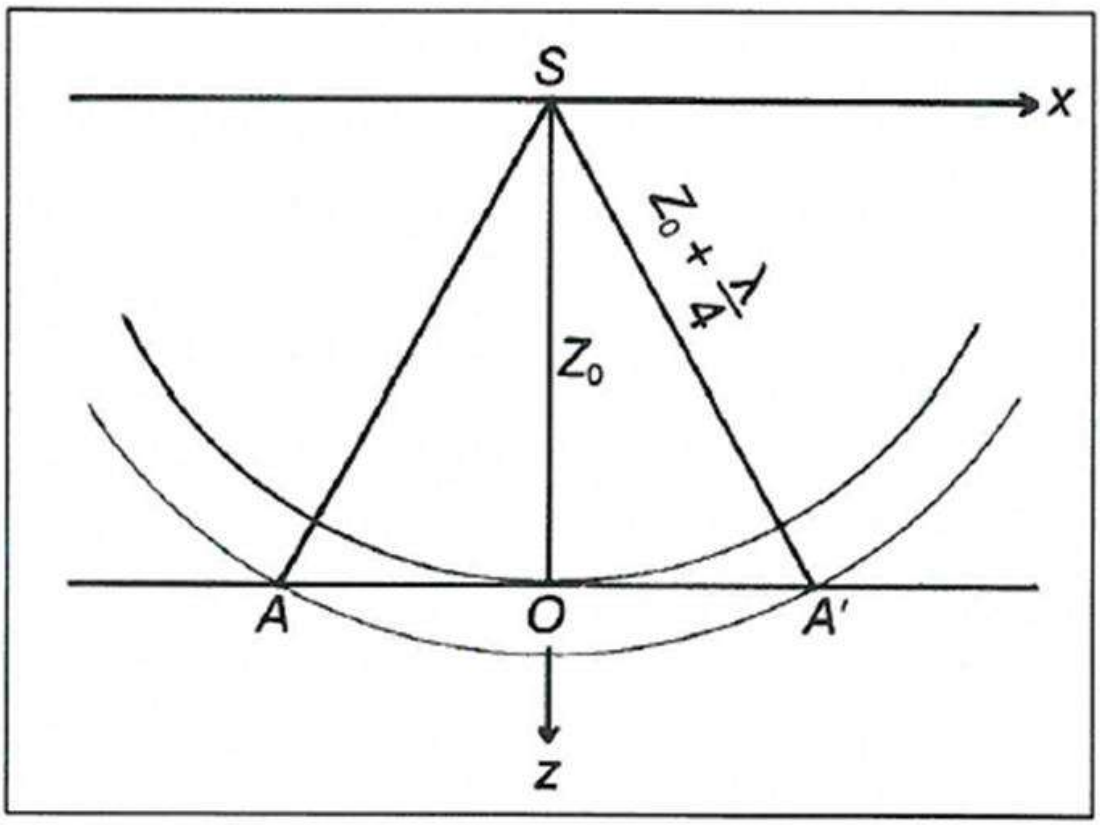


Figure 3.5: *An illustration of the Fresnel zone (A – A') where Z_0 is the reflection depth, λ is the dominant frequency and S is the source (Yilmaz, 2001; Nanda, 2016).*

Fresnel zone radius can be calculated by solving for R (Figure 3.5– OA' or OA), using Pythagorean Theorem:

$$\left(Z_0 + \frac{\lambda}{4}\right)^2 = {Z_0}^2 + R^2 \tag{14}$$

where Z_0 is the reflection depth and λ is the dominant frequency.

Horizontal resolution depends not only on the Fresnel zone but also on the type of boundary between two different types of geological layers. The boundary with a width less than λ/4 cannot be resolved thus defining the limit for resolution (Nanda, 2016). The Fresnel zone is small at a shallow depth but gradually increases to a greater depth. Resolution can be enhanced during the acquisition by deploying a broadband wavelet as a source and by recording with smaller sample intervals (~2 ms) (Chopra et al., 2006; Nanda, 2016).

3.4 Processing

The objectives of seismic data processing are (1) to suppress incoherent and coherent noise (Manzi et al., 2012a), (2) to remove unwanted waveforms from the field data, (3) to isolate and enhance pure primary reflection events, (4) to enhance weak reflection events by adding together individual recordings to produce a final stacked seismic section, (5) to remove the effects of land surface topography and other geometrical artifacts by the processes of migration to migrate seismic reflections to their true positions in time and space, and (6) to produce the best possible image of the subsurface (Brabham et al., 2005; Manzi et al., 2012a). Some of the processing sequence/steps that are followed in the reflection seismic method are shown in Figure 3.6, and they are taken from profiles OK-212 and OK-213 of chapter 6.

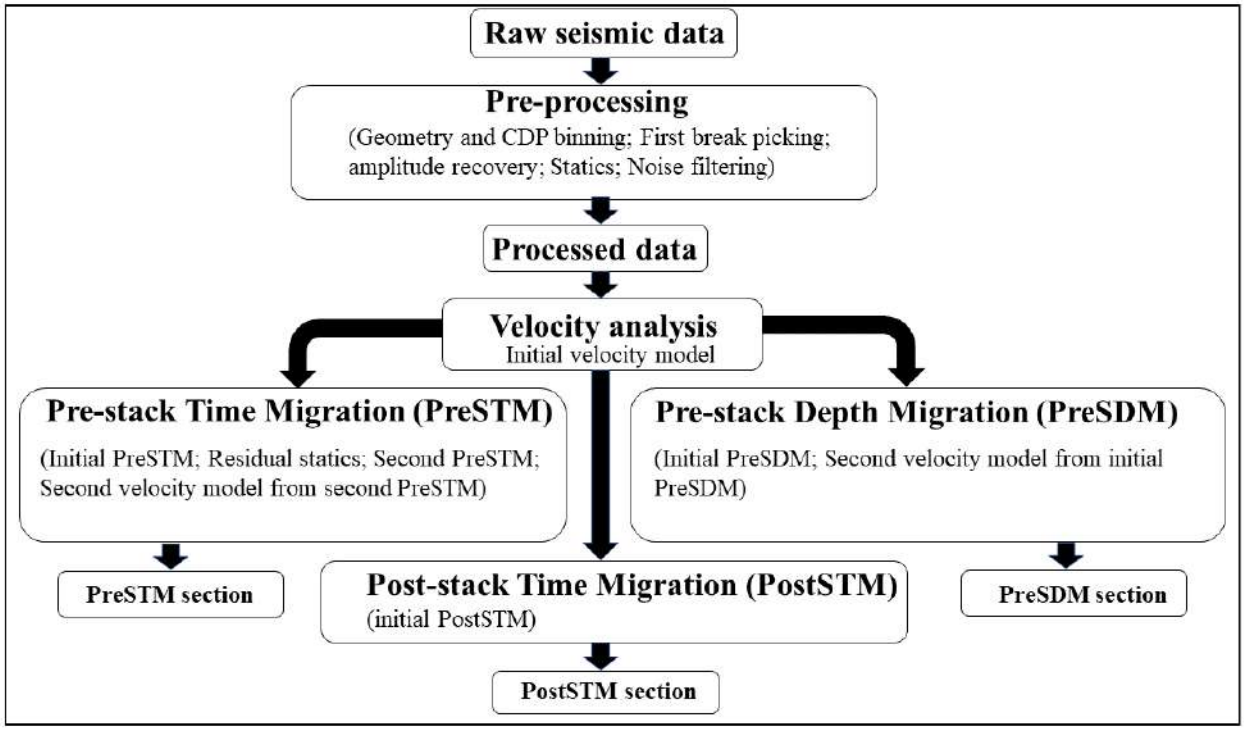


Figure 3.6: *Example of seismic reflection processing workflow used for profiles 1 and 2 presented in chapter 6 (Table 3.1; Mutshafa et al., 2022).*

Geometry set-up

Before the reprocessing of the legacy reflection seismic data, the data must undergo preliminary preparation. This is due to the possibility that the method in which the legacy data were kept does not adhere to the present standard of procedure and may cause problems when processing with modern processing programs. The legacy seismic data must thus be examined and modified before processing. For example, certain trace headers could be kept somewhere other than the contemporary norm outlined by Hagelund and Levin (2017). The trace headers must thus be carefully examined and, if required, manually edited. For example, using a seismic profile from Paper II (chapter 7), it was observed that the trace headers from the raw legacy data had no receiver and source height (REC_HT and SOURCE_HT = 0), while the x coordinates of the source and receiver were wrong (REC_X and SOURCE_X) (see Figure 3.7

highlighted by red outline). The Shuttle Radar Topography Mission (SRTM) data from the United States Geological Survey (USGS) was downloaded to get the elevation of source and receiver.

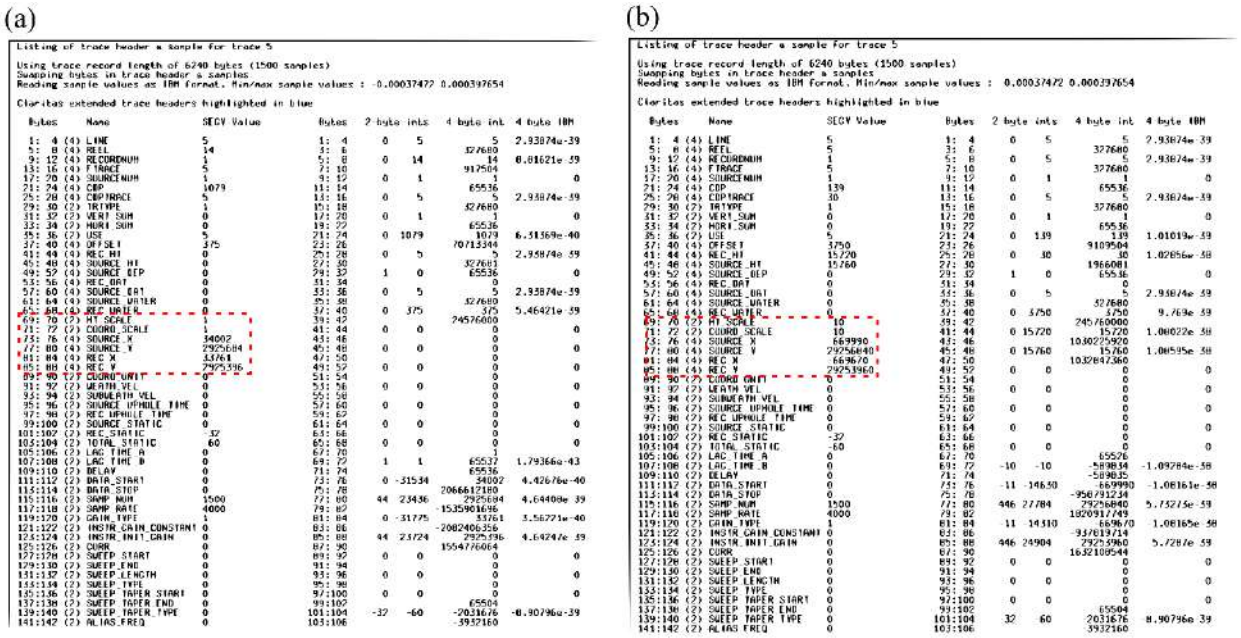
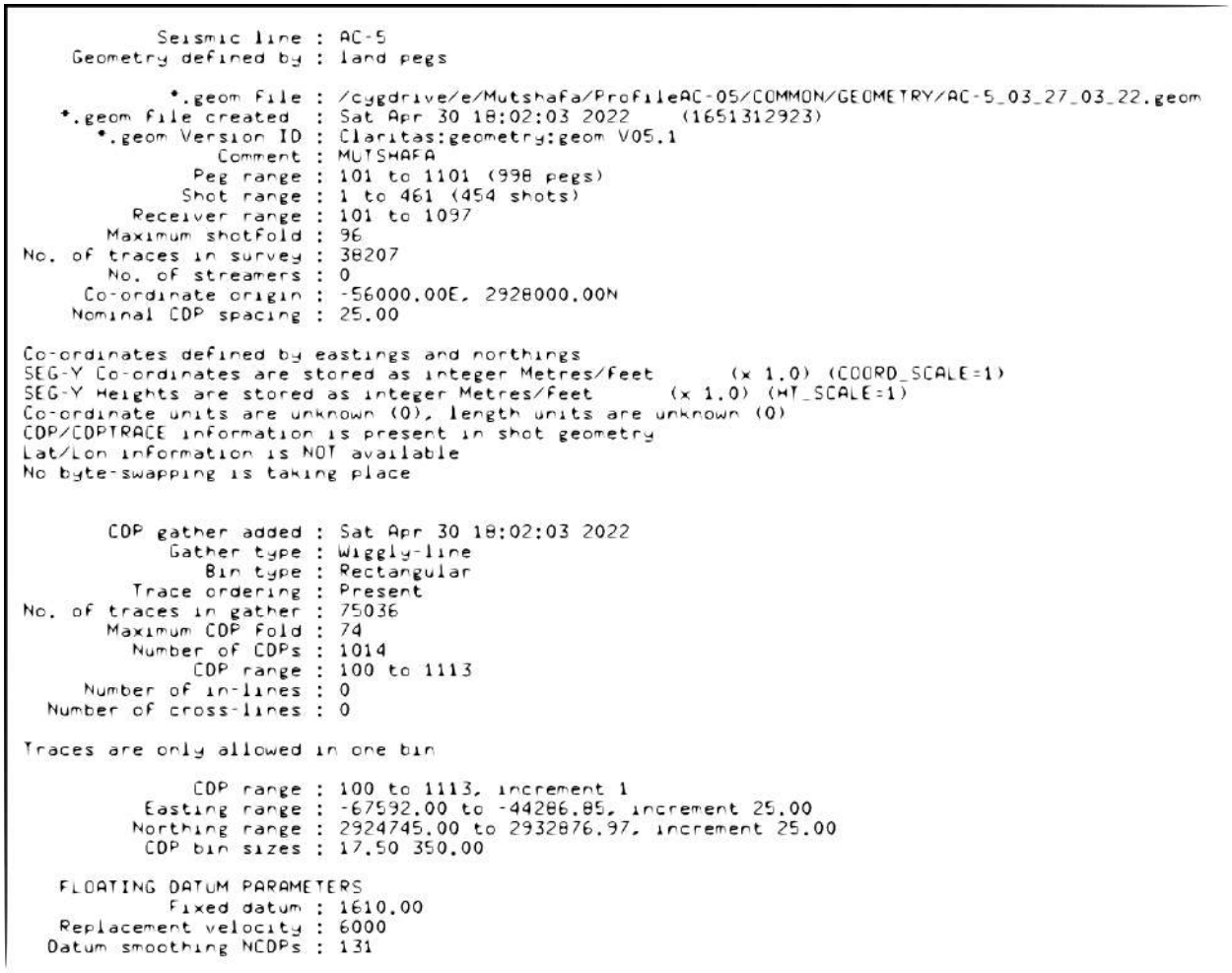


Figure 3.7: *List of headers information from profile AC_05 (chapter 7). (a) Trace from raw legacy data, and (b) trace from legacy data after reassigning the x coordinates of the source and receiver and assigning their elevation.*

Once the trace header information for the legacy profile is fixed and corrected, the geometry is created. The geometry of each profile is verified and if it is correct (Figure 3.8), the geometry is merged with the SGY seismic data.



```
          Seismic line : AC-5
    Geometry defined by : land pegs

           *.geom file : /cygdrive/e/Mutshafa/ProfileAC-05/COMMON/GEOMETRY/AC-5_03_27_03_22.geom
   *.geom file created  : Sat Apr 30 18:02:03 2022     (1651312923)
     *.geom Version ID : Claritas:geometry:geom V05.1
               Comment : MUTSHAFA
             Peg range : 101 to 1101 (998 pegs)
            Shot range : 1 to 461 (454 shots)
        Receiver range : 101 to 1097
       Maximum shotfold : 96
No. of traces in survey : 38207
       No. of streamers : 0
     Co-ordinate origin : -56000.00E, 2928000.00N
    Nominal CDP spacing : 25.00

Co-ordinates defined by eastings and northings
SEG-Y Co-ordinates are stored as integer Metres/Feet       (x 1.0) (COORD_SCALE=1)
SEG-Y Heights are stored as integer Metres/Feet       (x 1.0) (HT_SCALE=1)
Co-ordinate units are unknown (0), length units are unknown (0)
CDP/CDPTRACE information is present in shot geometry
Lat/Lon information is NOT available
No byte-swapping is taking place


       CDP gather added : Sat Apr 30 18:02:03 2022
            Gather type : Wiggly-line
              Bin type : Rectangular
         Trace ordering : Present
No. of traces in gather : 75036
       Maximum CDP fold : 74
         Number of CDPs : 1014
              CDP range : 100 to 1113
     Number of in-lines : 0
  Number of cross-lines : 0

Traces are only allowed in one bin

              CDP range : 100 to 1113, increment 1
          Easting range : -67592.00 to -44286.85, increment 25.00
         Northing range : 2924745.00 to 2932876.97, increment 25.00
          CDP bin sizes : 17.50 350.00

   FLOATING DATUM PARAMETERS
            Fixed datum : 1610.00
   Replacement velocity : 6000
  Datum smoothing NCDPs : 131
```

Figure 3.8: *Quality control check of the geometry set-up. Example from the legacy profile in Paper II (chapter 7).*

Velocity analysis

To get high-resolution images of the subsurface, velocity analysis should be carried out. Velocity verification can be done on either common shot gathers data or common midpoint data (Anderson et al., 1998). The common midpoint (CMP) is the point where different traces reach the same point. The velocity analysis is derived from the selected CMP gathers, which are the group of reflection seismic events with the same midpoints between a receiver (g) and source (s) (Manzi, 2014; Figure 3.9).

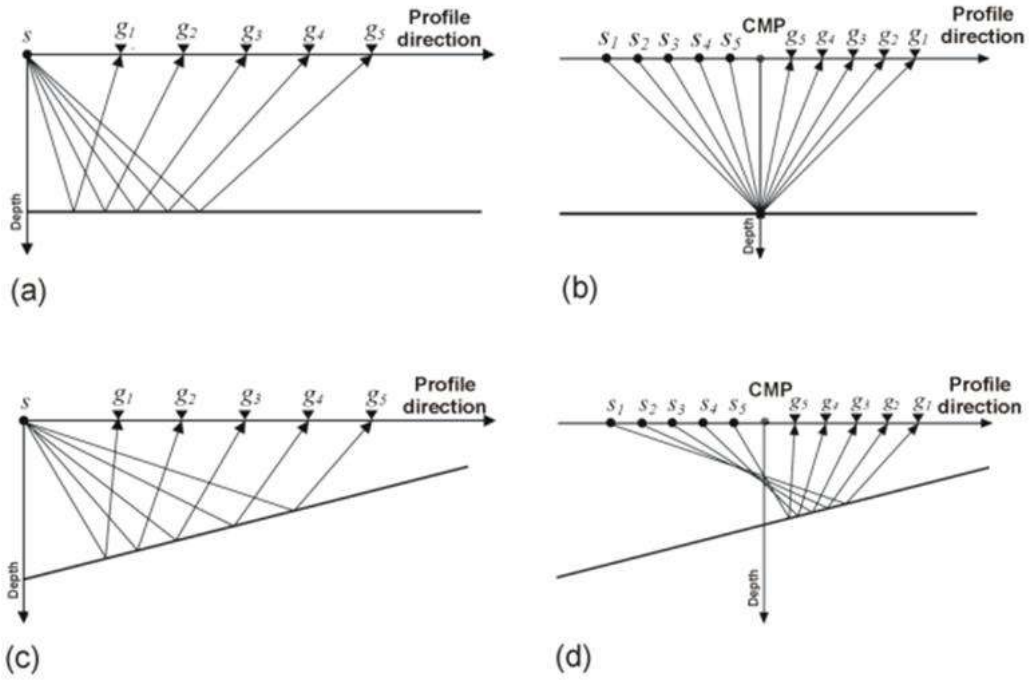


Figure 3.9: *Seismic survey geometry. (a) Horizontal layer with multiple receivers (g) and single source (s), (b) Common midpoint (CMP) gather for a horizontal layer, (c) Dipping layer with a single source and multiple receiver/geophones, (d) Common midpoint gather for dipping layer. The seismic wave travels from the source (s) to the subsurface reflector and is reflected in the geophones/receivers (g) where it is recorded (Manzi, 2014).*

After the CMP is located and sorted, then a Normal Move-out (NMO) correction is applied. An NMO is a time correction that is done on a reflection time section which moves traces to their correct position (Sheriff, 2002; van der Kruk, 2005). The NMO allows all the traces to be moved to the same level (Figure 3.10). The CMP traces are then stacked to improve the signal-to-noise ratio (Yilmaz, 2001; Manzi, 2014).

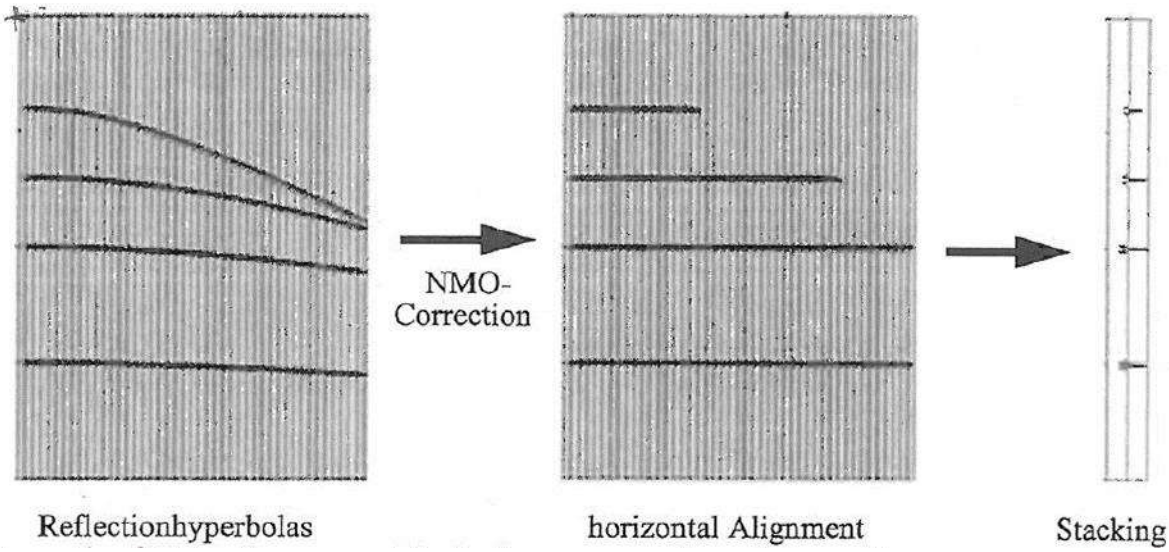


Figure 3.10: *A representation of the Normal Move-out correction principle. For a horizontal stratification, an averaged velocity termed the 'root mean square' (V_{RMS}) is the correct velocity and not a linearly averaged velocity over depth or transit time, and the V_{RMS} is stacked (van der Kruk, 2005).*

An approximation of the velocity analysis enables the flattening of the hyperbolic events and provides the best possible result when the seismic reflections are stacked. Yilmaz (2001) defined the approximation of a hyperbolic travel-time curve as:

$$t^2(h,V) = {t_0}^2 + \frac{4h^2}{V^2} \tag{15}$$

where t is the two-way travel time, V is the velocity of the layer, t_0 is the observed two-way travel time at zero-offset, and h is the half-offset (distance between the receiver and a source) defined by $(s+g)/2$, where s and g are a source and a receiver respectively.

Stacking involves velocity stacks of the traces in a CMP gather with a range of constant velocities by picking the velocity that provides the best lateral continuity of the reflection event (Yilmaz, 2001; Manzi, 2014). The hyperbolic approximation formula for the stacking velocity as derived from Equation 15 is given by:

$$t^2(h,V_{stk}) = {t_{0\,stk}}^2 + \frac{4h^2}{{V_{stk}}^2} \tag{16}$$

where V_{stk} is the stacking velocity, t is the stacking path, $t_{0\,stk}$ is the two-way zero-offset time associated with the best-fit hyperbola, and h is the distance between the source and a receiver.

Migration

Migration moves dipping reflections to their true sub-surface positions; collapses diffractions and increases spatial resolution (Yilmaz, 2001; Ristow et al., 2003; Gray, 2016; Crutchley and Kopp, 2018; Wadas, 2018). After migration, Yilmaz (2001) observed that migration (1) shortens dipping reflectors, (2) steepens reflectors, and (3) moves reflections in the up-dip direction and unties bowties on the stacked section and turns them into synclines. The goal of migration is to make the stacked section appear like the geologic cross-section in depth along a seismic traverse. Migration techniques can be applied either, in time or the depth domain, pre-stack or post-stack migration (Yilmaz, 2001; Manzi, 2014).

Migration algorithms

Migration of seismic data requires strategies concerning the type of migration algorithm, appropriate parameters for the algorithm, and migration velocities (Yilmaz, 2001; Cameron et al., 2008; Cocher et al., 2017). Migration strategies may include the following (see Figure 3.11):

(1) 2-D versus 3-D migration,

(2) Post- versus pre-stack migration, and

(3) Time versus depth migration.

Type of migration		Case
Time	time migration	dipping events
	prestack migration	conflicting dips with different stacking velocities
	3D migration	3D behavior of fault planes and salt flanks
Depth	depth migration	strong lateral velocity variations associated with complex oveburden structures
	prestack migration	complex nonhyperbolic moveout
	3D migration	3D structures

Figure 3.11: *Examples of migration strategies (modified from Yilmaz, 2001).*

Migration algorithms are classified into three main categories:

(1) Algorithms based on integral methods (Kirchhoff migration),

(2) Algorithms based on differential methods (finite-difference migration), and

(3) Algorithms implemented in the F-K domain (frequency-wavenumber migration).

The Kirchhoff migration

The diffraction summation that incorporates the obliquity spherical spreading and wavelet shaping factors is called the Kirchhoff summation (Yilmaz, 2001; Fu, 2002; Nainggolan and Subarsyah, 2014). The Kirchhoff migration method is relatively cheaper than finite-difference migration and has been used in the oil and gas industry for time and depth imaging (Sheriff, 2002; Manzi, 2014). The Kirchhoff migration can handle all dips up to 90 degrees but is unable to handle lateral velocity variations (Yilmaz, 2001). The method is non-recursive and makes use of the Kirchhoff integral equation given by:

$$u(r,t) = \frac{1}{2\pi}\int dt_0 \int \frac{dA_0 cos\beta}{r}\left[\left(\frac{1}{V}\right)u'(r_0,t_0) + \left(\frac{1}{r}\right)u(r_0,t_0)\right] \qquad (17)$$

where $t_0 = t - \left(\frac{r}{V}\right)$ is the travel time at zero-offset, A_0 is the amplitude of the wave at the source (zero-offset), V is the interval velocity, β is the angle dependent on the amplitude of the wave, r and r_0 is the distance traveled by the wave and the length of the wave at the source respectively.

In Kirchhoff migration, the diffraction hyperbola collapses when summing the amplitudes, and then placing them at the apex. The algorithm then sums all data values along a diffraction that is centered on each point on the output migrated section. Migration aperture width is the critical parameter in Kirchhoff migration, e.g., a small aperture width causes the destruction of steeply dipping events and rapidly varying amplitude changes. (Yilmaz, 2001; Manzi, 2014). The advantage of the Kirchhoff migration is its ability to compensate for amplitude due to spherical divergence or spreading factor obliquity and wavelet shaping factors before summing (Manzi, 2014).

Finite-difference migration

Finite-difference migration is a recursive, wave-equation-based method that employs the wavefield downward continuation principle. At each stage of downward continuation, the data is migrated (Yilmaz, 2001; Muijs et al., 2007). Finite-difference algorithms can handle all types of velocity variations, but they have different degrees of dip approximations. Disadvantages of this method include its inability to handle steep dips. The finite-difference equation is given by:

$$\frac{P(t+\Delta t)-P(t)}{\Delta t} = aP(t) \tag{18}$$

where $P(t+\Delta t)$ is the explicit operator, Δt is an arbitrary increment of time, a is the matrix coefficient, and P is the scalar wave equation. The depth size is an important parameter when computing a finite-difference migration (Yilmaz, 2001).

Frequency-wavenumber (F-K) migration

Frequency-wavenumber (F-K) migration was first developed by R.H. Stolt in 1978 and is also known as Stolt migration (Stolt, 1978). F-K migration involves solving the scalar wave equation based on knowledge of the wavefield on the surface and the assumption that only up-coming waves exist (Gilmore et al., 2006). The method transforms the data from the time domain to the frequency-wavenumber domain, where the wave velocity and direction can be estimated. This information is then used to correct the wave bending and spreading that occurs as seismic waves travel through subsurface media. The frequency-wavenumber algorithm is limited in the ability to resolve velocity variation (Yilmaz, 2001).

Post-stack versus pre-stack time migration

In pre-stack migration, seismic data are adjusted before the stacking sequence occurs. In the pre-stack time migration, the Kirchhoff wave-equation algorithm is often an algorithm of choice in complex structural environments (Manzi, 2014). Pre-stack Kirchhoff migration provides the flexibility to output selected CMP gathers in their migrated positions. The technique is useful in refining and estimating the root mean square (RMS) velocity model (Yilmaz, 2001; Manzi, 2014). Post-stack migration operates on the stacked section, which is assumed to be a zero-offset section. Post-stack migration takes a shorter computation time

compared to pre-stack migration and has a high signal-to-noise ratio (Figure 3.12). However, it does not produce correct images of reflectors in geologically complex areas that have strong lateral velocity variations (Yilmaz, 2001; Manzi, 2014).

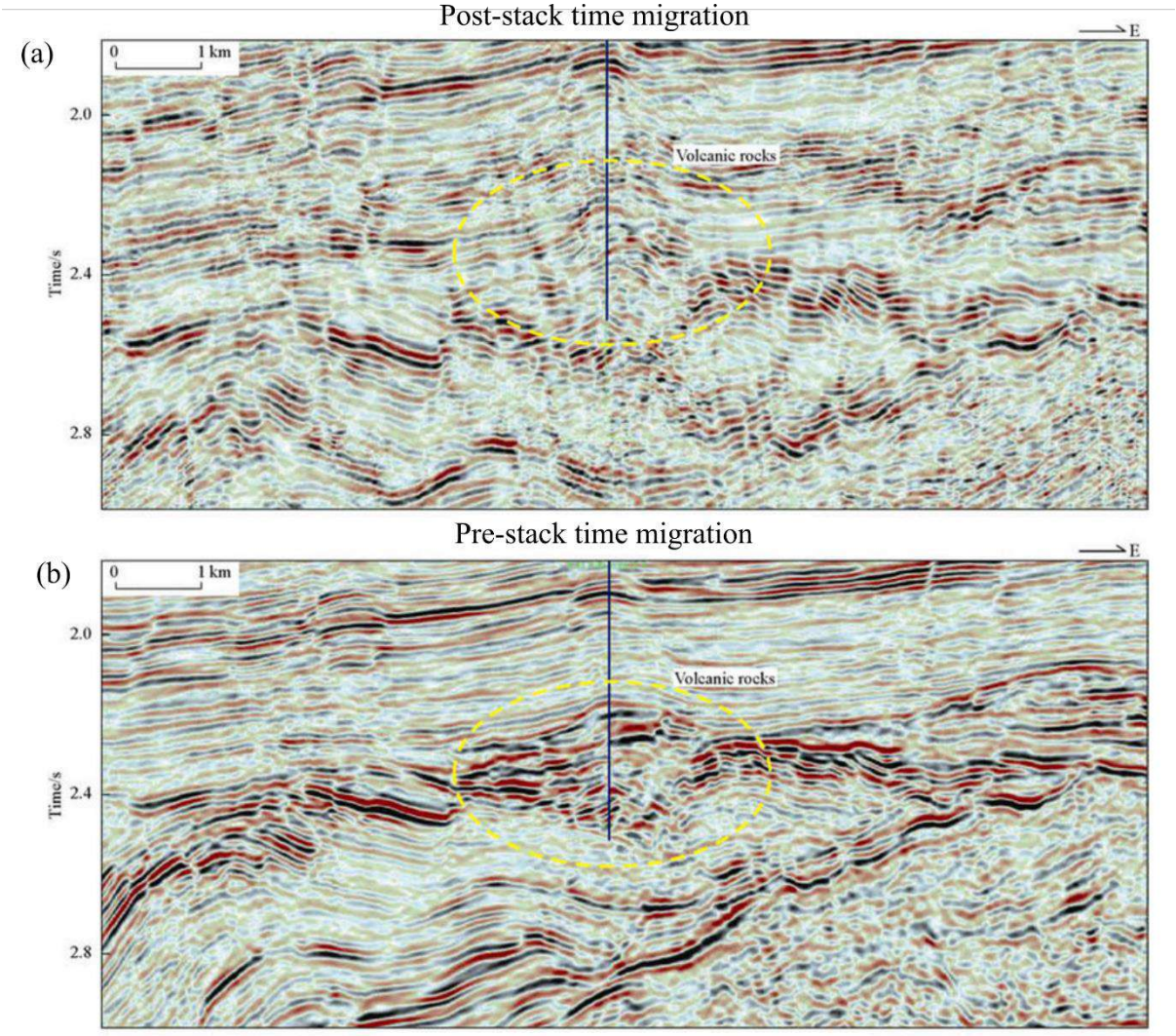


Figure 3.12: *Example of post-stack migration and pre-stack migration of the same section (after Longde et al., 2015).*

3.5 Interpretation

Once the data are processed, the next stage is to interpret the seismic data in such a way that it gives a geological representation of the Earth's subsurface. The quality of the seismic interpretation is dependent on the accuracy and the quality of the processing done in the seismic data. When it comes to the conventional interpretation of reflection seismic data, strong seismic reflectors are identified and picked on each inline, crossline, and time or depth slices (in the

case of 3D data). The conventional interpretation has a shortcoming in that it does not allow for better delineation of geological features below the seismic resolution limit (i.e., one-quarter dominant wavelength).

Conventional 3D seismic interpretation

The conventional seismic interpretation begins with the picking and tracking/mapping of clear, strong, and laterally consistent reflective seismic horizons of the migrated seismic sections (Dentith and Mudge, 2014). Seismic horizons are the reflectors/seismic events picked on individual profiles. The reflectors represent a change in rock properties (seismic velocity and density) across a boundary between two layers of rock, unconformities, or the upper and lower contacts of mineralized units/reefs (Callaway et al., 2013). Interpreters track horizon surfaces according to the amplitude, phase, and continuity patterns of seismic events in the seismic data. The amplitude of a seismic horizon is influenced by the contrast in the acoustic impedance across an interface, it can reveal/provide variations in lithology. On the seismic sections, the reflective horizons are defined as the maximum positive (peak) or maximum negative (trough) amplitudes. A horizon's selection as a peak or trough is based on the polarity of the data. In the European picking standard, a peak denotes a decrease in acoustic impedance across an interface, whereas a trough denotes an increase (Bacon et al., 2003; Brown, 2001; 2011).

Auto-tracking and manual picking

Picking is an interpretation method that involves tracking a reflective horizon on seismic sections using the interpretation software package. Depending on the data quality and continuity of the horizon, this can be done manually or automatically (auto-tracking) (Herron, 2011; Herron, 2014).

Since the early 1980s, interactive interpretation systems have used auto-picking techniques. Auto-picking technique uses a computer algorithm to pick the peak amplitude accurately and efficiently along the horizon. The idea behind auto-picking is straightforward. The interpreter sets seed picks on inline and crossline sections along the selected horizon. These seed points are then used as initial controls for the correlation. On a nearby trace, the program searches for a similar feature. It selects that trace and proceeds on to the next trace if it discovers such a feature within the given limitations (Herron, 2014). Figure 3.13 is a sketch showing how an auto-picker works. The auto-tracker halts tracking at that trace if any of the search conditions

are not satisfied (amplitude out of range, absence of a comparable feature in the dip window, etc.).

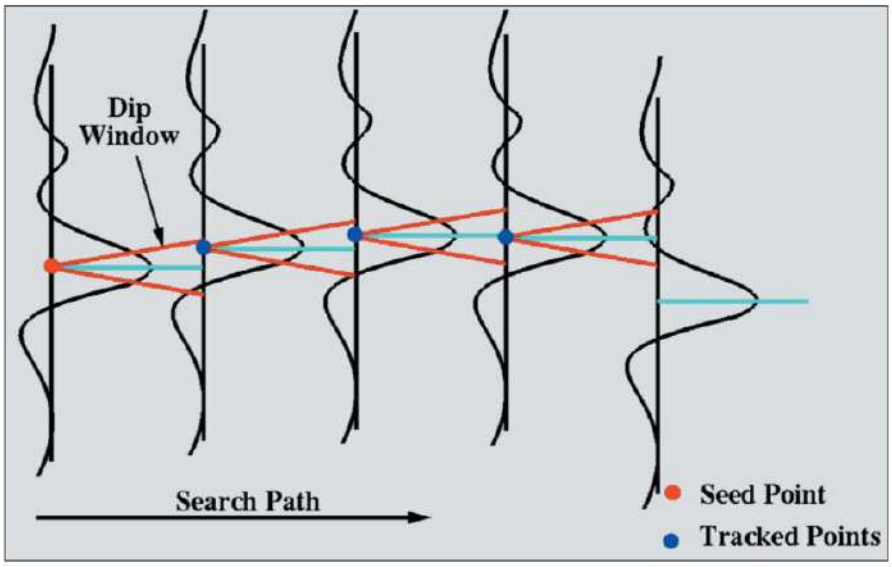


Figure 3.13: *A sketch of an auto-picker's operation (after Dorn, 1998).*

The auto-picker is classified into two classes, (1) feature trackers and (2) correlation trackers. The feature tracker does not compute any correlations between traces; instead, it looks for a similar arrangement of samples within the dip window. From trace to trace, it tries to follow a pattern of data on the seismic trace that characterizes a peak, trough, zero crossing, etc.

A correlation tracker compares a section of the seismic trace at the seed pick to a nearby trace over a series of lag intervals that are limited by the dip search window. The pick on the new trace is accepted and the picker continues to the next trace if a lag time is discovered with an appropriate correlation quality factor. The correlation auto-picker requires a lot more processing power than the feature tracker (Dorn, 1998).

However, auto-tracking may not work at all locations on the horizons in regions with complex faulting, low signal-to-noise ratio, and changes in the data polarity. As a result, manual picking is carried out on every inline and crossline to enable detailed structural interpretation. This method is the most well-known. In terms of the time and effort required by the interpreter, it is also by far the least effective horizon interpretation technique.

Seismic attributes

To help with the interpretation, seismic attributes are used to improve or enhance the mapping of the geological features that are below the seismic resolution limit (Taner et al., 1979; Taner, 2001; Chopra and Marfurt, 2007; Liner, 2016). The importance of seismic attributes in the interpretation of seismic sections was discovered in the late 1960s and early 1970s (Barnes, 2007; Chopra and Marfurt, 2007). A seismic attribute, according to Barnes (1999), is "a descriptive and quantifiable characteristic of seismic data that can be displayed at the same scale as the original data". Sheriff (2002) went on to state that a seismic attribute is a measurement based on time, amplitude, frequency, and attenuation readings.

Complex-trace attributes

Complex trace attributes typically refer to attributes derived from the analysis of seismic waveforms along individual traces or seismic signal segments. Frequently, complex-trace attributes are used to uncover information that is hidden in migrated seismic sections (Taner, 2001; Chopra et al., 2006; Chopra and Marfurt, 2007; Manzi et al., 2013). They are also called instantaneous attributes and are one of the commonly used attributes for seismic interpretation (Barnes, 1999; 2016). The complex trace consists of two parts mathematically, the real (or amplitude) part and the imaginary (or Hilbert trace) part. The concept of the complex seismic trace is illustrated in Figure 3.14.

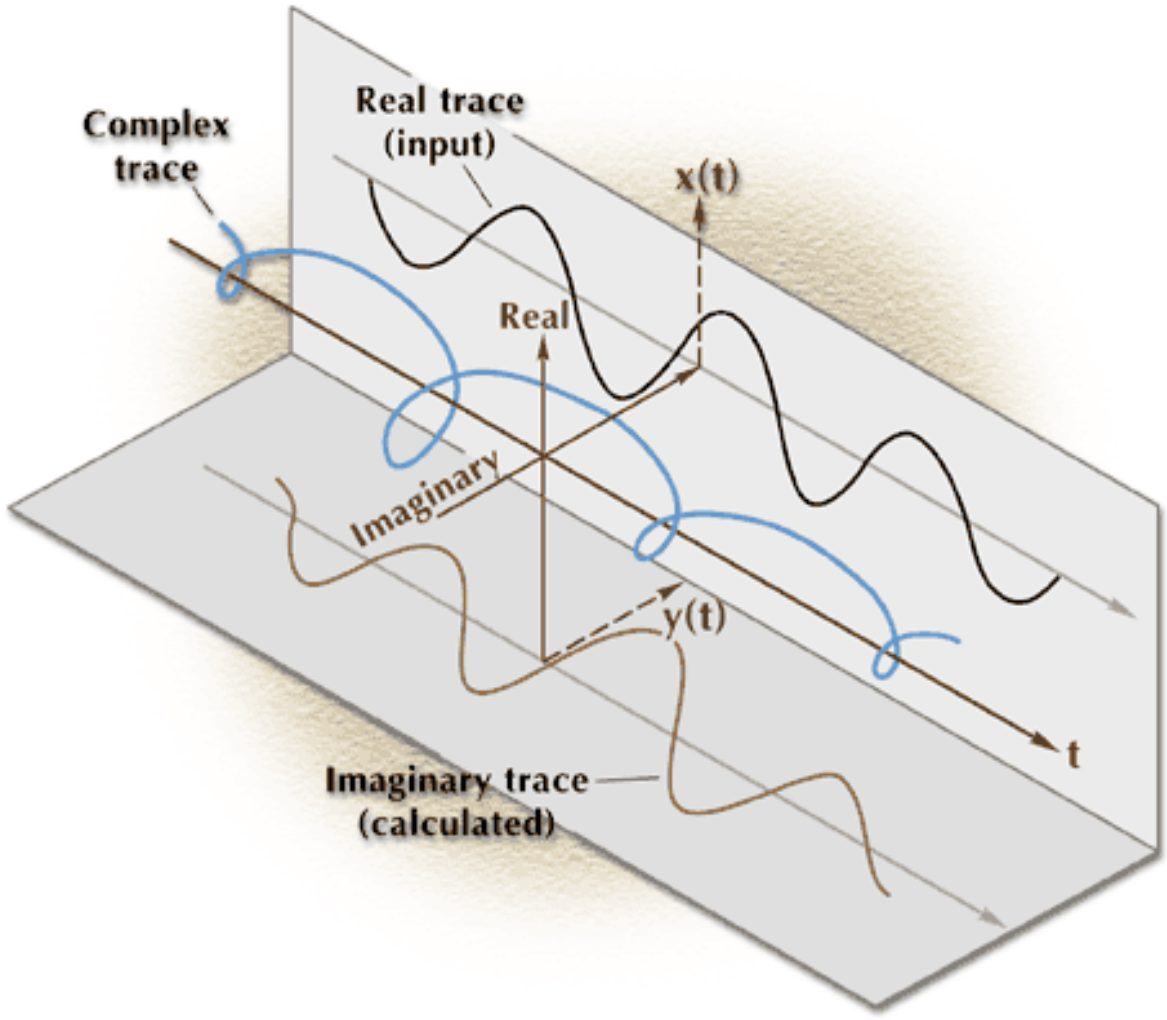


Figure 3.14: *A complex seismic trace. The seismic time axis is t. The real part x (t) of the complex trace is the actual seismic trace; the imaginary part y (t) is a mathematical function calculated from the real trace by a Hilbert transform process (after Taner et al., 1979).*

Separating the phase information from the amplitude information in the seismic data is the fundamental step in computing a complex-trace analysis (Taner et al., 1979; Barnes, 2016). The amplitude and the phase spectra can be represented by the cosine and the sine spectra of the Fourier transform (i.e., X(f) and Y(f) respectively) (Taner et al., 1979; Renè et al., 1986), given by:

$$X(f) = A(f)cos\varphi(f) \tag{19}$$

$$Y(f) = A(f)sin\varphi(f) \tag{20}$$

where the $A(f)$, is related to the amplitude and $\varphi(f)$ is the phase component.

A seismic trace x(t) can be split into two attributes, (1) instantaneous amplitude attribute, a(t), and (2) the cosine of the instantaneous phase $\varphi_i(t)$ attribute (Figures 3.14 and 3.15), e.g.

$$x(t) = a(t)cos\varphi_i(t) \tag{21}$$

But Equation 21 relates two unknown functions to one known: as a result, the quadrature trace y(t), is given by:

$$y(t) = a(t)sin\varphi_i(t) \tag{22}$$

and is described as the seismic trace's Hilbert transform and given as follows:

$$y(t) = h(t) * x(t) \tag{23}$$

where h(t) is the Hilbert transform operator that produces the quadrature trace y(t) by subtracting 90 degrees of phase from the seismic trace x(t).

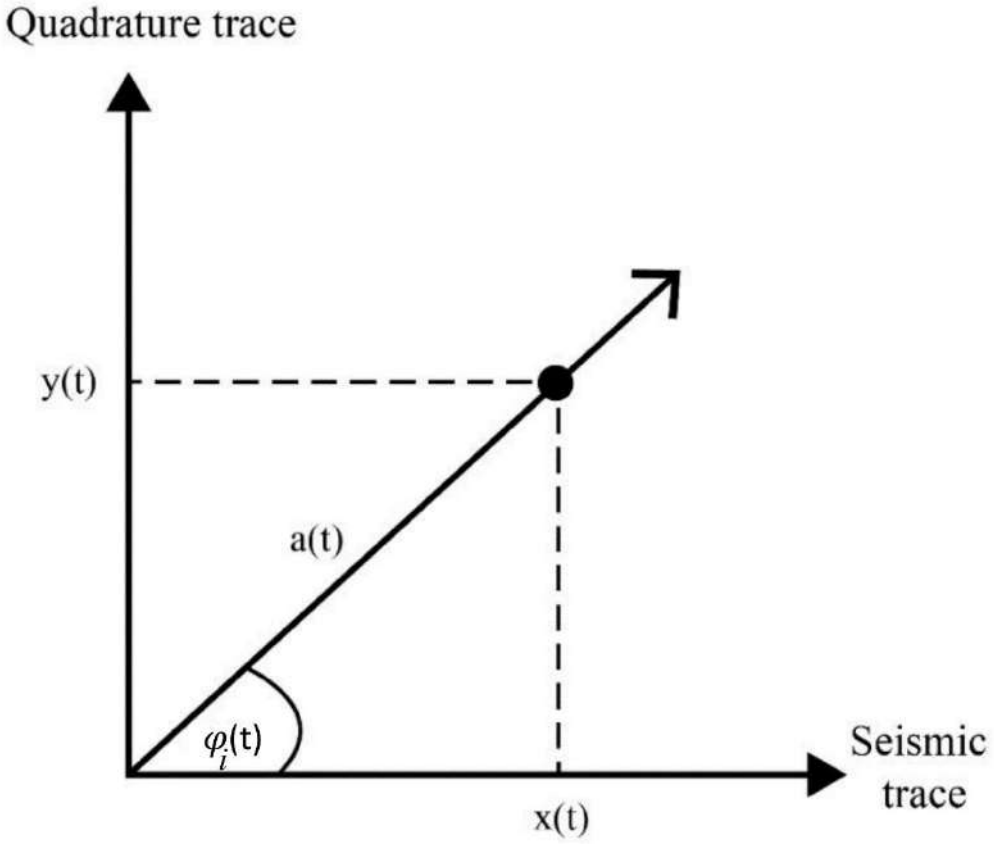


Figure 3.15: *An illustration of the relationship between the seismic trace (x(t)) and the quadrature (y(t)) in Cartesian coordinates. The amplitude and phase attributes represent the point in polar coordinates, the seismic and quadrature traces represent the point in polar coordinates, while the seismic and quadrature traces represent the point in Cartesian coordinates.* $\varphi_i(t)$ *is the cosine of the instantaneous phase and a(t) is the instantaneous amplitude attribute (after Sehoole, 2019).*

The Cartesian to Polar coordinate transform can be used to determine the instantaneous amplitude and phase from the seismic and quadrature trace (Figure 3.15):

$$a(t) = \sqrt{x^2(t) + y^2(t)} \tag{24}$$

$$\varphi_i(\mathrm{t}) = tan^{-1}\left[\frac{y(t)}{x(t)}\right] \tag{25}$$

Equations 23 and 24 form the basis of all other complex-trace attributes. The phase signal $\varphi_i(\mathrm{t})$ changes with time, and then we estimate the instantaneous frequency as the change of phase with time. This is the first derivative of phase over time. There are numerous methods for calculating derivatives, but the one that is frequently used is as follows:

$$f(\mathrm{t}) = \frac{d\varphi}{dt} = \frac{1}{a(t)}\left[x(t)\frac{dy(t)}{dt} - y(t)\frac{dx(t)}{dt}\right] \tag{26}$$

where square brackets indicate the square of the Euclidean distance. $f(\mathrm{t})$ is the instantaneous frequency attribute.

Horizon-based attributes

Amplitude Attributes

According to Herron (2011), the amplitude attribute uses changes in acoustic impedance to reflect geological changes. This measures the energy that is reflected within a specified window and eliminates any undesirable phase effects that are found when picking amplitudes (Manzi et al., 2013). Some of the amplitude attribute examples include reflection strength, root mean square (RMS) amplitude, maximum amplitude, average absolute amplitude, and total energy. The amplitude attribute has the limitation of failing to image small-scale lithological changes in thin beds (i.e., layers with thicknesses less than the tuning thickness) and small-scale faults that are below the seismic resolution limit (Herron, 2011; Barnes, 2016).

Dip-magnitude and dip-azimuth

Dalley et al. (1989) defined dip and dip azimuth attributes as the amount of inclination of a horizon in the subsurface and the direction of this inclination measured from a local reference direction, respectively. Dip and dip-azimuth were simply re-defined by Rijks and Jauffred (1991) as the magnitude (or amount of inclination of a horizon) and direction of the time gradient computed at each sample trace of the interpreted horizon grid, respectively. The

calculations are done by fitting a plane through neighboring data points and placing the computed values at the central data point. Dip and dip azimuth have the following mathematical expressions:

$$Dip\ magnitude = \sqrt{\left(\frac{dt}{dx}\right)^2 + \left(\frac{dt}{dy}\right)^2} \tag{27}$$

$$Dip\ azimuth = \arctan\left(\frac{\frac{dt}{dy}}{\frac{dt}{dx}}\right) \tag{28}$$

where $\frac{dt}{dx}$ and $\frac{dt}{dy}$ are the dip in the x and y direction, respectively (Marfurt and Chopra, 2007).

Calculating dip and dip azimuth on an interpreted seismic horizon is useful for revealing small-scale faults that would be less noticeable on migrated seismic sections. The degree to which the fault dip differs from the horizon dip determines how well dip and dip azimuth work to detect faults. To enable the detection of faults using the dip azimuth attribute, the dip direction of the fault should also differ from that of the horizon. To fix the issue of dip-magnitude and dip-azimuth detectability differences a combination of dip and dip-azimuth variations is applied to overcome these limitations (Manzi et al., 2012b).

Edge detection attribute

The edge detection attribute is a combination of dip and azimuth variations that are normalized to the local noise of the interpreted horizon grid (Manzi et al., 2012b). The edge detection attribute measures the changes in the signal amplitude variations within the horizon. By adjusting the color bar, the edge detection technique can be used to detect small-scale faults and fault complexities more effectively, such as fault continuity and fault interconnectivity. Due to its sensitivity to small amplitude variations in the data, this attribute has the significant advantage of not introducing artifacts through smoothing (Randen et al., 2001; Manzi et al., 2012a). When compared to the dip and dip azimuth attributes, the edge detection attribute is a more potent tool for highlighting intricate structural detail on horizons.

4. 3D SEISMIC IMAGING: ATTRIBUTE ANALYSIS

The Kloof (now Kloof-Driefontein Complex East (KDC East) and South Deep mines are located in the West Rand goldfields of the Witwatersrand Basin. The basin is one of the world's biggest primary producers of gold. Several 2D seismic profiles (Pretorius et al., 2003) and tens of 3D seismic surveys (Manzi et al., 2012a) were acquired in the 1990s across the Witwatersrand Basin to delineate gold reefs under the thick cover of the Transvaal and Ventersdorp Supergroups. The results from these surveys demonstrated the effectiveness of reflection seismics for deep targeting in hard-rock settings. One of these surveys is the Kloof-South Deep 3D seismic survey, which was acquired in 2003 for deep mine planning and designs. The KDC East mine is situated west of the West Rand Fault and is one of the largest mines in the West Rand goldfield. The most important gold deposits at the KDC East mine are the Ventersdorp Contact Reef (VCR) and Black Reef (BLR), which are located at depths between 0.5 km and 3.5 km below ground surface. The South Deep mine lies to the east of the West Rand Fault (Figure 4.1) and the mine exploits the Upper Elsburg Reefs (UERs) and the VCR.

The Kloof-South Deep 3D seismic was designed to cover both Kloof (KDC East mine) and South Deep mines to image the major structures such as the West Rand Fault (WRF) and delineate deep-seated gold-bearing horizons (> 0.5 km depths) such as the Black Reef (BLR) and Ventersdorp Contact Reef (VCR). The 3D seismic data cover an area measuring ~15 km east-west and ~18 km north-south. The survey was conducted by Compagnie Générale de Géophysique (CGG) and processed by Velseis Pty Ltd. in 2004 and Manzi et al. (2012a). The seismic volume extends to about 11 km in depth and was processed using both pre-stack and post-stack time-migration workflows (Manzi et al., 2012a). The 3D seismic data have been the subject of several studies (e.g., Manzi et al., 2012a, b; Manzi et al., 2013a, b) given their unique nature in terms of quality in imaging complex geological structures.

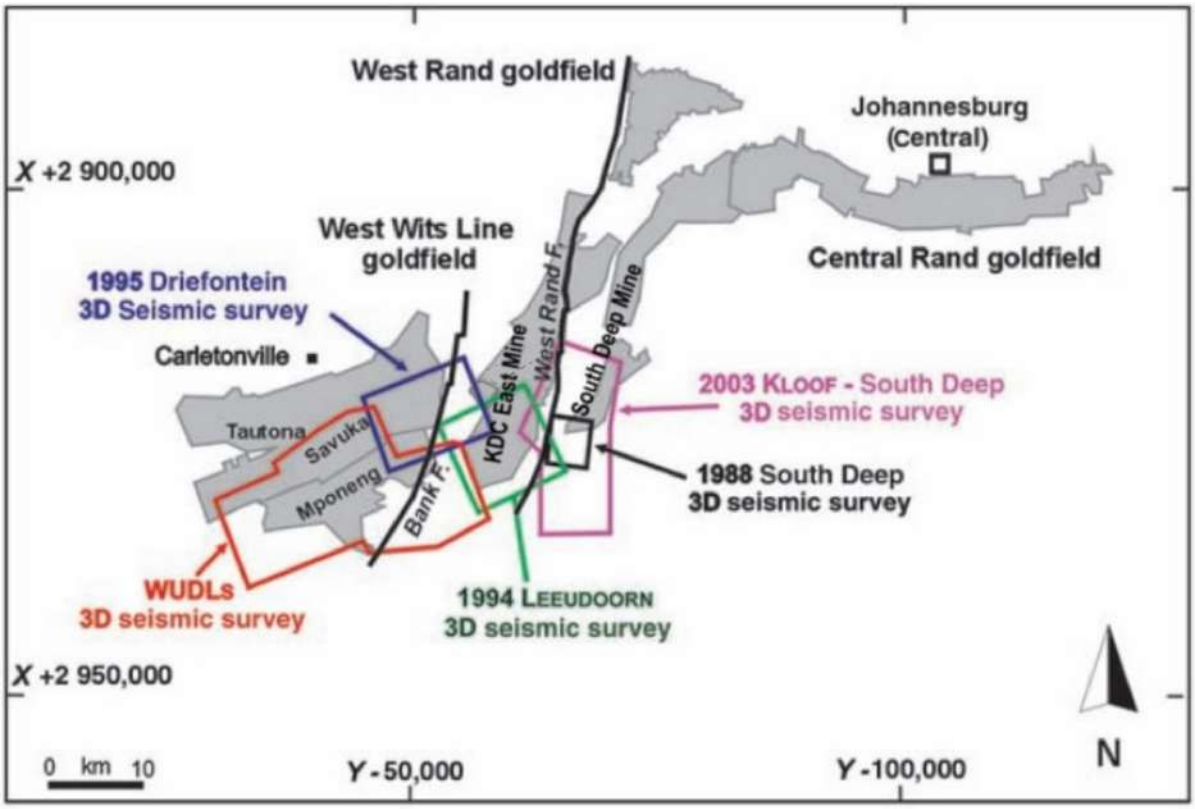


Figure 4.1: *The location of historical surveys over the West Rand and West Wits Line goldfields (after Manzi et al., 2012a). The survey of interest for this study is the 2003 Kloof-South Deep seismic survey.*

The seismic dataset was re-processed again by HiSeis in 2020 using today's standard processing workflow to improve the quality of the data. The processing of the seismic data by HiSeis focused on pre-stack depth imaging using reverse time migration (RTM), while the legacy processing focused on depth imaging using Kirchhoff migration (Manzi et al., 2022a, b). The details of the processing steps undertaken during the re-processing of the cube was not available to the candidate, thus these are not discussed in this chapter. However, the final processed seismic volume was given to the candidate to test seismic interpretation techniques for structural delineation. Figure 4.2 shows an example of the legacy (Figure 4.2a) and 2022 reprocessed seismic section (Figure 4.2b). In summary, the 2020 reprocessing provided:

(1) Enhanced resolution throughout the stratigraphic sequence,

(2) Clearly defined VCR and BLR horizons, and

(3) Cleary defined geological structures.

The overall aims of the current work (in this chapter) were to investigate (1) the application of seismic attributes to the reprocessed 3D seismic data for structural enhancement, and (2) effectiveness of horizon attributes on reprocessed data in defining the geometry of faults and

gold-bearing horizons. It is worth noting that this work only presents preliminary results, and more detailed seismic interpretation will be conducted by the candidate which may lead to the publication of the results.

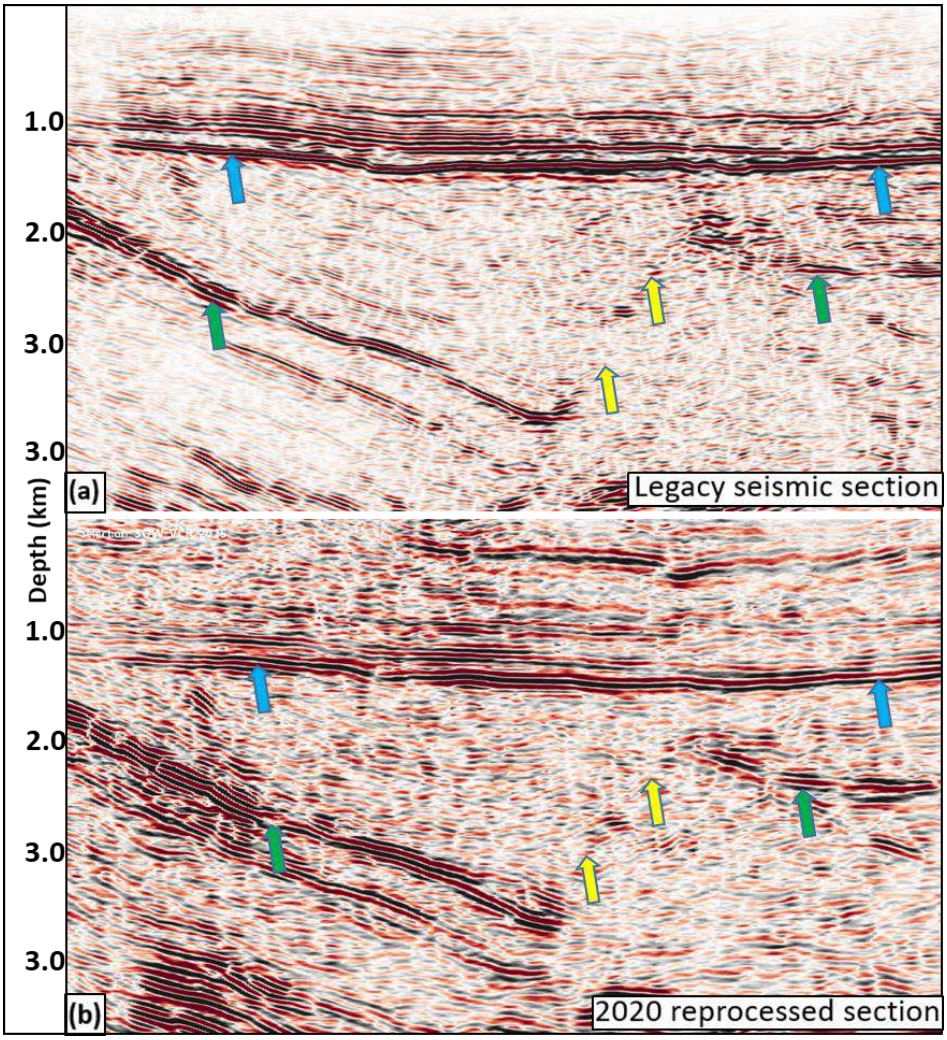


Figure 4.2: *Depth-converted seismic sections. (a) The legacy post-stack Kirchhoff time migrated (PostSTM) section. (b) The 2020 reprocessed section - pre-stack reverse time migrated (PreSTM) section. Note that 2020 PreSTM shows better resolution relative to the legacy PostSTM. Blue arrows indicate Black Reef, green arrows indicate Ventersdorp Contact Reef, while yellow arrows indicate fault zone.*

The 2020 re-processed 3D seismic data were imported to Schlumberger's Petrel software as an SEG-Y file using present parameters and the WGS_1984_UTM_ZONE_34S coordinate reference system. A 2D profile from Paper II was also imported and cut through a 3D seismic cube as shown in Figure 4.3. The seismic reflectors (VCR and BLR) were

prominent across the re-processed seismic volume and were mapped in order to resolve fault zones.

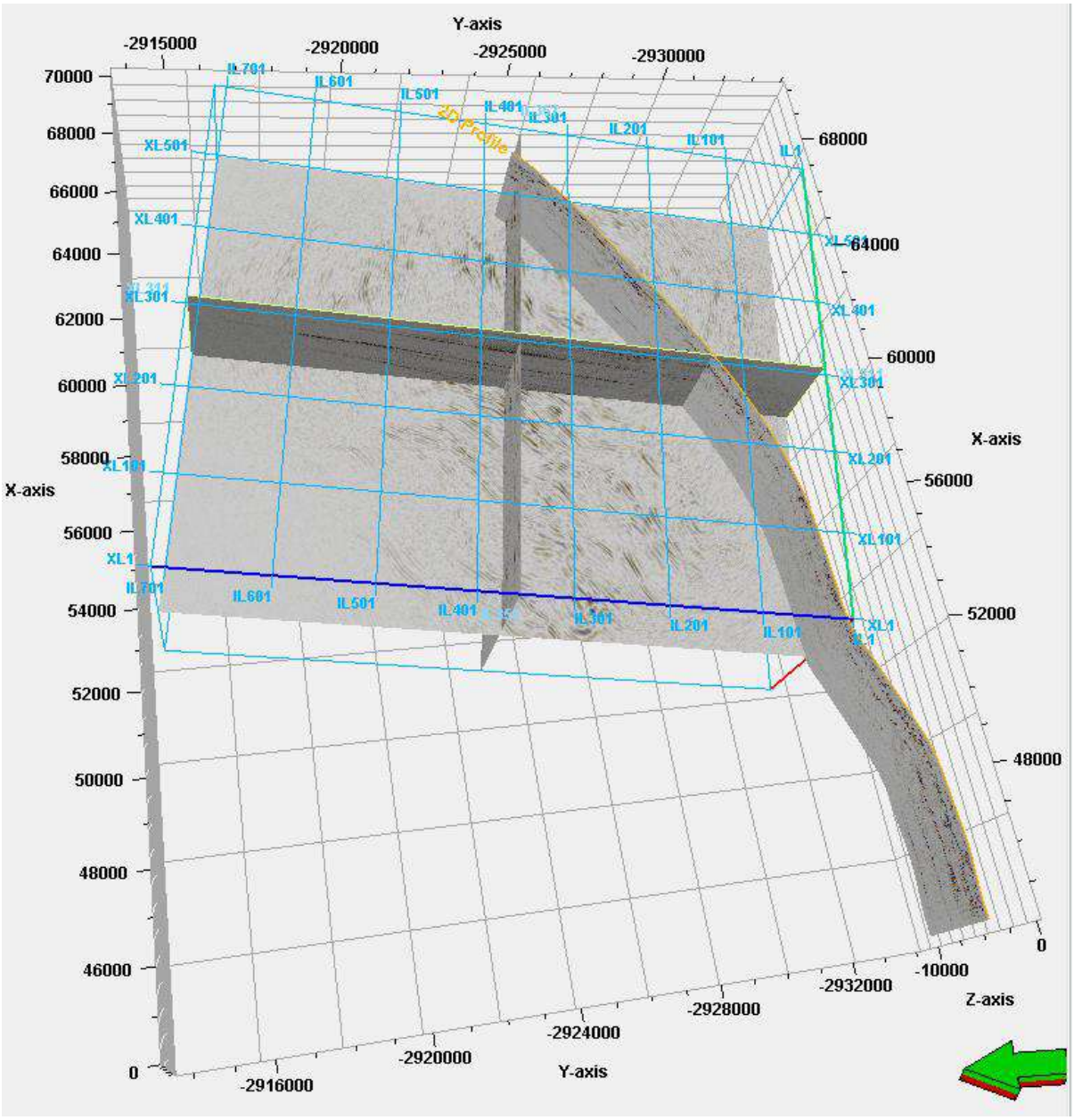


Figure 4.3: *Three-dimensional visualization of Kloof-South Deep seismic survey and 2D seismic profile. The 3D seismic cube displays the inline (y-axis), crossline (x-axis), and depth slice (z-axis) sections.*

4.1 Picking horizons

Seismic horizons (VCR and BLR) were picked on 2D and 3D windows every 10th inline, crossline, and random lines using manual and seeded auto-tracking techniques (Figures 4.4a and 4.5a). The combined confidence classification horizon-based attribute was applied to the

picked VCR and BLR horizons to validate the initial interpretation (Figures 4.4b and 4.5b). The combined confidence classification map shows the level of confidence in a horizon identification, with red representing high levels, green representing moderate levels, and blue representing low levels. The combined confidence classification map comprises the surface stability index and the thick-slice volume amplitude. The surface stability index is defined as the estimated confidence in the surface based on comparing depths at adjacent locations, indicating areas where the surface changes in elevation. While the thick-slice volume amplitude is defined as a histogram equalization of root-mean-square (RMS) amplitude (Schlumberger, 2015). The VCR horizon showed a good delineation of distinct north-northeast trending fault as a linear feature with a low confidence zone (blue color) (Figure 4.4b), while the BLR horizon mapped most of the faults represented as linear features (Figure 4.5a). The confidence level at the BLR horizon is much higher in the western region than in the eastern region due less structurally complexity (Figure 4.5b).

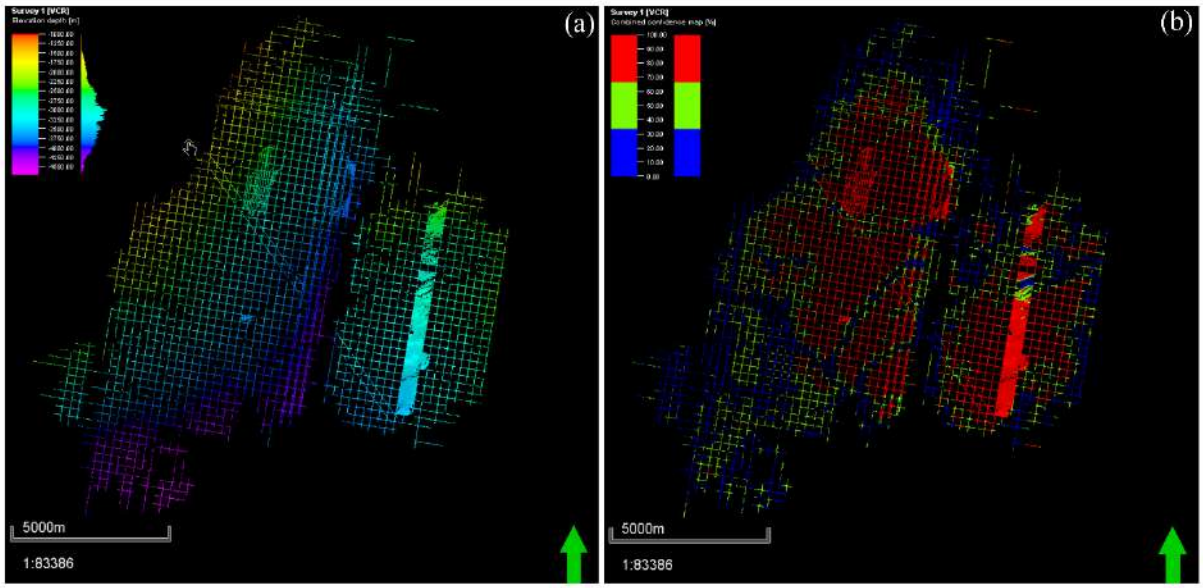


Figure 4.4: *Horizon picking on Ventersdorp Contact Reef (VCR). (a) 2D manual interpretation for VCR. (b) Combined confidence classification map to validate the identification of VCR. The red, green, and blue colors show high, intermediate, and low levels of confidence, respectively.*

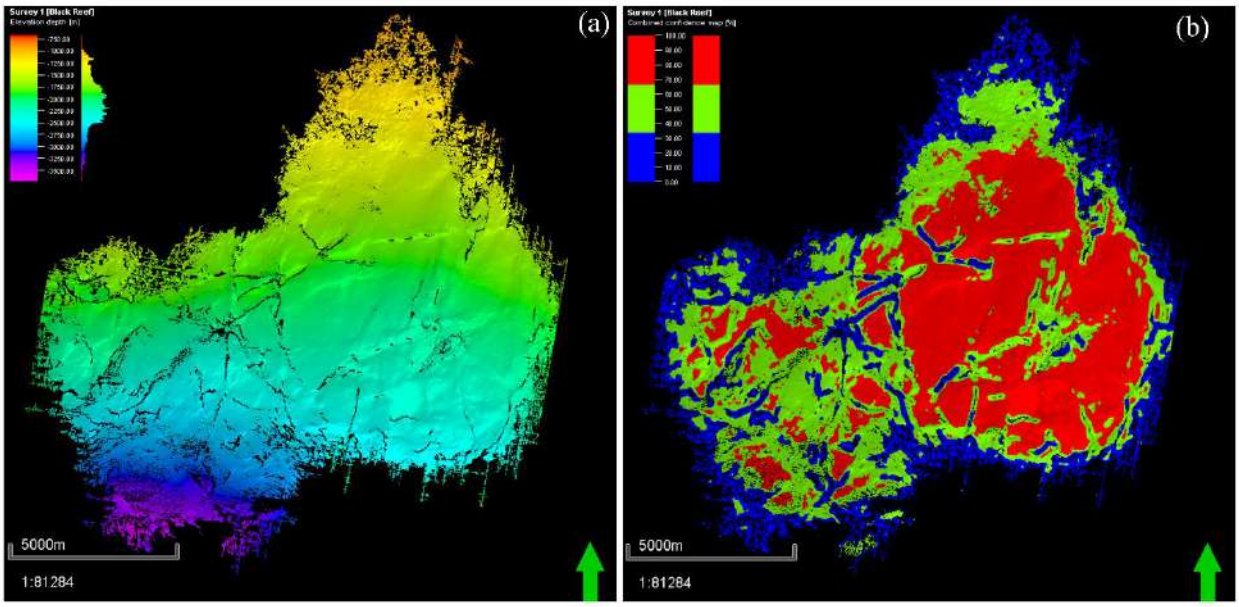


Figure 4.5: *Horizon picking on Black Reef (BLR). (a) 3D auto-tracking interpretation of BLR. (b) Combined confidence classification map to validate the interpretation of BLR. The red, green, and blue colors show high, intermediate, and low levels of confidence, respectively.*

4.2 Surface creation

Figure 4.6 shows the depth map created after picking horizons. The map shows that the faults were not mapped adequately using the depth map. A confidence classification horizon-based attribute was used before creating a surface from a horizon interpretation (see Figures 4.4b and 4.5b). The picked horizons were gridded and contoured. Gridding is a method of spatially regularizing irregularly spaced data through interpolation and filling in horizon gaps. The grid size and position of the created surface were automatically obtained from the input of the horizon picked with X and Y direction grid increments of 50 m. For both VCR and BLR horizons, the elevation depth ranges from 1500 to 2500 m. Figure 4.6a shows the closely spaced contour lines representing a steep slope as indicated by the white arrow, while Figure 4.6b shows relatively widely spaced contour lines representing a gentle slope as indicated by black arrows.

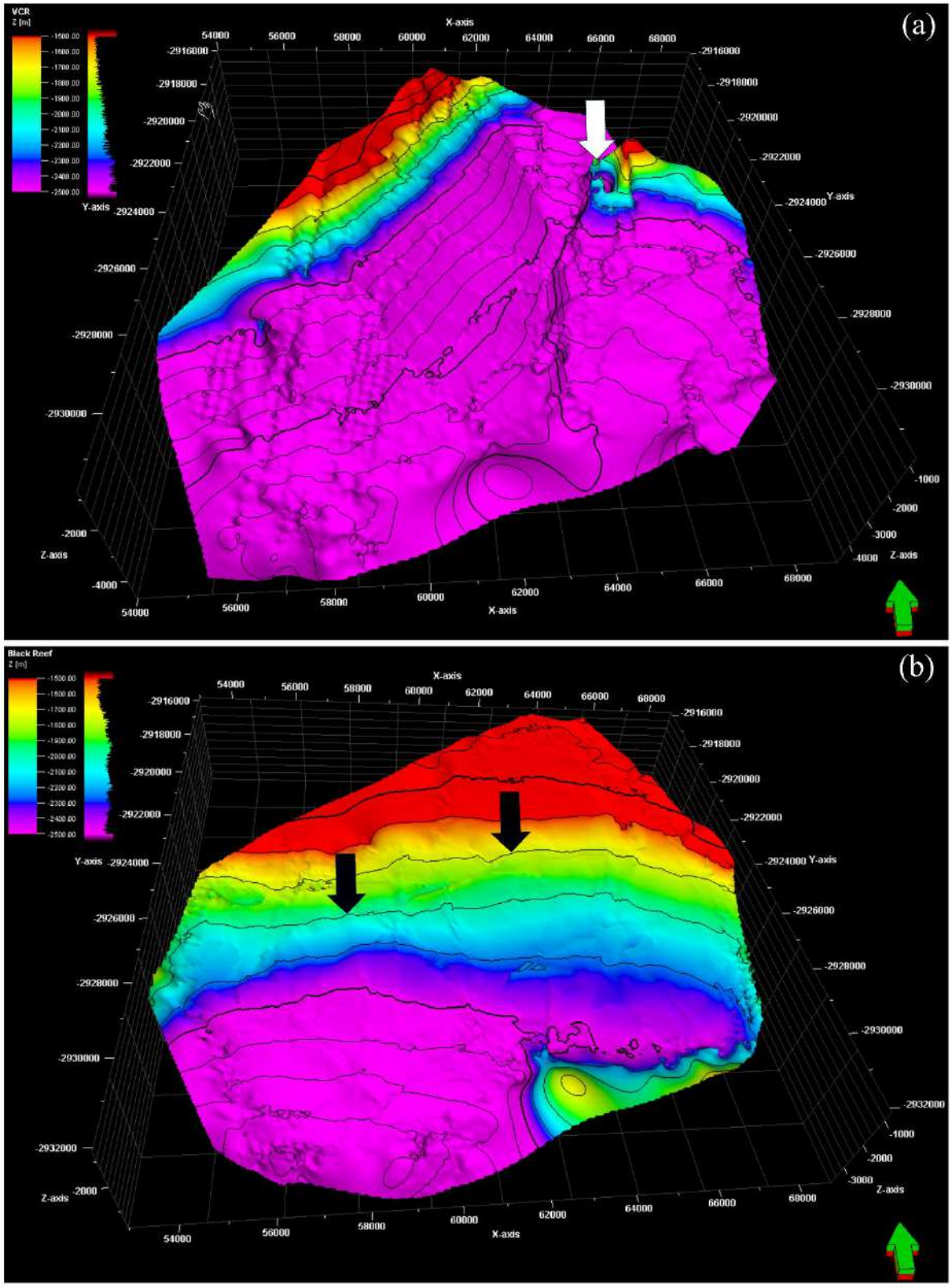


Figure 4.6: *Depth maps generated from the picked horizons. (a) VCR surface, and (b) BLR surface. The color bar is given in meters. The elevation depth ranges from 1500 to 2500 m. BLR: Black Reef, VCR: Ventersdorp Contact Reef.*

4.3 Surface attributes

To better delineate faults, surface attributes were applied on the created surfaces (VCR and BLR). Surface attributes are used to improve or enhance the mapping of geological features that are below the seismic resolution limit (Chopra and Marfurt, 2007; Liner, 2016). Numerous faults of many orientations were clearly mapped on the influential data map compared to the depth map for both VCR and BLR surfaces (Figure 4.7a-c). The influential data attribute highlights areas of rapid 3D geometric change. Both high positive (red) and corresponding negative (blue) values imply large variations in geometry. In Figure 4.7b, the influential data attribute is shown to enhance areas with a great magnitude of displacement and north-northeast trending faults. This shows that the influential data map is more effective in highlighting regional-scale variations rather than local-scale variations (Figure 4.7b, d).

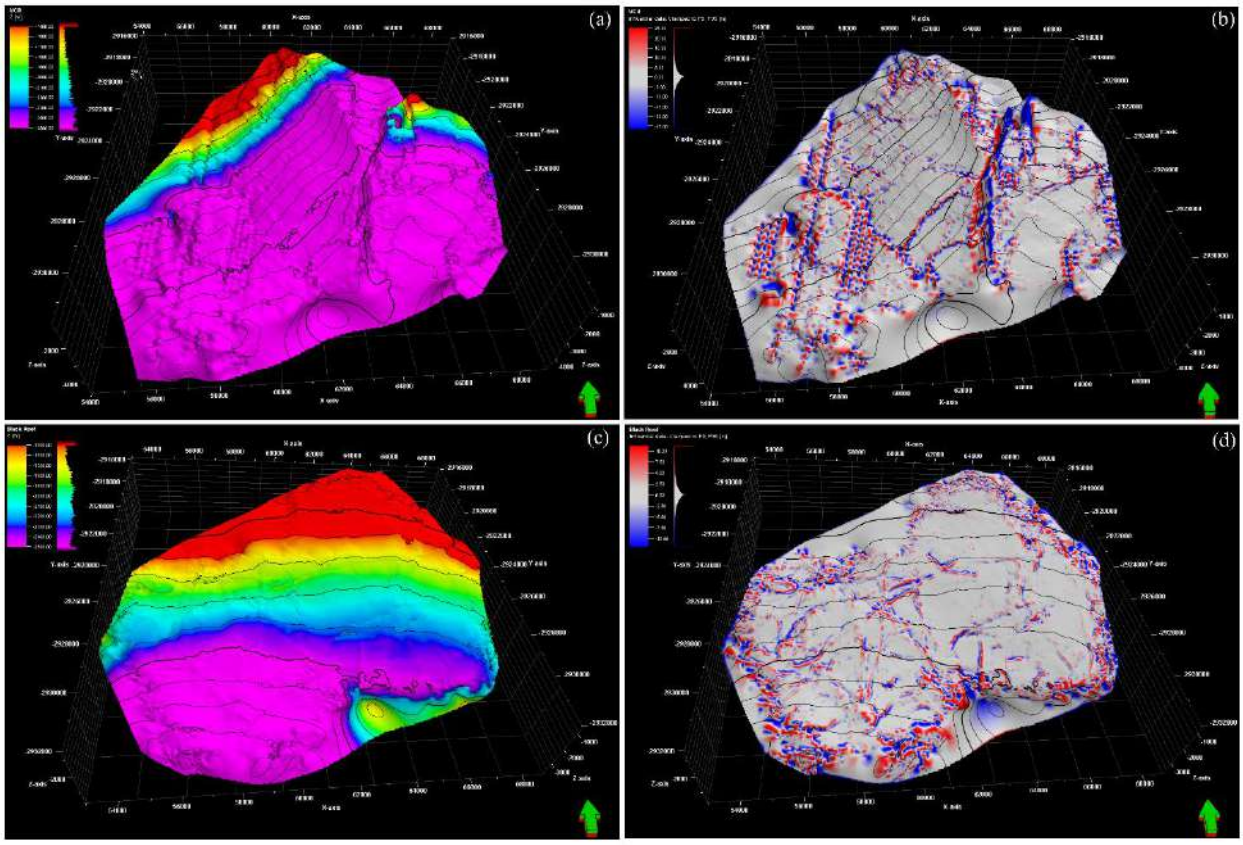


Figure 4.7: *Comparison between the depth map and influential data attribute. (a) VCR depth map, and (b) VCR influential data map, and (c) BLR depth map, (d) BLR influential data map. The elevation depth ranges from 1500 to 2500 m. BLR: Black Reef, VCR: Ventersdorp Contact Reef.*

Figure 4.8 shows the dip and dip azimuth applied to the VCR surface. The horizon is characterized by dip angle values ranging between 0 and 90 degrees (Figure 4.8a). The dip angle attribute shows a linear feature (fault) indicated by a white arrow with dip values greater than 80 degrees compared to the rest of the horizon. Figure 4.8b shows the VCR dip azimuth map characterized by linear features with higher dip azimuth values ranging from 125 to 300 degrees. The fault indicated by the white arrow has a dip azimuth of ~275 degrees.

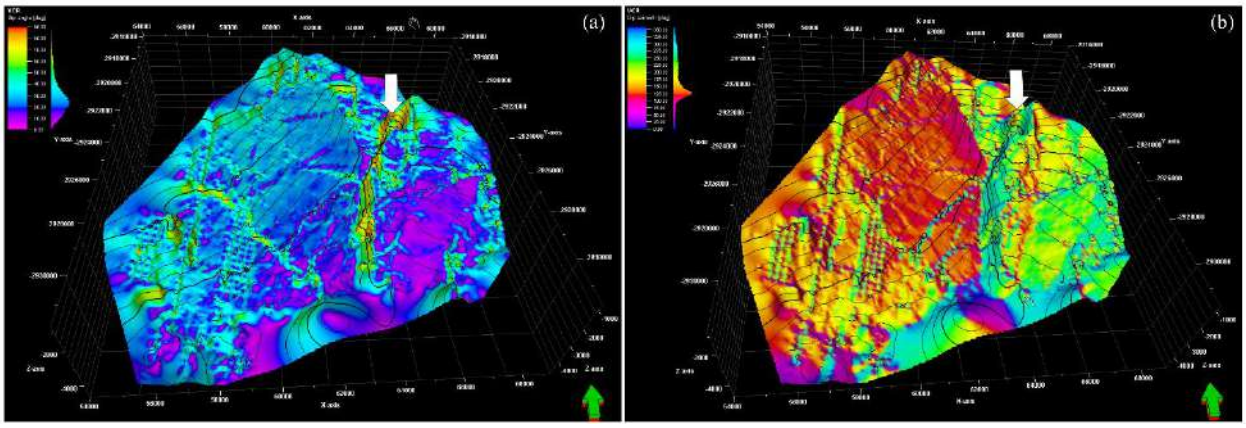


Figure 4.8:*The dip angle (a) and dip azimuth (b) attributes computed on the VCR surface highlighting faults features. A major feature is indicated by a white arrow in both attributes. VCR: Ventersdorp Contact Reef.*

From the BLR dip angle attribute, the horizon is characterized by dip angle values ranging from 0 to 80 degrees and most linear features have a dip angle of ~30 degrees (Figure 4.9a). In the BLR dip azimuth map, the attribute was able to highlight linear features better in the region indicated by the white circle compared to the dip angle attribute map. The BLR dip azimuth values range from 0 to 350 degrees.

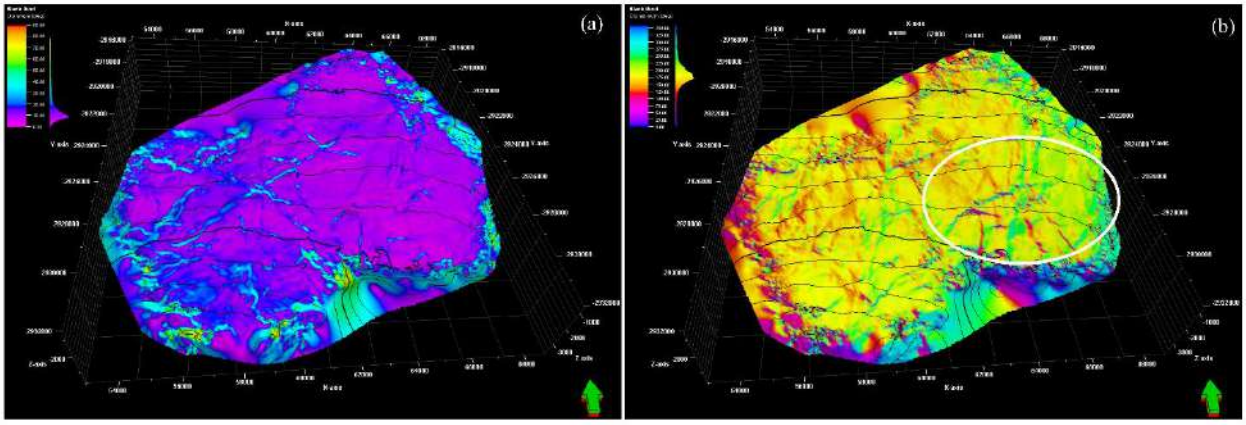


Figure 4.9: *The dip angle (a) and dip azimuth (b) attribute computed on the BLR surface highlighting faults features. The map is dominated by dip azimuth values ranging from 180 to 360 degrees). BLR: Black Reef.*

4.4 Fault mapping

The major West Rand Fault and Wrench Fault zones displace the VCR horizon by several kilometers (Figure 4.10). However, no displacement of the BLR is discernable on a seismic section (Figure 4.11). Edge detection attributes were computed for the VCR and BLR horizons to investigate possible subtle faults that appear at both elevation levels. Edge detection is a surface attribute that combines the dip and dip azimuth properties and smooths them to the local noise of the surface. The edge detection attribute shows traces of linear features throughout the horizon, which are interpreted as faults. The VCR edge detection attribute highlights the irregularity or structural complexity of the VCR. The map exhibits a dominant north-northeast trending fault known as the West Rand Fault with a lower edge surface percentage (5% - 30%) (Figure 4.10).

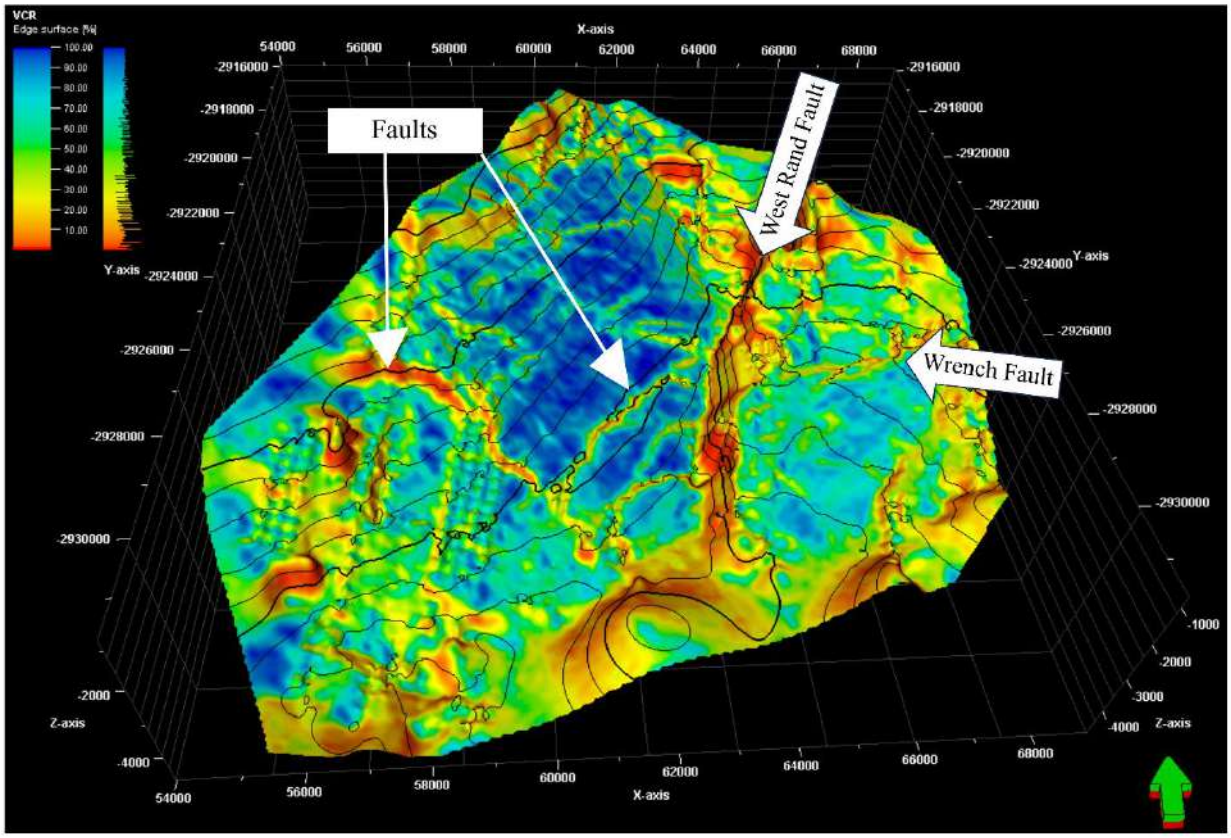


Figure 4.10: *Edge detection attribute map showing high-resolution imaging of the faults on the VCR surface. The edge detection attribute color bar is given in %. Areas where the surface is faulted, appear red and orange, between 0 – 40 %. The horizon is faulted with known faults such as the West Rand Fault and Wrench Fault. VCR: Ventersdorp Contact Reef.*

Figure 4.11 shows the BLR edge detection attribute map dominated by areas of low percentages ranging from 10% to 30%. The horizon is dominated by linear features interpreted as faults. Even though low percentages are observed on the edges of the BLR horizon, these features can be interpreted as faults. The change in contour lines is still the same as the ones observed in the elevation depth map.

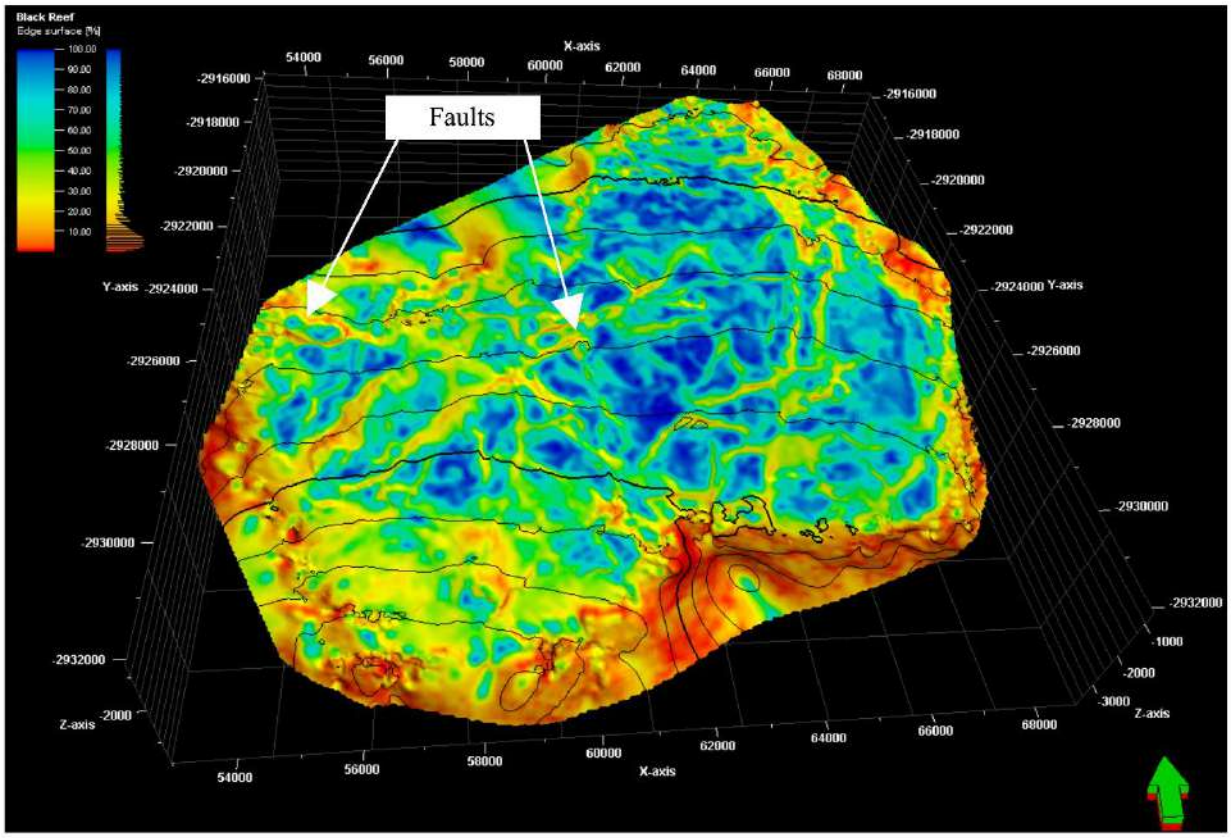


Figure 4.11: *Edge detection attribute map showing high-resolution imaging of the faults on the BLR surface. The edge detection attribute color bar is given in %. Areas where the surface is faulted, appear red and orange, between 0 – 20 %. BLR: Black Reef.*

Figure 4.12 presents the 3D model of the VCR edge detection attribute together with the structures that are interpreted to have displaced the VCR but not the BLR. This confirms the interpretation made in Paper II (Chapter 7 of the thesis) of the 2D seismic line that cuts through the edge of the 3D seismic cube. The fault surfaces in Figure 4.12 were derived from the manually picked faults and remodeled to correlate with the VCR topographic breaks revealed by edge detection attributes. If there are faults that are projected from the VCR to the BLR horizons, they may be faults that were reactivated during the post-BLR deformation event (Manzi et al., 2012b).

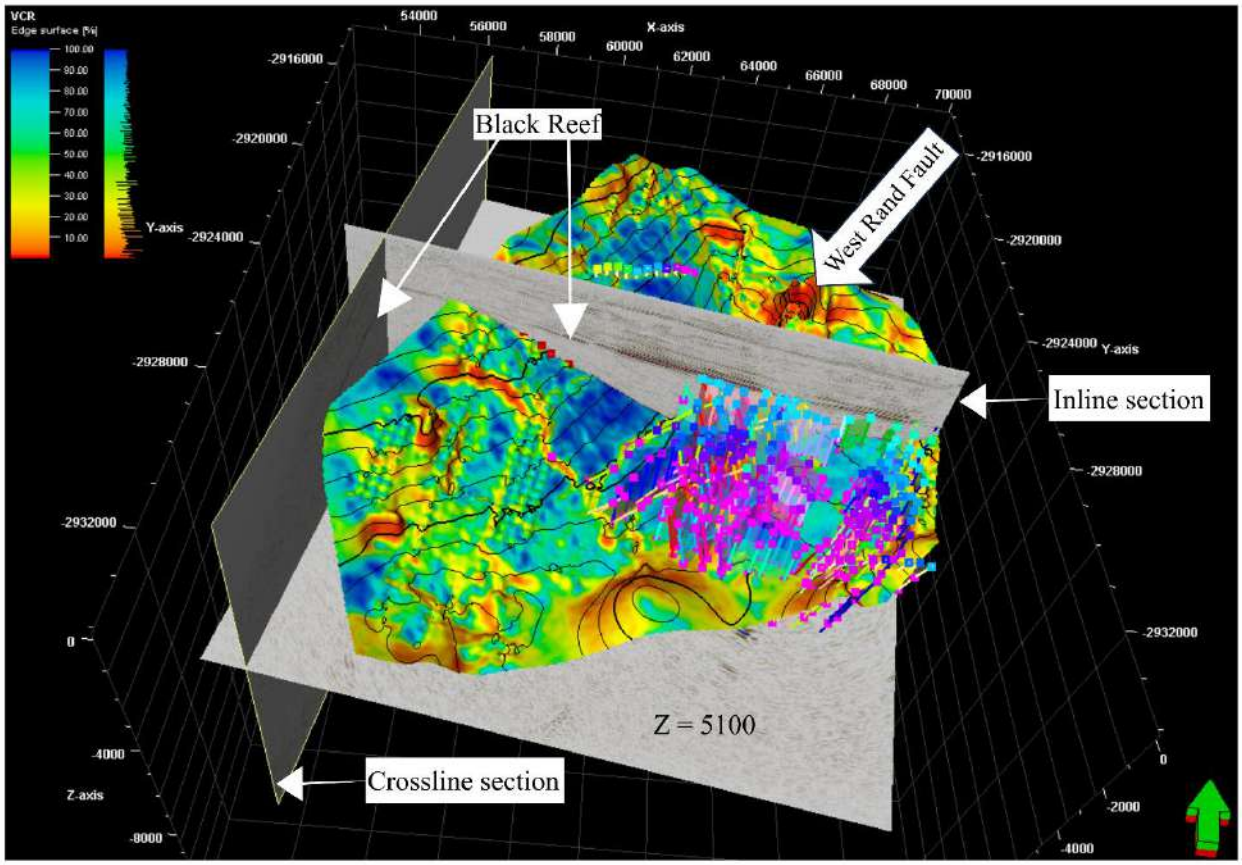


Figure 4.12: *Three-dimensional visualization of combined 3D VCR edge detection surface and modeled faults (color bar for edge detection attribute is given in%). These faults do not offset the BLR on seismic sections. BLR: Black Reef, VCR: Ventersdorp Contact Reef.*

4.5 Implications for mining

Reprocessing of the 2003 using the latest processing algorithms has delivered improved VCR, BLR and structural imaging for KDC East and South Deep gold mines. The preliminary attribute analysis shows that both the VCR and Black Reef ore bodies are cross-cut by several geological structures (mainly faults) of various dips and orientations. This enables more structural analysis to be conducted on the data and be incorporated into future mine planning and designs to reduce structural risk in strategic mine planning. Several structures were under-sampled in previous interpretations on the legacy 3D seismic data due to the poor quality of the original data, especially in structurally complex geological terrains. The preliminary test results demonstrate the value of interpreting legacy seismic data using advanced seismic attributes. These results must be incorporated into the geology maps at depth for KDC East and South Deep mines to draw attention to where possible mining obstacles, increased possibility in fall-of-ground events, and changes ore content could be expected.

5. REFERENCES

Ahmadi, O. (2015). Application of the Seismic Reflection Method in Mineral Exploration and Crustal Imaging: Contributions to Hardrock Seismic Imaging (Doctoral dissertation, Acta Universitatis Upsaliensis).

Anderson, N., Shoemaker, M., and Hatheway, A. (1998). Overview of the Shallow Seismic Reflection Technique: in Highway Applications of Engineering Geophysics with an Emphasis on Previously Mined Ground. Missouri Department of Transportation, publishers., Jefferson City, Missouri.

Armstrong, R. A., Compston, W., Retief, E. A., Williams, I. T., and Welke, H. J. (1991). Zircon ion microprobe studies bearing on the age and evolution of the Witwatersrand triad. Precambrian Research, **53**, 243-266.

Bacon, M., Simm, R., and Redshaw, T. (2003). 3-D Seismic Interpretation. Cambridge University Press. 234pp.

Barrie, W. M. (1981). The Stratigraphy And Sedimentology Of The West Rand Basin In The Western Transvaal (Doctoral dissertation, Witwatersrand University).

Barton, E. S., Compston, W., Williams, I. S., Bristow, J. W., Hallbauer, D. K., and Smith, C. B. (1989). Provenance ages for the Witwatersrand Supergroup and the Ventersdorp contact reef; constraints from ion microprobe U-Pb ages of detrital zircons. Economic Geology, **84**, 2012-2019.

Bowen, T. B., Marsh, J. S., Bowen, M. P., and Eales, H. V. (1986). Volcanic rocks of the Witwatersrand triad, South Africa. I: Description, classification and geochemical stratigraphy. Precambrian Research, **31**, 297-324.

Brabham, P.J., Thomas, J., and McDonald, R.J. (2005). The terrestrial shallow seismic reflection techniques applied to the characterization and assessment of shallow sedimentary environments. Journal of Engineering Geology and Hydrogeology, **38**, 23 – 38.

Brown, A. (2001). Understanding seismic attributes. Geophysics, **66**, 47-48.

Brown, A. R. (2011). Interpretation of three-dimensional seismic data. Society of Exploration Geophysicists and American Association of Petroleum Geologists.

Burger, H. R. (1992). Exploration Geophysics of Shallow Subsurface Prentice-Hall. Eaglewood Cliffs, NJ, 489pp.

Button, A. (1986). The Transvaal sub-basin of the Transvaal Sequence. In: Anhaeusser, C.R. and Maske, S., Editors, 1986. Mineral Deposits of Southern Africa, Geological Society of South Africa, Johannesburg, 811–817.

Callaway, J. C., Cahoon, D. R., and Lynch, J. C. (2013). The surface elevation table–marker horizon method for measuring wetland accretion and elevation dynamics. Methods in biogeochemistry of wetlands, **10**, 901-917. https://doi.org/10.2136/sssabookser10.c46.

Cameron, M., Fomel, S., and Sethian, J. (2008). Time-to-depth conversion and seismic velocity estimation using time-migration velocity. Geophysics, **73**, VE205-VE210.

Carcione, J. M., Herman, G. C., and Ten Kroode, A. P. E. (2002). Seismic modeling. Geophysics, **67**, 1304-1325. https://doi.org/10.1190/1.1500393.

Cawthorn, R.G., and Webb, S.J. (2001). Connectivity between the western and eastern limbs of the Bushveld Complex. Tectonophysics, **330**, 195-209.

Cerveny, V. (1987). Ray tracing algorithms in three-dimensional laterally varying layered structures. Seismic tomography, **5**, 99-133.

Cheraghi S., Malehmir, A., and Bellefleur, G. (2012). 3D imaging challenges in steeply dipping mining environment: new lights on acquisition geometry and processing from the Brunswick No. 6 seismic data, Canada. Geophysics, **77**, WC109–WC122.

Chopra, S., Castagna, J., and Portniaguine, O. (2006). Thin-bed reflectivity inversion. In SEG Technical Program Expanded Abstract. Society of Exploration Geophysicists, 2057-2061.

Chopra, S., and Marfurt, K.J. (2007). Seismic Attribute for Prospect Identification and Reservoir Characterization: Geophysical Developments Series. U.S.A: Society of Exploration Geophysicist, 1 – 22.

Clendenin, C. W. (1989). Tectonic influence on the evolution of the early Proterozoic Transvaal Sea, southern Africa. Ph.D. Thesis (unpublished.), University of the Witwatersrand, Johannesburg, South Africa.

Cocher, E., Chauris, H., and Plessix, R. É. (2017). Seismic iterative migration velocity analysis: Two strategies to update the velocity model. Computational Geosciences, **21**, 759-780.

Coward, M., Spencer, R., and Spencer, C. (1995). Development of the Witwatersrand Basin, South Africa. Geological Society, London, Special Publications, **95**, 243-269.

Crutchley, G. J., and Kopp, H. (2018). Reflection and refraction seismic methods. Submarine geomorphology, 43-62.

Dan, M.F.M., Mohamad., E.T., and Komooc, I. (2016). Characteristics of boulders formed in tropical weathered granite: A review. Jurnal Teknologi, **78**, 23-30. https://doi.org/10.11113/jt.v78.9635.

Dankert, B. T., and Hein, K. A. (2010). Evaluating the structural character and tectonic history of the Witwatersrand Basin. Precambrian Research, **177**, 1-22.

De Beer, J. H. (Ed.). (2016). The History of Geophysics in Southern Africa. African Sun Media.

Dentith, M. and Mudge, S. (2014). Geophysics for the Mineral Exploration Geoscientist. New York: Cambridge University Press. 425pp.

Donoso, G. A., Malehmir, A., Pacheco, N., Araujo, V., Penney, M., Carvalho, J., Spicer, B., and Beach, S. (2020). Potential of legacy 2D seismic data for deep targeting and structural imaging at the Neves–Corvo massive sulphide-bearing deposit, Portugal. Geophysical Prospecting, **68**(1-Cost-Effective and Innovative Mineral Exploration Solutions), 44-61.

Dorn, G. A. (1998). Modern 3-D seismic interpretation: The Leading Edge, **17**, 1262-1272.

Ebrom, D., Li, X., McDonald, J., and Lu, L. (1995). Bin spacing in land 3-D seismic surveys and horizontal resolution in time slices. The Leading Edge, **14**, 37-40.

Eriksson, P. G., and Altermann, W. (1998). An overview of the geology of the Transvaal Supergroup dolomites (South Africa). Environmental geology, **36**, 179-188.

Eriksson, P. G., Hattingh, P. J., and Altermann, W. (1995). An overview of the geology of the Transvaal Sequence and Bushveld Complex, South Africa. Mineralium Deposita, **30**, 98-111.

Eriksson, P.G., and Reczko, B.F.F. (1995). The sedimentary and tectonic setting of the Transvaal Supergroup floor rocks to the Bushveld Complex. Journal of African Earth Sciences, **21**, 487–504.

Eriksson, P. G., Schweitzer, J. K., Bosch, P. J. A., Schereiber, U. M., Van Deventer, J. L., and Hatton, C. J. (1993). The Transvaal sequence: an overview. Journal of African Earth Sciences (and the Middle East), **16**, 25-51.

Fu, L. Y. (2002). Born dispersion equation and Kirchhoff migration in laterally heterogeneous media. In SEG Technical Program Expanded Abstracts, Society of Exploration Geophysicists, 1113-1116.

Gebrande, H. (1976). A seismic-ray tracing method for two-dimensional inhomogeneous media. In Explosion seismology in Central Europe: data and results. Berlin, Heidelberg: Springer Berlin Heidelberg, 162-167.

Gillot E., Gibson M., Verneau D. and Laroche S. (2005). Application of high-resolution 3D seismic to mine planning in shallow platinum mines. First Break, **23**, 59–64.

Gilmore, C., Jeffrey, I., and LoVetri, J. (2006). Derivation and comparison of SAR and frequency-wavenumber migration within a common inverse scalar wave problem formulation. IEEE transactions on geoscience and remote sensing, **44**, 1454-1461.

Gray, S.H. (2016). Seismic imaging. In Encyclopedia of Exploration Geophysics. Society of Exploration Geophysicists. S1-1.

Hagelund, R., Levin, S. A. (2017). Seg-y_r2. 0: Seg-y Revision 2.0 Data Exchange Format. Society of Exploration Geophysicists, Houston.

Hamilton, J. (1977). Isotope and trace element studies of the Great Dyke and Bushveld mafic phase and their relation to Early Proterozoic magma genesis in southern Africa. Journal of Petrology, **18**, 24–52.

Hardage, B. A. (1997). Principles of onshore 3-D seismic design (No. 5). Bureau of Economic Geology, University of Texas at Austin.

Harmer, R. E., and Farrow, D. (1995). An isotopic study on the volcanics of the Rooiberg Group: age implications and a potential exploration tool. Mineralium Deposita, **30**, 188-195.

Herron, D. (2011). First steps in seismic interpretation: Geophysical monograph series no. 16, Tulsa: Society of Exploration Geophysicists. 203pp.

Herron, D. (2014). Pitfalls in horizon autopicking. Interpretations, **3**, SB1-SB4.

Hunt, J.P. (2006). Geological Characteristics of Iron Oxide-Copper-Gold (IOCG) Type Mineralisation in the Western Bushveld Complex (Master's by dissertation). University of the Witwatersrand, Johannesburg.

Jackson, M. C. (1992). A review of the late Archean volcano-sedimentary Dominion Group and implications for the tectonic setting of the Witwatersrand Supergroup, South Africa. Journal of African Earth Sciences (and the Middle East), **15**, 169-186.

Jahn, B. M., Bertrand-Sarfati, J., Morin, N., and Mace, J. (1990). Direct dating of stromatolitic carbonates from the Schmidtsdrif Formation (Transvaal Dolomite), South Africa, with implications on the age of the Ventersdorp Supergroup. Geology, **18**, 1211-1214.

Jones, M. Q. W. (2018). Virgin rock temperatures and geothermal gradients in the Bushveld Complex. Journal of the Southern African Institute of Mining and Metallurgy, **118**, 671-680.

Kallweit, R. S., and Wood, L. C. (1982). The limits of resolution of zero-phase wavelets. Geophysics, **47**, 1035-1046.

Kearey, P., Brooks, M., and Hill, I. (2002). An Introduction to Geophysical Exploration, 3rd ed. ix + 262 pp. Oxford: Blackwell Science. Price 29.95 (paperback). ISBN 0 632 04929 4. DOI: 10.1017/S0016756803378021.

Keydar, S., Shtivelman, V., and Arzi, A. (2018). Three–Dimensional Seismic Diffraction Imaging for Detecting Near-Surface Inhomogeneities. Geophysics.

Kinnaird, J. A. (2005). The Bushveld Large Igneous Province. The Review Paper, The University of the Witwatersrand, South Africa. Retrieved from http://www.largeigneousprovinces.org/sites/default/files/BushveldLIP.pdf

Kirk, J., Ruiz, J., Chesley, J., Walshe, J., and England, G. (2002). A major Archean, gold-and crust-forming event in the Kaapvaal Craton, South Africa. Science, **297**, 1856-1858.

Koivisto E., Malehmir A., Heikkinen P., Heinonen S., and Kukkonen I. (2012). 2D reflection seismic investigations in the Kevitsa Ni-Cu-PGE deposit, northern Finland. Geophysics **77**, WC149–WC162.

Kositcin, N., McNaughton, N. J., Griffin, B. J., Fletcher, I. R., Groves, D. I., and Rasmussen, B. (2003). Textural and geochemical discrimination between xenotime of different origin in the Archaean Witwatersrand Basin, South Africa. Geochimica et Cosmochimica Acta, **67**, 709-731.

Lenhardt, N., and Eriksson, P.G. (2012). Volcanism of the Palaeoproterozoic Bushveld Large Igneous Provinces: the Rooiberg Group, Kaapvaal Craton, South Africa. Precambrian Research special volume for Wulf Mueller, 3 – 11.

Longde, S. U. N., Chaoliang, F. A. N. G., Liming, S. A., Ping, Y., and Zandong, S. U. N. (2015). Innovation and prospect of geophysical technology in the exploration of deep oil and gas. Petroleum Exploration and Development, **42**, 454-465.

Malan, S. P. (1959). The Petrology and Mineralogy of the Rocks of the Dominion Reef System near Klerksdorp. (Doctoral dissertation, University of the Witwatersrand).

Malehmir, A., Durrheim, R., Bellefleur, M., Urosevic, M., Juhlin, C., White, D., Milkerit, B., and Campbell, G. (2012a). Seismic methods in mineral exploration and mine planning: A general overview of past and present case histories and a look into the future. Geophysics, **77**, WC173–WC190.

Malehmir, A., Bergman, B., Andersson, B., Sturk, R., and Johansson, M. (2018). Seismic imaging of dyke swarms within the Sorgenfrei–Tornquist Zone (Sweden) and implications for thermal energy storage. Solid Earth, **9**, 1469-1485.

Malehmir, A., Donoso, G., Markovic, M., Maries, G., Dynesius, L., Brodic, B., Pecheco, N., Marsden, P., Bäckström, E., Penney, M., and Araujo, V. (2019). Smart Exploration: from legacy data to state-of-the-art data acquisition and imaging. First Break, **37**, 71-74.

Manzi, M.S.D., Gibson, M.A.S., Hein, K.A.A., King, N. and Durrheim, R.J. (2012a). Application of 3D seismic techniques to evaluate ore resources in the West Wits Line goldfield and portions of the West Rand goldfield, South Africa. Geophysics, **77**, 163 –171.

Manzi, M.S.D., Durrheim, R.J., Hein, K.A.A., and King, N. (2012b). 3D edge detection seismic attributes used to map potential conduits for water and methane in deep gold mines in the Witwatersrand basin, South Africa. Geophysics, **77**, 133 – 147.

Manzi, M. S., Hein, K. A., King, N., and Durrheim, R. J. (2013a). Neoarchaean tectonic history of the Witwatersrand Basin and Ventersdorp Supergroup: New constraints from high-resolution 3D seismic reflection data. Tectonophysics, **590**, 94-105.

Manzi, M. S. D., Hein, K. A. A., Durrheim, R., and King, N. (2013b). Seismic attribute analysis to enhance detection of thin gold-bearing reefs: South Deep gold mine, Witwatersrand basin, South Africa. Journal of Applied Geophysics, **98**, 212-228.

Manzi, M. S., Hein, K. A., Durrheim, R. J., and King, N. (2014). The Ventersdorp Contact Reef model in the Kloof Gold Mine as derived from 3D seismics, geological mapping and exploration borehole datasets. International Journal of Rock Mechanics and Mining Sciences, **66**, 97-113.

Manzi, M., Malehmir, A., and Durrheim, R. J. (2018). Improved Subsurface Imaging through Re-processing of Legacy 2D Seismic Data-A Case Study from a Deep South African Gold Mine. European Association of Geoscientists and Engineers. In 2nd Conference on Geophysics for Mineral Exploration and Mining, **1**, 1-5.

Manzi, M., Malehmir, A., and Durrheim, R. (2019). Giving the legacy seismic data the attention they deserve. First Break, **37**, 89-96.

Markovic, M., Maries, G., Malehmir, A., von Ketelhodt, J., Bäckström, E., Schön, M., and Marsden, P. (2020). Deep reflection seismic imaging of iron-oxide deposits in the

Ludvika mining area of central Sweden. Geophysical Prospecting, **68**(1-Cost-Effective and Innovative Mineral Exploration Solutions), 7-23.

Martini, J.E.J. (1979). A copper-bearing bed in the Pretoria Group in the northeastern Transvaal. Special Publication Geological Society of South Africa**, 6**, 65–72.

Milkereit, B., Eaton, D., Wu, J., Perron, G., Salisbury, M. H., Berrer, E. K., and Morrison, G. (1996). Seismic imaging of massive sulfide deposits; Part II, Reflection seismic profiling. Economic Geology, **91**, 829-834.

Mondol, N.H. (2010). Seismic exploration. Petroleum Geoscience, **1**, 375-402.

Moore, J. M., Tsikos, H., and Polteau, S. (2001). Deconstructing the Transvaal Supergroup, south Africa: implications for Palaeoproterozoic palaeoclimate models. Journal of African Earth Sciences, **33**, 437-444.

Muijs, R., Robertsson, J. O., and Holliger, K. (2007). Prestack depth migration of primary and surface-related multiple reflections: Part I—Imaging. Geophysics, **72**, S59-S69.

Mutshafa, N., Manzi, M. S., Westgate, M., James, I., Brodic, B., Bourdeau, J. E., Durrheim, R.J., and Linzer, L. (2022). Seismic imaging of the gold deposit and geological structures through reprocessing of legacy seismic profiles near Kloof–Driefontein Complex East Mine, South Africa. Geophysical Prospecting. *http://dx.doi.org/10.1111/1365-2478.13283*

Myers, R. E., McCarthy, T. S., and Stanistreet, I. G. (1990). A tectono-sedimentary reconstruction of the development and evolution of the Witwatersrand Basin, with particular emphasis on the Central Rand Group. South African Journal of Geology, **93**, 180-201.

Nainggolan, T.B., and Subarsyah, S. (2014). Suppressing Diffraction Effect Using Kirchhoff Pre-stack TIME Migration On 2D Seismic Multichannel Data At Flores Sea. Bulletin of the Marine Geology, **29**, 71-80, doi:10.32693/bomg.v29i2.67.

Nanda, N. C. (2016). Seismic data interpretation and evaluation for hydrocarbon exploration and production: A practitioner's guide. Springer.

Nel, L. T., Jacobs, H., Allan, J. T., and Bozzoli, G. R. (1937). Wonderstone. Geological Series Bull. Union of South African Geological Survey, **8**.

Ofterdinger, U., MacDonald, A. M., Comte, J.C., and Young, M. E. (2019). Groundwater in fractured bedrock environments: managing catchment and subsurface resources – an introduction. Geological Society, London, Special Publications, **479**, 1-9. https://doi.org/10.1144/SP479-2018-170.

Onyebueke, E. O., Manzi, M. S. D., and Durrheim, R. J. (2018). High-resolution shallow reflection seismic integrated with other geophysical methods for hydrogeological prospecting in the Nylsvley Nature Reserve, South Africa. Journal of Geophysics and Engineering, **15**, 2658-2673.

Pretorius C.C., Muller M.R., Larroque M. and Wilkins C. (2003). A review of 16 years of hardrock seismics on the Kaapvaal Craton, Hardrock Seismic Exploration. In: Developments in Geophysics Series. (ed. Eaton, D., Salisbury, M. and Milkereit, B.) SEG, Houston. 2003, 247–268. https://doi.org/10.1190/1.9781560802396.ch16.

Randen, T., Pedersen, S.I., and Sønneland, L. (2001). Automatic Extraction of Fault Surfaces from Three-Dimensional Seismic Data. SEG Technical Program Expanded Abstracts, 551–554.

Rijks, E.J.H., and Jauffred, J.C.E.M. (1991). Attribute extraction: An important application in any detailed 3D interpretation study. The Leading Edge of Exploration, **10**, 11–19.

Ristow, D., Hinz, K., Hauschild, J., Gindler, T., Berhorst, A., and Bönnemann, C. (2003). Imaging the subsurface with 2-D and 3-D seismic data. Ocean Margin Systems, 33-55.

Rogers, D. V. (2015). Types of Earthquakes waves. Retrieved 15 May 2019, from https://allshookup.org/quakes/waveprop.htm.

Rost, S., and Thomas, C. (2009). Improving seismic resolution through array processing techniques. Surveys in Geophysics, **30**, 271-299.

Robb, L. J., and Meyer, F. M. (1995). The Witwatersrand Basin, South Africa: geological framework and mineralization processes. Ore Geology Reviews, **10**, 67-94.

Rundle, C. C., and Snelling, N. J. (1977). The geochronology of uraniferous minerals in the Witwatersrand Triad; an interpretation of new and existing U-Pb age data on rocks and minerals from the Dominion Reef, Witwatersrand and Ventersdorp Supergroups. Philosophical Transactions of the Royal Society of London. Series A, Mathematical and Physical Sciences, **286**, 567-583.

Russer, P., and Russer, J. A. (2015). Some remarks on the transmission line matrix (TLM) method and its application to transient EM fields and to EMC problems. Computational Electromagnetics-Retrospective and Outlook: In Honor of Wolfgang JR Hoefer, 29-56.

Salisbury, M. H., Milkereit, B., and Bleeker, W. (1996). Seismic imaging of massive sulfide deposits; Part I, Rock properties. Economic Geology, **91**, 821-828.

Sehoole, L.T.C. (2019). Application of 3D seismics to enhance mapping of potholes in the western Bushveld Complex, South Africa (Master's by dissertation). University of the Witwatersrand, Johannesburg.

Stevenson, F., and Durrheim, R. J. (1997). Reflection seismic for gold, platinum and base metal exploration and mining in Southern Africa. In Proc. of Exploration, **97**, 391-398.

Schlumberger. (2015). The Oilfield Glossary: Where the oil field meets the dictionary. Retrieved from: http://www.glossary.oilfield.slb.com/Terms/v/velocity_analysis.aspx.

Schmelzbach, C., Horstmeyer, H., and Juhlin, C. (2007). Shallow 3D seismic-reflection imaging of fracture zones in crystalline rock. Geophysics, **72**, B149-B160.

Schweitzer, J. K., Hatton, C. J., and De Waal, S. A. (1995). Economic potential of the Rooiberg Group: volcanic rocks in the floor and roof of the Bushveld Complex. Mineralium Deposita, **30**, 168-177.

Shao, J., Zhang, Q., Wu, X., Lei, Y., Wu, X., and Wang, Z. (2020). Investigation on the water flow evolution in filled fracture under seepage-induced erosion. Water, **12**, 3188pp. https://doi.org/10.3390/w12113188.

Sheriff, R. E. (2002). Encyclopedic dictionary of applied geophysics. U.S.A: Society of exploration geophysicists, 25-400.

Skursch, O., Corfu, F., Tegner, C., Lesher, C. E., Andreasen, R., Hagen-Peter, G. A., and Vervoort, J. D. (2022). Zircon U–Pb chronology and Hf isotopes of the Lebowa Granite Suite and petrogenesis of the Bushveld Complex, South Africa. Contributions to Mineralogy and Petrology, **177**, 26.

Smith, G. D., Smith, G. D., and Smith, G. D. S. (1985). Numerical solution of partial differential equations: finite difference methods. Oxford university press.

South African Committee for Stratigraphy (SACS). (1980). Stratigraphy of South Africa. Part I: Lithostratigraphy of the Republic of South Africa, South West Africa/ Namibia and the Republics of Bophuthatswana, Transkei and Venda. Handbook of the Geological Survey of South Africa, **8**, 690pp.

Spitzer, R., Green, A. G., and Nitsche, F. O. (2001). Minimizing field operations in shallow 3-D seismic reflection surveying. Geophysics, **66**, 1761-1773.

Stolt, R. H. (1978). Migration by Fourier transform. Geophysics, **43**, 23-48.

Taner, M. T., Koehler, F., and Sheriff, R. E. (1979). Complex seismic trace analysis. Geophysics, **44**, 1041-1063.

Taner, M. T. (2001). Seismic attributes: Canadian Society of Exploration Geophysicists Recorder, **26**.

Tankard, A. J., Jackson, M. P. A., Eriksson, K. A., Hobday, D. K., Hunter, D. R. and Minter, W. E. L. (1982). Crustal evolution of southern Africa: 3.8 billion years of Earth history. Springer-Verlag, N. Y., Berlin, 423pp.

Terracin, M., and Manzi, M. (2017). Spatial corrections for post-stack time migrated legacy 2D seismic data: a case study from the Witwatersrand Basin, South Africa. In South African Geophysical Association Biennial Conference, Sommerset West, Cape Town.

van der Kruk, J. (2005). Reflection seismic I (University of the Witwatersrand Geophysics Honours notes 2015). Zurich, Germany: Institut fur Geophysik.

Van der Westhuizen, W. A., De Bruiyn, H., and Meintjes, P. G. (1991). The Ventersdorp supergroup: an overview. Journal of African Earth Sciences (and the Middle East), **13**, 83-105.

van Veldhuizen, E. J. (2006). Integrated approach to 3-D seismic acquisition geometry analysis: Emphasizing the influence of the inhomogeneous subsurface.

Visser, J. N. J. (1971). The deposition of the Griquatown Glacial Member in the Transvaal Supergroup. South African Journal of Geology, **74**, 187-199.

von Backstrom, J. W. (1981). Dominion reef group, Western Transvaal, South Africa (No. USGS-PP--1161-A-BB).

von Ketelhodt, J. K., Manzi, M. S., and Durrheim, R. J. (2019). Post-stack denoising of legacy reflection seismic data: implications for coalbed methane exploration, Kalahari Karoo Basin, Botswana. Exploration Geophysics, **50**, 667-682.

Wadas, S. H. (2018). High-resolution shear wave reflection seismics and borehole seismics as tools for the imaging and the characterization of near-surface subrosion structures. Technische Universitaet Berlin (Germany).

Walraven, F. (1987). Textural, geochemical and genetic aspects of the granophyric rocks of the Bushveld Complex. Memoir 72, Geological Survey South Africa, **145**.

Walraven, F., and Martini, J. (1995). Zircon Pb-evaporation age determination of the Oak Tree Formation sequence: Implications for Transvaal-Griqualand West basin correlations. South African Journal of Geology, **98**, 58-67.

Watchorn, M. B. (1981). Continental sedimentation and volcanism in the Dominion Group of the Western Transvaal: a review. South African Journal of Geology, **84**, 67-73.

Widess, M. B. (1973). How thin is a thin bed?. Geophysics, **38**, 1176-1180.

Wilson, J., Ferré, E. C., and Lespinasse, P. (2000). Repeated tabular injection of high-level alkaline granites in the eastern Bushveld, South Africa. Journal of the Geological Society, **157**, 1077-1088.

Winter, H. D. (1976). A lithostratigraphic classification of the Ventersdorp succession. South African Journal of Geology, **79**, 31-46.

Yilmaz, Ö. (2001) Seismic Data Analysis: Processing, Inversion, and Interpretation of Seismic Data. Society of Exploration Geophysicists.

Zhang, H., Krooswyk, S., and Ou, J. (2015). High speed digital design: design of high speed interconnects and signaling. Elsevier.

6. SUMMARY OF SCIENTIFIC CONTRIBUTIONS

Paper I (Published): *"Mutshafa, N., Manzi, M. S., Westgate, M., James, I., Brodic, B., Bourdeau, J. E., Durrheim, R.J., and Linzer, L. (2022). Seismic imaging of the gold deposit and geological structures through reprocessing of legacy seismic profiles near Kloof-Driefontein Complex East Mine, South Africa" Geophysical Prospecting* http://dx.doi.org/10.1111/1365-2478.13283

The paper presents the reprocessing results of the 1988 legacy seismic data acquired in the West Rand goldfield (South Africa) for deep mineral exploration and mine planning. These legacy 2D seismic data were reprocessed using the latest processing algorithms to improve imaging of the gold deposit and complex geological structures down to 3.5 km depth below the ground surface. Various migration workflows were tested, namely, pre-stack time migration (PreSTM), pre-stack depth migration (PreSDM), and post-stack time migration (PostSTM). The PreSDM provided better imaging of the deep-seated orebody due to its ability to honour complex lateral variations in the velocity field, whereas the PreSTM and PostSTM enhanced the continuity of the near-surface reflections below the dolomitic rocks.

As the primary author, I created the geometry of the two legacy profiles that came with unreliable source and receiver elevations using Globe Claritas software. I used Shuttle Rader Topography Mission (SRTM) data to determine reliable elevations. I also prepared the manuscript, generated the figures used in the manuscript, with input from the second author Musa Manzi (Supervisor). The third author assisted with the processing and provided the code to compute the 1D synthetic seismogram using MATLAB software. The fourth author assisted with the computation of the first breaks traveltime tomograms and reprocessing data up to migration. Authors five to eight assisted with reviewing the manuscript. Additionally, I interpreted the seismic profiles and integrated them with the surface geology.

Paper II (Under review): *"Mutshafa, N., Manzi, M. S., James, I. Seismic imaging of deep-seated gold deposit and host rocks through reappraisal of legacy seismic data in the Fochville mining area, South Africa"* (submitted to *Geophysical Prospecting*).

The manuscript demonstrates how the reappraisal of legacy reflection seismic data may be beneficial in mineral exploration by applying cutting-edge seismic processing methods to improve imaging resolution. A detailed interactive velocity analysis guided by constant

velocity stacks were performed to construct a velocity model for dip-moveout and then subjected the stack section to F-x deconvolution to increase the signal-to-noise ratio. The Kirchhoff pre-stack time migration results showed that we can explore the deep-seated mineralization (Ventersdorp Contact Reef) at depth greater than 3 km and the results are in agreement with the borehole logs. Comparing the results with the 2D legacy data, the reprocessed seismic section shows significant improvements in imaging and reflector delineation that were produced using modern processing techniques. The comparison was only made with the unmigrated stacked seismic section. Borehole logs and surface geological information were used to constrain the interpretation of the 2D legacy reflection seismic data.

I prepared the manuscript and generated the figures with input from the second author. The third author assisted with the computation of the first breaks travel-time tomograms and reprocessing data. The third author also helped with reviewing the manuscript. I reprocessed the profile, from reconstructing coordinates and elevation of receivers and sources to create geometry. I was also responsible for the interpretation of the seismic data which was constrained by borehole logs and surface geology.

Paper III (Published): *"Gomo S., Rapetsoa M. K., Manzi M. S. D., Onyebueke E., Dildar J., Sihoyiya M., Mutshafa, N., Harrison W., Bourdeau J E., Brovko, O., James I., Cooper G. R. J., Scheiber S., Durrheim R. J. (2023). Integrated geophysical methods for boulder delineation to improve mining*" *Geophysical Prospecting* *http://dx.doi.org/10.1111/1365-2478.13322*

The manuscript employs an integrated geophysical approach, using magnetics, electrical resistivity tomography, seismic refraction tomography, ground penetrating radar and borehole data, to map boulders and geological features (e.g., lithologies, fractures, iron-rich ultramafic pegmatites, weathering zones, and thickness of the topsoil) that have the potential to impede mining operations at a mine in the Bushveld Complex, South Africa. Such features often pose a challenge for mining activities as they introduce complexities and delays in mining, drilling, blasting and excavation programs, which subsequently increase mining costs.

I was part of the crew that acquired all the datasets used on this manuscript. The 8th author and I assisted with the processing of resistivity data. The 2nd author and I assisted with the geometry set up of the seismic data, first break picking and processing. I reviewed the manuscript, while the first author prepared the manuscript and generated the figures used. The 10th author assisted with magnetic 3D modeling. The 11th author assisted with producing P-

wave tomography inversions; The 4th author assisted with GPR data processing and interpretation. The 3rd and 9th to 14th authors assisted with the manuscript supervision and others assisted with manuscript review.

Paper IV (Under review): *"Rapetsoa, M. K., Gomo, S., Manzi, M. S. D., James, I., Dildar, J., Sihoyiya, M., Mutshafa, N., Durrheim, R.J. Multi-geophysical methods for characterizing fractures in an open pit mine, western Bushveld Complex, South Africa"* (submitted to *Geophysical Prospecting*).

The manuscript demonstrates that multi-geophysical methods can be utilized to delineate fractures and faults in an active open pit mine, western Bushveld Complex, South Africa. Open pit mines are faced with a challenge of rock slope stability due to geological structures (fractures, faults and dykes) that compartmentalize the rock mass. Geophysical surveys (seismic, magnetic and electrical methods) were conducted in an open pit area at Tharisa mine, Marikana, Northwest Province, with the goal to delineate fractures that may be potential conduits for water migration into the pit. The data have revealed fractures within the open pit, suggesting multiple factors that contributed to the fracture system such as (1) geologically induced fractures that were reactivated during the intrusion of dykes, and (2) induced fractures due to mine blasting. The use of multiple geophysical methods was useful in the interpretation and imaging of structures with different geometry and orientation at different depths.

I participated as part of the crew that acquired all the datasets used on this manuscript. I assisted with the processing and interpretation of resistivity data. The 1st author prepared the manuscript and generated the figures with the guidance of 3rd author. The 4th author assisted with producing P-wave tomography inversions and processing seismic data. The 8th author assisted with the review of the manuscript. Other authors assisted with reviewing the manuscript and were also part of the crew that acquired the data sets used in this manuscript.

Paper V (Under review): *"Gomo, S., Mutshafa, N., Manzi, S.D., Bourdeau, J. E., Brodic, B., James, I., Cooper, R.J., Durrheim, R. J. Integration of ground geophysical methods to characterize near-surface groundwater aquifers within an active mine"* (submitted to *Near Surface Geophysics*).

The manuscript demonstrates the potential of near-surface geophysics for hydrological purposes in an open pit mine. To map and better understand the weathered aquifer system in the region and its relation to mine fissure inflow, we conducted seismic refraction tomography (SRT), multichannel analysis of surface waves (MASW) and electrical resistivity tomography (ERT) surveys. The study objectives are (1) to image and understand the weathered aquifer zone in the top ~35 meters of the ground, (2) to assess the overlying materials to infer the interaction between surface and groundwater, and (3) to determine the potential impact of mining activity on near-surface aquifers in the region. The study successfully demonstrates that geophysical methods can help bridge hydrological knowledge gaps, offering valuable insights for water-stressed countries such as South Africa. For all sites, the results reveal the prevalence of extensive and deep weathering, possible high hydraulic conductivity zones, and the variation in weathering with depth, mainly associated with the overburden zone, semi-weathered bedrock zone (which hosts the semi-weathered aquifer), and the crystalline bedrock zone, where aquifers are associated with joints and fractures. However, these variations generally show a strong correlation with each other.

I was part of the crew that acquired all the datasets used on this manuscript. I assisted with the processing and interpretation of resistivity data, and I also assisted with the geometry set up of the seismic data, first break picking. I reviewed the manuscript, while, the first author wrote the manuscript under the supervision of the 3rd to 8th authors, and generating figures. The 6th author assisted with producing P-wave tomography inversions.

7. Paper I: Seismic imaging of the gold deposit and geological structures through reprocessing of legacy seismic profiles near Kloof–Driefontein Complex East Mine, South Africa

Ndamulelo Mutshafa[1], Musa S.D. Manzi[1*], Michael Westgate[1], Ian James[1,2], Bojan Brodic[1,3], Julie E. Bourdeau[4], Raymond J. Durrheim[1], Lindsay Linzer[1,5]

[1]*School of Geosciences, University of the Witwatersrand, PBag 3, WITS, Johannesburg 2050, Republic of South Africa,*

[2] *Southern Geoscience Consultants, West Perth, WA, Australia,*

[3]*Department of Earth Sciences, Uppsala University, Sweden,*

[4]*Geological Survey of Canada, 601 Booth Street, Ottawa, Ontario, K1A 0E9, Canada.*

[5]*SRK House, 265 Oxford Rd, Illovo, Johannesburg, 2196, Republic of South Africa*

**E-mail:* musa.manzi@wits.ac.za

ABSTRACT

Two legacy reflection seismic profiles were acquired in 1988, north of the Kloof-Driefontein Complex East (KDC East) Mine in the West Rand goldfield (South Africa), for the purpose of gold exploration and mine planning. These legacy 2D seismic data have been reprocessed using the latest processing tools to improve imaging. Special interest is given to the Black Reef Formation, which hosts a known gold orebody. The original legacy data are of poor quality, especially in areas that are dominated by dolomitic outcrops. To improve the quality of the data, special attention was given to the refraction static correction to enhance the continuity of the reflections below dolomitic rocks. Refraction seismic tomograms from both profiles exhibit three-layer P-wave velocity models: 1) topsoil (1 000 - 2 000 m/s), 2) a weathered layer ranging from ca. 100 to 300 m in thickness (2 000 - 5 000 m/s), 3) and bedrock (> 5 000 m/s). Seismic profile OK-212 shows poor imaging of the Black Reef Formation because of the scattering of seismic energy in the near-surface due to dolomites from the Transvaal Supergroup, while seismic profile OK-213 exhibits south-dipping reflections that are associated with the Black Reef Formation. To improve the structural imaging resolution, we tried pre-stack time migration (PreSTM), pre-stack depth migration (PreSDM), and post-stack time migration (PostSTM) using the Kirchhoff algorithm. Pre-stack depth migration most improved the imaging of deeper reflections due to its ability to honour complex lateral variations in the

velocity field. Both PreSTM and PostSTM enhanced the continuity of the near-surface reflections below the dolomitic rocks.

Keywords: Seismics, data processing, imaging, mining, exploration

INTRODUCTION

The mining industry has long relied on traditional geological mapping and drilling for mine planning. However, there is a growing recognition that high-resolution exploration techniques for deep targeting (such as reflection seismic) must be employed if the mineral exploration and mining industry are to maintain long-term profitability (Milkereit *et al*. 1996; Salisbury *et al*. 1996; Malehmir *et al*. 2012). The seismic reflection method is a geophysical method that uses the reflection of seismic waves to obtain images of the Earth's subsurface (Yilmaz, 2001; Manzi *et al*. 2012). Compared to other geophysical methods, which lose resolution with increasing depth, seismic methods provide high-resolution images of deep-seated geologic structures that may host mineral deposits at depths exceeding 1 km (Malehmir *et al*. 2012; Manzi *et al*. 2012). This property, among others, led the mining industry to take advantage of the seismic reflection method and seek solutions to prospecting problems (Malehmir *et al*. 2012; Manzi *et al*. 2012). Since the early reports of Reid *et al*. (1979), the seismic reflection method has proven its capability in mineral exploration and mine planning, mainly in Europe, South Africa, Australia and Canada (i.e., Eaton *et al*. 2003; Malehmir *et al*. 2012; Markovic *et al*. 2020, and references therein). Stevenson and Durrheim (1997) presented seminal case studies on the application of reflection seismology for gold, platinum and base metal exploration in southern Africa in the early 1980s. Following these case studies, both 2D and 3D reflection seismic studies have been conducted for mineral exploration and mine planning purposes across South Africa (Pretorius *et al*. 1989; Campbell *et al*. 1990; Campbell, 2011; Manzi *et al*. 2012; 2013; 2014).

Although acquiring new data has benefits, among others, from instrumentation that have a wider dynamic range and a large number of channels, the reappraisal of legacy reflection seismic data has shown to deliver value, particularly if they are from a brownfield setting, near or even above active mines (Malehmir *et al*. 2014; 2020). Legacy data have advantages such as: 1) being less contaminated by noise from mining activities (e.g., blasting, drilling, rock crushing, etc.); 2) being less contaminated by electric/electromagnetic noise; 3) have been

acquired in places that presently may be unavailable for new surveys; and 4) ultimately coming at a lower cost compared to new acquisition campaigns (i.e., Donoso *et al.* 2020 and references therein). Reprocessing of reflection seismic legacy data using the latest processing tools can provide valuable new information for both mineral exploration and mine planning purposes (Malehmir *et al.* 2019; Manzi *et al.* 2019; Donoso *et al.* 2020). South African hard rock reflection seismic data, in particular, is worthy of reappraisal. More than 20 000 line-km of 2D data were acquired in the 1980s and 1990s, covering several important mining regions (Durrheim, 2016; Terracin and Manzi 2017; von Ketelhodt *et al.* 2019). New insights obtained from legacy data may profit future mine planning operations by finding new ore deposits or constraining discovered ones with greater accuracy, ultimately giving a superior estimation of resources and providing information that may assist with, for example, siting and sinking future shafts (Manzi *et al.* 2019; Westgate, 2020). In addition, applying modern processing algorithms to legacy seismic data results in improved structural resolution and more accurate delineation of deeper ore deposits (Manzi *et al.* 2018a, b).

In this paper, we present the results from re-processing two legacy 2D reflection seismic profiles acquired near the Kloof-Driefontein Complex (KDC) East Mine in the West Rand goldfield (Witwatersrand Basin, South Africa). We show the processing results from pre-stack time migration (PreSTM), pre-stack depth migration (PreSDM), and post-stack time migration (PostSTM) approaches using the Kirchhoff algorithm. Seismic delineation of the Black Reef (BLR) Formation is of particular interest in this study because of its potential economic significance, and the fact that it is one of the few shallow (< 2 km) ore deposits targeted for future mining. Application of different migration algorithms allowed for improved mapping of the BLR and its associated geological structures. The results from this study clearly demonstrate the benefits of recovering and reprocessing legacy seismic data using the latest seismic processing tools to improve mineral exploration and mining.

GEOLOGICAL SETTING

The Kaapvaal Craton of southern Africa is one of the world's best-preserved Archean-aged crustal segments (Fig. 1a). The oldest rocks (hereon referred to as basement rocks) of the craton are 3.66 to 3.11 Ga granitoid-greenstone terranes (Brandl *et al.* 2006; Kröner *et al.* 2019).

Overlying the granitoid-greenstone terranes are metasedimentary sequences belonging to the Mesoarchean-aged Witwatersrand Basin, which is world-renowned for its gold endowment (Frimmel, 2019). At the base of the basin lies the Dominion Group rocks dated variously at 3 086 ± 3 (Armstrong *et al*. 1991) and 3 074 ± 6 Ma (Robb *et al*. 1992) which consist of a thin basal siliciclastic unit as well as a bimodal volcanic sequence. Overlying the Dominion Group is the Witwatersrand Supergroup, which is further divided into the West and Central Rand groups (Figs. 1 and 2). The West Rand Group consists mainly of marine quartzite and shale with minor conglomerate beds (Barton *et al*. 1989; Myers *et al*. 1990; Frimmel, 2019), while the Central Rand Group is mainly characterized by fluvial to fluvio-deltaic quartzite and conglomerate units, which are separated by erosional unconformities (Barton *et al*. 1989; Catuneanu, 2001). Altogether, the Witwatersrand Supergroup has produced about one-third of all gold mined in history (ca. 53 000 t Au; Frimmel, 2019). Most of the gold is found in thin beds of quartz-pebble conglomerates, locally referred to as "reefs".

The predominantly volcanic Neoarchean to Paleoproterozoic Ventersdorp Supergroup unconformably overlies the Witwatersrand Supergroup (Van der Westhuizen *et al*. 1991; Rundle and Snelling, 1977; Manzi *et al*. 2014). Most notably, the Ventersdorp Contact Reef (VCR) at the base of the Ventersdorp Supergroup is gold-bearing and currently mined southeast of Johannesburg (West Rand goldfield; Manzi *et al*. 2013, 2014).

The Ventersdorp Supergroup is in turn unconformably overlain by the Neoarchean to Paleoproterozoic Transvaal Supergroup sediments (2.64 – 2.06 Ga; SACS, 1980; Eriksson *et al*. 1995, 2006; Manzi *et al*. 2013; Tucker *et al*. 2016). The Transvaal Supergroup is further subdivided into (from stratigraphic bottom to top): 1) Protobasinal rocks, 2) Black Reef Formation (BLR), 3) Chuniespoort Group, and 4) Pretoria Group. Protobasinal rocks (a descriptive term rather than a formal group) are characterized by mudrocks, sandstones, and basaltic to rhyolitic volcanic rocks. The BLR (2.59 Ga; Henry and Master, 2008) is characterized by mature quartz arenites with lesser amounts of conglomerates and mudrocks (Nwaila *et al.* 2020). Within the BLR is a thin, gold-endowed conglomerate bed that is referred to as the Black Reef orebody. This orebody resembles Witwatersrand-type gold deposits in terms of mineralogy and economic concentration of gold (Fuchs *et al*. 2016). Sedimentary rocks of the BLR were deposited under fluviatile conditions and later in a shallow epicratonic marine environment (Els *et al.* 1995).

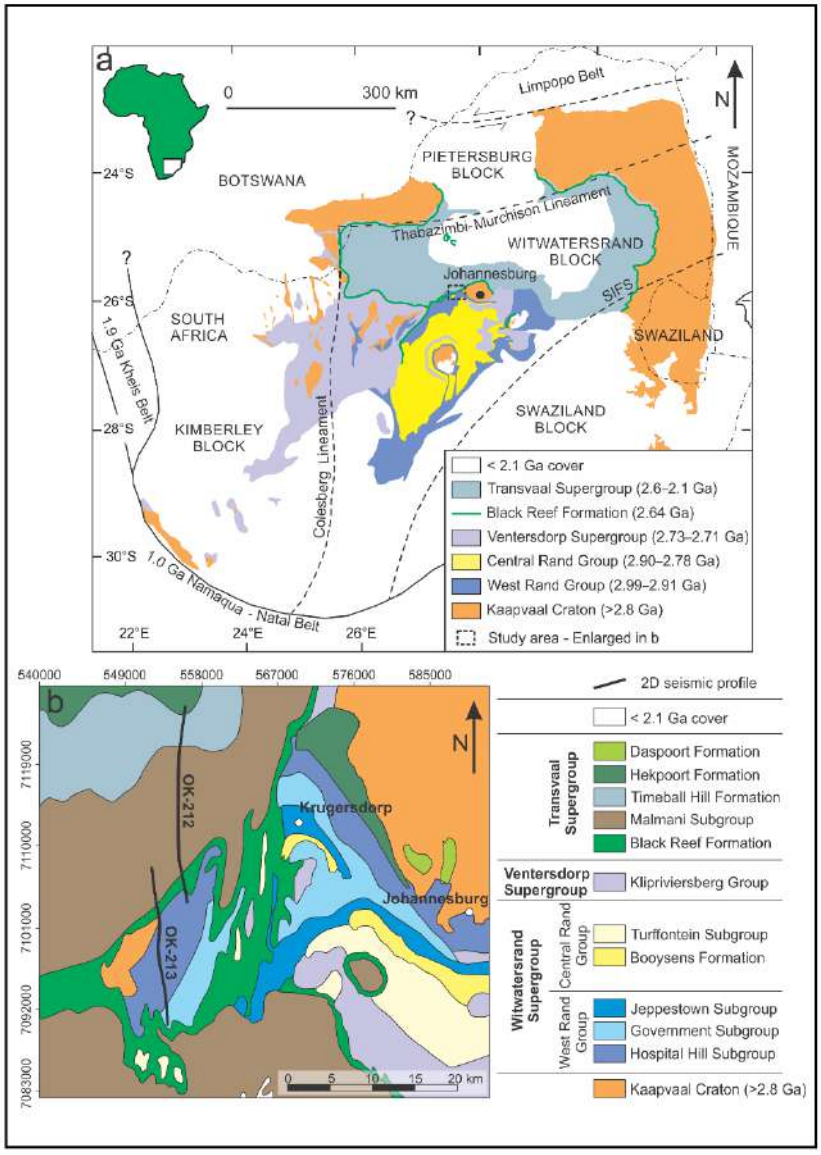


Figure 1 (a) Simplified geological map of the Kaapvaal Craton in southern Africa with the distribution of the Witwatersrand (West and Central Rand groups), Ventersdorp and Transvaal supergroups. The map includes the location of the study area in the West Rand goldfields. Figure modified after Frimmel (2014). (b) Simplified geological map of the study area showing the position of the 2D seismic profiles. The KDC East Mineshaft is found ~20 km south of the study area.

It is located at depths between 0 and 2 km and is crosscut by a series of dykes and faults of various orientations and ages. The BLR remains the least explored gold deposit in South Africa, although it was discovered in the 1880s (Penning, 1891). The Chuniespoort Group (2.06 – 2.04 Ga; Eriksson *et al*. 2006) consists of dolomites (Malmani Subgroup), chert, limestones, shales, and banded iron formations (Walraven, 1995). Finally, the Pretoria Group rocks (ca. 2.22 Ga; Burger and Coertze, 1975; Els *et al.* 1995) unconformably overlie the Chuniespoort Group and

are characterized by mudrocks alternating with sandstones, basaltic-andesitic lavas (Hekpoort Formation), and minor conglomerates.

Geology of the study area, KDC East Mine

The study area is located in the West Rand goldfield, on the north-western rim of the Witwatersrand Basin (Fig. 1). Both seismic profiles (OK-213 and OK-212) are located ~20 km north of the KDC East Mine shaft. The lithology and stratigraphic succession within the study area consist of (from bottom to top; Fig. 2): 1) granitoid basement rocks of the Kaapvaal Craton, 2) quartzites, shales and minor conglomerates of the Hospital Hill and Government subgroups, West Rand Group, Witwatersrand Supergroup, 3) quartz arenites of the BLR, Transvaal Supergroup, 4) dolomites of the Malmani Subgroup, Chuniespoort Group, Transvaal Supergroup, and 5) mudrocks and sandstones of the Timeball Hill Formation, and basaltic-andesitic lavas of the Hekpoort Formation, Pretoria Group, Transvaal Supergroup. Both the Ventersdorp Supergroup and Central Rand Group are absent in the study area as they have been eroded (Fig. 2).

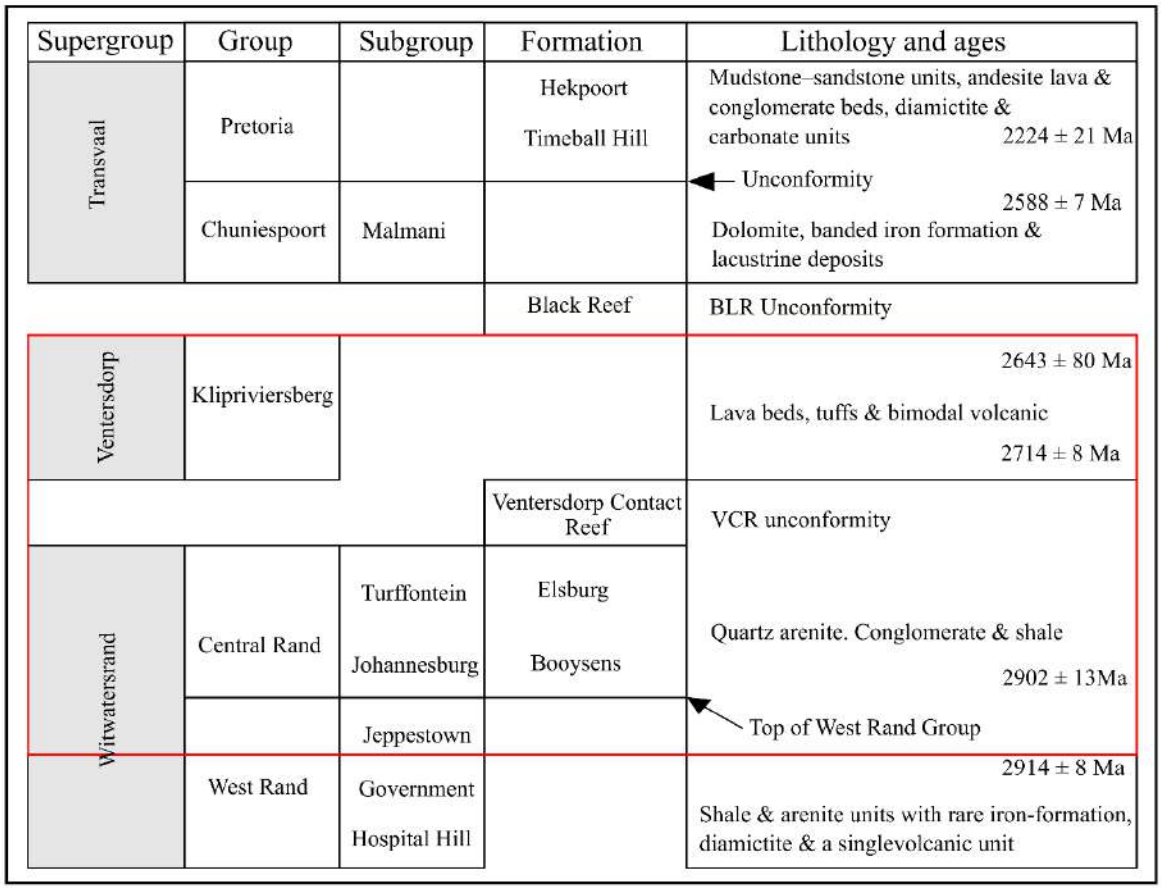


Figure 2 Simplified stratigraphic succession of the study area near the KDC East Mine. Units in the outlined red rectangle are not observed in the seismic section (after Manzi *et al*., 2012).

KDC East Mine is a well-established intermediate to an ultra-deep-level (2.5 and 3.5 km) gold mine. The mine is currently experiencing high operational costs related to great mining depths and the structural complexity of the orebodies. For example, mining at these depths is complicated by hazards such as rockbursts, the inrush of flammable gas and water, and high temperatures (Ranjith *et al*. 2017). To mitigate the risks, minimize the costs and extend the 'Life of Mine', the mine is currently seeking to extend its mining operations to the north-western portion (the study area) and exploit the BLR orebody, which is found at shallow depths (0.5 – 1 km).

NUMERICAL MODELLING AND SEISMIC REFLECTIVITY

The target of the study is to map the BLR, as well as the relationship between the Government and Hospital Hill subgroups (West Rand Group), and between the Hospital Hill Subgroup and basement rocks, as shown in Figure 1 for profile OK-213. In order to create a numerical model, the average values of P-wave velocity and density were obtained from previous studies in the Witwatersrand Basin (Manzi *et al*. 2012; 2015; Tucker *et al*. 2016; Nkosi *et al*. 2017). To investigate the seismic response of the BLR, the 2D acoustic finite-difference forward modelling was performed using the Tesseral software, with the densities and velocities of the geological units summarized in Table 1.

Table 1 Average P-wave velocities and density values used for the study area, located near KDC East Mine. Values adapted from previous studies (Manzi *et al*. 2012; 2015; Tucker *et al*. 2016; Nkosi *et al*. 2017).

Rock type	P-wave velocity (m/s)	Density (kg/m^3)
Quartzite	5 733	2 610
Shale	5 748	2 900
Dolomite	6 700	3 000
Quartzite (BLR)	6 125	2 690
Granite	5 700	2 605

Figure 3 shows the velocity model used as one of the modelling inputs with different velocities corresponding to the geological units and their structural relations. The model has a length of 15.7 km and a depth of 3.5 km. The acoustic finite-difference response was calculated along the profile with receivers moving with the source, to match the acquisition spread used for acquiring the legacy data reprocessed here. The total number of shots computed was 158 with a source spacing of 100 m. A maximum of 3 100 ms TWT was chosen for the numerical modelling with a Ricker wavelet of 55 Hz at a sampling rate of 4 ms. The profile was computed with 124 receivers per shot and 50 m receiver spacing. These parameters are summarised in Table 2.

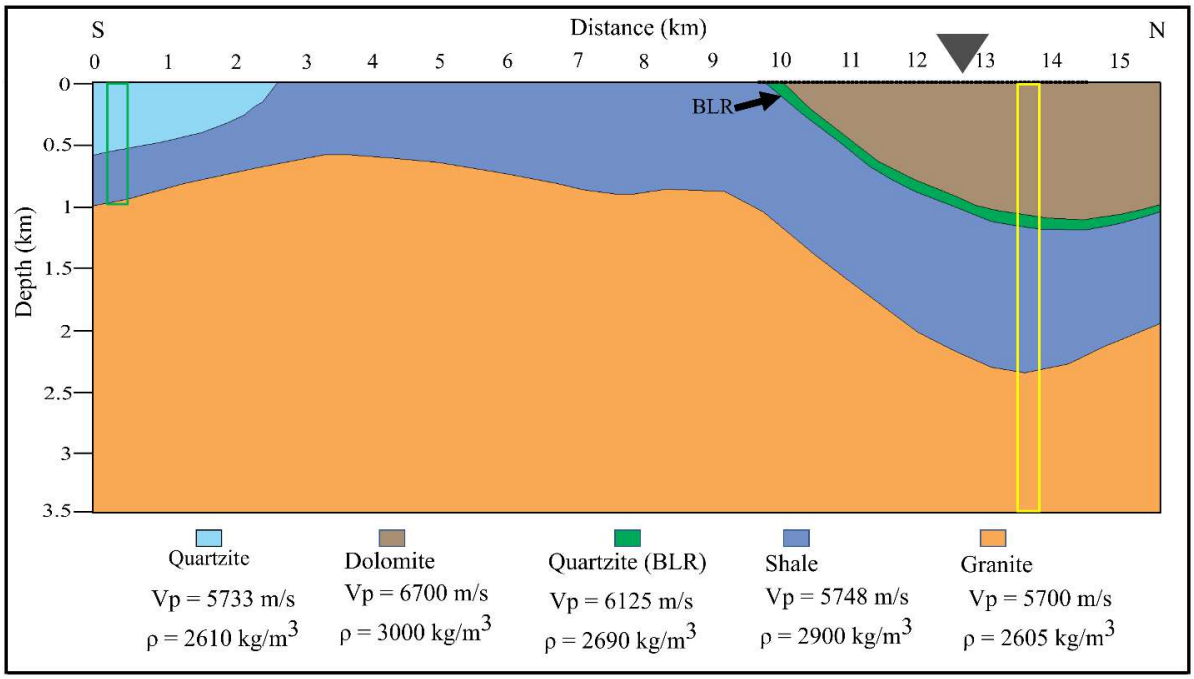


Figure 3 The 2D velocity model used for acoustic finite-difference forward modeling purposes. Different velocities correspond to known geological units as encountered by the legacy profile OK-213. The target of this study is the Black Reef (BLR) horizon. The green (left) and yellow (right) rectangles represent possible scenarios to test the sources of seismic reflectivity in the study area and create 1D synthetic seismograms. The shaded inverted triangle shown at the distance of approximately 12.8 km represents the location of a shot shown in the synthetic shot gather used to compare with legacy data and the black line represents a range of receivers.

Table 2 2D acoustic modelling parameters used for seismic profile OK-213.

Modelling parameters	
Profile length	15 700 m

Sampling rate	4 ms
Recording length	3 100 ms
Source spacing	100 m
Source	Vertical (Z)
Number of shot points	158
Receiver spacing	50 m
Receiver per shot	124
Frequency	55 Hz
Wavelet	Ricker
Surface mode	Free surface
Grid cell (dx, dz)	5.3 m
Grid time increment (dt)	1.1 ms

Figure 4 compares the synthetic shot gather (at the 12.8 km mark shown in Figure 3 with an inverted shaded triangle) generated via acoustic finite-difference forward modelling (Fig. 4a) and the raw shot gather (Fig. 4b) for profile OK-213. The P-wave first breaks in synthetic gather are highlighted in Figure 4a using red arrows. The reflection indicated by blue arrows in both shot gathers (Fig. 4a, b) is produced by the lithological contact between the Hospital Hill Subgroup and basement rocks. The green arrows correspond to the reflections related to the BLR, located between the Malmani and Hospital Hill subgroups (Fig. 2).

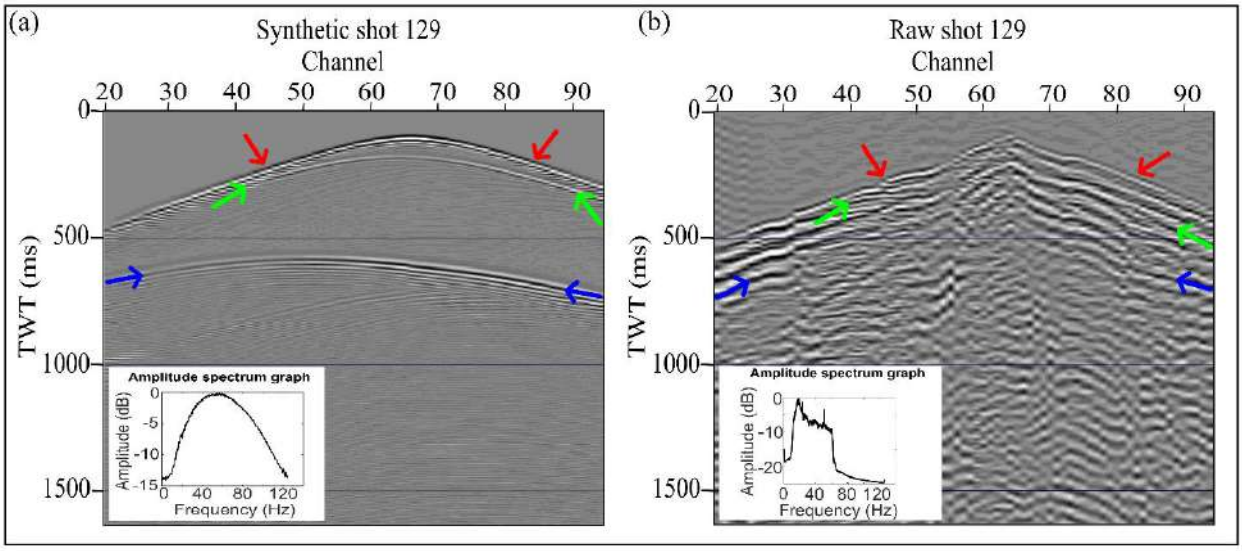


Figure 4 Comparison between the synthetic shot gather (a), and raw, real shot gather (b) with the corresponding amplitude spectrum graphs for profile OK-213 at the distance of approximately 12.8 km mark shown in Figure 3 with an inverted shaded triangle. The red arrows show the first breaks; the green arrows show the Black Reef (BLR) horizon reflection. The blue arrows represent the reflection between the basement rocks (Kaapvaal Craton) and the West Rand (Witwatersrand Supergroup) metasediments contrast.

Additional sources of seismic reflectivity in the study area were investigated and 1D synthetic seismograms were calculated. Two possible scenarios corresponding to geological conditions at two different locations along the profile were tested; 1) near the south end of the 2D acoustic finite-difference velocity model, as represented by a green rectangle, and 2) towards the north end of the model, as represented by a yellow rectangle in Figures 3 and 5. A sampling rate of 4 ms and a Ricker wavelet with the dominant frequency of 55 Hz were used to compute the synthetic seismograms. Figure 5 shows the computed synthetic seismogram with the acoustic impedance contrast between various lithologies.

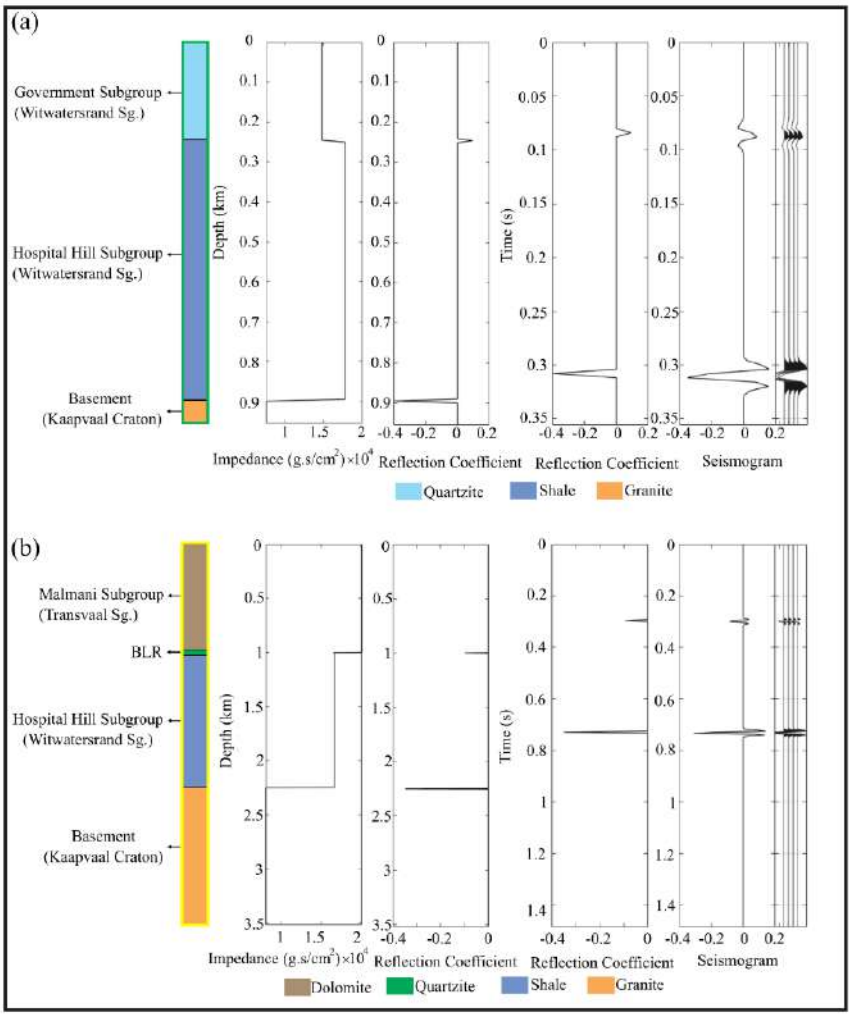


Figure 5 Calculated acoustic impedances, reflection coefficients as a function of depth and time, and synthetic seismograms for two stratigraphic sequences encountered at different locations along the profile shown in Figure 3. (a) A strong reflection is observed at the base of the profile and is associated with the interface between the basement and Hospital Hill Subgroup. Another reflection is observed at the interface between the Government and Hospital Hill subgroups. (b) A strong reflection is observed at the interface between the basement and Hospital Hill Subgroup. The generated reflection between the Malmani and Hospital Hill subgroups is associated with the BLR horizon for the synthetic seismogram computed from the end of the profile. Both 1D synthetic seismograms were computed using reflection coefficient with Ricker wavelet (55 Hz) at a sampling rate of 4 ms. BLR: Black Reef; Sg: Supergroup.

Significant acoustic impedance contrasts occur between the Hospital Hill Subgroup and basement rocks (Fig. 5a, b), the Government and Hospital Hill subgroups (Fig. 5a), and the Hospital Hill and Malmani subgroups (Fig. 5b), all of which produce strong seismic reflections.

Notably, the BLR is also associated with a strong seismic reflection since it occurs at the reflective interface between the overlying dolomites of the Malmani Subgroup and the underlying shale and minor quartzites of the Hospital Hill Subgroup (Fig. 5b). The reflection between the Hospital Hill Subgroup and the basement rocks in Figure 5a is similar to the reflection observed in Figure 4 (blue arrows).

LEGACY 2D SEISMIC DATA

Seismic data acquisition

The legacy 2D reflection seismic data were provided by Sibanye Stillwater to the Wits Seismic Research Centre for research and teaching purposes. The data were received as raw shot gathers in SEG-Y format, and the acquisition information was obtained from field observer's reports as well as from header information. The two reflection seismic profiles (OK-212 and OK-213) were acquired in 1988 by the Gold Division of Anglo American as part of a large gold exploration campaign (Pretorius *et al*. 2003; Manzi *et al*. 2018b). Vibroseis trucks were used as seismic sources with profile lengths of 16.9 km and 15.7 km, respectively (Fig. 1b). The acquisition parameters are summarized in Table 3. Both profiles were acquired with a sweep length of 18 s and a sweep frequency of 8 – 62.5 Hz at a sampling rate of 4 ms. The sweeps were recorded in-field and cross-correlated with pilot traces for each shot location. The correlated traces were then saved in SEG-D format before being converted to SEG-Y format. Seismic profiles OK-212 and OK-213 have a total of 176 and 145 shots, respectively, with 124 receivers per shot, 50 m receiver spacing, and 100 m shot spacing for both profiles.

Table 3 Main acquisition parameters for profiles OK-212 and OK-213.

Acquisition parameters		
Survey parameters	OK-212	OK-213
Type of survey	2D	2D
Year	1988	1988
Profile length	16.9 km	15.7 km
Trend	S-N	N-S
Spread	2,975–25–X–25–2,975 (m)	2,975–25–X–25–2,975 (m)
Nominal fold	25	25
Average fold	37	38
Recording system		

Recording device	CS2502 SN368	CS2502 SN368
Sampling rate	4 ms	4 ms
Recording length	6 s	6 s
Sweep length	18 s	18 s
Sweep frequencies	8 – 62.5 Hz	8 – 62.5 Hz
Source information		
Source spacing	100 m	100 m
Source type	Vibroseis	Vibroseis
Receiver information		
Receiver spacing	50 m	50 m
Geophone type	10 Hz (SM4)	10 Hz (SM4)

The receivers had a natural frequency of 10 Hz, and the data were recorded with an 8 Hz low-cut filter. The resulting average common midpoint (or CMP) fold for seismic profile OK-212 and OK-213 is 37 and 38, respectively, and the bin size is 25 m.

Seismic data reprocessing

The processing sequence applied for each of the legacy seismic profiles is given in Figure 6. As we were unable to retrieve the original processing results, either in digital or analogue form, we are unfortunately not able to do a side-by-side comparison between the new and legacy processing results. Nonetheless, reprocessing of the legacy profiles is important for future mine planning and evaluation of the shallow-seated deposits currently of interest.

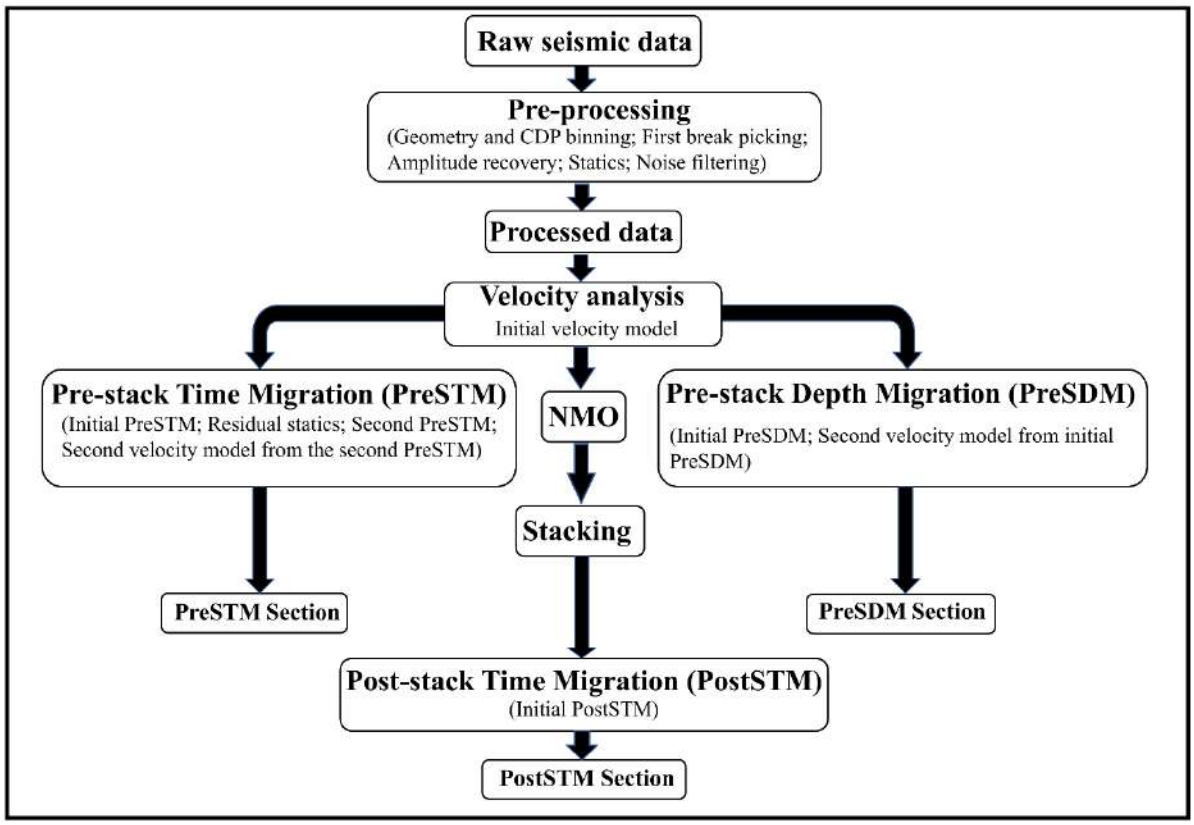


Figure 6 The processing workflow used for the 2D seismic profiles OK-212 and OK-213.

The reprocessing work started with a careful review of existing observer reports on the acquisition parameters to ensure that recovered geometry, found in the raw shot gather trace headers, was as accurate as possible. Some of the headers, such as the source depth and source up-hole, had false values of -9999 that were zeroed when edited, and some headers were not stored under the conventional titles and had to be extracted from their byte locations.

Next, we fixed the geometry; while the source and receiver locations were correct, their elevation values were not in agreement and appeared offset. This issue, which is pertinent with the legacy seismic data, was encountered and documented by Westgate *et al.* (2020). To correct this, we used Shuttle Radar Topography Mission (SRTM) data to determine reliable elevations. The source elevations were found to be the more accurate and reliable as they agreed with the SRTM data. We used nearest-neighbour interpolation to interpolate the receiver elevations from the source elevations and cross-validated the obtained elevations versus the SRTM data. Given the relatively flat topography along the profiles, together with the 50 m receiver spacing, the approach used is considered appropriate since elevations obtained are accurate to the nearest meter and did not change significantly from station to station.

Following these pre-conditioning steps, each profile was processed separately with individually adjusted parameters. Both the elevation datum and replacement velocity were kept consistent to preserve the continuity of the seismic reflections across the profiles. Both profiles OK-212 and OK-213 exhibit 50 Hz noise, likely caused by nearby AC power lines in the region (Fig. 7a, c). The noise was filtered out using a notch filter. After correcting the geometry, the traces were binned into common midpoint bins by fitting a spline curve through the cloud of common midpoints containing the highest number of traces and placing bins along this line every 25 m.

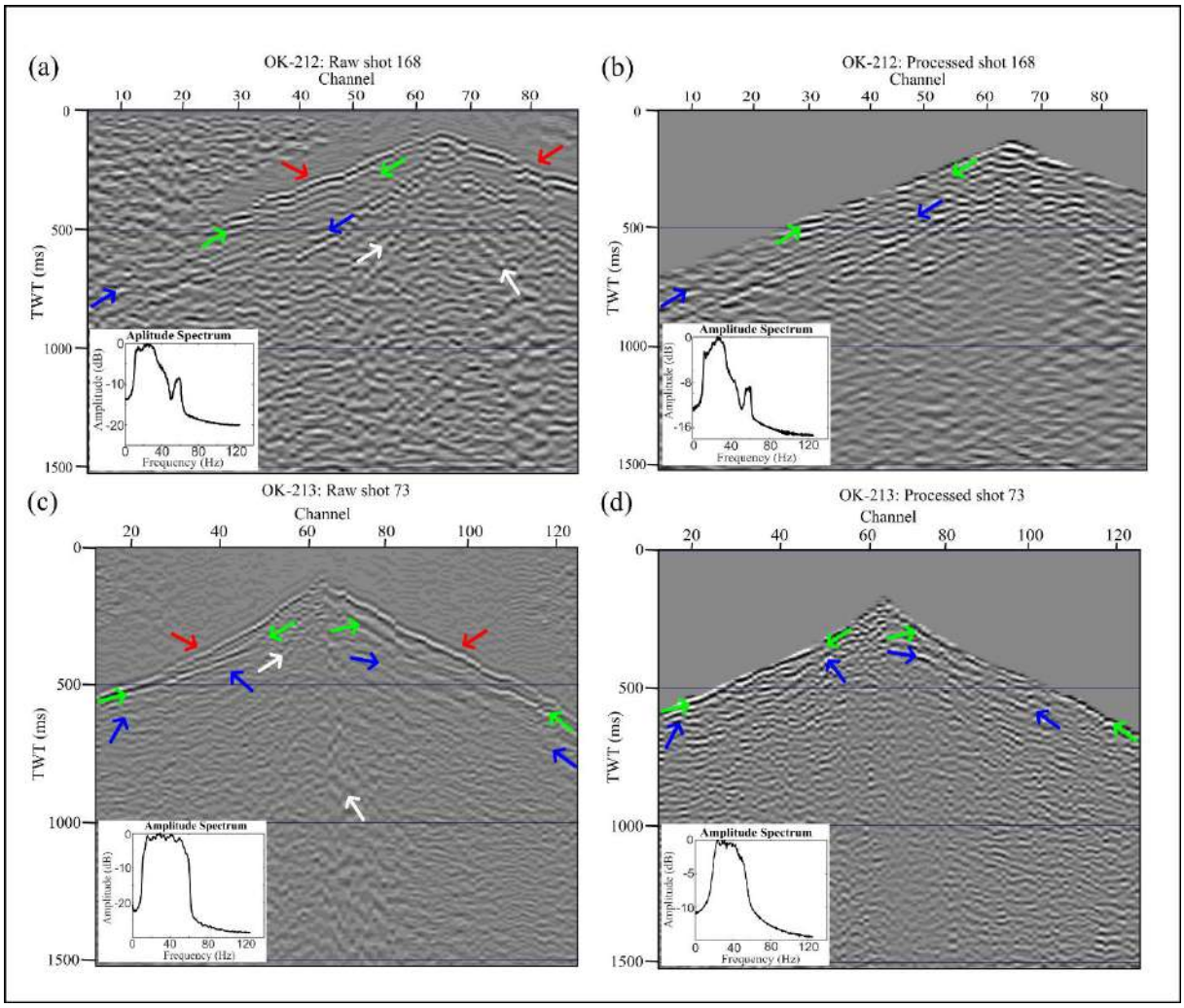


Figure 7 Comparison of shot gathers from profile OK-212 (a) before and (b) after applying the pre-stack processing, as well as from profile OK-213 (c) before and (d) after pre-stack processing, along with the respective amplitude spectra of each gather. Red arrows indicate first breaks. White arrows indicate noise (including ground-roll and airwave energy) that has been attenuated after pre-processing. Blue arrows indicate possible reflections, and the BLR seismic reflection is indicated by the green arrows.

For profiles OK-212 and OK-213, a total of 5 977 and 12 152 first breaks were picked, respectively, to compute refraction statics in order to correct for the effect of the variable thickness and lateral velocity variation of the weathering layer. Floating datum statics were applied to both profiles (OK-212 and OK-213). The reference datum elevation of 1 700 m above mean sea level was chosen for both profiles along with a replacement velocity of 5 500 m/s as seen from the refracted arrivals velocity. Figure 7 shows examples of the recorded shot gather before (Figs. 7a, c) and after (Figs. 7b, d) the initial processing. Automatic gain control (or AGC) with a window length of 250 ms was applied to the shot gathers to recover attenuated amplitudes (Fig. 7b, d). Clear first breaks, as indicated by red arrows in Figure 7a, c, as well as possible reflections, as indicated by blue arrows in Figure 7, were observed in most of the shot gathers. The BLR reflection is indicated by green arrows in Figure 7. In both profiles, OK-212 and OK-213, the data was acquired with a split spread geometry and a near offset trace at ±175 m resulting in the first break at 50 – 100 ms at the closest trace to the source array (see Fig. 7).

Pre-stack processing includes frequency filtering, f-k filtering, and predictive deconvolution. A bandpass filter was applied to attenuate frequencies not contained in the sweep (i.e., 8 – 62.5 Hz). Most of the airwave and ground-roll energy (indicated by white arrows in Fig. 7a, c) were removed by applying an f-k mute. Predictive deconvolution was applied on the data with the operator length and prediction gap being specified every tenth shot and then interpolated for intermediate shots. For both profiles (OK-212 and OK-213), the deconvolution parameters varied across the length of the profile. Profile OK-212 had an average of 60 ms prediction gap and ranged from 30 ms to 96 ms, and the operator length had an average of 40 ms and range of 4 ms to 70 ms. Profile OK-213 had an average of 47 ms prediction gap and ranged from 20 ms to 84 ms, and the operator length had an average of 52 ms and range of 17 ms to 80 ms. The different gaps and operator lengths were tried, and these gave the best results.

Velocity analysis was performed using constant velocity stacks to generate a velocity model for Dip-Moveout (DMO) corrections. The Kirchhoff pre-stack time migration (PreSTM), pre-stack depth migration (PreSDM), and Kirchhoff post-stack time migration (PostSTM) were tested in our data for comparison purposes. PostSTM provided better results in the shallow region of the data, whereas PreSDM provided better structural imaging in the deeper portion

of the data due to the structural complexity of geology at depth, and the complex lateral changes in the velocity field.

RESULTS AND INTERPRETATION

In general, the data exhibit a good signal-to-noise ratio from which a reliable seismic stratigraphy can be derived. The refraction tomographic velocity models were computed using picked first breaks up to a depth of ~500 m for OK-212 and ~600 m OK-213 (Fig. 8) and were used to characterize the P-wave velocities. The P-wave velocities, displayed in Figure 8, range from 1 000 m/s to 6 500 m/s. The upper ~100 m and ~80 m for profiles OK-213 and OK-212 (Fig. 8a, c), respectively, correspond to topsoil, with P-wave velocities ranging from ~1 000 – 2 000 m/s. Beneath the topsoil is a 100 – 300 m weathered layer, with velocities between 2 000 and 5 000 m/s. The base of the tomographic velocity models corresponds to bedrock with velocities greater than 5 000 m/s.

The PostSTM section for profile OK-212 is shown in Figure 9 with close-up areas (red and blue rectangles) showing possible visible seismic reflections. For profile OK-212, the subsurface could not be clearly imaged below the dolomites belonging to the Malmani Subgroup (see Fig. 1b).

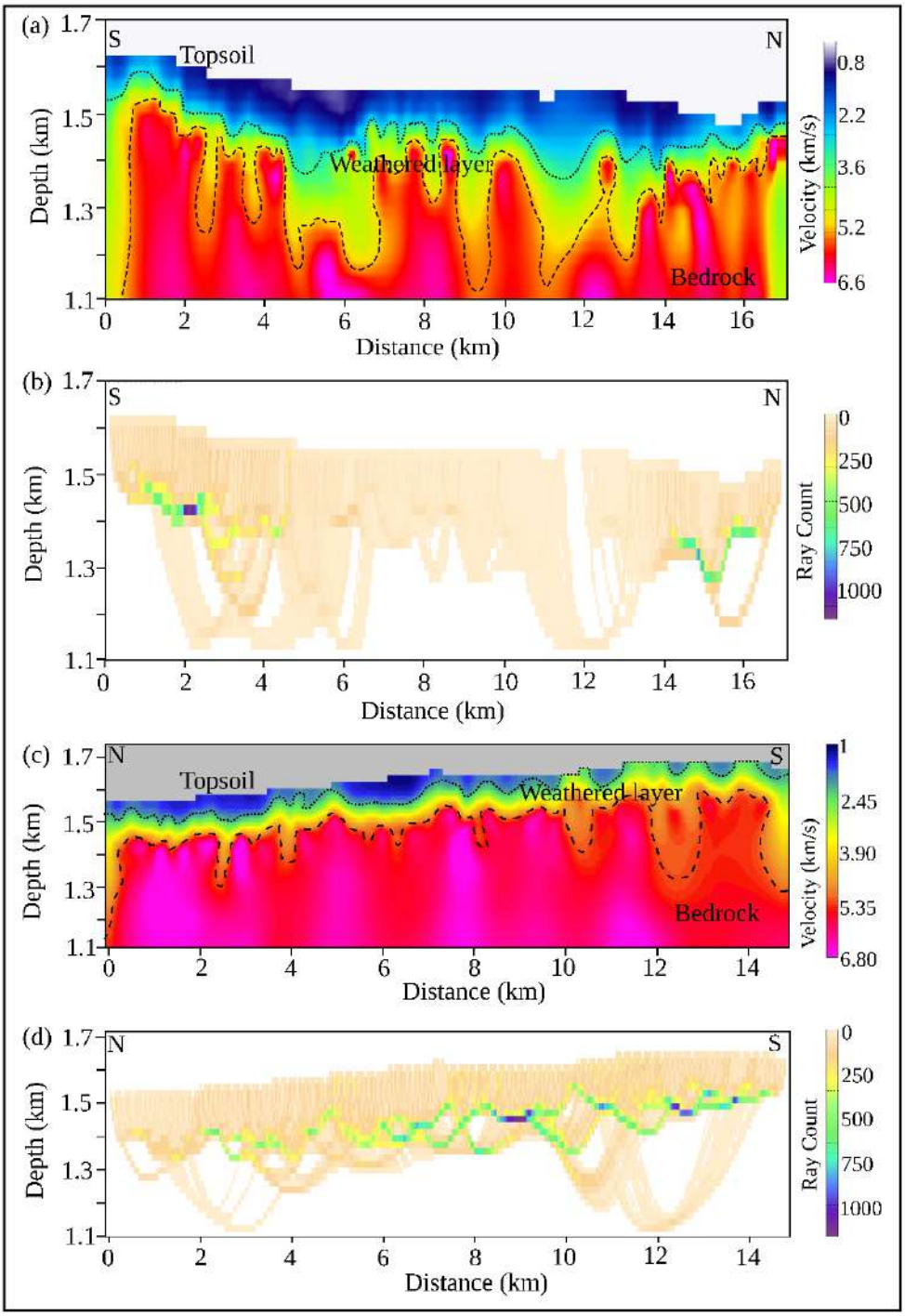


Figure 8 Refraction tomographic velocity model calculated for profile OK-212 (a), as well as the associated ray path model showing ray coverage of the velocity model (b). The same is shown for profile OK-213 (c - d). Both profiles show three distinct layers: topsoil, weathered layer, and bedrock.

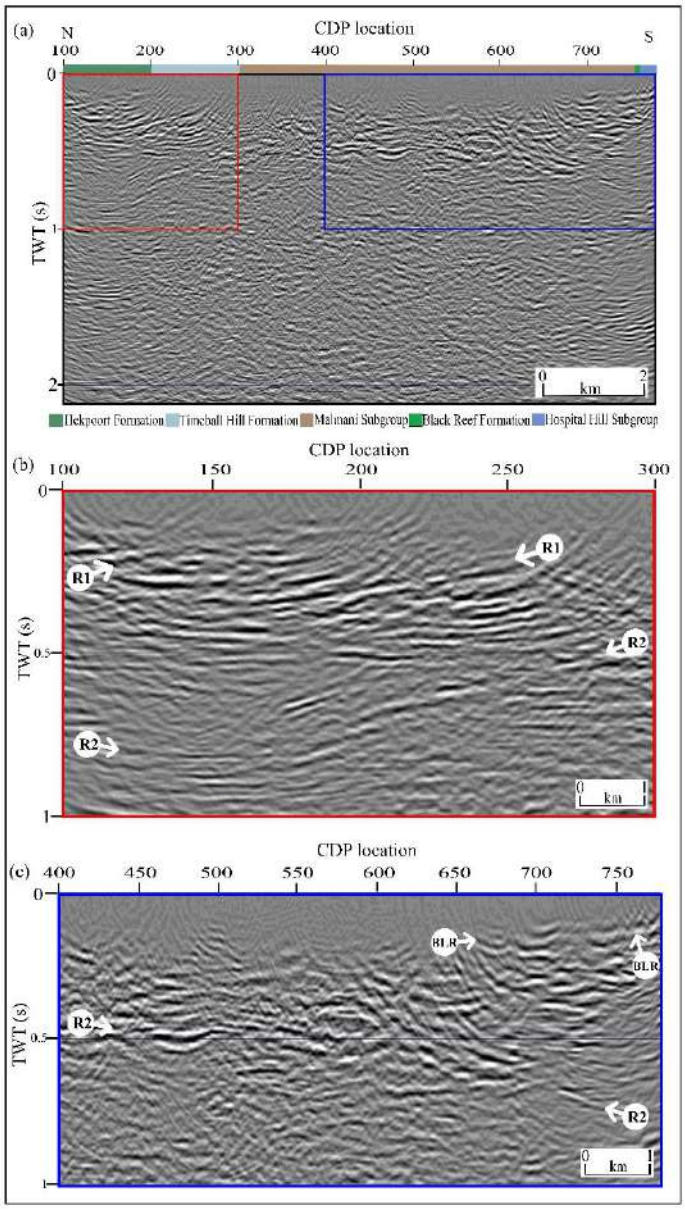


Figure 9 (a) Post-stack time migrated section for profile OK-212. The surface geology is displayed above the seismic section. Outlined red and blue rectangles, enlarged in (b) and (c), respectively, highlight visible seismic reflections. Reflections are attenuated beneath dolomitic outcrops belonging to the Malmani Subgroup. (b) Enlarged post-stack time migrated section indicating visible reflections R1 and R2. (c) Enlarged post-stack time migrated section indicating the reflection associated with the Black Reef Formation (BLR) and R2.

Dolomites are known to cause scattering of seismic energy in the near-surface, thus preventing energy propagation into the subsurface (Manzi *et al.* 2012). Two packages of reflections (R1 and R2) are seen in the shallower part of the OK-212 section, between 0 and 1 s two-way travel time (TWT), and between CDP 100 and 300 (Fig. 9b). Both R1 and R2 are located at the northern end of the OK-212 section and appear to dip to the north. The significant acoustic

impedance contrast between the Hekpoort and Timeball Hill formations produces the reflection R1. The R2 reflection is produced by the interface between the Timeball Hill Formation and Malmani Subgroup. The reflection attributed to the BLR is located at the southern end of the section, dipping to the north between 0 and 0.2 s TWT (Fig. 9c).

Figure 10 shows the PostSTM section for profile OK-213 with close-up areas (blue and red rectangles) showing possible visible seismic reflections. Visible reflections are located towards the northern part of the profile. Towards the southern part of the profile, there are no clear or visible reflections. We identified six groups (BLR and R3 to R7) of reflections. Seismic reflectors R3, R4 and BLR in Figure 10b dips towards the north from the near-surface, between CDP 200 and 625, and at ~0.6 s TWT. The other three reflections (R5, R6 and R7) are found at greater depths and are gently dipping towards the south, between CDP 420 and 620, at 2 – 3.5 s TWT (Fig. 10c).

The PreSTM and PreSDM results for profiles OK-212 and OK-213 are shown in Figures 11 and 12, respectively. Packages of seismic reflections (R1, R2 and BLR; denoted by white arrows) for profile OK-212 are visible in Figure 11, notably away from the dolomites belonging to the Malmani Subgroup. All the reflections from profile OK-212 dip towards the north.

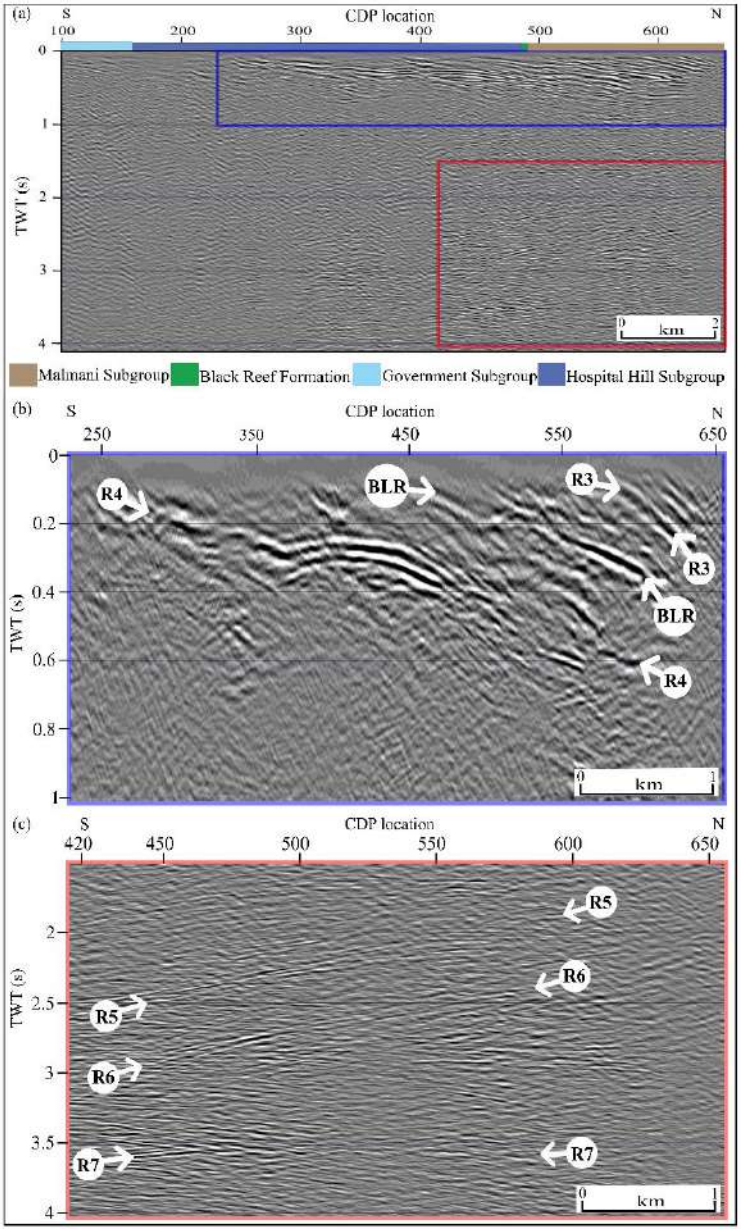


Figure 10 (a) Post-stack time migrated section for profile OK-213. The surface geology is displayed above the seismic section. Outlined blue and red rectangles, enlarged in (b) and (c), highlight visible seismic reflections. (b) The enlarged post-stack time migrated section indicates visible reflections R3, R4 and BLR (Black Reef Formation). (c) Enlarged post-stack time migrated section indicating visible reflections R5, R6 and R7. Note that the vertical exaggeration differs between (b) and (c).

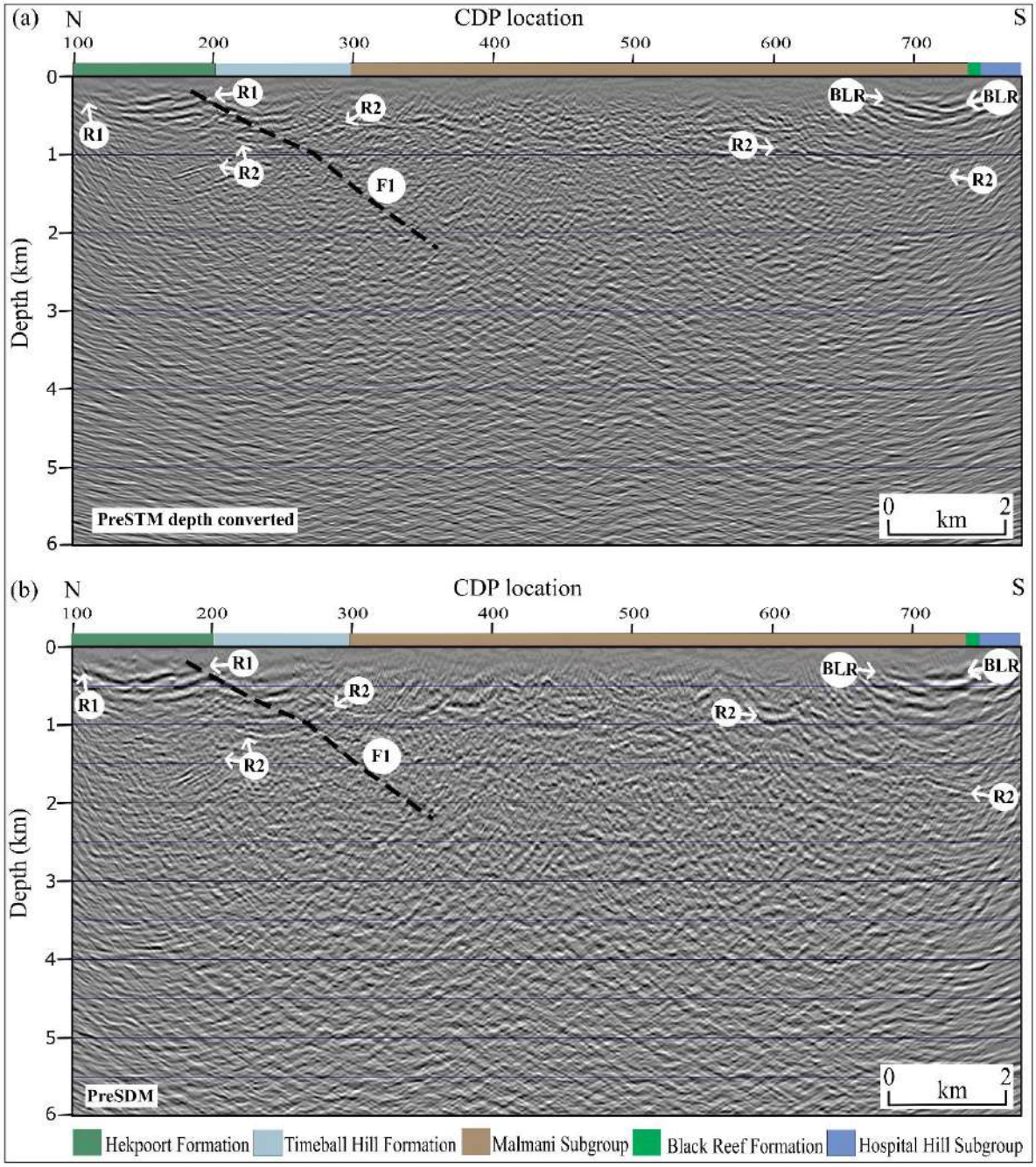


Figure 11 Comparison between (a) PreSTM and (b) PreSDM sections for seismic profile OK-212. The surface geology is displayed above the seismic sections. Possible visible reflectors R1, R2 and BLR (Black Reef Formation) are indicated by white arrows. F1 (black dashed line) is a fault cross-cutting reflector R2. PreSTM: Pre-stack time migration; PreSDM: Pre-stack depth migration.

The lithological contact between Hekpoort Formation and the underlying Timeball Hill Formation corresponds to the reflection marked R1. The reflection labelled R2 is produced by the lithological contact between the younger Timeball Hill Formation and the underlying Malmani Subgroup. The BLR is dipping towards the north from the near-surface to about CDP

750 (Fig. 11). For profile OK-213, presented in Figure 12, the R4 reflector and BLR dip towards the north. The reflector marked by R4 represents the contact between the Government Subgroup and the underlying Hospital Subgroup.

In both Figures 11 and 12, it is evident that the PreSDM performs better than the PreSTM imaging. The notable difference between the two methods is that PreSDM enhances the delineation of deeper reflections, while PostSTM shows a clear definition of shallow reflections (e.g., compare Fig. 12a to b). Specifically, reflectors BLR and R4 are enhanced by the PreSDM up to a depth of 2.1 km (Fig. 12b). Additionally, the R4 reflector, enhanced in the PreSDM image suggests lateral velocity changes, possibly related to thrusting with the basement (see Manzi *et al*. 2013; Beach and Smith, 2007; Frimmel, 2005). Furthermore, the PreSDM image confirms that the BLR and other reflections (Fig. 11b) are crosscut and displaced by mainly normal faults (see interpreted PreSDM section in Fig. 13). As seen in Figure 11b, reflector R2 is crosscut by a fault (F1) which dips south.

PostSTM shows better imaging at shallow depths compared to both PreSDM and PreSTM imaging. For example, the reflector marked R3 is clearly imaged in the PostSTM in Figure 10b, compared to both PreSDM and PreSTM images in Figure 12.

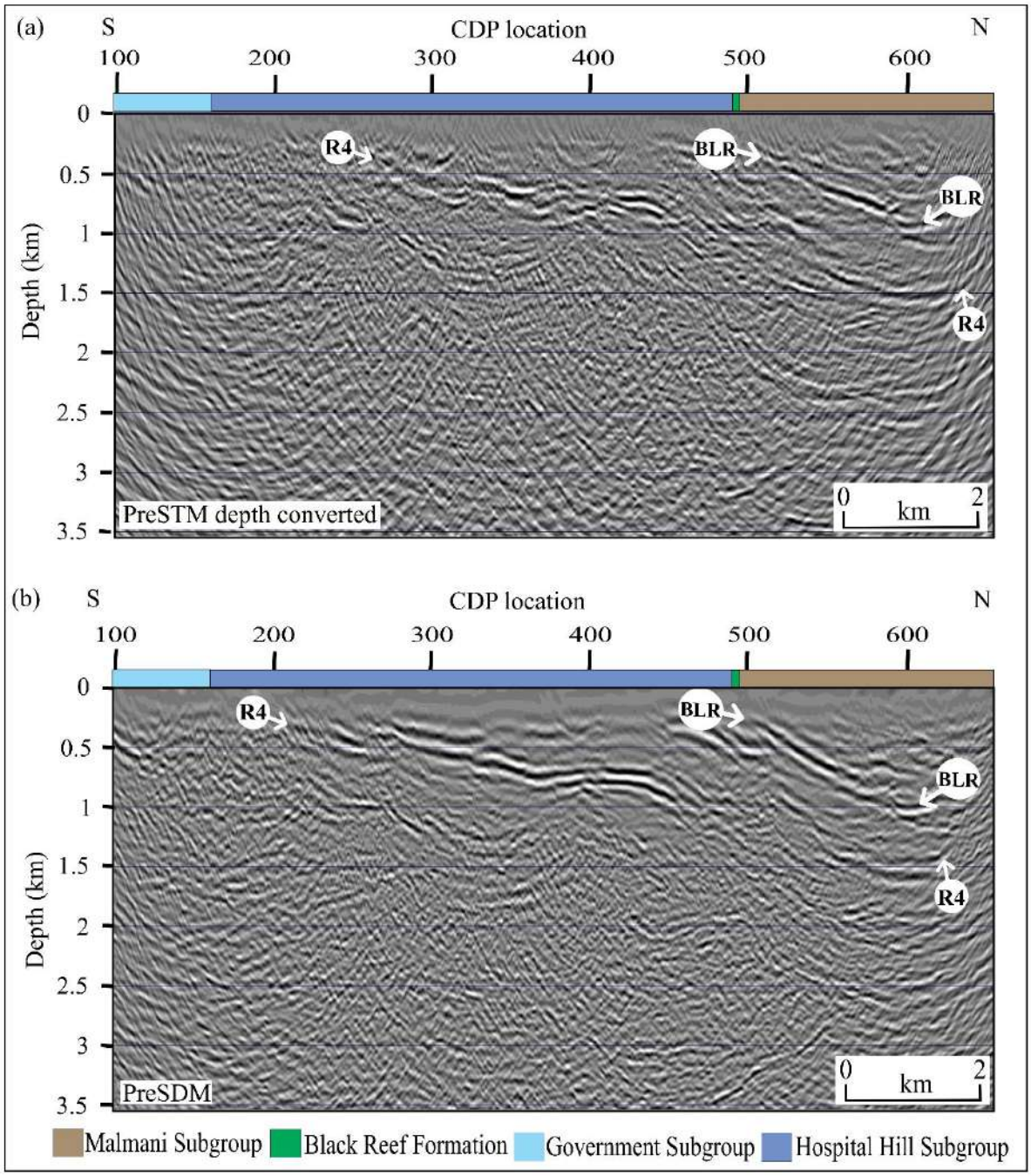


Figure 12 Comparison between (a) PreSTM and (b) PreSDM for seismic profile OK-213 with possible reflectors (R4 and BLR). The surface geology is presented above the seismic section. PreSTM: Pre-stack time migration; PreSDM: Pre-stack depth migration; BLR: Black Reef.

In general, the application of PostSTM and PreSDM clearly enhances the continuity of reflections (marked R4 and BLR) in Figures 10b and 12b, from CDP 280 – 620 in the seismic profile of OK-213.

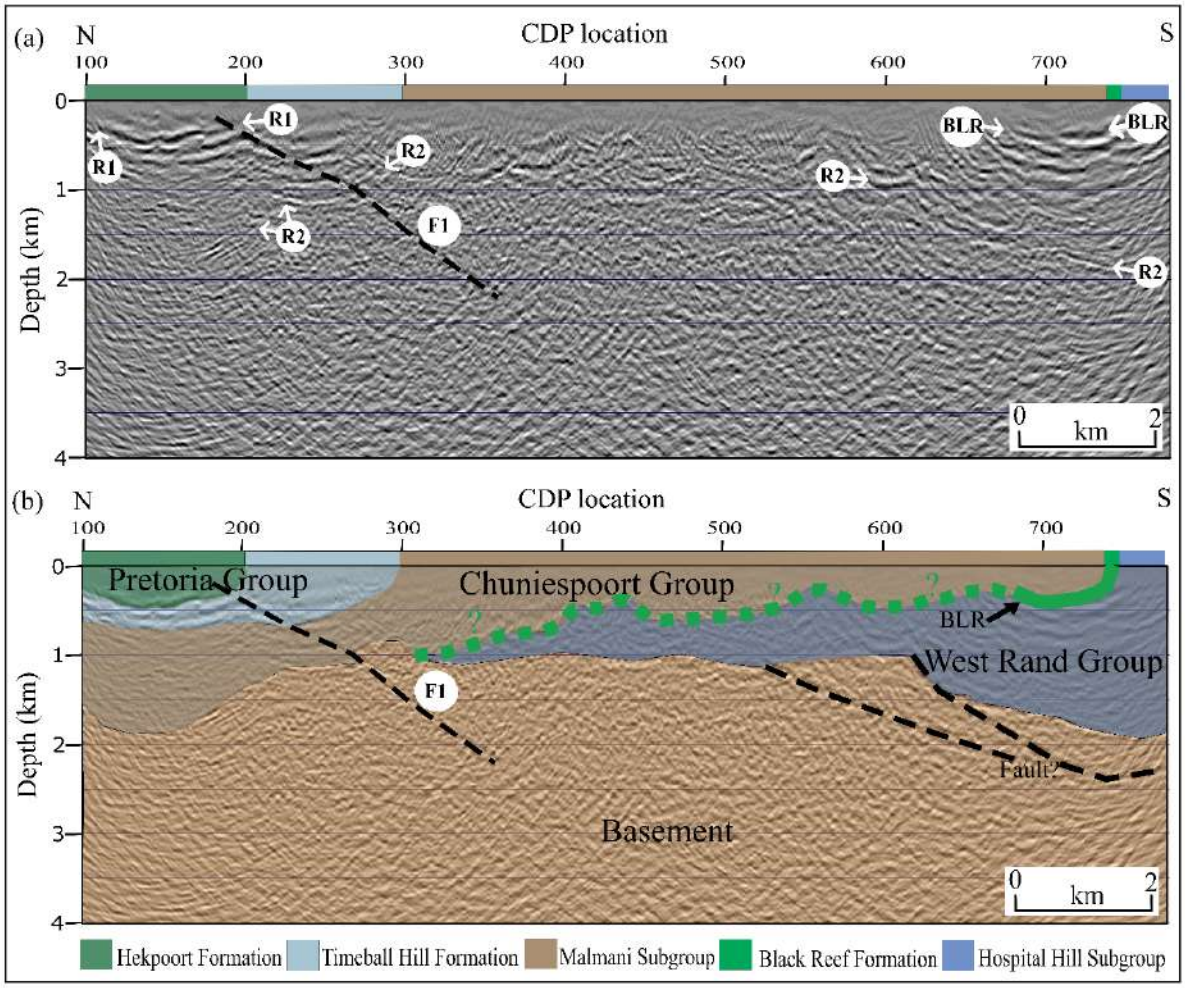


Figure 13 (a) Uninterpreted final pre-stack migrated depth (PreSDM), and (b) interpreted PreSDM sections overlaid with a geological model for profile OK-212. The surface geology is presented above the seismic sections. Fault F1 displaces the Timeball Hill and Malmani subgroups, as well as the BLR, Hospital Hill Subgroup and the basement rocks.

The comparison between the uninterpreted and final depth-interpreted seismic sections (PreSDM) is shown in Figures 13 and 14 for profiles OK-212 and OK-213, respectively. The interpreted (PreSDM) section for profile OK-212 (Fig. 13) shows the following: 1) the lithological contact between andesitic lavas (Hekpoort Formation) and quartzites (Timeball Hill Formation); 2) a fault (F1) that displaces Timeball Hill Formation, Malmani Subgroup, and Hospital Hill Formation; and 3) the delineation of the BLR, aided by the lithological contact between dolomites (Malmani Subgroup) and quartzites and shales (Hospital Hill Subgroup). Below the Hospital Hill Formation, the section demonstrates a delineation of strong reflections within basement rocks (Kaapvaal Craton) that may be related to thrusting (Fig. 13b) (see Manzi *et al.* 2013; Beach and Smith, 2007; Frimmel, 2005). The interpreted (PreSDM) section for profile OK-213 is presented in Figure 14. To the south, the observed reflections

correspond to lithological contact between the Government and Hospital Hill subgroups. The delineation of the BLR is aided by the lithological contact between the overlying dolomitic rocks of the Malmani Subgroup and the underlying quartzites and shales of the Hospital Hill Subgroup. Below the Hospital Hill Subgroup, the top of the basement is well defined with possible reflections within the unit (pointed by white arrows in Fig. 14b). The low-angle reflections may be related to thrusting (see Manzi *et al*. 2013; Beach and Smith, 2007; Frimmel, 2005).

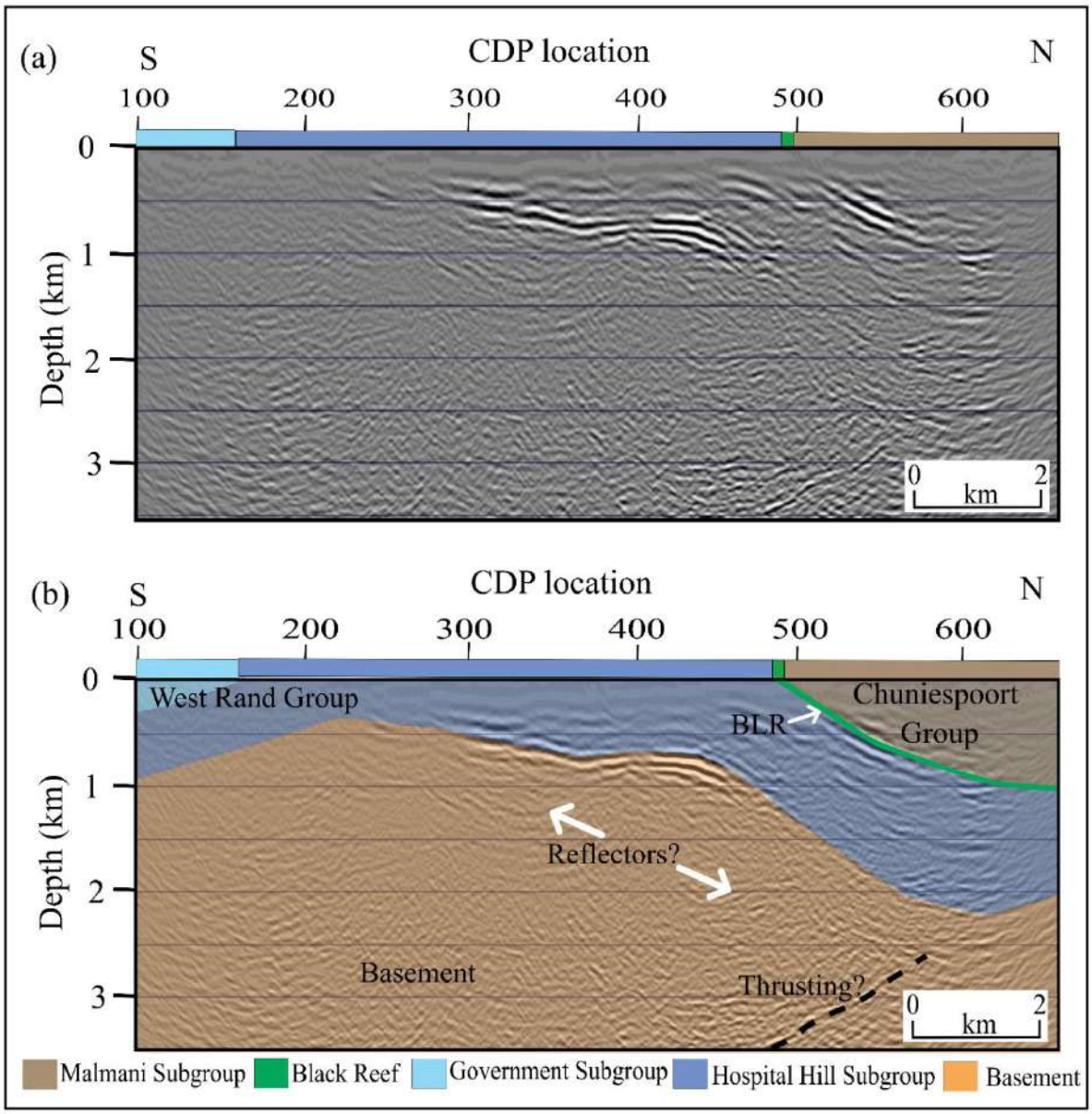


Figure 14 (a) Uninterpreted final pre-stack migrated depth (PreSDM), and (b) interpreted PreSDM sections overlaid with a geological model for profile OK-213. The surface geology is presented above the seismic sections. The interpreted section shows the Hospital Hill Subgroup

dipping both north in the northern part of the section, and south in the southern part of the section. Possible thrusting in the basement is represented by a black dashed line.

DISCUSSION

The surface geology of the two 2D legacy seismic profiles contains areas of dolomitic outcrops belonging to the Malmani Subgroup. Seismic imaging of the subsurface orebodies relies on: 1) near-surface rocks; 2) impedance contrast of the target bodies and their host; 3) design of the seismic survey; 4) sources of noise in the area; and 5) thickness, depth and geometry of the targets (Eaton *et al.* 2003). The main purpose of this study is to image the BLR which is intended to be mined at KDC East Mine. The BLR exhibits a strong reflection that is generated due to a significant acoustic impedance contrast between the overlying dolomites of the Malmani Subgroup with high velocity (6 700 m/s) and high density (~3 000 kg/m^3), and the underlying relatively lower-velocity (~5 733 m/s), less dense (~2 610 kg/m^3) Hospital Hill Subgroup which is dominated by quartzites (Manzi *et al.* 2012).

The seismic resolution limit refers to both the vertical and horizontal resolution and is a critical parameter that guides the interpretation of the seismic data. The dominant frequency of our data across the targeted reflector (BLR) is 55 Hz for both profiles OK-212 and OK-213. Assuming an average P-wave velocity of 6 000 m/s, the dominant frequency yields a dominant wavelength of ~109 m for profiles OK-212 and OK-213. This implies that the Rayleigh resolution limit (1/4 dominant wavelength) is ~ 27 m for both profiles, and the Widess limit (1/8 dominant wavelength for the data with a high signal-to-noise ratio) is ~13.6 m (Widess, 1973). This indicates that we cannot resolve geological features below this limit. However, smaller features can still be detected, but the detection limit will be dependent on the shape, and geometry of the targets, as well as the signal-to-noise ratio of the data. In the study area, the gold-bearing horizon in the BLR is generally thinner than 1 m (Nwaila *et al.* 2020; 2022), meaning that it cannot be resolved. However, the BLR can still be mapped due to the strong seismic reflection between the overlying dolomites of the Malmani Subgroup and the underlying quartzites of the Hospital Hill Subgroup, this reflector serving as a proxy for the location of the gold-bearing horizon.

The horizontal resolution is simply described as the ability to detect two laterally displaced features as two distinct adjacent events (Sheriff, 1997). In terms of lateral resolution, with BLR

located at depths between 500 and 2 000 m, the Fresnel-zone width is between 165 and 330 m, respectively. This horizontal resolution assumes that the 2D seismic data are un-migrated (Yilmaz, 2001). However, after migration, the limit of resolvability can be enhanced to approximately half the dominant wavelength, which is equivalent to ~55 m for profiles OK-212 and OK-213.

Our overall results indicate that the PreSDM performed better than the PreSTM approach and that PreSTM sections for both seismic profiles are inadequate for accurate geological interpretation of subsurface structures at the mine scale (Figs. 11 and 12). In areas of rapid vertical and lateral velocity changes, energy is dispersed in such a way that PreSTM and PostSTM data cannot provide the desired resolution (Kosloff *et al*., 1996; Zhou, 2002). PostSTM assumes that the stack section is of zero-offset input which is not valid for complex subsurface settings. The PreSDM approach enhances the image of the subsurface in areas where both the vertical and lateral velocity models are changing. Better handling of the velocity model can therefore assist in improving the quality of the data when imaging at depth.

Although raw data show a relatively good signal-to-noise ratio with good quality first breaks seen at all offsets, the imaging of reflections clearly is hampered by scattering of the seismic energy due to karst weathering of the dolomite outcrops belonging to the Malmani Subgroup.

CONCLUSION

We have re-processed two 2D legacy seismic datasets acquired in 1988, near KDC East Mine using modern processing algorithms. The data benefited from careful processing using post-stack time, pre-stack time, and pre-stack depth migration approaches, and handling of velocity analysis. In particular, careful application of refraction static corrections for near-surface velocity characterization was key in producing clear near-surface images. The processing of the legacy seismic data show the good quality imaging of downdip and lateral continuation of the BLR, down to a depth of 2 km. The data also enables the delineation of different dipping structures, i.e., north-south trending and steeply dipping normal faults that crosscut and displace the BLR and low-angle thrusts within the basement rocks. The performance of Kirchhoff PreSTM, PreSDM, and PostSTM imaging approaches was tested on both profiles. We found that the PreSDM approach is efficient in imaging deeper, while PostSTM works better on shallow reflections. Our processing results of the legacy seismic data show that the

added value of legacy data reprocessing is significantly high, encouraging mining companies in South Africa and worldwide to revive their old seismic data using the latest processing tools.

ACKNOWLEDGEMENTS

The donation of 2D legacy seismic data by Sibanye Stillwater is acknowledged and greatly appreciated. The Council of Geosciences, Research Office Carnegie Bursary, and National Research Foundation are acknowledged for financial support. We wish to thank HiSeis for funding a license for the GLOBE Claritas seismic processing software package, Tesseral Technologies for sponsoring the licenses for Tesseral seismic modelling software, Schlumberger for Petrel licenses, and the Seismic Research Center at the University of the Witwatersrand for MATLAB licenses.

DATA AVAILABILITY

Seismic research data that support the findings of this study are available on request from the corresponding author. The data are not publicly available due to privacy restrictions. Geological outcrop data can be found on the website of The Council for Geoscience, South Africa. (https://maps.geoscience.org.za/portal/apps/sites/?fromEdit=true#/interactivewebmap)

REFERENCES

Armstrong, R.A., Compston, W., Retief, E.A., Williams, I.T. and Welke, H.J., 1991. Zircon ion microprobe studies bearing on the age and evolution of the Witwatersrand triad. *Precambrian Research*, *53*(3-4), pp.243-266.

Barton, E.S., Compston, W., Williams, I.S., Bristow, J.W., Hallbauer, D.K. and Smith, C.B., 1989. Provenance ages for the Witwatersrand Supergroup and the Ventersdorp contact reef; constraints from ion microprobe U-Pb ages of detrital zircons. *Economic Geology*, *84*(7), pp.2012-2019.

Beach, A. and Smith, R., 2007. Structural geometry and development of the Witwatersrand Basin, South Africa. *Geological Society, London, Special Publications*, *272*(1), pp.533-542.

Burger, A.J. and Coertze, F.J., 1975. Age determinations–April 1972 to March 1974. *Annals of the Geological Survey of South Africa*, *10*, pp.135-141.

Brandl, G., Cloete, M. and Anhaeusser, C.R., 2006, Archaean greenstone belts, in Johnson, M.R., Anhaeusser, C.R., and Thomas, R.J., eds., The geology of South Africa: Pretoria, Geological Society of South Africa, Johannesburg and Council for Geoscience, v. 51, p. 9–56.

Campbell, G. and Crotty, J.H., 1990. 3-D seismic mapping for mine planning purposes at the South Deep Prospect. In: D.A.J. Ross-Watt and P.D.K, Robinson (Eds). *Proceedings International Deep Mining Conference:* SAIMM Symposium Series, S1O(2), pp. 569-597.

Campbell, G., 2011. Exploration geophysics of the Bushveld Complex in South Africa. *The Leading Edge*, *30*(6), 622–638. https://doi.org/10.1190/1.3599148

Catuneanu, O., 2001. Flexural partitioning of the late Archaean Witwatersrand foreland system, South Africa. *Sedimentary Geology*, *141*, pp.95-112.

Donoso, G.A., Malehmir, A., Pacheco, N., Araujo, V., Penney, M., Carvalho, J., Spicer, B. and Beach, S., 2020. Potential of legacy 2D seismic data for deep targeting and structural imaging at the Neves–Corvo massive sulphide-bearing deposit, Portugal. *Geophysical Prospecting*, *68*(1-Cost-Effective and Innovative Mineral Exploration Solutions), pp.44-61. doi:10.1111/1365-2478.12861.

Durrheim, R.J., 2016. Hard rock reflection seismics. *The History of Geophysics in Southern Africa*, p.237.

Eaton, D.W., Milkereit, B. and Salisbury, M.H. eds., 2003. Hardrock seismic exploration. Society of Exploration Geophysicists.

Els, B.G., Van den Berg, W.A. and Mayer, J.J., 1995. The Black Reef Quartzite Formation in the western Transvaal: sedimentological and economic aspects, and significance for basin evolution. *Mineralium Deposita*, *30*(2), pp.112-123.

Ericksson, P.G., Hattingh, P.J. and Altermann, W., 1995. An overview of the geology of the Transvaal Sequence and Bushveld Complex, South Africa. *Mineralium Deposita*, *30*(2), pp.98-111. https://doi.org/10.1007/BF00189339.

Ericksson, P.G., Alterman, W. and Hartzer, F.J., 2006. The Transvaal Supergroup and its percursors. *Johnson MR, Anhaeusser CR and Thomas RJ (eds.) The Geology of South Africa. Geological Society of South Africa, Johannesburg/Council for Geoscience, Pretoria*, pp.461-499.

Frimmel, H.E., 2005. Archaean atmospheric evolution: evidence from the Witwatersrand gold fields, South Africa. *Earth-Science Reviews*, *70*(1-2), pp.1-46.

Frimmel, H.E., 2014. A giant Mesoarchean crustal gold-enrichment episode: Possible causes and consequences for exploration. Society of Economic Geologists, Special Publication 18, pp. 209–234.

Frimmel, H.E., 2019. The Witwatersrand Basin and its gold deposits. In *The Archaean geology of the Kaapvaal craton, southern Africa* (pp. 255-275). Springer, Cham.

Fuchs, S., Williams-Jones, A.E. and Przybylowicz, W.J., 2016. The origin of the gold and uranium ores of the Black Reef Formation, Transvaal Supergroup, South Africa. *Ore Geology Reviews*, *72*, pp.149-164.

Henry, G. and Master, S., 2008. Black reef project. *Council for Scientific and Industrial Research (CSIR) and University of the Witwatersrand, Johannesburg*.

Kosloff, D., Sherwood, J., Koren, Z., Machet, E. and Falkovitz, Y., 1996. Velocity and interface depth determination by tomography of depth migrated gathers. *Geophysics*, *61*(5), pp.1511-1523.

Kröner, A., Hoffmann, J., Wong, J.M., Geng, H.Y., Schneider, K.P., Xie, H., Yang, J.H. and Nhleko, N., 2019. Archaean crystalline rocks of the Eastern Kaapvaal Craton. In *The Archaean Geology of the Kaapvaal Craton, Southern Africa* (pp. 1-32). Springer, Cham. https://doi.org/10.1007/978-3-319-78652-0_1.

Malehmir, A., Durrheim, R., Bellefleur, G., Urosevic, M., Juhlin, C., White, D.J., Milkereit, B. and Campbell, G., 2012. Seismic methods in mineral exploration and mine

planning: A general overview of past and present case histories and a look into the future, Seismic methods for mineral exploration. *Geophysics*, *77*(5), pp.WC173-WC190.

Malehmir, A., Koivisto, E., Manzi, M., Cheraghi, S., Durrheim, R.J., Bellefleur, G., Wijns, C., Hein, K.A. and King, N., 2014. A review of reflection seismic investigations in three major metallogenic regions: The Kevitsa Ni–Cu–PGE district (Finland), Witwatersrand goldfields (South Africa), and the Bathurst Mining Camp (Canada). *Ore Geology Reviews*, *56*, pp.423-441.

Malehmir, A., Donoso, G., Markovic, M., Maries, G., Dynesius, L., Brodic, B., Pecheco, N., Marsden, P., Bäckström, E., Penney, M. and Araujo, V., 2019. Smart Exploration: from legacy data to state-of-the-art data acquisition and imaging. *First Break*, *37*(8), pp.71-74.

Malehmir, A., Manzi, M., Draganov, D., Weckmann, U. and Auken, E., 2020. Introduction to the special issue on "Cost-effective and innovative mineral exploration solutions". *Geophysical prospecting*, *68*(1), pp.3-6.

Manzi, M.S., Durrheim, R.J., Hein, K.A. and King, N., 2012. 3D edge detection seismic attributes used to map potential conduits for water and methane in deep gold mines in the Witwatersrand basin, South Africa. *Geophysics*, *77*(5), pp.WC133-WC147.

Manzi, M.S., Hein, K.A., King, N. and Durrheim, R.J., 2013. Neoarchaean tectonic history of the Witwatersrand Basin and Ventersdorp Supergroup: New constraints from high-resolution 3D seismic reflection data. *Tectonophysics*, *590*, pp.94-105.

Manzi, M.S., Hein, K.A., Durrheim, R.J. and King, N., 2014. The Ventersdorp Contact Reef model in the Kloof Gold Mine as derived from 3D seismics, geological mapping and exploration borehole datasets. *International Journal of Rock Mechanics and Mining Sciences*, *66*, pp.97-113.

Manzi, M., Cooper, G., Malehmir, A., Durrheim, R. and Nkosi, Z., 2015. Integrated interpretation of 3D seismic data to enhance the detection of the gold-bearing reef: Mponeng Gold mine, Witwatersrand Basin (South Africa). *Geophysical Prospecting*, *63*(4-Hard Rock Seismic imaging), pp.881-902.

Manzi, M., Malehmir, A. and Durrheim, R.J., 2018a. 3D Reflection Seismics for Deep Platinum Exploration in the Bushveld Complex, South Africa. In *2nd Conference on*

Geophysics for Mineral Exploration and Mining (Vol. 2018, No. 1, pp. 1-5). European Association of Geoscientists and Engineers.

Manzi, M., Malehmir, A. and Durrheim, R. J., 2018b. Improved Subsurface Imaging through Re-processing of Legacy 2D Seismic Data-A Case Study from a Deep South African Gold Mine. In *2nd Conference on Geophysics for Mineral Exploration and Mining* (Vol. 2018, No. 1, pp. 1-5). European Association of Geoscientists and Engineers.

Manzi, M., Malehmir, A. and Durrheim, R., 2019. Giving the legacy seismic data the attention they deserve. *First Break*, *37*(8), pp.89-96.

Markovic, M., Maries, G., Malehmir, A., von Ketelhodt, J., Bäckström, E., Schön, M. and Marsden, P., 2020. Deep reflection seismic imaging of iron-oxide deposits in the Ludvika mining area of central Sweden. *Geophysical Prospecting*, *68*(1-Cost-Effective and Innovative Mineral Exploration Solutions), pp.7-23.

Milkereit, B., Eaton, D., Wu, J., Perron, G., Salisbury, M.H., Berrer, E.K. and Morrison, G., 1996. Seismic imaging of massive sulfide deposits; Part II, Reflection seismic profiling. *Economic Geology*, *91*(5), pp.829-834.

Myers, R.E., McCarthy, T.S. and Stanistreet, I.G., 1990. A tectono-sedimentary reconstruction of the development and evolution of the Witwatersrand Basin, with particular emphasis on the Central Rand Group. *South African Journal of Geology*, *93*(1), pp.180-201.

Nkosi, N.Z., Manzi, M.S., Drennan, G.R. and Yilmaz, H., 2017. Experimental measurements of seismic velocities on core samples and their dependence on mineralogy and stress; Witwatersrand Basin (South Africa). *Studia Geophysica et Geodaetica*, *61*(1), pp.115-144.

Nwaila, G.T., Durrheim, R.J., Jolayemi, O.O., and Maselela, H.K., 2020. Significance of granite-greenstone terranes in the formation of Witwatersrand-type gold mineralisation – a case study of the Neoarchaean Black Reef Formation, South Africa. *Ore Geology Reviews, 121*, 103572.

Nwaila, G.T., Manzi, S.D., Zhang, S.E., Bourdeau, J.E., Bam, L.C., Rose, D.H., Maselela, K., Reid, D.L., Ghorbani, Y. and Durrheim, R.J., 2022. Constraints on the geometry and gold distribution on the Black Reef Formation of South Africa using 3D reflection seismic data and micro-X-ray computed tomography. *Natural Resources Research*, in press.

Penning, W.H., 1891. A Contribution to the Geology of the Southern Transvaal. *Quarterly Journal of the Geological Society*, *47*(1-4), pp.451-463.

Pretorius, C.C., Jamison, A. and Irons, C., 1989. Seismic exploration in the Witwatersrand basin, Republic of South Africa. In *Proceedings of Exploration* (Vol. 87, pp. 241-253). Ontario Geol. Sur.

Pretorius C.C., Muller M.R., Larroque M. and Wilkins C., 2003. A review of 16 years of hardrock seismics on the Kaapvaal Craton, Hardrock Seismic Exploration. In: Developments in Geophysics Series. (ed. Eaton, D., Salisbury, M. and Milkereit, B.) SEG, Houston. 2003, 247–268. https://doi.org/10.1190/1.9781560802396.ch16.

Ranjith, P.G., Zhao, J., Ju, M., De Silva, R.V., Rathnaweera, T.D. and Bandara, A.K., 2017. Opportunities and challenges in deep mining: a brief review. *Engineering*, *3*(4), pp.546-551.

Reid, A.B., Polome, L.G. and Greene, B.W., 1979. Ultra-high resolution reflection seismics in chromite detection. In *49th Annual International Meeting. New Orleans: SEG*.

Robb, L.J., Davis, D.W., Kamo, S.L. and Meyer, F.M., 1992. Ages of altered granites adjoining the Witwatersrand Basin with implications for the origin of gold and uranium. *Nature*, *357*(6380), pp.677-680.

Rundle, C.C. and Snelling, N.J., 1977. The geochronology of uraniferous minerals in the Witwatersrand Triad; an interpretation of new and existing U-Pb age data on rocks and minerals from the Dominion Reef, Witwatersrand and Ventersdorp Supergroups. *Philosophical Transactions of the Royal Society of London. Series A, Mathematical and Physical Sciences*, *286*(1336), pp.567-583.

Salisbury, M.H., Milkereit, B. and Bleeker, W., 1996. Seismic imaging of massive sulfide deposits; Part I, Rock properties. *Economic Geology*, *91*(5), pp.821-828.

South African Committee for Stratigraphy (SACS)., 1980. Stratigraphy of South Africa. Part I: Lithostratigraphy of the Republic of South Africa, South West Africa/ Namibia and the Republics of Bophuthatswana, Transkei and Venda, Handb. Geol. Surv. S. Afr. 8.

Sheriff, R.E., 1997. Seismic resolution a key element. *AAPG Explorer*, *18*(10), pp.44-51.

Stevenson, F and RJ Durrheim, 1997. Reflection seismics for gold, platinum and base metal exploration and mining in southern Africa, Proc. Exploration 97: 4th Decennial International Conference on Mineral Exploration, G. Gubins (ed.), 391-398.

Terracin, M. and Manzi, M., 2017. Spatial corrections for post-stack time migrated legacy 2D seismic data: A case study from the Witwatersrand Basin, South Africa. *15th Biennial Conference and Exhibition, SA Geophys. Assn,* 10-13 September 2017, Somerset West. Published online, paper 2017-107.

Tucker, R.F., Viljoen, R.P. and Viljoen, M.J., 2016. A review of the Witwatersrand Basin–The world's greatest goldfield. *Episodes*, *39*(2), pp.105-133.

Van der Westhuizen, W.A., De Bruiyn, H. and Meintjes, P.G., 1991. The Ventersdorp supergroup: an overview. *Journal of African Earth Sciences (and the Middle East)*, *13*(1), pp.83-105. https://doi.org/10.1016/0899-5362(91)90045-Z.

von Ketelhodt, J.K., Manzi, M.S. and Durrheim, R.J., 2019. Post-stack denoising of legacy reflection seismic data: Implications for coalbed methane exploration, Kalahari Karoo Basin, Botswana. *Exploration Geophysics*, *50*(6), pp.667-682.

Walraven, F., 1995. Zircon Pb-evaporation age determinations of the oak tree formation, Chuniespoort group, Transvaal sequence: implications for Transvaal-Griqualand west basin correlations. *South African Journal of Geology*, *98*(1), pp.58-67.

Westgate, M., Manzi, M.S., James, I. and Harrison, W., 2020. New insights from legacy seismic data: reprocessing of legacy 2D seismic data for imaging of iron-oxide mineralization near Sishen Mine, South Africa. *Geophysical Prospecting*, *68*(7), pp.2119-2140.

Westgate, M., 2020. Reappraisal of legacy reflection seismic data using advanced processing techniques and seismic attributes. Ph.D. Thesis. University of the Witwatersrand, South Africa.

Widess, M.B., 1973. How thin is a thin bed?. *Geophysics*, *38*(6), pp.1176-1180.

Yilmaz, Ö., 2001. *Seismic data analysis: Processing, inversion, and interpretation of seismic data*. Society of Exploration Geophysicists.

Zhou, H.W., 2002, October. Kirchhoff reflection tomography: Concept and preliminary result. In *2002 SEG Annual Meeting*. OnePetro.

8. Paper II: Seismic imaging of deep-seated gold deposit and host rocks through reappraisal of legacy seismic data in the Fochville mining area, South Africa

Ndamulelo Mutshafa[1*], Musa S.D. Manzi[1], Ian James[1, 2]

[1]*School of Geosciences, University of the Witwatersrand, Private Bag 3, WITS, Johannesburg 2050, Republic of South Africa*

[2] *Southern Geoscience Consultants, West Perth, WA, Australia*

*** E-mail:** Ndamulelo.Mutshafa@students.wits.ac.za

Abstract

Reappraisal of legacy reflection seismic data have shown to deliver value in mineral exploration, particularly in brownfield settings. In this work, we demonstrate how the reappraisal and processing of legacy reflection seismic data can be advantageous in the mineral exploration industry by using today's standard seismic processing tools to improve the imaging of deep and complex geological structures that host mineral deposits. The recovered and processed 25.3 km long legacy seismic profile in this study was acquired in 1983 by the Gold Division of Anglo-American in as part of the Witwatersrand Goldfields exploration program. This study aims to improve the imaging of the Ventersdorp Contact Reef (VCR) gold-bearing horizon (termed reef), a world-class gold deposit (2 m thick) situated at depths between ~2400 and ~4100 m below the ground surface near South Deep mine in Fochville, South Africa. The final processing results from the pre-stack time and phase-shift migration approaches clearly reveal a dipping reflection associated with the gold-bearing horizon and major steeply dipping faults that crosscut and displace the deposit. The final results are integrated with borehole information, 1D synthetic modeling, and aeromagnetic data to constrain the structural interpretation. In particular, 1D synthetic simulation and borehole data constrain the depth position of the gold deposit. The magnetic data provide additional constraints on the complex

faulted blocks of the host rocks that may have a direct impact on ore resources and evaluation. The mining companies, such as South Deep gold mine, operating closer to the seismic profiles can use this new structural information to update the current geological models and improve future mine planning and designs, thus providing some insight into the prospectivity of unmined ground.

Keywords: Exploration; seismic; imaging; mining; processing

INTRODUCTION

The reflection seismic method is a powerful geophysical technique that uses the reflection of seismic waves to obtain an image of the Earth's subsurface (Yilmaz, 2001). Reflected seismic waves bring information about the rocks and geological structures in the subsurface (Ahmadi, 2015). Active seismic methods are widely employed by the seismic and mineral exploration industry. Traditionally, the primary aim of seismic exploration has been to study geological sources of large lateral extent, such as boundaries of geologic formation, and oil and gas deposits (Keydar et al., 2018). Numerous case studies using seismic reflection for hard rock mineral exploration have been published by researchers from all over the world (Manzi et al., 2012b; Manzi et al., 2018; Malehmir et al., 2012; 2014, 2020; Markovic et al., 2020; Ahmadi et al., 2013; Ziramov et al., 2023). These examples demonstrate the growing use of seismic reflection techniques for mineral exploration. As a result of the decline in the number of deposits found at shallow depths, subsurface exploration has gradually shifted towards deposits at greater depths (> 500 m). A method with higher resolution and a deep penetration depth is needed to distinguish between deposits and their structures at depth (Malehmir et al., 2012 and references therein). The seismic reflection method provides the highest resolution subsurface images (compared to other geophysical methods) of geological structures hosting mineral deposits and can, in favorable geology, be used to directly detect minerals deposits at depths greater than 1 km (Malehmir et al., 2012; Manzi et al., 2012b).

Seismic data have proven capability in mineral exploration and mine planning (Markovic et al., 2020). Reappraisal of legacy reflection seismic data have shown to deliver value, particularly if they are from a brownfield setting, near or even above active mines (Malehmir et al., 2014; 2020). Legacy data have advantages such as being less contaminated by noise from mining activities (e.g., blasting, drilling, rock crushing, etc.); being less contaminated by electric/electromagnetic noise; have been acquired in places that presently may be unavailable for new surveys; and ultimately coming at a lower cost compared to new acquisition campaigns (i.e., Donoso et al., 2020 and references therein).

The study's main objective is to image the gold orebody known as the Ventersdorp Contact Reef (VCR, ca. ~1.5 – 2 m thickness) at depths between 2400 and 3900 m below the surface near South Deep Gold mine in Fochville of the West Rand goldfield. More focus will be on imaging the VCR orebody, its continuity, and the faults that intersect it. The VCR occurs at a strong seismic reflective interface between the Ventersdorp Supergroup and Central Rand Group of the Witwatersrand Supergroup, thus a good candidate for seismic imaging (Manzi et al., 2012a, b). South Deep gold mine uses a mechanized mining method and exploits the Upper Elsburg conglomerates (multi-stacked reefs) located a few meters below the VCR orebody. The mine plans to extend its deep mining operations towards the south of the current mining activities; therefore, a better imaging of the VCR may enable the mine to understand the structural complexity of the VCR and the underlying orebodies at depths down to 4200 below surface.

GEOLOGICAL SETTINGS

Many scholars have documented the geological background of the West Rand goldfield in the Witwatersrand Basin, including Gibson et al., (2000), Jolley et al., (2004), McCarthy (2006), Beach and Smith (2007), Dankert and Hein (2010), and Nwaila et al., (2021). Due to its

supremacy in global gold production, the Witwatersrand Basin has drawn scholars for over a century (Robb and Myer, 1995). The Witwatersrand Basin hosts some of the world's largest and deepest gold mines, with reefs (e.g., VCR) exploited at depths ranging from 500 to 4200 m below the earth's surface (Mkhabela and Manzi, 2017). The Ventersdorp Contact Reef (VCR) is one of the basin's most economically important gold-bearing orebodies.

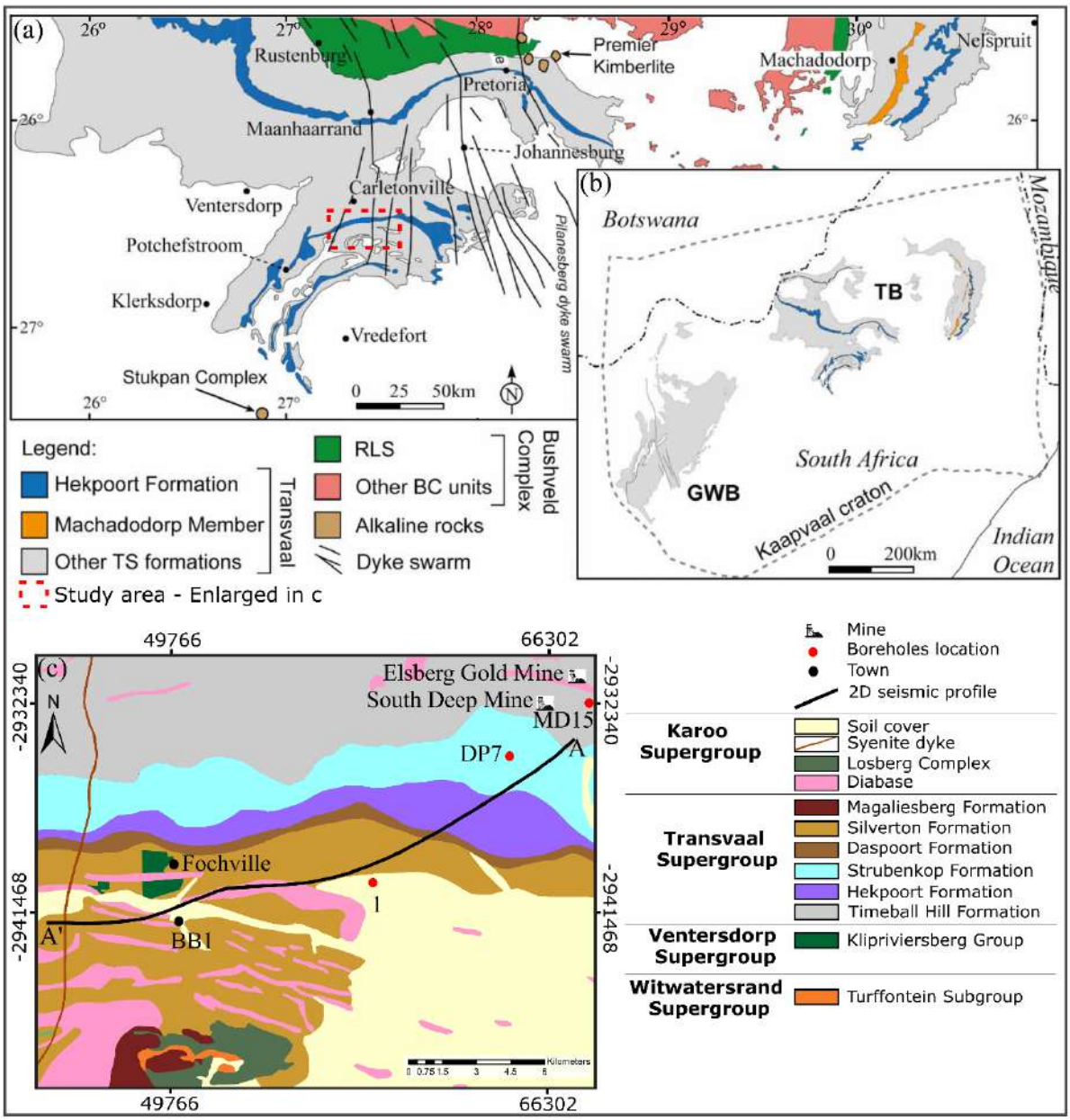


Figure 1. (a) Location map showing the local geology including the Transvaal Supergroup (TS), with an emphasis on its strata-bound igneous unit i.e., Hekpoort Formation, other TS

formations, and Bushveld Complex (BC) in the Transvaal sub-basin (TB). (b) The Kaapvaal Craton boundaries and preserved extent of the TS are mainly distributed within two sub-basins, the TB and the Griqualand West sub-basin (GWB). (c) Simplified geological map of the study area showing the position of the 2D seismic profile (A – A'). Figure modified after Humbert et al., 2020.

The Witwatersrand Supergroup (Figure 1) is a 7000-8000-meter-thick metasedimentary basin that formed between 2985 and 2849 Ma. It unconformably overlies the Dominion Group and is separated into the lower West Rand Group and the upper Central Rand Group (McCarthy, 2006; Dankert and Hein, 2010; Mkhabela and Manzi, 2017). The lower West Rand Group (5150 m thick) is comprised of shale and quartzite units with minor conglomerate beds, restricted to the upper part of the group (Frimmel, 2019; Nwaila et al., 2021), while the upper Central Rand Group (2880 m thick) is made up of alternating quartzite and conglomerate and was deposited around 2902 Ma. The upper Central Rand Group is subdivided into the Johannesburg and subsequent Turffontein subgroups, and it hosts almost more than 90% of the ore gold deposits found in the Witwatersrand Basin. Lavas from the Ventersdorp Supergroup cover the Central Rand Group, with the Venterspost Formation's VCR at the base. The VCR conformably underlies the basaltic rocks of the overlying Klipriviersberg Group and the acoustic impedance contrast at the interface between the high velocity, dense ultramafic lavas (6457 m/s, 2.98 g/cm^3) of the Ventersdorp Supergroup and the low-velocity, less dense quartzites (5899 m/s, 2.75 g/cm^3) of the Central Rand Group creates a strong seismic reflector that correlates with the VCR (Gibson et al., 2000; Manzi et al., 2015; Pretorius et al., 1997; Figure 2). The Ventersdorp magmatic activity was followed by the continuous deposition of a relatively thin Black Reef (BLR) Formation, which is the basal lithostratigraphic unit of the Transvaal Supergroup (Beach and Smith, 2007). The BLR is a strong seismic marker due to its

location between the significant acoustic impedance contrasting hangingwall (dolostone) and footwall (basaltic lavas) rocks.

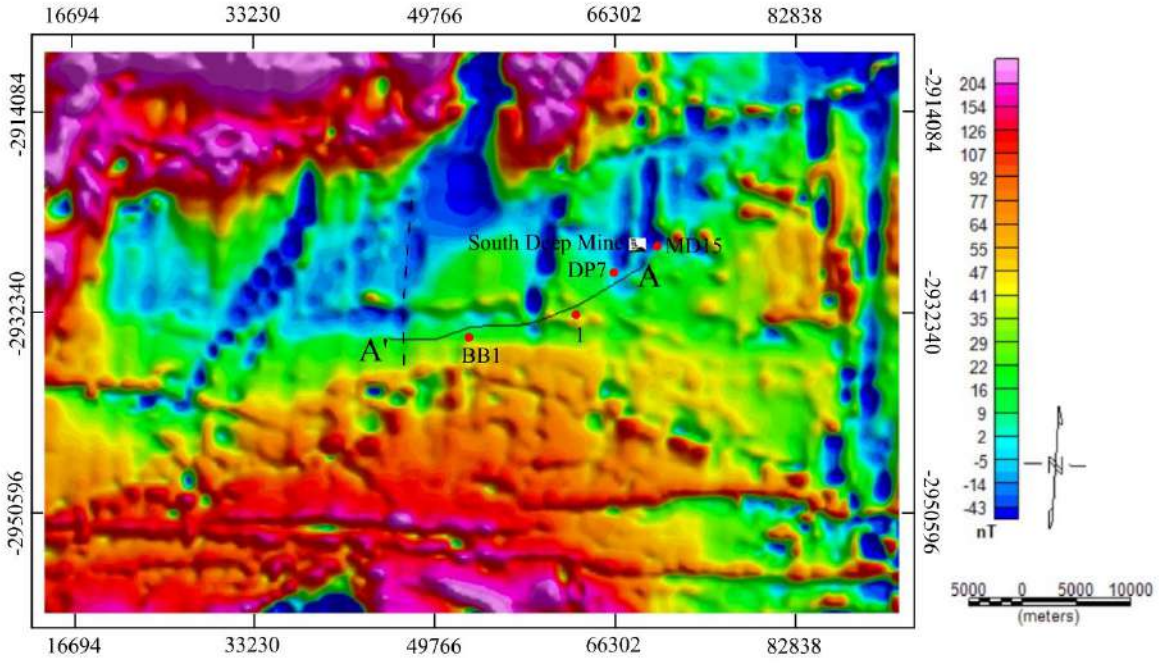


Figure 2. Aeromagnetic map with the location of the seismic profile. The stripes with strong magnetic low-blue seem to be dykes with remanent magnetization.

The West Rand goldfield has experienced several tectonic events, which have been confirmed through previous studies (Coward et al.,1995, Beach and Smith, 2007, Dankert and Hein, 2010, Jolley et al., 2007; Manzi et al., 2013a). For example, the gold deposits in the Fochville mining region are mainly affected by (1) major faulting and folding attributed to extensional tectonics that occurred during the deposition of the Ventersdorp Supergroup, and (2) several steeply dipping dolerite sills and dykes that are attributed to Karoo (150 Ma), Pilanesburg (1.3 Ga), Transvaal (2.20 Ga), and Ventersdorp (2.60 Ga) volcanic activities. The sills and dykes trend north-south and east-west near the study area as observed in the regional aeromagnetic map in Figure 2. These structures, if not properly mapped, can complicate the extraction of ore by removing or interrupting portions of the mineral deposits. Figure 3 shows

the boreholes drilled close to the profile in the survey area (see Figure 1c for borehole locations), which were used to constrain seismic processing and interpretation.

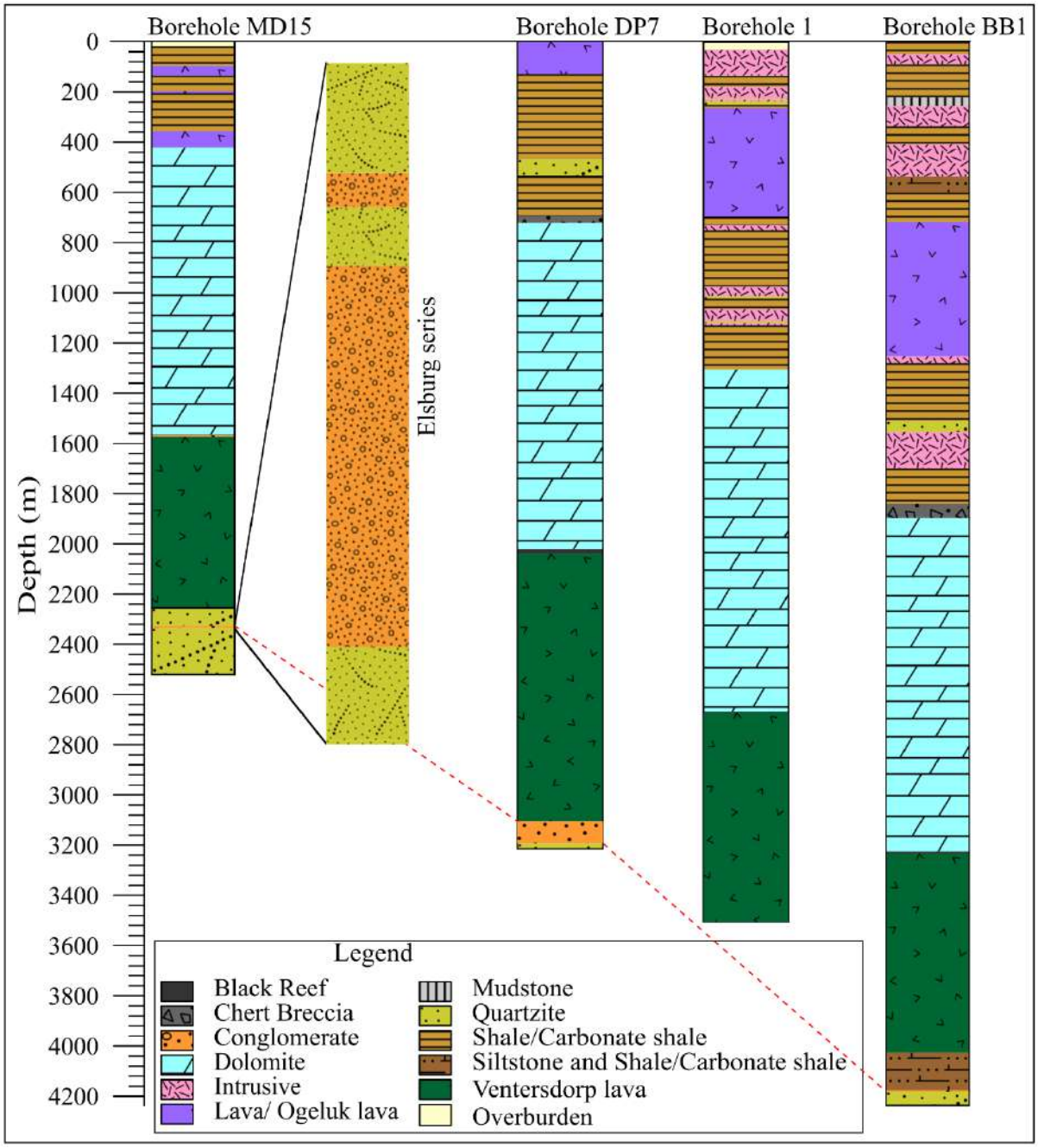


Figure 3. Borehole logs were drilled in our survey area. Four borehole logs are presented (i.e., boreholes MD15, DP7, 1, and BB1). The data shows all boreholes intersect the lithological unit Black Reef Formation. The deepest borehole (BB1) was drilled up to 4.2 km. The red and blue dotted lines show the tracing of the mineralization across the boreholes.

LEGACY 2D SEISMIC DATA

Seismic data acquisition

The legacy seismic data were acquired in 1983 by the Gold Division of Anglo-American as a part of a major gold exploration programme in the Kaapvaal craton (Manzi et al., 2018). The acquisition parameters of the seismic survey are summarized in Table 1.

Table 1. Main Acquisition parameters for the profile.

Acquisition parameters	
Type of survey	2D
Year	1983
Profile length	25.3 km
Trend	NE-SW
Field spread	End-on × - 175 – 4975 m
Recording system	
Recording device	SN338 HR/ ADDIT III/ CMA I
Sampling rate	4 ms
Recording length	6 s
Sweep length	26 s
Sweep frequencies	10 – 90 Hz
Number of sweeps	8
Source information	
Source spacing	50 m
Source type	Vibroseis

Source array	4 vibroseis trucks, inline
Receiver information	
Receiver spacing	50 m
Number of channels	96
Geophone type	10 Hz (SM4)
Pattern wiring	4 strings of 6

The survey had to follow a crooked line geometry along the local roads due to the field surface conditions and terrain. The seismic profile was acquired using eight sweeps generated by four vibroseis trucks inline as a source with a sweep frequency of 10 – 90 Hz over a 26 s sweep length, at a sampling rate of 4 ms. The data were received as raw shot gathers that had been correlated in-field and the detailed acquisition information was obtained from field observer's reports as well as from headers. The profile has a receiver and source station spacings of 50 m. The 2D seismic data have a profile length of 25.3 km with a NE-SW trend direction (Figure 1c). The seismic profile has a total of 461 shots with 96 channels per shot set up as 4 strings of 6 geophones in an inline linear array. The receivers had a natural frequency of 10 Hz (vertical single component), and the data were recorded with a low-cut filter of 8 Hz.

Seismic data reprocessing

There is no record of any publication from this profile. The data were received from Anglo Gold Ashanti as raw data together with some documentation such as field notes and observer's reports. Before setting up the geometry of the profile for processing, we first investigated the quality of the recorded gathers. The 2D seismic data had no source and receiver elevations from the headers. We then used Shuttle Radar Topography Mission (or SRTM) data to

determine reliable elevations and tied them to the source and receiver locations. We have been able to reconstruct coordinates, acquisition geometry, field pegs, and shot records for the profile. A summary of the preparation and processing steps applied to the data are given in Figure 4.

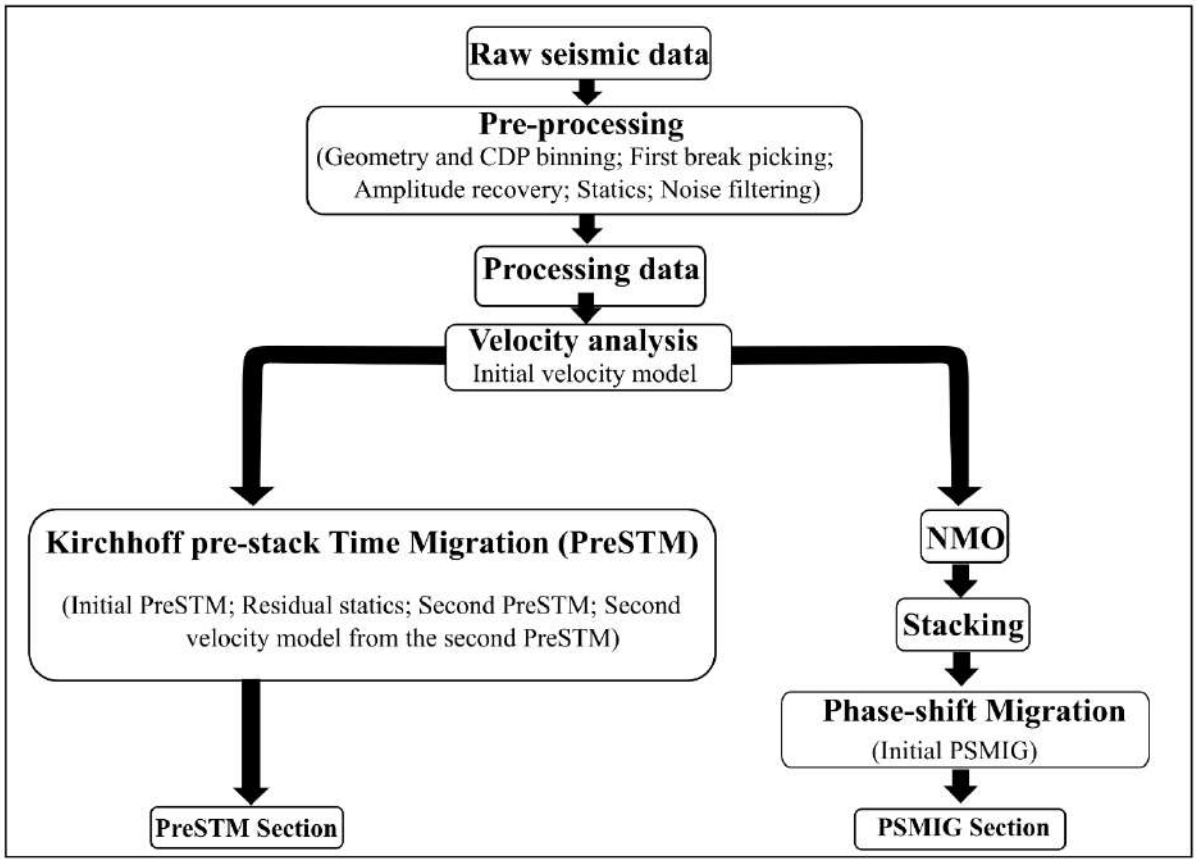


Figure 4. Schematic diagram of processing sequence used for the 2D seismic profile.

After successfully creating the geometry, we merged the trace headers with the geometry. The traces were binned into common midpoint (CMP) bins by fitting a spline curve through the cloud of common midpoints containing the highest number of traces and positioning bins along the line every 25 m. The resulting nominal common depth point (CDP) fold is 74 using the crooked line geometry with a bin size of 25 m. An automatic gain control

(AGC) was applied with a window length of 750 ms to recover attenuated amplitudes to all shot gathers. Figure 5 shows examples of the recorded shot gathers before and after initial processing with their frequency spectra. Generally, the seismic data are of good quality, with clear P-wave first breaks (highlighted by red arrows in Figure 5a, b) observed in most of the shot gathers and possible reflections above the orebody (e.g., R1-R3; BLR) in the top 1.5 s (TWT) and orebody-generated reflection (VCR) indicated by purple arrows between 2 and 3 s (TWT) (Figure 5). As indicated by black arrows, ground roll energy was removed by applying an f-k mute filter. Furthermore, reflections from fault systems are observed, dipping to the opposite side of the mineralization (VCR) and even possibly crossing the mineralization (Figure 5) as indicated by dash lines.

A total of 37941 P-wave first breaks were manually picked to compute refraction statics to correct the effect of the variable thickness and lateral velocity variation of weathering. Floating datum statics were applied with a reference datum elevation of 1650 m above mean sea level (amsl) along with a replacement velocity of 6000 m/s as observed from the refracted P-wave arrivals velocity. After pre-stack processing steps including CDP binning, floating datum and refraction statics corrections, frequency filtering (adaptive notch and bandpass), f-k filtering, and predictive deconvolution, the processed shot gathers clearly show enhanced reflections with high-signal-noise ratio (SNR). An adaptive notch filter was utilized to eliminate a prominent 50 Hz component of the data, which was most likely caused by the presence of power lines providing AC current near survey areas. A bandpass filter was used to attenuate frequencies that were not included in the sweep (10 - 90 Hz). An f-k mute was used to eliminate most of the airwave and ground-roll energy (shown by black arrows in Figure 5a, b). The data were subjected to predictive deconvolution, with the operator length and prediction gap defined per tenth shot and then interpolated for intermediate shots.

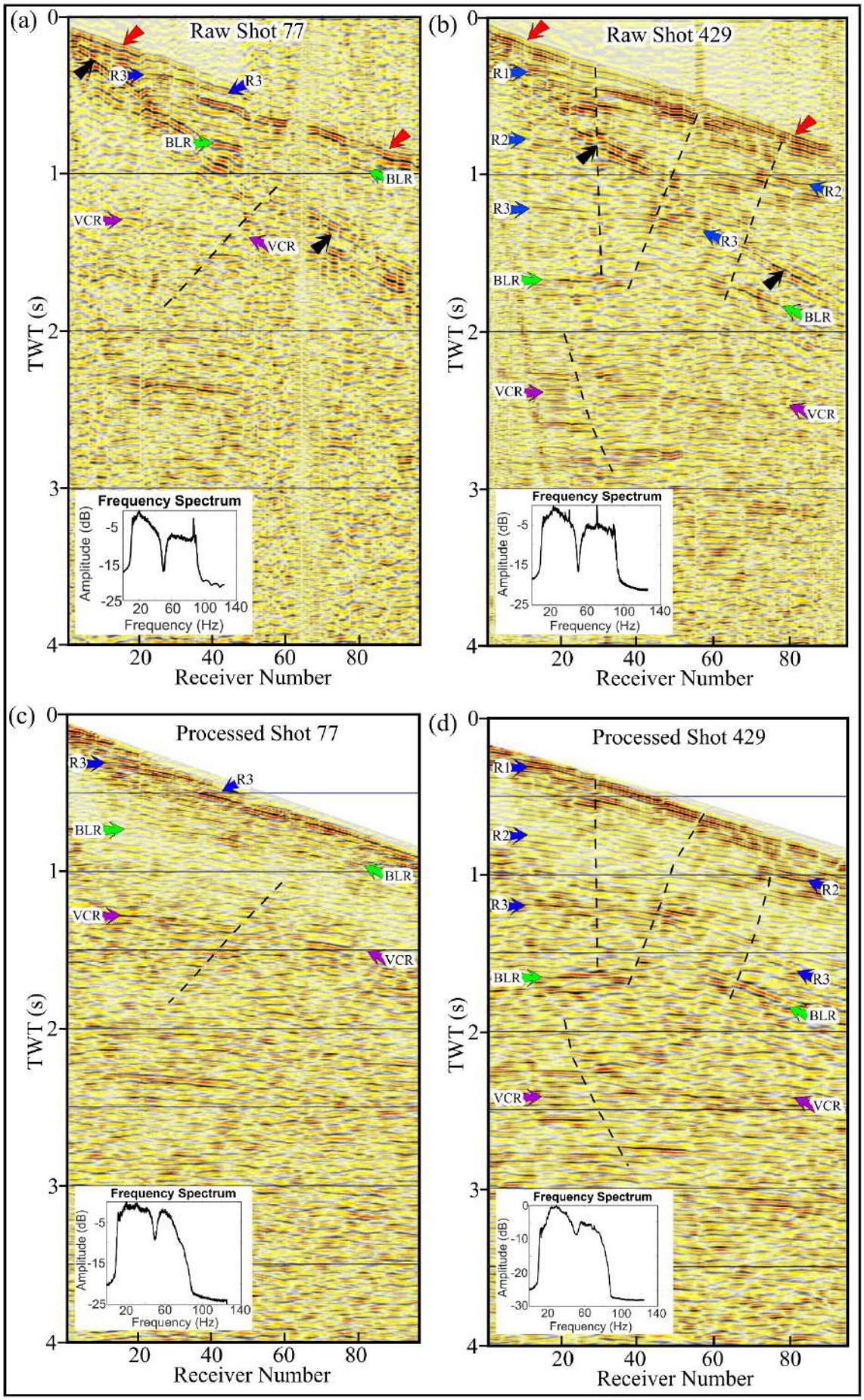

(a)
Raw Shot 77
R3
R3
BLR
BLR
VCR
VCR
Frequency Spectrum
Amplitude (dB)
-5
-15
-25
20 60 100 140
Frequency (Hz)
TWT (s)
0
1
2
3
4
20 40 60 80
Receiver Number
(b)
Raw Shot 429
R1
R2
R2
R3
R3
BLR
BLR
VCR
VCR
Frequency Spectrum
Amplitude (dB)
-5
-15
-25
20 60 100 140
Frequency (Hz)
TWT (s)
Receiver Number
(c)
Processed Shot 77
R3
R3
BLR
BLR
VCR
VCR
Frequency Spectrum
Amplitude (dB)
-5
-15
-25
20 60 100 140
Frequency (Hz)
TWT (s)
Receiver Number
(d)
Processed Shot 429
R1
R2
R2
R3
R3
BLR
BLR
VCR
VCR
Frequency Spectrum
Amplitude (dB)
0
-10
-20
-30
20 60 100 140
Frequency (Hz)
TWT (s)
Receiver Number

Figure 5. Example of shot gathers before (a, b) and after (c, d) applying the pre-stack processing, along with the respective amplitude spectra of each gather. Some shot gathers already applied a notch filter from the field. First breaks are indicated by red arrows; airwaves that are removed after processing are indicated by black arrows, and blue arrows indicate possible reflections (R1 – R3). Green arrows indicate reflection BLR and purple arrows indicate VCR orebody. BLR: Black Reef, and VCR: Ventersdorp Contact Reef.

A detailed interactive velocity analysis was performed and guided by constant velocity stacks (CVS) to construct a velocity model for dip-moveout (DMO). A series of residual static adjustment passes were performed to improve reflection coherency prior to DMO corrections. Following an offset-time domain Kirchhoff dip-moveout (DMO), the data were stacked along the CDP line with an 80% stretch mute. To increase the SNR of the data, the stacked section was subjected to F-x deconvolution. The post-stack -Phase shift migration (PSMIG) and the Kirchhoff pre-stack time migration (PreSTM) were tested on the dataset, and both provided good subsurface images for final interpretation. The Kirchoff PreSTM technique was chosen due to account for conflicting dips with different stacking velocities (Yilmaz, 2001) since the orebody is known to dip in the SW direction, while the PSMIG method is good at handling vertically varying velocities and dipping events of up to 90 degrees. Other migration algorithms tested included pre-and-post-stack finite difference and Stolk migration; however, these showed no improvement on the data. The final decision was then made to conduct the final structural interpretation on PSMIG, which was converted to depth using a constant velocity of 6000 m/s.

RESULTS AND INTERPRETATION

To better understand the seismic response and the source of seismic reflectivity of the different

lithologies in the study area, 1D-synthetic seismograms were conducted by calculating the acoustic impedances, and reflection coefficients as a function of depth and time (Figure 6). Four borehole logs from the study area were used to generate the synthetic seismograms (for the location of boreholes, see Figure 1).

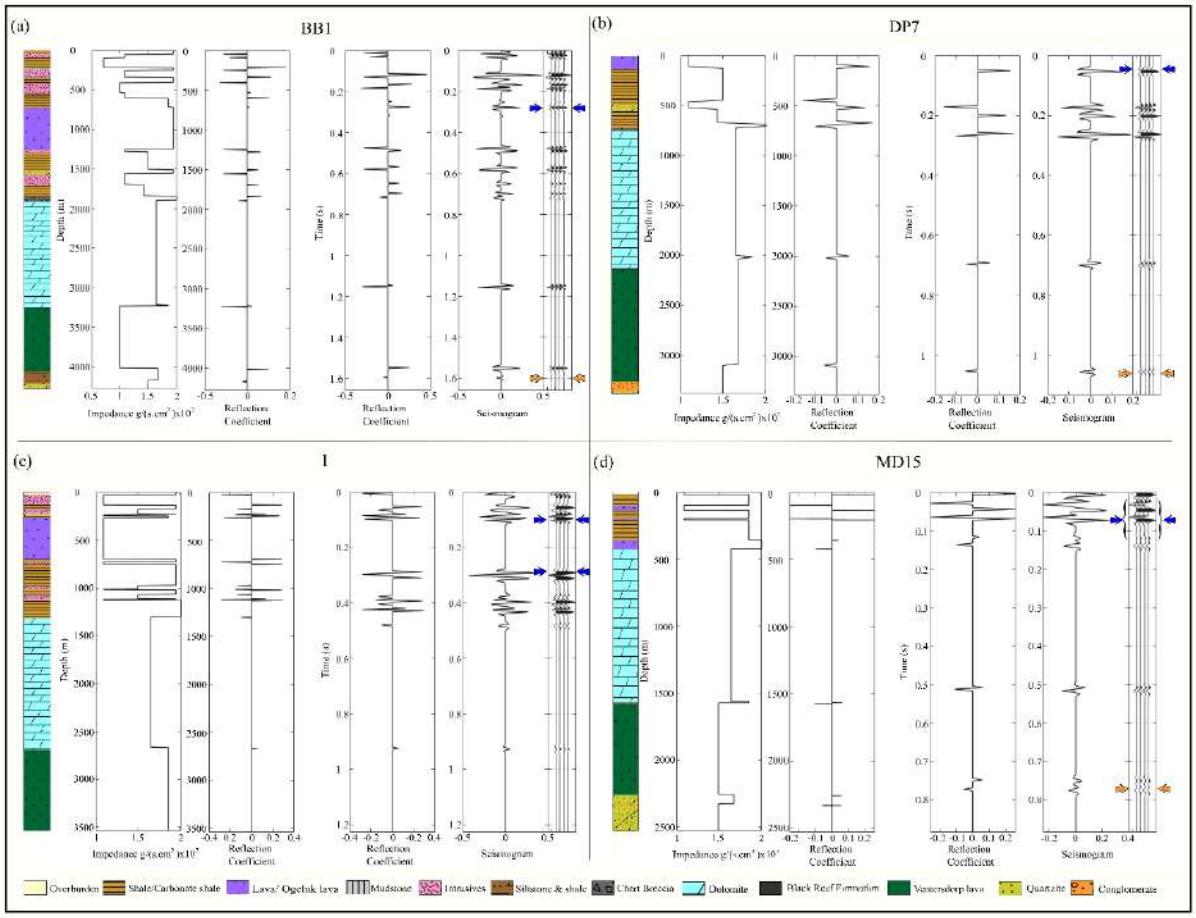


Figure 6. Calculated acoustic impedances, reflection coefficients as a function of depth and time, and synthetic seismograms for (a) borehole BB1, (b) borehole DP7, (c) borehole 1, and (d) borehole MD15 in the study area. All the 1D-synthetic seismograms were computed using a reflection coefficient with Ricker wavelet (55 Hz) at a sampling rate of 4 ms. Strong reflections are observed in all the synthetic seismograms and are associated with the interface between the shale and lavas units.

A sampling rate of 4 ms and a Ricker wavelet with a dominant frequency of 55 Hz was used to compute the synthetic seismograms. The results show a significant seismic response due to the conglomerate and the host rock for boreholes BB1, DP7, and MD15 (indicated by orange arrows in Figure 6a, b, d). Figure 6c shows that borehole 1 did not intersect the targeted orebody. All the 1D synthetic seismograms show strong reflections and are associated with the interface between the shale and lavas units (indicated by blue arrows). BB1 intersects the VCR at a depth of ~4180 m, DP7 intersects the VCR at a depth of ~3170 m, and MD15 intersects the VCR at a depth of ~2330 m.

For quality check, the first break picks and travel time residuals for the P-wave velocity tomogram are given in Figure 7a, b respectively. They are both plotted as a function of offset.

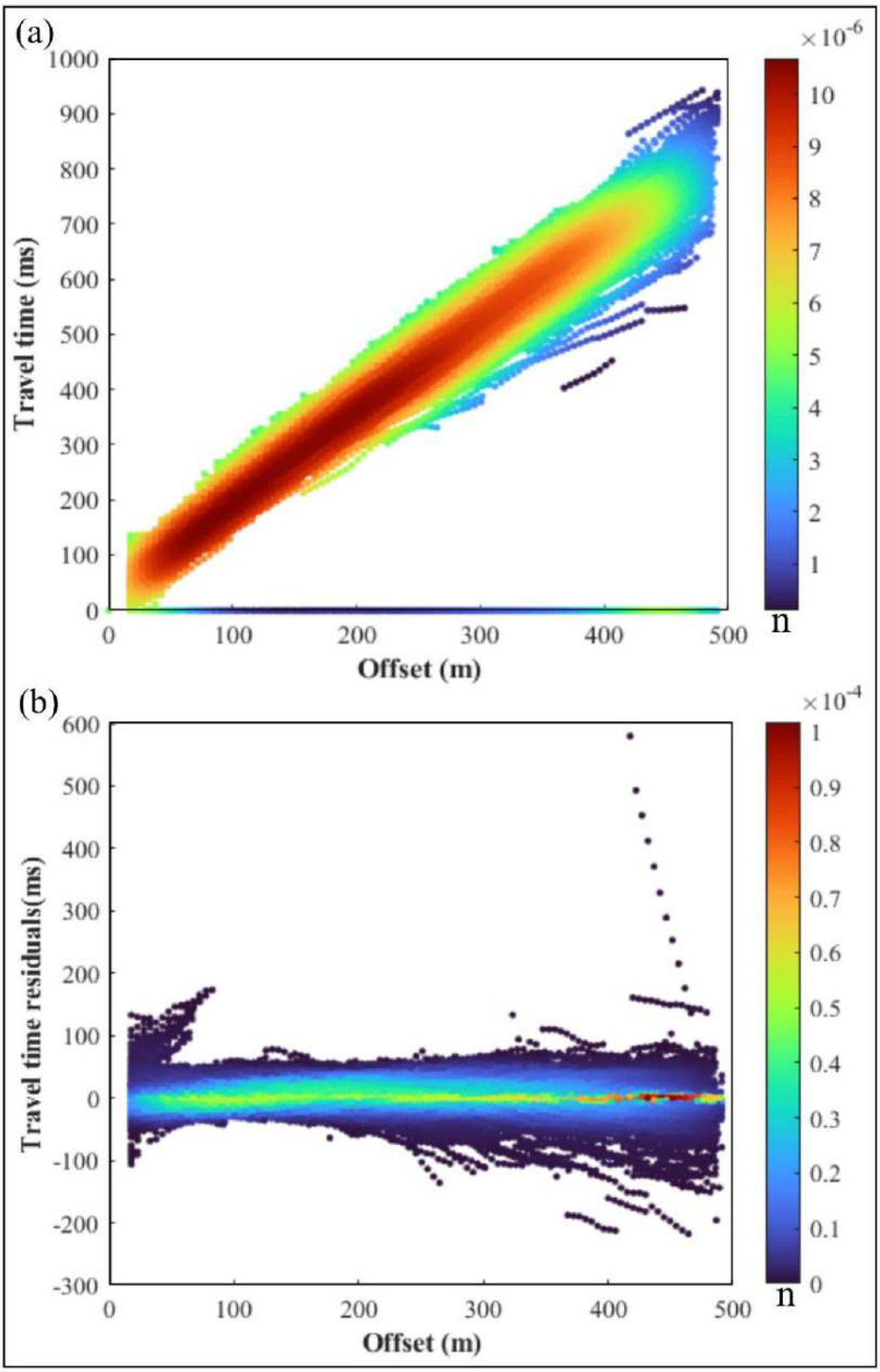

(a)
Travel time (ms)
Offset (m)
×10^-6
n
(b)
Travel time residuals(ms)
Offset (m)
×10^-4
n

Figure 7. Quality check of the first breaks and inverted tomographic model. First breaks (a) and travel time residuals (b) plots for the profile; plotted as a function of offset, where n is the number of points within a range.

Refraction tomography was calculated to aid the interpretation of the seismic profile up to a depth of 1600 m, the velocity model and the ray path coverage are displayed in Figure 8a, b. The uppermost layer of the initial model (blue-green color), largely observed within the top 50 m, is not interpreted in this study due to a lack of seismic resolution at these depths (Figure 8a). The second layer (yellow-orange color), underlying the first layer, has velocities ranging from 2500 to 5000 m/s and, largely, a thickness of 120 m. The third layer (red-pink color) is representing the host rock or basement with velocities of around 5000 m/s and greater. It is worth noting that the depth to the surface of the identified layers varies moving across the profile.

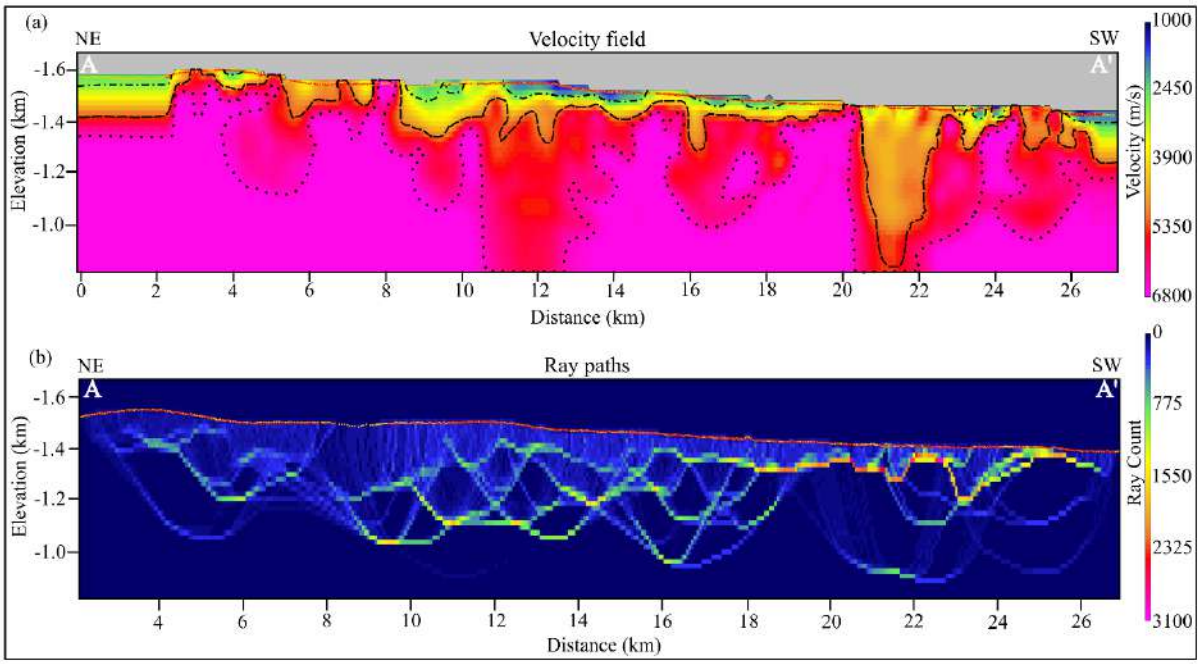


Figure 8. (a) Refraction tomographic velocity model calculated and (b) the associated ray path model showing ray coverage of the velocity model. The velocity model shows three distinct

layers; layer 1 (blue-green colour) with velocities ranging from 1000 – 2500 m/s, layer 2 (yellow-orange color) with velocities ranging from 2500 – 5000 m/s, and layer 3 (red-pink color with a velocity greater than 5000 m/s. A – A' is the path of the seismic profile (see Figure 1c).

The data generally have a good SNR from which a credible seismic interpretation can be generated. Figure 9 shows the results of the processed unmigrated stack sections up to 3.5 s (TWT). Outlined black and blue rectangles highlight the visible, and continuity of seismic reflections for the processed stacked section. The outlines (up to 1.5 s TWT) are enlarged in Figure 10 for better representations/visualizations.

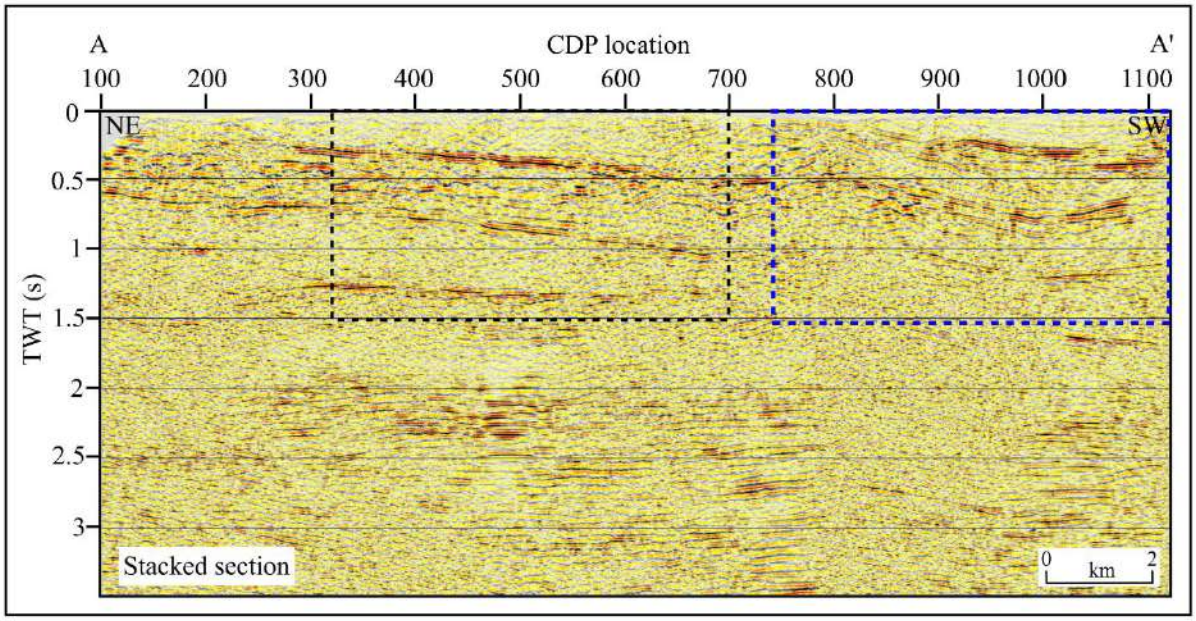


Figure 9. Results of processed unmigrated stacked section for the 2D profile. Outlined black and blue rectangles highlight the visible, and continuity of seismic reflections. And they are enlarged in Figure 10 for better visualizations.

Figure 10a shows good imaging and clear continuity of reflections from the stacked section with a black outline (Figure 9). We observe the delineation of faults (black solid lines)

cross-cutting the entire strata in the processed stacked section shown by the blue outline (Figure 10b).

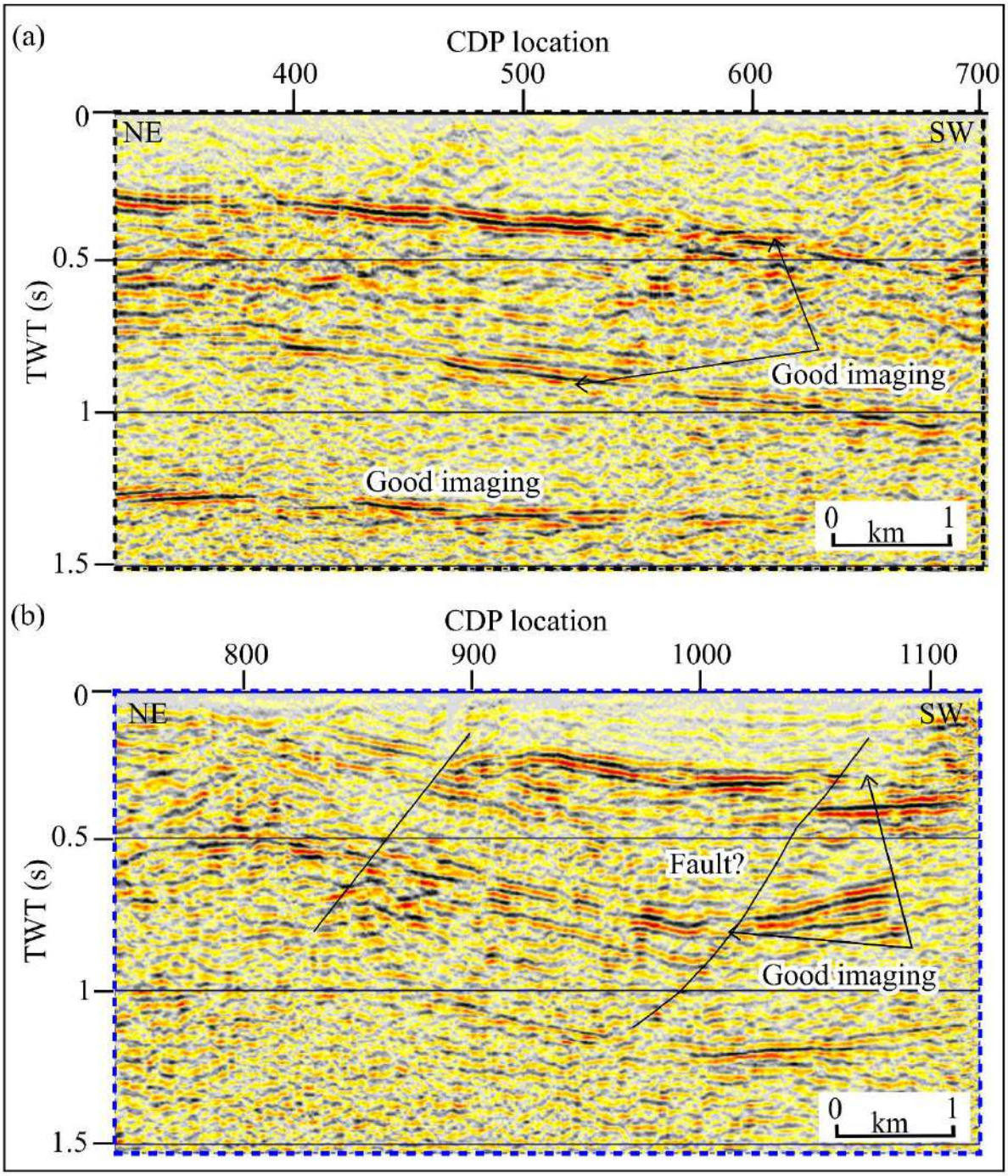


Figure 10. Enlarged results of processed stacked section from Figure 9. The processed stack sections (a, b) show good imaging, continuity of reflections, and possibility of fault structures.

The comparison between the Phase shift migration (PSMIG) and Kirchhoff pre-stack time migration (PreSTM) results is presented in Figure 11. The notable difference between the two techniques is that the reflections in Kirchoff PreSTM are not as continuous as the PSMIG, for example, between the CDPs 100 and 200, the PSMIG clearly enhances the continuity of reflections as compared to the PreSTM. The dataset shows clear possible reflections (R1 – R3) dipping towards the SW direction, denoted by blue arrows.

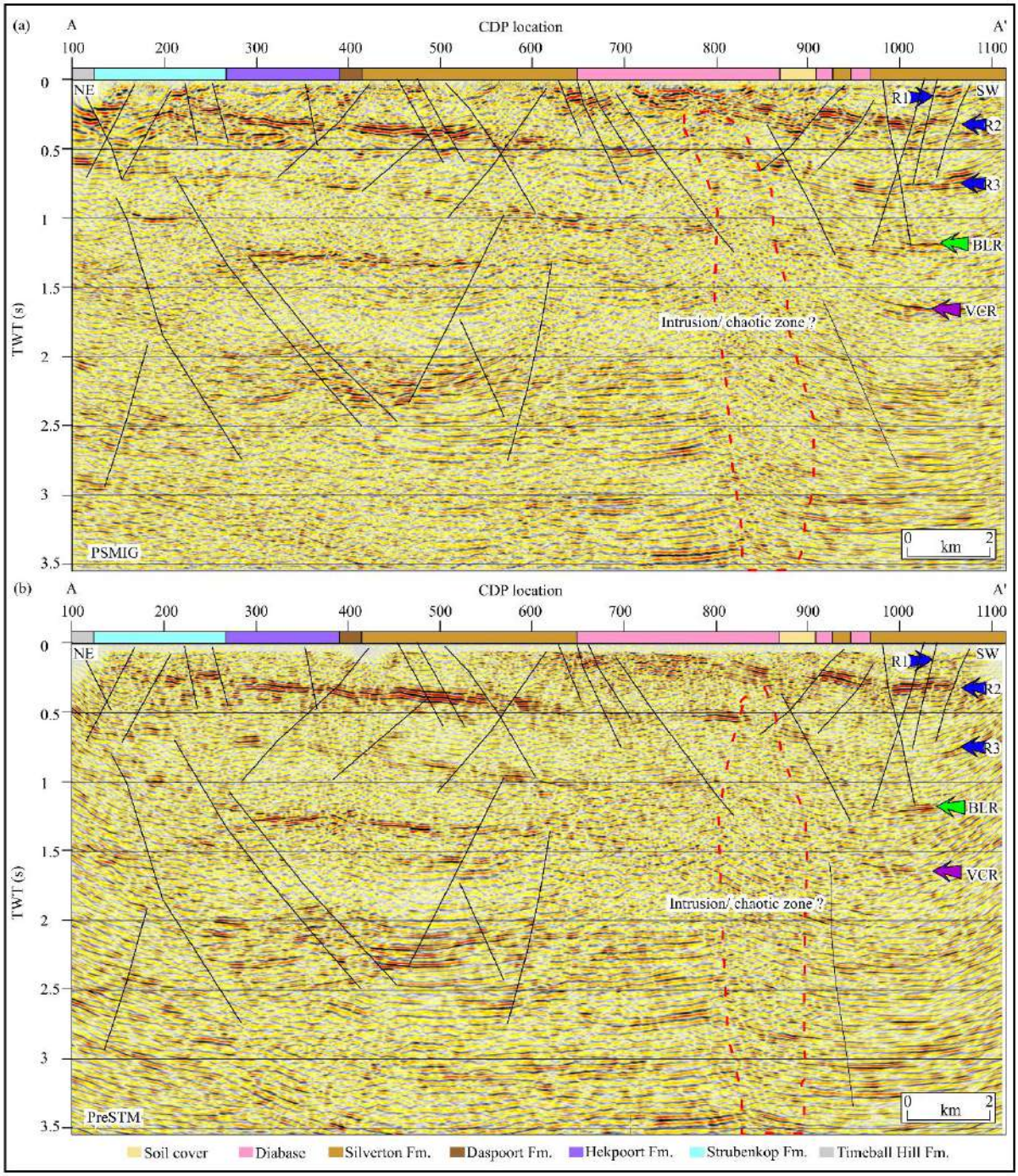


Figure 11. Comparison between the final (a) PSMIG and (b) PreSTM sections for seismic profile, with possible visible reflectors (R1 – R3) indicated by blue arrows, horizon BLR indicated by green arrow, and the zone of the target mineralization (VCR) represented by purple arrow. Fault systems cross-cutting reflectors and orebody are represented by black solid lines. The red dash line represents intrusion or chaotic zone. Outcrops are presented above the seismic section. PSMIG: Phase shift migration; PreSTM: Pre-stack time migration.

The acoustic impedance contrast between the Silverton and Hekpoort formations produces the reflection denoted by R1. The R2 reflection is produced by the lithological contact between the Hekpoort and Timeball Hill formations. The interface between the Chuniespoort Group and Timeball Hill Formation produces the reflection R3. The reflections seem to be crosscut by faults. Faults between CDPs 200 – 400 and 500 – 700 are dipping in the same direction (SW) of the seismic reflections. From approximately 0.5 – 1.75 s TWT, the Black Reef and VCR (orebody) are well-defined in the seismic section. Between CDPs 800 and 900, there seems to be an intrusion caused by the diabase also known as dolerite, and this feature is circulated by red dash lines in Figure 11.

We used borehole logs and surface geology to constrain the interpretation of the profile. Four boreholes (see Figure 3) were drilled up to a depth of ~2.5 km for borehole MD15, ~3.2 km for borehole DP7, ~3.5 km for borehole 1, and ~4.2 km for borehole BB1. All boreholes intersect the Black Reef (BLR) reflector at different depths and thicknesses along the profile. From the NE direction (A), the logged boreholes intersect the BLR horizon at a 1563.20 – 1572.55 m depth range for MD15, 2020 – 2038 m for DP7, 2668.32 – 2671.88 m for 1, and 3224.85 – 3233.36 m for BB1. Borehole 1 did not intersect the Ventersdorp Contact Reef (VCR), whereas the other three boreholes intersect the VCR orebody at ~2330 m for MD15, ~3170 m for DP7, and ~4180 m for BB1.

The regional aeromagnetic map (Figure 2) was used to constrain seismic interpretation. The contractor of the aeromagnetic survey is unknown. According to Stettler (2009, personal. communication), the details about the parameters of the survey (flight height, line spacing, etc) are not known as this went missing at some point in the past. The aeromagnetic data maps the regional faults and dykes that crosscut the seismic profile. The uninterpreted final PSMIG depth converted section is shown in Figure 12a. Figure 12b shows the total magnetic intensity

along the seismic profile and the surface geology data are displayed on the bottom of the magnetic profile. The final interpreted PSMIG depth-converted seismic section is shown in Figure 12c with the geological model overlain. In terms of tectonic in the area, most of the faults that crosscut the orebody VCR, don't crosscut the horizon BLR, and also those that occurred post Black Reef Formation, don't crosscut the VCR orebody. However, faults and dykes crosscut all the strata. The observed reflector BLR is aided by the lithological contact between the overlying dolomitic rocks of the Chuniespoort Group and the underlying Ventersdorp basaltic lavas of the Ventersdorp Supergroup. The VCR reflector/mineralization is due to the strong contrast in seismic velocities and densities between overlying Ventersdorp basaltic lavas and the underlying Central Rand Group quartzite units.

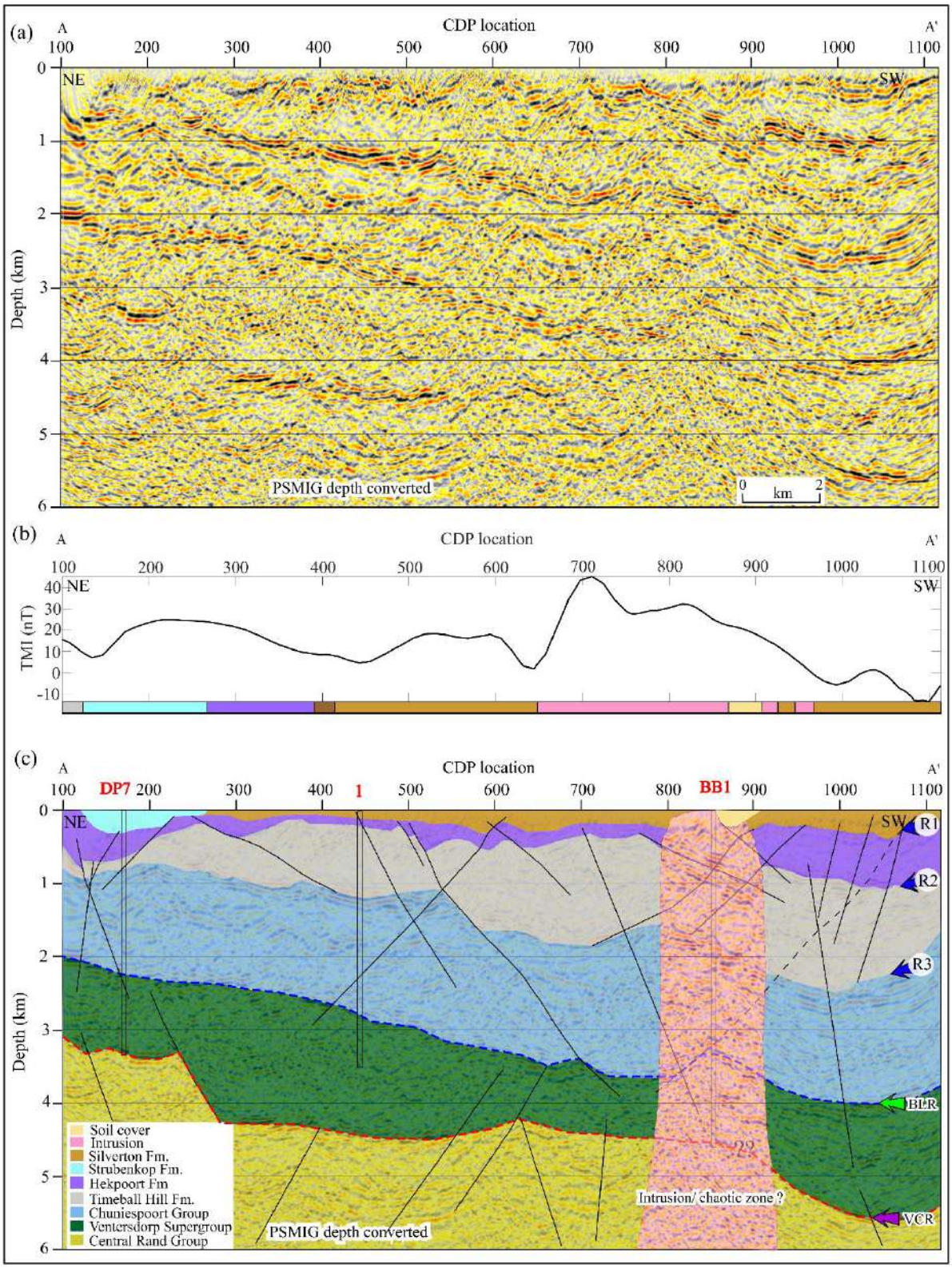


Figure 12. (a) Uninterpreted final PSMIG section of the profile, (b) Aeromagnetic data along the seismic profile used to constrain the interpretation, and (c) Interpreted PSMIG depth converted section overlaid with a basic geological model. Several faults displace the horizon

BLR and mineralization/ orebody VCR and other groups. Faults are represented by black solid lines. PSMIG: Phase-shift migration, BLR: Black reef; VCR: Ventersdorp Contact Reef; Fm: Formation.

DISCUSSION

The migrated seismic sections of the profile (Figure 11) demonstrate the superiority of the PSMIG (Figure 11a) over the Kirchhoff PreSTM (Figure 11b) for the migration of events having moderately varying lateral velocities. PSMIG handles steep dips and curved reflectors better than Kirchhoff PreSTM (Gazdag, 1978). The reflectors located at the CDPs between 100 to 300 of 0 – 1.5 s TWT region are better imaged by the PSMIG method compared to the PreSTM method. The reflector BLR is poorly imaged (Figure 11) due to the low acoustic impedance contrast between the overlying dolomites of Chuniespoort Group with a velocity of 6700 m/s and density of 3.0 g/cm^3 and the underlying Ventersdorp basaltic lavas with a velocity of 6400 m/s and density of 2.9 g/cm^3 (Manzi et al., 2013b; Westgate et al., 2020; Mutshafa et al., 2022). The contact between the Ventersdorp basaltic lavas and the underlying Central Rand Group quartzite (VCR) with relatively lower velocities (~5400 m/s) and densities (~2.67 g/cm^3) exhibits a significant acoustic impedance contrast (Manzi et al., 2015). From the exploration holes, the borehole BB1 information shows that the reflector R1 is intersected at a depth of 407.30 m (contact between shales from the Silverton Formation and basaltic rocks from the Hekpoort Formation) which corresponds to the observed depth position of the reflector on the PSMIG section (Figure 12a, c; Humbert et al., 2020). Reflector R2 is associated with mudstones from the Timeball Hill Formation and the basaltic lavas of the Hekpoort Formation. Reflector R3 is associated with the contact between the dolomitic rocks from the Chuniespoort Group and shales and quartzites from the Pretoria Group.

The borehole, MD15 (Figure 3) intersects the BLR horizon between 1563.20 – 1572.55 m depth, and the orebody (VCR) is embedded between the quartzites and lavas at 2255.09 – 2334.28 m depth of approximately 1.8 km away from the start of the seismic profile. The borehole log data confirm the SW-dipping reflections and their depth in the migrated seismic section (Figure 12b). This is encouraging and motivates the use of seismic methods in the exploration of deep-seated targets. A few faults are dipping towards NE in the opposite direction of the interpreted reflectors, while others are dipping in the SW direction. A dash line fault from the shallow surface crosscut the BLR reflector and other post-Black Reef Formation strata, and it might be interpreted as the syenite dyke (between CDP 1081 and 1082) with remanent magnetization by using the surface geological map and total magnetic intensity map (Figures 1c, 2, and 12), the position of the dyke is represented by the black dash line in Figure 2.

CONCLUSION

A profile from the 2D legacy seismic dataset acquired in 1983 near the South Deep mine (West Rand goldfield) was processed using today's processing algorithms. This study's results could benefit the mine in terms of exploring the deep-seated mineralization at a depth greater than 4 km as shown by the borehole log information and Phase shift migration (depth converted) seismic section. Applying today's processing algorithms to the legacy seismic data results in more accurate delineation of deeper mineralization and improved structural resolution. Borehole logs, magnetic data, and surface geological information were used to constrain the interpretation of the seismic reflection data. The final seismic sections show several reflections associated with the orebody dipping towards the SW and suggest their continuation to depths of greater than 4 km. The study illustrates that processing legacy data can help to gain new insights and is advantageous as the datasets are less contaminated by noise from mining

activities (i.e., drilling and blasting).

Comparing the migration results of the processed seismic sections shows the improvements in imaging and delineation of reflectors produced using today's processing techniques. Both post-stack-Phase shift and Kirchhoff pre-stack time migration techniques play a vital role in improving subsurface imaging, enhancing geological interpretations, and aiding in mitigating exploration risks. The findings are positive and can be used to process legacy seismic data in hard-rock conditions.

ACKNOWLEDGEMENTS

The donation of 2D legacy seismic data by Sibanye Stillwater is acknowledged and greatly appreciated. The Council of Geosciences, Research Office Carnegie Bursary, and National Research Foundation are acknowledged for financial support. We wish to thank HiSeis Pty Ltd. for funding a license for the GLOBE Claritas seismic processing software package, Schlumberger for Petrel licenses, and the Wits Seismic Research Center at the University of the Witwatersrand for MATLAB licenses.

DISCLOSURE STATEMENT

No potential conflict of interest was reported by the author(s).

DATA AVAILABILITY

Due to privacy restrictions, the seismic and borehole logs data are not publicly available. Geological outcrop data can be found on the website of The Council for Geoscience, South Africa. https://maps.geoscience.org.za/portal/apps/sites/?fromEdit=true#/interactivewebmap.

FUNDING

This work was supported by the Council of Geosciences, Research Office Carnegie Bursary, and National Research Foundation.

REFERENCES

Ahmadi, O., Juhlin, C., Malehmir, A., and Munck, M. (2013). High-resolution 2D seismic imaging and forward modeling of a polymetallic sulfide deposit at Garpenberg, central SwedenSeismic imaging at Garpenberg. *Geophysics*, *78*(6), B339-B350.

Ahmadi, O. (2015). *Application of the Seismic Reflection Method in Mineral Exploration and Crustal Imaging: Contributions to Hardrock Seismic Imaging* (Doctoral dissertation, Acta Universitatis Upsaliensis).

Beach, A., and Smith, R. (2007). Structural geometry and development of the Witwatersrand Basin, South Africa. *Geological Society, London, Special Publications*, *272*(1), 533-542.

Coward, M. P., Spencer, R. M., and Spencer, C. E. (1995). Development of the Witwatersrand Basin, South Africa. *Geological Society, London, Special Publications*, *95*(1), 243-269.

Dankert, B. T., and Hein, K. A. (2010). Evaluating the structural character and tectonic history of the Witwatersrand Basin. *Precambrian Research*, *177*(1-2), 1-22.

Donoso, G.A., Malehmir, A., Pacheco, N., Araujo, V., Penney, M., Carvalho, J., Spicer, B., and Beach, S. (2020). Potential of legacy 2D seismic data for deep targeting and structural imaging at the Neves–Corvo massive sulphide-bearing deposit, Portugal. *Geophysical Prospecting*, *68*(1-Cost-Effective and Innovative Mineral Exploration Solutions), pp.44-61. https://doi:10.1111/1365-2478.12861.

Gazdag, J. (1978). Wave equation migration with the phase-shift method. *Geophysics*, *43*(7), 1342-1351.

Gibson, M. A., Jolley, S. J., and Barnicoat, A. C. (2000). Interpretation of the Western Ultra Deep Levels 3-D seismic survey. *The Leading Edge*, *19*(7), 730-735.

Humbert, F., Elburg, M.A., Agangi, A., Belyanin, G., Akoh, J., Smith, A.J.B., Chou, Y.M., and Beukes, N.J. (2020). A~ 1.4 Ga alkaline mafic sill from the Carletonville area: connection to the Pilanesberg Alkaline Province?. *South African Journal of Geology 2020*, *123*(4), 597-614. https://doi.org/10.25131/sajg.123.0039.

Jolley, S.J., Freeman, S.R., Barnicoat, A.C., Phillips, G.M., Knipe, R.J., Pather, A., Fox, N.P.C., Strydom, D., Birch, M.T.G., Henderson, I.H.C., and Rowland, T.W. (2004). Structural controls on Witwatersrand gold mineralization. *Journal of Structural Geology*, 26(6-7), 1026 – 1086.

Jolley, S. J., Stuart, G. W., Freeman, S. R., Knipe, R. J., Kershaw, D., McAllister, E., Barnicoat, A.C., and Tucker, R. F. (2007). Progressive evolution of a late orogenic thrust system, from duplex development to extensional reactivation and disruption: Witwatersrand Basin, South Africa.

Keydar, S., Shtivelman, V., and Arzi, A. (2018). Three-dimensional seismic diffraction imaging for detecting near-surface inhomogeneities. *Geophysics*.

Malehmir, A., Durrheim, R.J., Bellefleur, M., Urosevic, M., Juhlin, C., White, D., Milkerit, B., and Campbell, G. (2012). Seismic methods in mineral exploration and mine planning: A general overview of past and present case histories and a look into the future. Geophysics, 77(5), WC173–WC190.

Malehmir, A., Koivisto, E., Manzi, M., Cheraghi, S., Durrheim, R.J., Bellefleur, G., Wijns, C., Hein, K.A., and N. King. (2014). A review of reflection seismic investigations in three major metallogenic regions: The Kevitsa Ni–Cu–PGE district (Finland), Witwatersrand

goldfields (South Africa), and the Bathurst Mining Camp (Canada). *Ore Geology Reviews*, *56*, 423-441.

Malehmir, A., Manzi, M., Draganov, D., Weckmann, U., and Auken, E. (2020). Introduction to the special issue on "Cost-effective and innovative mineral exploration solutions". *Geophysical prospecting*, *68*(1), 3-6.

Manzi, M. S., Durrheim, R. J., Hein, K. A., and King, N. (2012a). 3D edge detection seismic attributes used to map potential conduits for water and methane in deep gold mines in the Witwatersrand basin, South Africa3D seismic imaging in mining. *Geophysics*, *77*(5), WC133-WC147.

Manzi, M. S., Gibson, M. A., Hein, K. A., King, N., and Durrheim, R. J. (2012b). Application of 3D seismic techniques to evaluate ore resources in the West Wits Line goldfield and portions of the West Rand goldfield, South Africa Application of 3D seismic techniques. *Geophysics*, *77*(5), WC163-WC171.

Manzi, M. S., Hein, K. A., Durrheim, R. J., and King, N. (2014). The Ventersdorp Contact Reef model in the Kloof Gold Mine as derived from 3D seismics, geological mapping and exploration borehole datasets. *International Journal of Rock Mechanics and Mining Sciences*, *66*, 97-113.

Manzi, M. S., Hein, K. A., King, N., and Durrheim, R. J. (2013a). Neoarchaean tectonic history of the Witwatersrand Basin and Ventersdorp Supergroup: New constraints from high-resolution 3D seismic reflection data. *Tectonophysics*, *590*, 94-105.

Manzi, M. S. D., Hein, K. A. A., Durrheim, R., and King, N. (2013b). Seismic attribute analysis to enhance detection of thin gold-bearing reefs: South Deep gold mine, Witwatersrand basin, South Africa. *Journal of Applied Geophysics*, *98*, 212-228.

Manzi, M., Cooper, G., Malehmir, A., Durrheim, R., and Nkosi, Z. (2015). Integrated interpretation of 3D seismic data to enhance the detection of the gold-bearing reef:

Mponeng Gold mine, Witwatersrand Basin (South Africa). *Geophysical Prospecting*, *63*(4), 881-902.https://doi/10.1111/1365-2478.12273.

Manzi, M., Malehmir, A., and Durrheim, R. J. (2018). Improved Subsurface Imaging through Re-processing of Legacy 2D Seismic Data-A Case Study from a Deep South African Gold Mine. In *2nd Conference on Geophysics for Mineral Exploration and Mining* (Vol. 2018, No. 1, pp. 1-5). EAGE Publications BV. https://doi.org/10.3997/2214-4609.201802705.

Markovic, M., Maries, G., Malehmir, A., von Ketelhodt, J., Bäckström, E., Schön, M., and Marsden, P. (2020). Deep reflection seismic imaging of iron-oxide deposits in the Ludvika mining area of central Sweden. *Geophysical Prospecting*, *68*(1-Cost-Effective and Innovative Mineral Exploration Solutions), 7-23.

Mutshafa, N., Manzi, M.S., Westgate, M., James, I., Brodic, B., Bourdeau, J.E., Durrheim, R.J., and Linzer, L. (2022). Seismic imaging of the gold deposit and geological structures through reprocessing of legacy seismic profiles near Kloof–Driefontein Complex East Mine, South Africa. *Geophysical Prospecting*.

McCarthy, T.S. (2006). The Witwatersrand Supergroup. In: *The Geology of South Africa* (eds M.R. Johnson, C.R. Anhaeusser and R.J. Thomas), 155– 186. Geological Society of South Africa, Johannesburg/Council for Geosciences, Pretoria.

Mkhabela, M., and Manzi, M. (2017). Detection of potential methane gas pathways in deep South African gold mines. *Journal of Geophysics and Engineering*, *14*(4), 960-974.

Nwaila, G.T., Bourdeau, J.E., Jinnah, Z., Frimmel, H.E., Bybee, G.M., Zhang, S.E., Manzi, M.S.D., Minter, W.E.L., and Mashaba, D. (2021). The Significance of Erosion Channels on Gold Metallogeny in the Witwatersrand Basin (South Africa): Evidence from the Carbon Leader Reef in the Carletonville Gold Field. *Economic Geology*, *116*(2), 265-284.

Pretorius, C.C., Trewick, W.F., and Irons, C. (1997). Application of 3D seismic to mine planning at Vaal Reefs gold mine, number 10 shaft, Republic of South Africa Proc. *Exploration 97: 4th Decennial Int. Conf. on Mineral Exploration (Toronto)*, 399–408.

Robb, L.J., and Meyer, F.M. (1995). The Witwatersrand Basin, South Africa: geological framework and mineralization processes. *Ore Geology Reviews*, *10*(2), 67-94.

Westgate, M., Manzi, M.S., James, I., and Harrison, W. (2020). New insights from legacy seismic data: reprocessing of legacy 2D seismic data for imaging of iron-oxide mineralization near Sishen Mine, South Africa. *Geophysical Prospecting*, 68(7), 2119–2140. https://doi.org/10.1111/1365-2478.12996.

Yilmaz, Ö. (2001). *Seismic data analysis: Processing, inversion, and interpretation of seismic data*. Society of exploration geophysicists.

Ziramov, S., Young, C., Kinkela, J., Turner, G., and Urosevic, M. (2023). Pre-stack depth imaging techniques for the delineation of the Carosue Dam gold deposit, Western Australia. *Geophysical Prospecting*, 00, 1– 19. https://doi.org/10.1111/1365-2478.13314.

9. Paper III: Integrated geophysical methods for boulder delineation to improve mining

Sikelela Gomo[1], Moyagabo K. Rapetsoa[1], Musa S. D. Manzi[1]*, Emmanuel Onyebueke[1], Jureya Dildar[1], Mpofana Sihoyiya[1], **Ndamulelo Mutshafa**[1], Wesley Harrison[3], Julie E. Bourdeau[2], Oleg Brovko[1], Ian James[1] Gordon R. J. Cooper[1], Stephanie Scheiber[1], Raymond J. Durrheim[1]

[1]School of Geosciences, University of the Witwatersrand, Johannesburg, Private Bag, Wits, 2050, Republic of South Africa.

[2]Geological Survey of Canada, 601 Booth Street, Ottawa, Ontario, K1A 0E8, Canada.

[3]SRK Consulting, SRK House, 265 Oxford Rd, Illovo, Johannesburg, 2196, Republic of South Africa.

*Email: musa.manzi@wits.ac.za

Abstract

Near-surface boulders can pose serious challenges to open-cast mining. They often introduce complexities, delays in drilling, blasting and excavation programs, which subsequently decrease mining efficiency, increase mining risks and costs. The location of subsurface boulders and the identification of other geological features that may impact mining activities (e.g., fractures, the presence of iron-rich ultramafic pegmatites, and the variation in weathering across a mining region) is necessary to reduce the challenges posed by these geological features, therefore optimizing mining efficiency. In this study, magnetics, electrical resistivity tomography, seismic refraction tomography, ground penetrating radar, and borehole data are integrated for boulder delineation and mapping of other geological features that may impact mining using an unmined section at Tharisa Mine, Bushveld Complex (South Africa), as a test site. The results obtained from the different geophysical techniques are found to complement each other, and successfully delineate boulders, fractures, iron-rich ultramafic pegmatites and the variation in weathering and layering across the area. The incorporation of geophysical results can thus improve mining efficiency, while reducing mining risks and costs.

KEYWORDSs: Boulders, Magnetics, Resistivity, Seismic refraction, Ground penetrating radar.

INTRODUCTION

The development of mines and the optimum exploitation of mineral resources are paramount factors for the economic, societal and environmental development of countries. The presence of boulders in mining operations is problematic as these represent obstacles that may decrease productivity (e.g., delay blasting, drilling and excavation), as well as increase mining and engineering costs, and risks (Felletti and Beretta, 2009; Dan et al., 2016; Shao et al., 2020). Boulders are defined as rock fragments with a diameter greater than 256 mm, which may occur in different sizes and shapes, and appear as a corestone surrounded by concentric shells and/or embedded in saprolite. They are formed by chemical (spheroidal weathering) and/or mechanical processes (e.g., blasting) (Udden, 1914; Dan et al., 2016; Shao et al., 2020). Boulders formed by chemical processes are referred to as subterranean boulders, while those caused by mechanical processes are referred to as subaerial boulders (Twidale and Romani, 2005).

It is therefore important to locate boulders beforehand to adequately plan, and thus minimise any deleterious effects on mining and engineering operations. Although there is a paucity of integrated geophysics studies to detect and map boulders, Jee and Ha (2007) discuss the viability of using electrical resistivity tomography (ERT), ground penetrating radar (GPR), seismic refraction tomography (SRT) and magnetics to delineate boulders during tunneling. Several other case studies, though not based on boulder delineation, also demonstrate the successful mapping of boulders and boulder zones using various geophysical techniques. For instance, Musil et al. (2002) employed seismic reflection and refraction combined with drilling to map the internal structure, including suspended boulders, of the lower boundary of the Muragl rock glacier (Switzerland). Cardarelli et al. (2010) applied both ERT and SRT to locate cavities in the near subsurface, which, when filled with air, have a response similar to boulders. Ettinger et al. (2014) used GPR to study the internal geometry of a volcaniclastic fan produced by aggradation during a lahar event from the Cotopaxi volcano (Ecuador). Interestingly, GPR results resolved boulders hosted within the volcaniclastic fan. In a similar study, Gomez et al. (2018) utilized GPR, along with other geospatial techniques, to study the spatial distribution of boulder-size clasts at the Semeru volcano (Indonesia), gaining insights on how their distribution relates to valley morphology and the dynamic deposition of lahars.

Subterranean boulders (corestones) in the weathered zone are often by-products of chemical weathering, appearing as more competent and less altered than the host rock (Durgin, 1977; Dan et al., 2016). These boulders are normally separated or compartmentalized by

fractures (joints and/or fault zones) and soft cemented materials with lower densities, compaction and competence (Jee and Ha, 2007). A number of such boulders have been observed in the Bushveld Complex of South Africa, where they became exposed by mining operations. The area of interest consists of anorthosite to norite boulders embedded in saprolite clays (weathered rock). The boulders are more competent and have higher magnetic susceptibility compared to the surrounding weathered rocks. As a result, the boulders are more resistive, dense and magnetic as compared to the surrounding weathered rocks.

In this paper, we present the results from integrated geophysical surveys (i.e., magnetics, ERT, SRT and GPR) that were conducted at an unmined section at the Tharisa Mine in the Bushveld Complex. The main aim of the integrated surveys was to delineate and characterise subsurface (or subterranean) boulders in saprolite clays. Generally, boulders measure between one and two meters across, however, in this study we designed our surveys to target boulders larger than four meters since smaller boulders can be easily disposed of by mining operations. A secondary aim was to map geological site features (e.g., lithologies, fractures) that could have a direct impact on mining operations which would ultimately facilitate effective mine planning (Onyebueke et al., 2018). The most significant feature that geophysical methods bring to mineral exploration and mining is the ability to map complex and subsurface geological features at greater resolution than any other geological method (Malehmir et al., 2012).

GEOLOGICAL BACKGROUND

The research was carried out at Tharisa Mine, an opencast Platinum Group Metals (PGMs) and chrome mine, situated in the south-western limb of the Bushveld Complex, which itself is located in the northern portions of the Kaapvaal Craton (Fig. 1a). The Bushveld Complex hosts the largest ultramafic-mafic layered intrusion in the world, with an aerial extent of about 66,000 km^2 and a thickness between 7-9 km (Cawthorn, 2015). The complex formed about 2.05 Ga and hosts stratiform PGM, chromium and vanadium deposits (Scoates et al., 2021). The Bushveld Complex was emplaced through a series of magma injection events, intruding at the unconformity separating the Transvaal Supergroup (Pretoria Group) sedimentary rocks and the Rooiberg Group volcanic rocks (Kruger, 2005, Perritt and Roberts, 2007; Cawthorn, 2015). The complex is subdivided into three major magmatic units, the: 1) Rustenburg Layered Suite (RLS), 2) Rashoop Granophyre Suite (RGS), and 3) Lebowa Granite Suite (LGS); and is split up into five limbs, i.e., four outcropping limbs (western, far-western, eastern and northern

limbs) and one buried limb (south-eastern limb) (Eales and Cawthorn, 1996; Cawthorn and Webb, 2001). The mafic-ultramafic rocks of the RLS host most of the PGM mineralization of the Bushveld Complex.

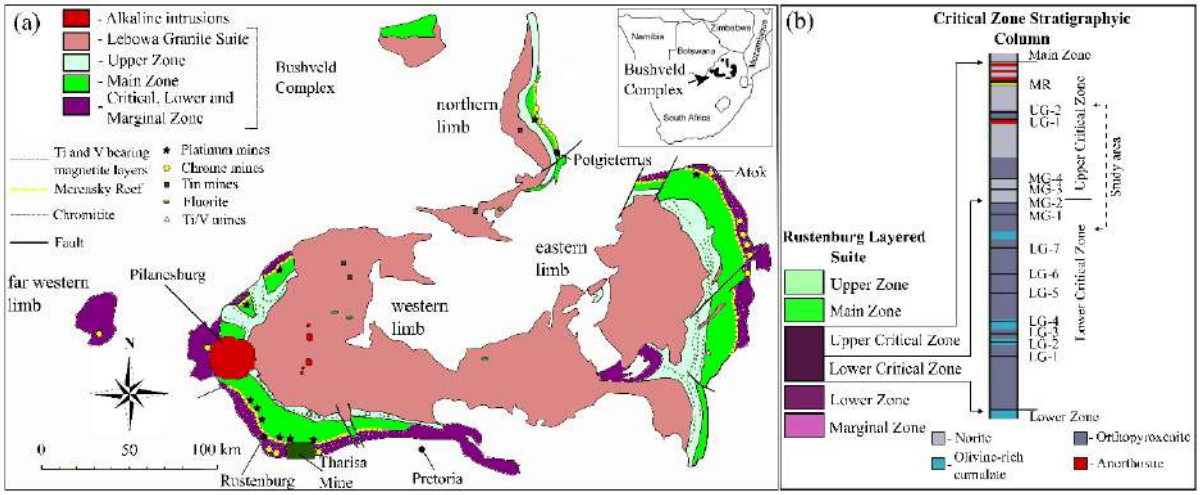


Figure 1: (a) Simplified geological map of the Bushveld Complex (modified from Taylor et al., 2009). (b) Simplified schematic stratigraphic column of the Critical Zone with its position within the Rustenburg Layered Suite. Included in the stratigraphic column is the location of Tharisa Mine, the Merensky Reef (MR), Upper Group (UP), Middle Group (MG) and Lower Group (LG) chromitite layers (modified from Hunt et al., 2018).

The RLS is subdivided into five zones known as the (from bottom to top): 1) Marginal (norites), 2) Lower (cyclic pyroxenite-harzburgite-dunite), 3) Critical (cyclic pyroxenite-norite-anorthosite-chromitite), 4) Main (gabbronorites), and 5) Upper zones (ferrogabbro-anorthosite-magnetitite and apatite-bearing diorites) (Fig. 1b; Barnes and Maier, 2002; Cawthorn, 2015). The economically significant PGM deposits are found in the Critical Zone, of which the Merensky Reef (MR) and Upper Group 2 chromitite (UG2) units define two of the world's largest platinum-bearing orebodies (Cawthorn et al., 2005; Fig. 1b). The Critical Zone is further subdivided into the Upper (cyclic orthopyroxenite, norite and anorthosite units) and Lower Critical zones (cyclic chromitite, harzburgite and pyroxenite units) (Fig. 1b; Barnes and Maier, 2002; Hunt et. al., 2018). The transition zone between the Upper and Lower Critical zones occurs where cumulus plagioclase first appears (Eales and Cawthorn, 1996; Barnes and Maier, 2002, Cawthorn, 2015).

Layered rocks of the RLS were subsequently disrupted by the intrusion/infiltration of iron-rich ultramafic pegmatite bodies (IRUPs) which crystallized from iron-rich intercumulus and residual melts (Scoon and Mitchell, 1994; Reid and Basson, 2002). IRUPs are coarse-

grained rocks that occur in the form of pipes, veins and occasionally, sub-concordant sheets. Furthermore, IRUPs are normally accompanied by numerous fractures and are predominantly found in the Upper Critical, Main and Upper zones. Tharisa Mine is stratigraphically located in the Critical Zone and is underlain by the Middle Group (MG) chromitite layers (Fig. 1a-b). The MG chromitite layer package is a deposit of five tabular chromitite layers named MG0, MG1, MG2, MG3 and MG4 (Fig. 1b). The main economic horizons of interest at Tharisa Mine are: MG1, MG2, MG3, MG4 and MG4A. In the past, the UG1 was also extracted at the mine, as both the UG2 and UG1 outcrop nearby. The major metal components mined by Tharisa Mine are platinum, followed by palladium and ruthenium.

OCCURANCE AND FORMATION OF BOULDERS

Igneous rocks often contain several fracture types (e.g., net, oblique, vertical and horizontal fractures) of variable origin (e.g., tectonic, thermal, epigenetic, anthropogenetic) (Jinghong et al., 2011; Vitale and Isaia, 2014). Fractures in the Bushveld Complex often consist of planar and non-planar joints, i.e., fractures or cracks with no characteristic shear displacement (Fig. 2a-d). The joins are ubiquitous, often planar in nature and occur in sets with approximately the same orientation. Their intensity varies widely across the complex and are largely attributed to tectonic stress (Wilson et al., 2005; Twidale and Romani, 2005; Roberts and Clark-Mostert, 2010). Some fractures observed in the Bushveld Complex (e.g., the prevalent layer-parallel faults and ramps) are interpreted to have formed due to crustal flexure (folding) caused by the intrusion of high-density mafic-ultramafic rocks (isostatic readjustment) (Eales et al., 1993; Cawthorn and Webb, 2001; Perritt and Roberts, 2007). According to Perritt and Roberts (2007), the Critical Zone commonly displays layered-parallel and ramp faults (duplex, frontal, and lateral ramps) with prominent striations or corrugations, which are subsurface features often exploited by near surface weathering processes to breakdown subsurface rocks.

Joint sets of varying orientation (cross cutting joint sets) often break down large masses of rock into separate fracture-bounded blocks (Fig. 2a). In subsurface environments, spheroidal weathering exploits these fractures (along with other rock features, such as crystal boundaries, cleavages, etc.) to break down the bedrock and initiate the formation of boulders (Fig. 2b-c; Twidale and Romani, 2005; Fletcher et al., 2006). The process is mainly driven by moisture from infiltrating meteoric waters, which contains gases, chemicals and biota, that altogether break down fresh bedrock into regolith (saprolite and boulders; Fig. 2c). The weathering

process decays the bedrock starting from the joints and moves inwards into the core of the fracture-bounded blocks, forming boulders (called subterranean boulders) embedded in saprolite. The amount of weathering, and thus the boulder size and shape all depend on prevalent fracture systems, shallow ground water chemistry, duration and intensity of weathering, as well as the rheology of the rock (Twidale and Romani, 2005; Dan et al., 2016). Along with subterranean boulders, subaerial boulders (blasting and excavation-induced boulders) are often present in opencast mining environments, including in the study area (Fig. 2d).

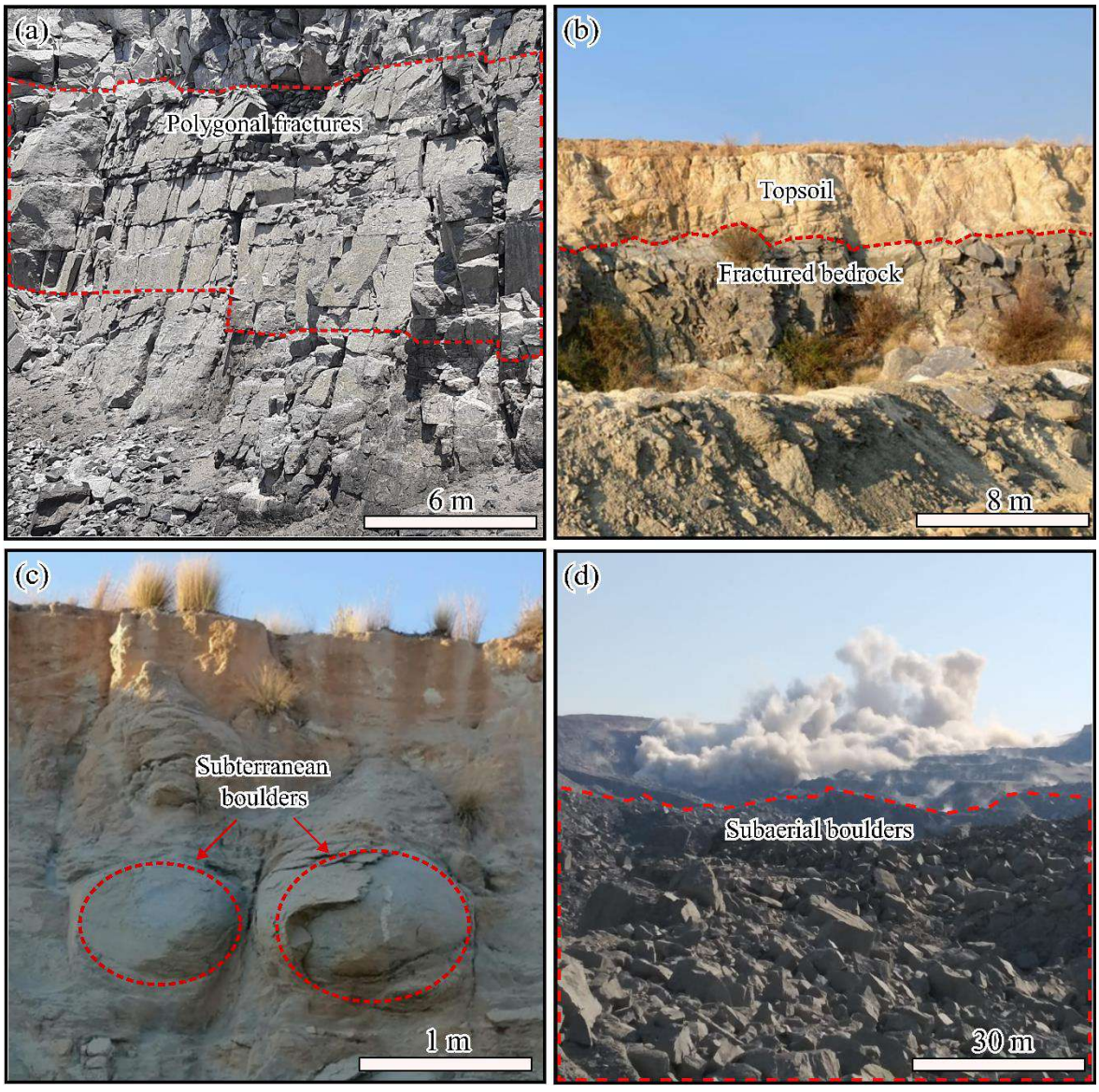


Figure 2: (a) Polygonal fractures in the norite and anorthosite rocks at Tharisa Mine, this image was taken inside the opencast mine pit. The red dotted line highlights a highly fractured zone. (b) Highwall face near the study area showing topsoil (highly weathered top zone) and fractured bedrock. (c) Subterranean boulders showing on the highwall face near the study area.

(d) Subaerial boulders (blasting induced boulders) inside the pit, at Tharisa Mine. The red dotted line highlights the zone with the subaerial boulders. The presented photos were taken by Hloniphani Hlongwa (11/10/2021).

GEOPHYSICAL SURVEYS

Prior to acquiring geophysical data, we collected rock samples and measured their physical properties, such as P-wave seismic velocity and magnetic susceptibility, to examine the feasibility of the study, and investigate if there is any significant physical property contrast between the boulders (fresh anorthosite and norite) and host rocks (weathered anorthosite and norite) (see Table 1). We conducted magnetic, electrical resistivity tomography (ERT), seismic refraction tomography (SRT) and ground penetrating radar (GPR) surveys to map boulders, weathered zones, fresh bedrock zones and other subsurface geological features (i.e., overburden, fractures and IRUPs in the top 10 – 40 m). Figure 3 shows the survey locations of the different geophysical techniques.

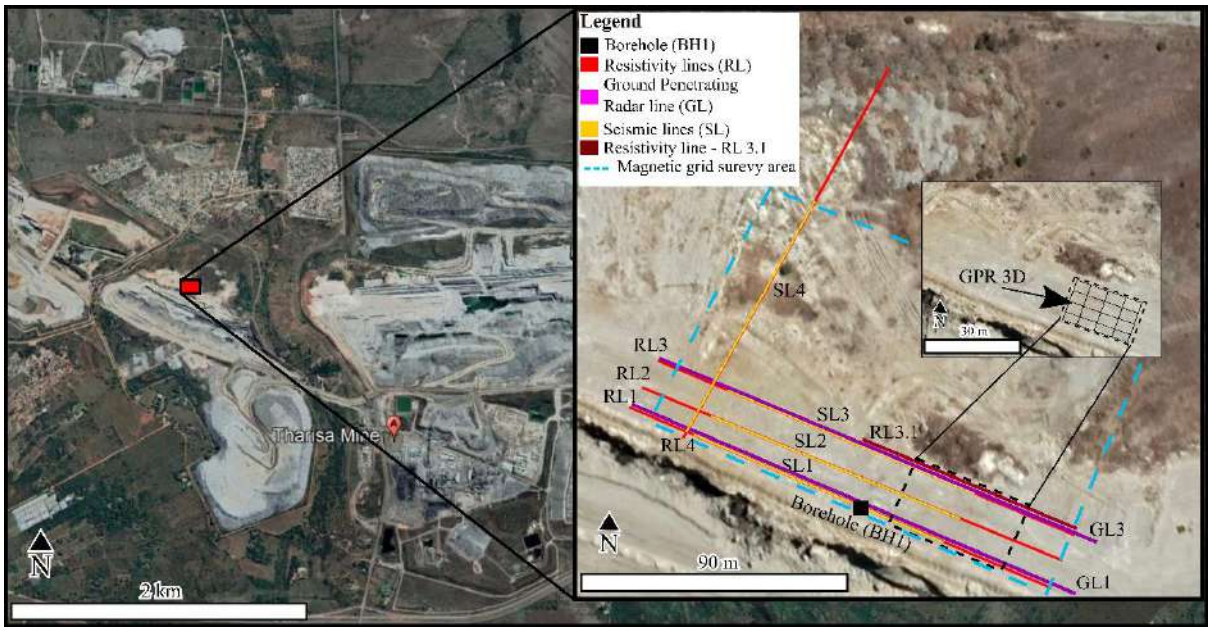


Figure 3: Google Earth image showing the location of the study area (marked with a red square) at Tharisa Mine and that of the magnetic, resistivity (RL), seismic (SL) and ground penetrating radar (GL and GPR 3D) grids collected over the study area (on the zoomed-in image of the study area).

Table 1: Weathered and fresh rock physical property measurements from samples collected in the study area. The resistivity measurements were taken from a study conducted by van Schoor and Fourier (2015) of rocks in South Africa.

Weathered norite rock measurements (Sample-X)			**Fresh norite rock measurements (Sample Y)**		
Number of measurements taken	Magnetic susceptibility (x10-3 SI)	P-wave seismic velocity (m/s)	Number of measurements taken	Magnetic susceptibility (x10-3 SI)	P-wave seismic velocity (m/s)
Sample-X 1	0.128	950	Sample-Y 1	5.84	5,710
Sample-X 2	0.137	1,090	Sample-Y 2	4.52	5,630
Sample-X 3	0.124	1,047	Sample-Y 3	5.09	5,610
Sample X Average	0.127	1,029	Sample Y Average	5.15	5,650
Weathered anorthosite resistivity			**Fresh anorthosite resistivity**		
Rock type		Resistivity (ohm.m)	Rock type		Resistivity (ohm.m)
Weathered anorthosite		~1,000 to 3,000	Fresh anorthosite		~5,000 to 10,000

Geophysical data acquisition and processing

Magnetic data

The magnetic data were acquired using three portable magnetometers, two G856 proton precession magnetometer and one G895 Cesium vapor magnetometer with an integrated GPS receiver (WGS 84, accuracy of ± 1 m). Both the proton precession magnetometers (G856) were used as base station magnetometers and were placed in separate areas with minimal noise. One of the magnetometers was set to collect data every 15 seconds and the other at every 30 seconds. The magnetometer with the best (least spikes) diurnal curve was used to correct the acquired field data. The Cesium vapor (G859) magnetometer was used as a rover magnetometer. In order to reduce the effect of near-surface magnetic materials and minerals,

the proton precision magnetometers were mounted on 2.5 m high vertically positioned, non-magnetic, aluminium poles. The rover magnetometer (G859) was carried on a non-magnetic backpack, with magnetic sensor and GPS receiver antenna heights of approximately 2 - 3 m and 1.7 - 2 m from surface, respectively. To obtain high-resolution data and avoid spatial aliasing, the magnetic data were acquired in a walking mode using a sampling rate of 1 second, line spacing of 2 m, over an area of 150 × 100 m. Seventy-five SSW – NNE, magnetic survey grid lines were collected over the magnetic grid survey area (Fig. 3).

Processing of the magnetic data involved removing diurnal variations, de-spiking and micro-levelling using the Fast Fourier Transform (FFT) frequency domain technique (which involves using the directional cosine filter and Butterworth filters) in order to reduce directional effects and remove long wavelength signals (detrending). Manual deculturing, as to prevent the removal of important shallow geological signals, of the original total magnetic intensity (TMI) grid and interpolation of the removed data points, using the minimum curvature technique, was subsequently carried out.

Magnetic enhancement techniques were applied to the data so as to correct and enhance specific characteristics of magnetic sources (e.g., magnetisation, position, limits and discontinuities). The reduction to magnetic pole (RTP) technique was applied to correct the position of the magnetic sources and their induced magnetization. The vertical tilt angle filter was applied to sharpen the edges of the magnetic sources (Cooper and Cowan, 2008; Von Dobeneck et al., 2021).

Electrical resistivity tomography data

The resistivity survey consisted of 5 survey lines (RL1 to RL4), with line RL3.1 being a high-resolution resistivity line collected over a smaller section of profile RL3 due to the observation of hard-rock anorthosite to norite boulders at the surface (Fig. 3). Four of the five resistivity lines (RL1, RL2, RL3 and RL3.1, WNW-ESE trending lines) were acquired on a graded sandy road, situated on the original surface of the opencast mine, close to the highwall. The lines were acquired perpendicular to the dip of the Bushveld Complex rocks in the area. Profile RL4, a SSW – NNE trending line, was acquired largely on partly loose sandy sediments, north of the road and parallel to the dip of the rocks in the area (Fig. 3). The data were acquired using an automated ABEM 1200 resistivity system and an electrode spacing of 1 m and 2 m. The profile length of the survey lines (excluding RL3.1) was 160 m, and that of RL3.1 was 80 m. The Dipole-Dipole and Schlumberger methods were used to acquire the data. The area along which

profiles RL1, RL2, RL3 and RL3.1 were collected was a flat graded area with negligible topographic variation. Survey RL4 was acquired over an area with slightly more sand cover and topographic variation (~1 m), especially in the northern side of the profile. Due to the effects of metal cased boreholes along profile RL4, the resistivity results of RL4 are not presented in the text.

The collected electrical resistivity tomography (ERT) data were first manually de-spiked and inverted to produce their inverted models. A weighted least-squares objective function coupled with linear filtering was used to carry out the inversion. Furthermore, an unstructured triangular finite element mesh, that allows for complicated model geometry, was used to produce the inverse models (Binley and Kemna, 2005; Blanchy et al., 2020). All the calculated resistivity inverse models reached the target root square mean error of ~1 in 3 to 4 iterations.

Seismic refraction tomography data

The seismic data, SL1 to SL4, were acquired along the resistivity survey lines for integration purposes (Fig. 3). The data were acquired using 48 (14 Hz) geophones connected to two 24-channel Geometric geode seismographs. To obtain high near-surface resolution, the data were collected using a geophone spacing of 2 m, yielding a common midpoint (CMP) of 1 m. Shots were taken at every receiver. An asymmetric split-spread geometry with fixed receiver location, at a sampling interval of 1 ms and a recording length of 1.5 seconds, were used to acquire the data. The ESS MINI Base System (weight-drop) mounted on a vehicle and/or 5 kg sledgehammer were used as seismic energy sources, and a 20 × 20 × 20 cm^3 aluminium metal base coupling plate was used to improve the source-to-ground coupling. A stack value of four was used to improve the signal-to-noise ratio. A high-cut filter of 250 Hz was used to eliminate the high frequencies that distort the acquired data. During the recording process, the acquired data were carefully monitored to avoid the introduction of noise generated by mining activities (e.g., drilling, blasting, moving vehicles and water pumps).

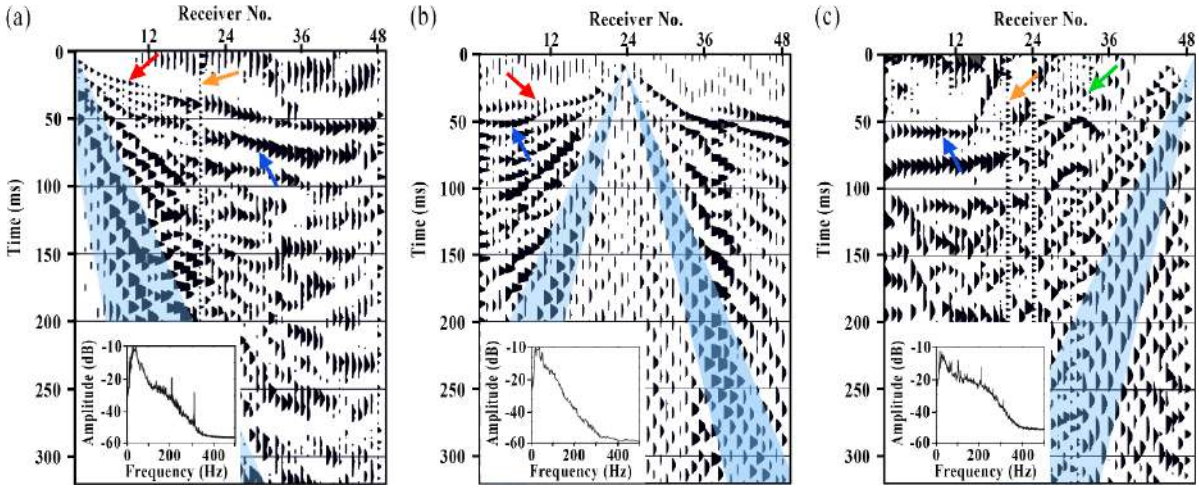


Figure 4: Raw seismic shot gathers (a-c) with corresponding frequency spectra. Bad traces (orange arrow) were removed from the shot gathers. The raw shot gathers show first arrivals (red arrows), reflections (blue arrow) that are masked by the surface waves and air waves (blue shaded areas). The green arrow in (c) corresponds to noise introduced by a secondary source, while the blue shaded area highlights the groundroll (surface wave) zone.

Figure 4(a-c) shows the comparison of raw seismic shot gathers of survey lines SL1, SL3 and SL4. Marked on the raw shot gathers are refracted (red arrows), possible reflected (blue arrows) that appear to be masked by surface waves, and air waves (blue shaded areas). Across all the gathered seismic data, the P-waves first breaks are present within the first 75 ms. Figure 4(c) (green arrow) shows an example of noise generated by drilling (between receiver 24 and 36) in seismic profile SL4. To construct the 2D P-wave refraction models, we used the 7,200 first arrival picks across profiles SL1, SL2 and SL3. The processing steps are summarized in Table 2. The first break data were picked manually. First break picks and travel-time residuals for the P-wave velocity tomograms are given in Figure 5(a, c, e) and Figure 5(b, d, f) respectively. Both the first break and travel-time residuals are illustrated as a function of offset. After 10 iterations, the final models for SL1, SL2, and SL3 profiles had an rms error of 4.6, 4.7 and 4.9, respectively (Fig. 5 b, d, f). Data acquired along the SL4 survey line are not presented in the text due to poor sensor-ground coupling caused by loose soil dumps along the survey line.

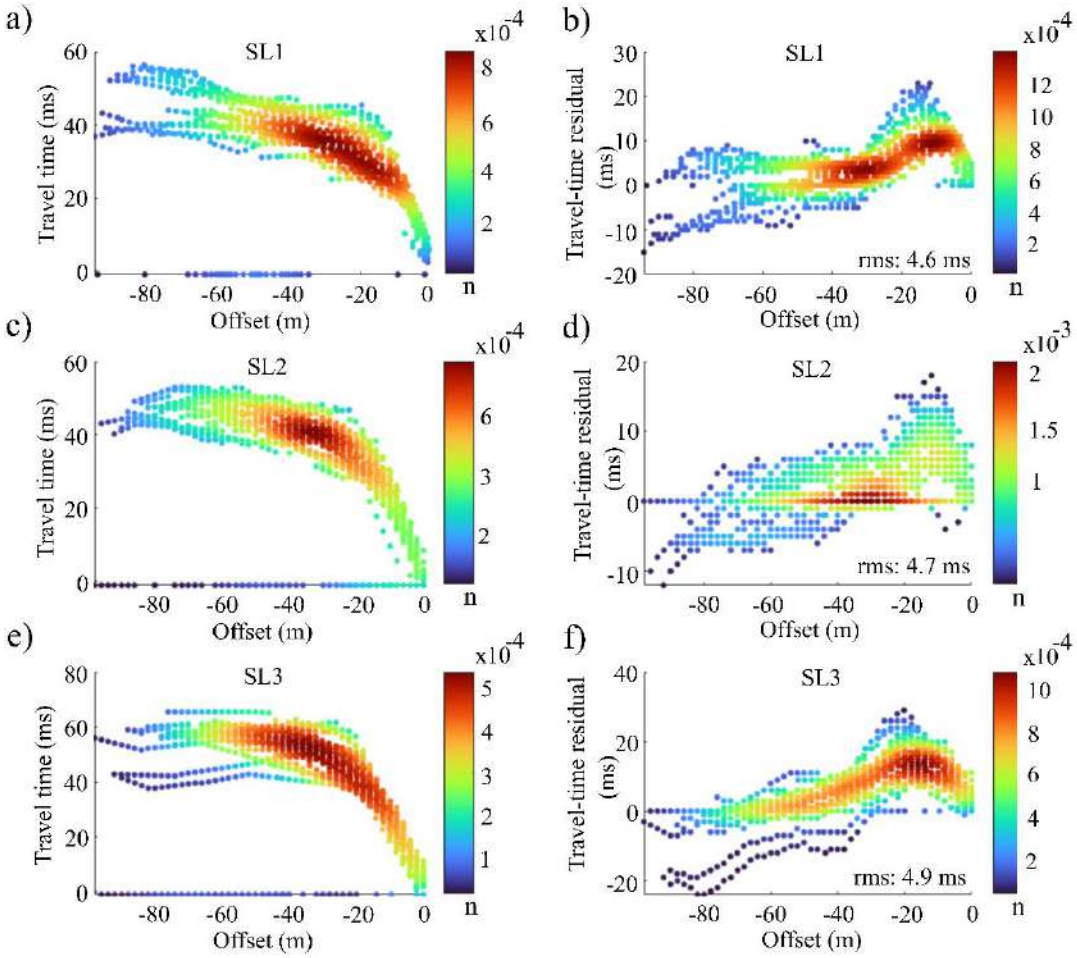


Figure 5: First break (a, c, e) and travel-time residuals (b, d, f) plots for seismic profiles SL1, SL2 and SL3. Both the first breaks and travel-time residuals are plotted as a function of offset, the colour scale used to illustrate the data represent the data density, where n – is the number of points within a range.

Table 2: Seismic data processing parameters.

Step	**2D processing flow**
1.	Read SEG-Y data
2.	Edit traces, Add geometry (X, Y, Z)
3.	Pick first P-wave breaks Traveltime-distance curve Inversion
4.	Refraction and elevation corrections Survey lines 1, 2, 3 and 4: Datum 1,224 m above mean seal level (msl).

Ground penetrating radar

Table 3 shows the geometry parameters used to acquire ground penetrating radar (GPR) data. The GPR data were acquired using the GSSI – SIR 4000 ground penetrating radar. The acquisition procedures involved moving the GPR cart across the 3D grid (GPR 3D) in zigzag direction and along the 2D lines GL1 and GL3 (Fig. 3). Common-offset reflection survey mode was used for data acquisition with 0.02 m trace spacing, 0.2 ns sampling interval and 120 ns listening time. To improve the signal-to-noise ratio, 10 vertical radargram were stacked at each sampling point.

The processing of the GPR data involved removing the acquisition delay time, applying energy decay gain to correct for the spherical spreading, and intrinsic attenuation of the signal. A bandpass filter (80 – 400 MHz) was used to attenuate unwanted frequency components. The dominant frequency is approximately 300 MHz. Subtract-mean (dewow) and subtracting average/background removal filters were applied to enhance the sub-vertical reflectors as well as suppressing the background noise and the direct arrivals. The synthetic reflection hyperbolas were matched with observed diffraction patterns emanating from underlaying boulders, so that a 2D velocity field can be created. The GPR profiles were migrated and converted to depth with a constant velocity of 0.1/0.2 m/ns.

Table 3: GPR acquisition parameters.

Acquisition item	3-D Grid/Line number parameters	
	GPR 3D	GL1 and GL3
Instrument:	GSSI – SIR 4000 GPR system	
Grid size/line length:	12 m × 15 m (X, Y)	200 m
Grid and trace spacing:	1 m × 0.02 m	0.02 m
Survey direction:	N - S	W - E
Survey pattern:	Zigzag	Along the profile
Dielectric:	9 F/m	
Processing steps		
Energy Decay:	0 – 150 ns time window	
Bandpass filter:	80 – 400 MHz	

Subtract-mean (dewow):	1 – 2 ns time window
Subtracting average/background removal:	10 – 20 average traces
Diffraction stack:	Summation width (10 – 20 traces); velocity (0.1 – 0.2 ns)
Time-depth conversion:	0.1 – 0.2 m/ns

RESULTS

Magnetics

Figure 6 presents the detailed total magnetic intensity map of the study area, including the results of the magnetic enhancement techniques.

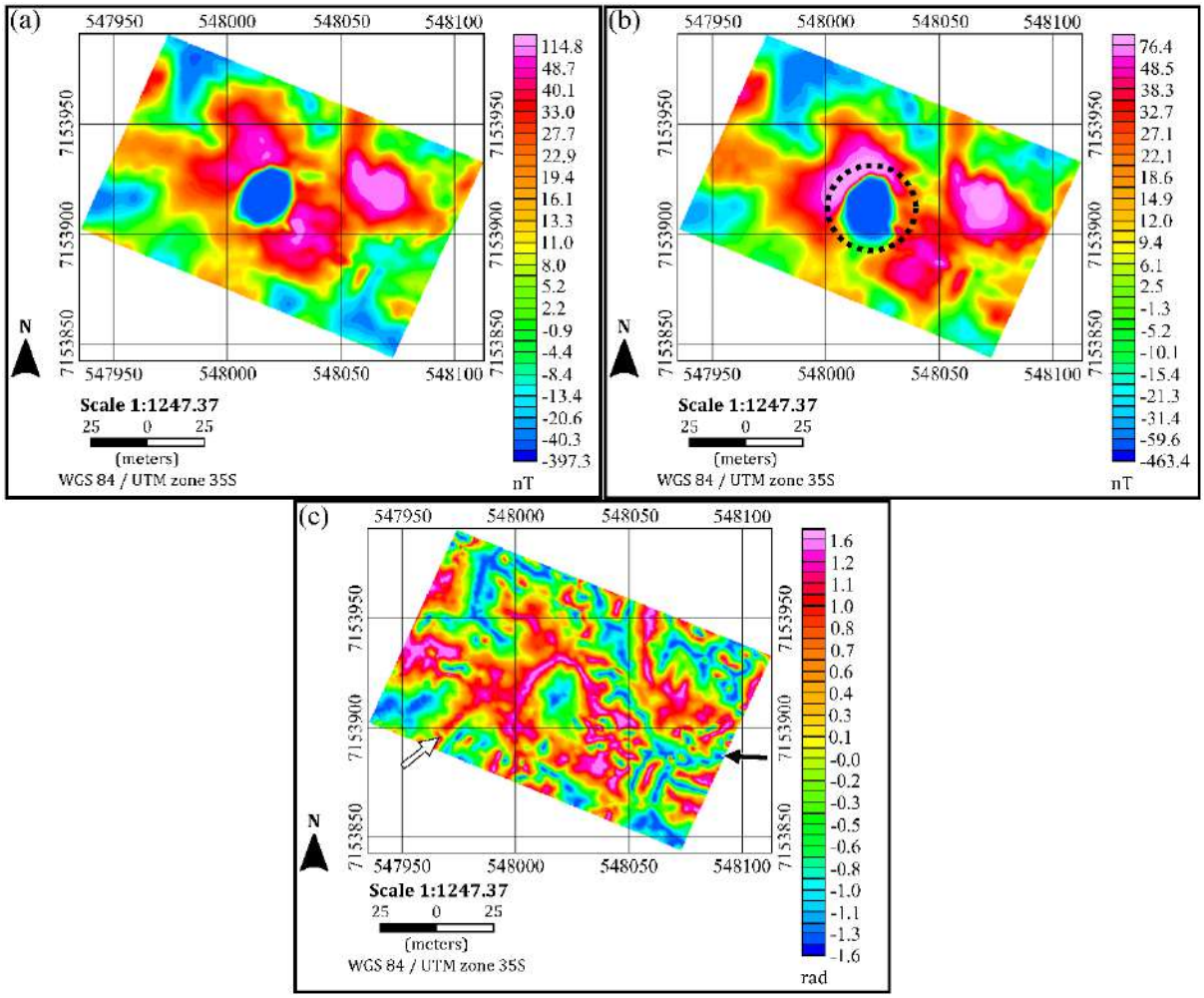


Figure 6: (a) Decultured, micro-levelled and detrended residual total magnetic intensity (TMI) map. (b) Reduced to magnetic pole (RTP) map, the black dotted circle shows the position of a body with remanent magnetisation found in the study area. (c) Vertical tilt angle of the RTP map. The black and white arrows show connected magnetic low zones and magnetic high zones.

Specifically, Figure 6(a-c) presents the total magnetic intensity (TMI), reduced to magnetic pole (RTP) and the vertical tilt angle maps of the study area, respectively. The TMI map, Figure 6(a), shows the variation and distribution of positive and negative magnetic anomalies in the study area. The application of the RTP technique provides the corrected position of the magnetic sources and their induced magnetization (Fig. 6b). From the computation of the RTP conversion, it is observed that a circular feature with remanent magnetisation is present (indicated by a black dotted circle). The vertical tilt angle filter sharpens the variation between the low and high magnetic intensity zones (Fig. 6c). The vertical tilt angle map reveals that, both the high and low magnetic intensity zones are largely interconnected (indicated by arrows in Fig. 6c). The black and white arrows in Figure 6(c) each demonstrate an example of a magnetic low and high zone, respectively. The effects of weathering (gradual variation in magnetic intensity moving from the magnetic low to high regions), the presence of fractures (zones that separate the red zones, also appearing as blue) and of a feature with remanent magnetisation are well captured in Figure 6(a-c).

Electrical resistivity tomography

The 160 m long survey lines acquired across the study area (Fig. 3) are observed to reach depths between 21 to 30 m, depending on the type of array used. The resistivity tomography results, shown in Figure 7, show a progressive increase of the resistivities of the rocks with depth. The near-surface (top ~6 to 5 m) is demarked by a conductive zone (low resistivity, blue coloured zone) with resistivities of ~3 – 40 ohm.m. The thickness of this low resistivity zone is observed to vary from one resistivity profile to another, but it is between 6 – 7 m (Fig. 7). This top resistivity low zone is underlain by a zone of much higher resistivities (~40 – 3,162 ohm.m), coloured as light green to yellow zone. The contrast observed between these two layers is representative of the sharp contrast observed at the topsoil-fractured bedrock interface, visible on the highwall present a few meters away from the study area (see Fig. 2b). Underlying the green to yellow zone is the light to dark red zone, a zone of much higher resistivity (~3,162 to ~10,000 ohm.m). The variation in the resistivity of these three observed zones is complex, both moving along and across the profiles (Fig. 7).

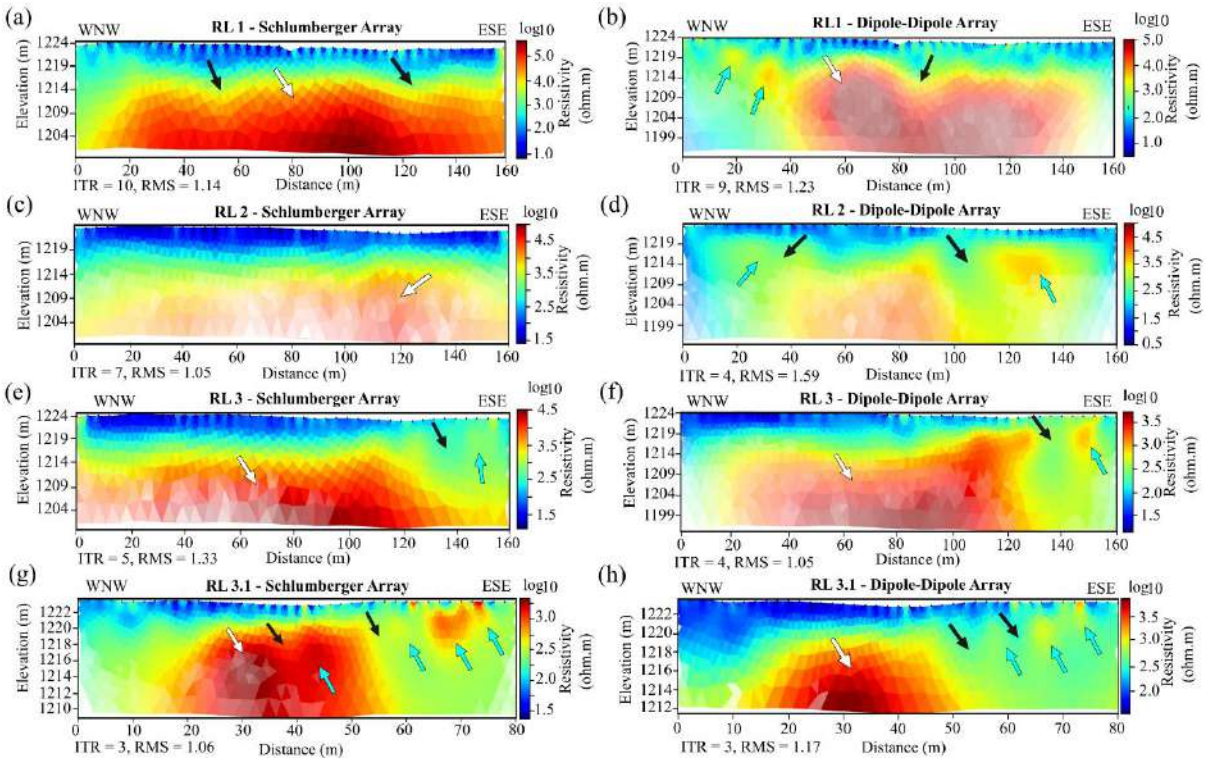


Figure 7: Schlumberger (a, c, e, g) and dipole-dipole (b, d, f, h) resistivity inverse models for electrical resistivity tomography survey RL1 – RL3.1. The white, black and blue arrows in the plots indicate the high resistivity, low resistivity and potential boulders, respectively. The elevation used to produce the resistivity tomographs is the elevation above sea level, while the resistivity variation is measured in ohm.m.

The Schlumberger array is observed to best demonstrate the resistivity variation across depth and the bedrock (high resistivity zones, indicated by white arrows) (Fig. 7a, c, e, g), while the dipole-dipole array (Fig. 7b, d, f, h) best demonstrates potential fractures, highly weathered zones (low resistivity zones separating high resistivity zones, indicated by black arrows) and boulders (semi-circular, high resistivity features in low resistivity zones, indicated by blue arrows).

Seismic refraction tomography

The P-wave refraction tomograms largely demonstrate an increase in P-wave seismic velocities with increasing depth. Figure 8 illustrates the final P-wave refraction models (Fig. 8a, c, e) for profiles SL1, SL2, and SL3, and their ray paths (Fig. 8b, d, f). The tomograms reveal the presence of roughly three P-wave seismic velocity zones (layers) of varying thickness, both along and across the seismic profiles (Fig. 8).

The near-subsurface seismic velocity zone, light brown zone (indicated by a white arrow), exhibits the maximum P-wave velocity of ~1,400 m/s. Based on the inversion models, the depth extent of the velocity low zone varies from surface to a maximum depth of about 20 m (Fig. 8). This top light brown layer is underlain by a yellow to green seismic P-wave velocity zone (indicated by a light blue arrow) of relatively higher velocities (~1,400 to ~4,000 m/s). The thickness of this layer varies across the profiles. The layer consists of semi-circles/ellipses of higher velocities embedded within it, which are interpreted as boulders. Underlying this second velocity zone is a light to dark blue seismic velocity zone of higher P-wave velocities (~4,000 to ~6,400 m/s, indicated by a black arrow). This light to dark blue seismic velocity zone exhibits variable depth from the surface. The observed seismic velocity zones consist of zones of disturbed layering, possible fracture (jointing and faulting) and boulder zones (Fig. 8).

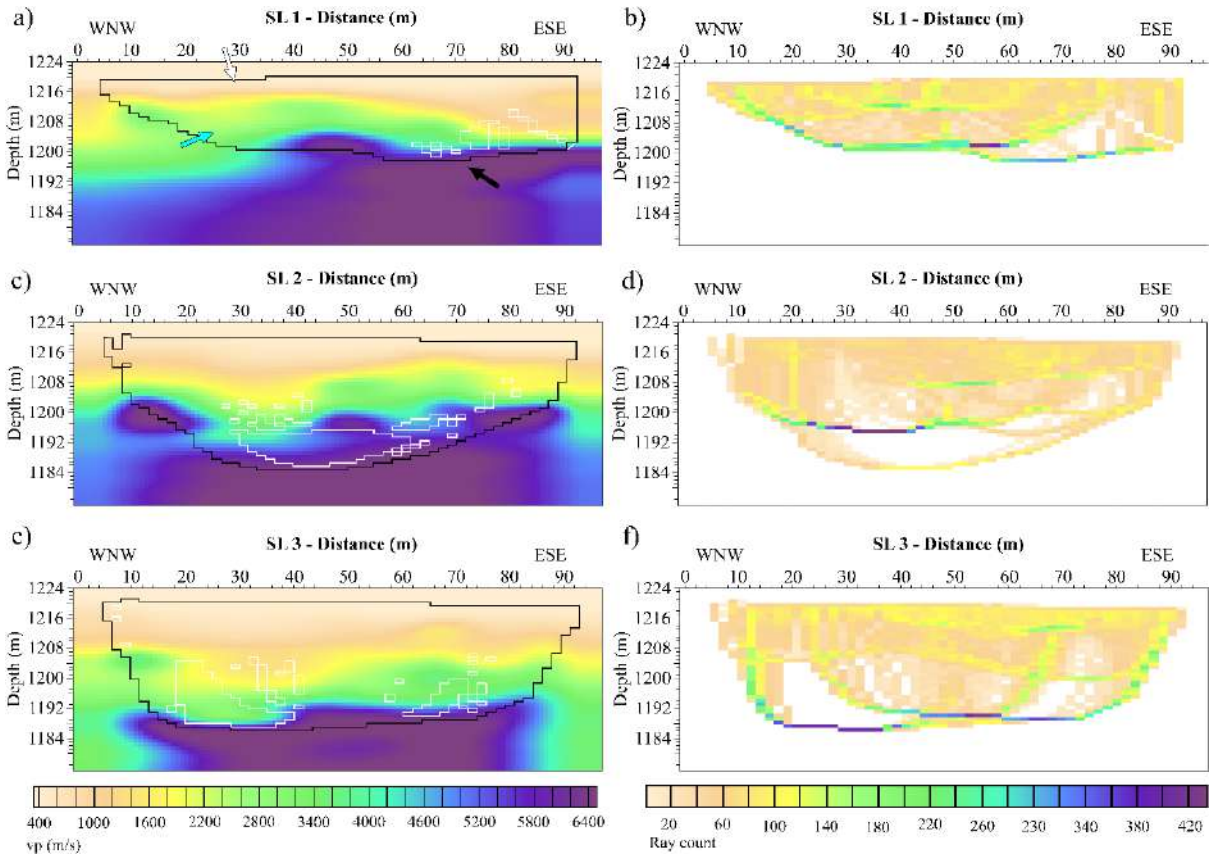


Figure 8: First break travel-time tomography model and their corresponding ray paths along profiles SL1 (a & b), SL2 (c & b), and SL3 (d & f). The outlines of the raypaths are drawn on the tomograms, the zones within the white borders are zones in which ray paths did not travel through. The tomograms display near-linear (top) to distorted (middle and bottom) seismic variations with increasing depth. The white, blue and black arrows show the three identified

seismic velocity layers, starting from the layer characterised by the lowest velocities to the layer with the highest velocities, respectively.

Ground penetrating radar

The ground penetrating radar (GPR) sections show radar traces (radargram) plotted against time and distance (Fig. 9). The x-axis represents the distance along the survey line while the y-axis represents the travel-time of the radar pulses. The radargrams show several reflections (dark blue arrows) and diffraction events (light blue arrows), probably emanating from buried boulders and loose soil cover, as well as from the background noise (Fig. 9).

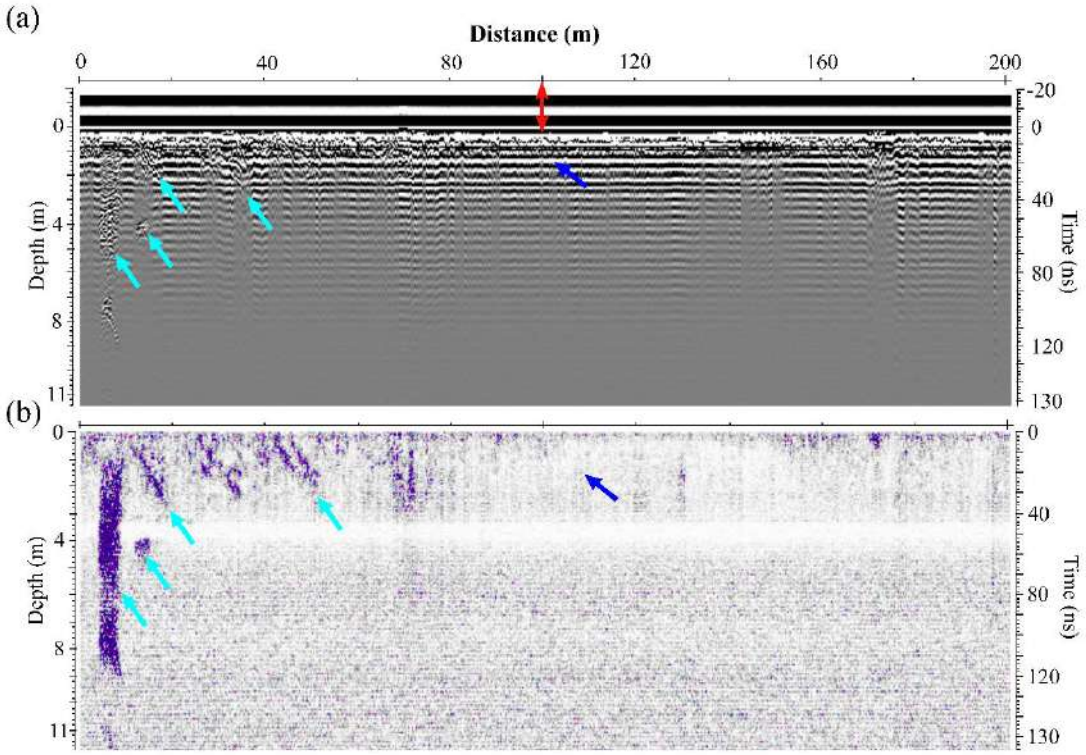


Figure 9: A sample of a raw (a) and processed 2D GPR sections (b) of profile GL1. The double headed red, light blue and dark blue arrows show the delay time, reflection and diffraction, and background noise, respectively. The observed reflection and diffraction events are possibly events originating from the contact of different lithologies and boulders.

INTERPRETATIONS AND DISCUSSION

Magnetic susceptibility inversion models

Noritic and anorthosite rocks can be magnetic due to the presence of accessory minerals such as magnetite and ilmenite (Dunlop et al., 2010; Soumya et al., 2017). The weathering of such

mafic rocks, i.e., norites and anorthosites, results in the formation of soil, with silicate minerals breaking down into clay minerals (conductive minerals), and iron-bearing minerals (e.g., magnetite and ilmenite) breaking down into iron oxides of varying magnetic susceptibility (Lu et al., 2008; von Dobeneck, 2021). The weathering of magnetite initially forms oxidized ferrimagnetic Fe-minerals, such as maghemite, followed by antiferromagnetic minerals such as hematite and goethite, which are far less magnetic (Lu et al., 2008; von Dobeneck, 2021). Both maghemite and hematite are observed at the mine site. In magnetic soils, however, magnetite can be weathered directly to hematite (Santana et al., 2001). Overall, there is a gradual loss of inherited thermoremanent and/or acquired chemical magnetization with progressive weathering, mainly associated with the alteration and the reduction of grain sizes of magnetic minerals in rocks (Lapointe et al., 1986; Harding et al., 1988; von Dobeneck et al., 2021). The reduction in magnetisation with weathering is observed in the magnetic susceptibility measured on hand samples in the laboratory (Table 1). Therefore, magnetic high zones (red- and pink-coloured zones) are interpreted to represent least-weathered areas, while low magnetic zones are interpreted to represent highly weathered areas (Figure 6). The high magnetic zones are caused by a shallow, fresher and less fractured bedrock component, and thus, these zones are likely to form blasting-induced boulders when blasted inadequately. Surrounding the high magnetic zones are lower magnetic intensity zones (green to dark blue-coloured zones; Fig. 6). The lower magnetic intensity zones represent highly weathered and fractured areas. The blue-coloured zones are thought to be the most weathered zones, where fractures in the rock accelerate chemical weathering processes. Thus, blue-coloured zones are where fresh rock was broken-down (e.g., formation of hematite and clay minerals) at a faster rate. The probability of finding isolated subterranean boulders surrounded by regolith should therefore be higher in such highly weathered zones.

The semi-circular, low magnetic intensity feature at the centre of the magnetic maps (blue-coloured; Fig. 6) is thought to be a weathered remnant of a magnetised iron-rich ultramafic pegmatite (IRUP) (Scoon and Mitchell, 1994).

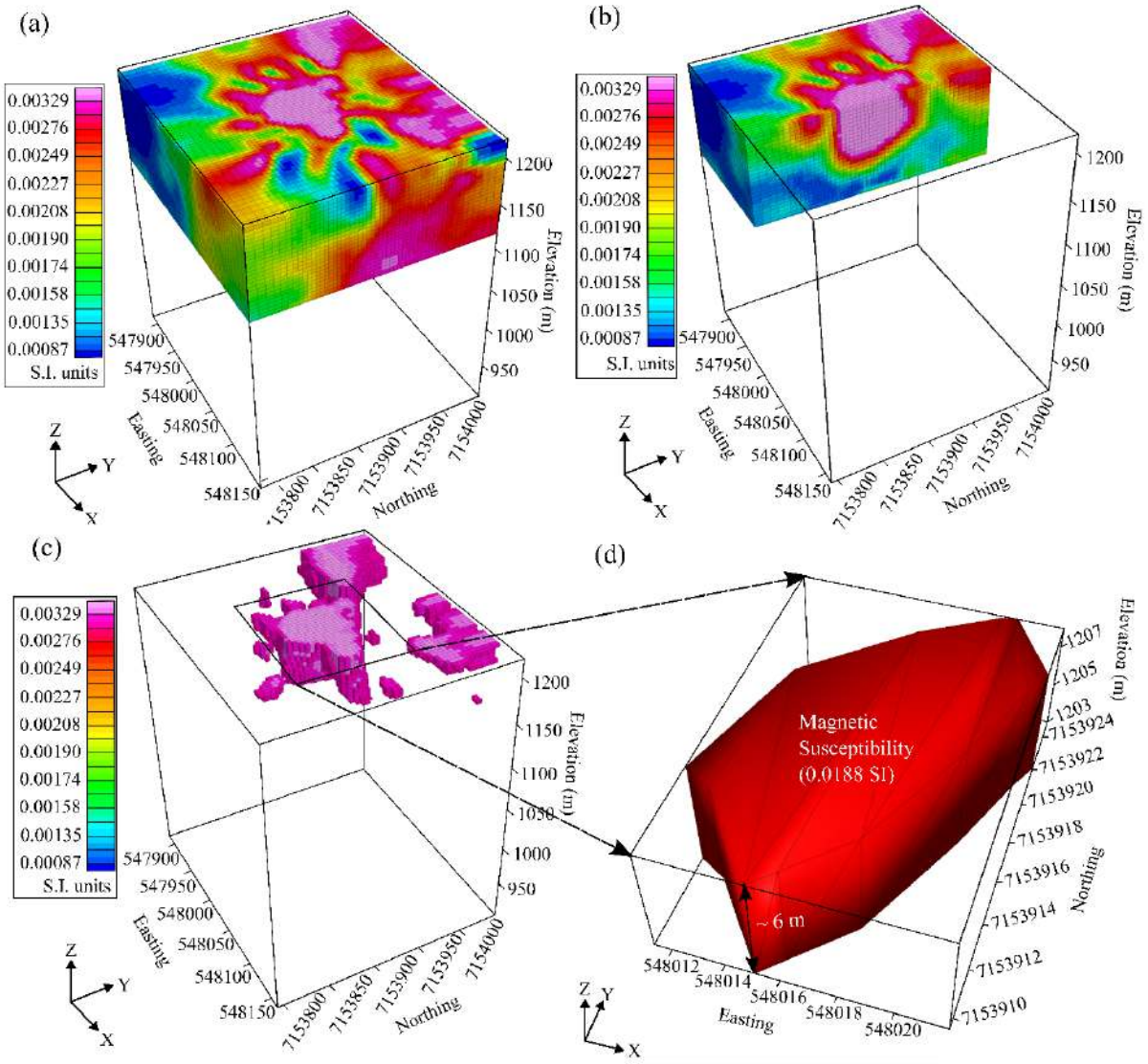


Figure 10: Susceptibility Magnetic Vector Inversion (MVI) model of the acquired TMI data in our study area. (a) Full MVI model of the magnetic data displaying the magnetic susceptibility of the rocks, including that of the IRUP (centre). (b) Clipped 3D susceptibility model showing the vertical nature of the IRUP. (c) Zones of high magnetic susceptibility around the IRUP are interpreted as potential boulders. (d) 3D best-fit ModelVision model of the IRUP.

IRUPs are typically weakly magnetic bodies (either positive or reverse magnetisation) that preferentially replace anorthosite-leuconorite lithologies (Scoon and Mitchell, 1994; Reid and Basson, 2002; Campbell, 2006). Such lithologies are noted at the Tharisa Mine. Furthermore, the semi-circular shape (when viewed perpendicular to layering) of the feature is consistent with the pipe-like shape (when viewed parallel to layering) often noted for IRUP bodies (Scoon and Mitchell, 1994). 3D models of the low magnetic susceptibility feature are presented in Figure 10(a-d), and confirm that the feature is indeed pipe-shaped. The models also reveal that

the feature is shallow (Fig. 10b), at a depth of about 10 m from surface with a vertical extent of roughly 6 m (Fig. 10c-d), and has a magnetic susceptibility of 0.0188 SI units. Given that the feature terminates at depth (Fig. 10b-d) suggests that it is of a replacement nature, which also corresponds to the hypothesized origin for IRUPs (Scoon and Mitchell, 1994). However, amplitude inversion models are often biased towards high amplitude anomalies, which in this case corresponds to the IRUP body. This existing bias results in the attenuation of lower amplitude features, meaning that they may not be well resolved. Thus, although Figure 10(c) appears to resolve small-scale semi-spherical features (possible boulders), it is possible that additional small-scale features are missed because of their lower magnetic susceptibility compared to the high amplitude IRUP. Considering the high level of weathering encountered in the top subsurface (10 – 30 m depth), combined with the presence of an IRUP, which is commonly accompanied by numerous fractures, these are promising factors for the presence of boulders in the area.

Integration of resistivity, seismic, and ground penetrating radar results

The electrical resistivity tomography (ERT), seismic refraction tomography (SRT) and ground penetrating radar (GPR) surveys acquired in this study were collected over an area of varying TMI; thus, over an area of variable weathering and magnetic susceptibility (Fig. 11). Figure 12 compares and correlates the inverted ERT, SRT and GPR sections across survey profile 1 (profile along which SL1, RL1 and GL1 where acquired) along with lithological data from a borehole (BH1) (Figs. 3 and 11).

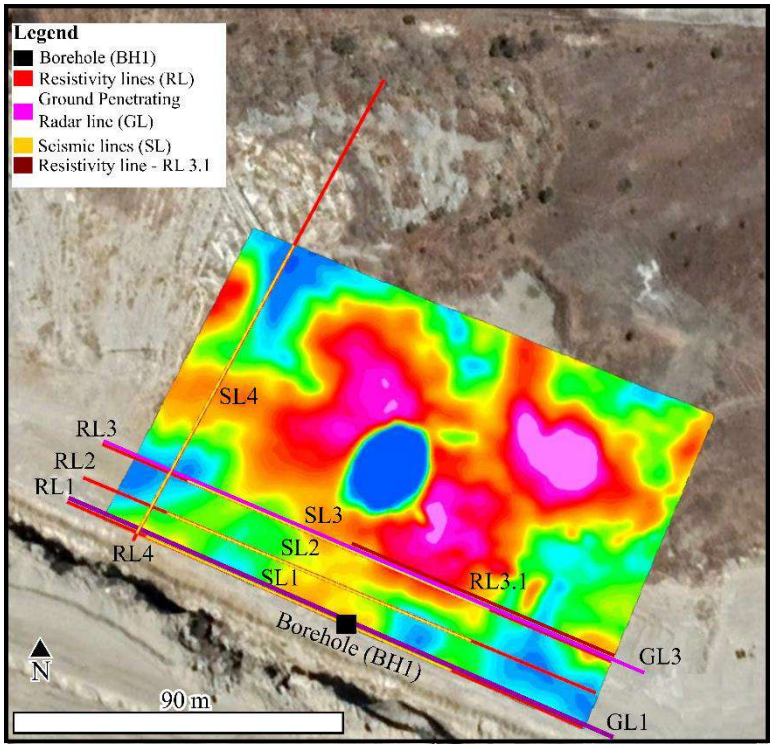


Figure 11: Seismic (SL), resistivity (RL) and ground penetrating radar (GL) 2D line locations overlain on the total magnetic intensity map of the study area. The seismic and resistivity profiles were placed on a zone with varying TMI to try map the observed magnetic variation in the subsurface rocks with depth.

Both the resistivity and seismic inversion results for profile 1 correlate with the borehole BH1 data. At the location of BH1, in both the resistivity and seismic sections, the dark to light blue and light brown zones corresponding to a low resistivity and seismic velocity zone, respectively, represent the top 6 m section (core-loss zone) of BH1 (Fig. 12b, c).

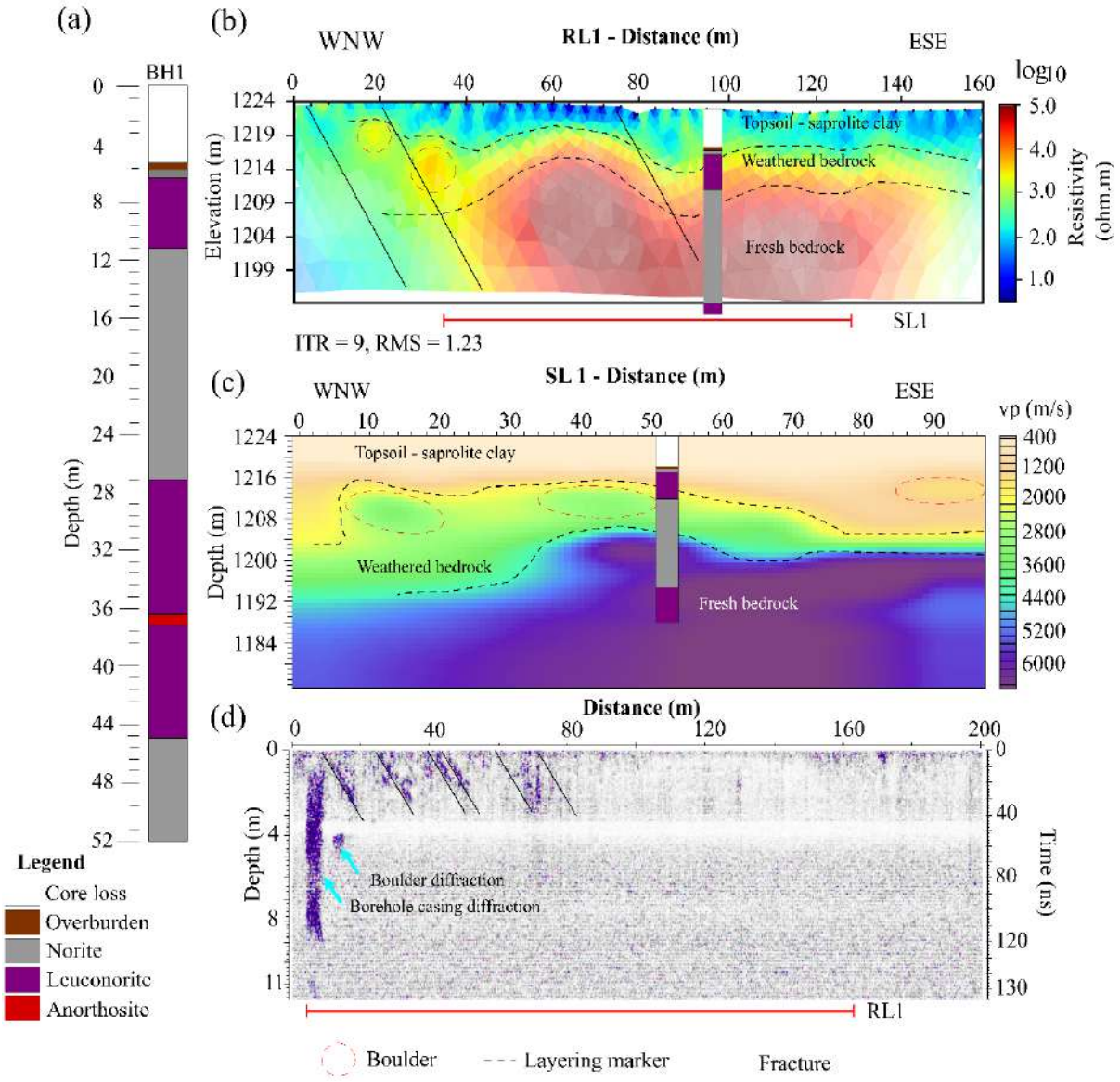


Figure 12: Interpretation and integration of methods for profile 1 (profile where SL1, RL1 and GL1 were acquired) 1. (a) Borehole (BH1) lithology along profile 1. The lithological log has been correlated with RL1 and SL1. (b) BH1 overlain on the electrical resistivity tomogram of RL1. (c) BH1 overlain on the seismic refraction tomogram of SL1. (d) Ground penetrating radar section of profile GL1. The dotted lines show the lithological boundaries between saprolite clay, weathered bedrock and fresh bedrock. The solid black lines correspond to joints, fractures, or fault lineaments.

The dark to light blue near-surface zone is characterized by resistivities of ≤40 ohm.m and P-wave velocities of ≤1,400 m/s. This zone is interpreted to be the saprolite clay – regolith zone, a zone of high weathering activity. With increasing depth, a large increase in resistivity and P-wave seismic velocity of the subsurface rocks is observed.

The overburn norite and leuconorite layers, situated below the core-loss zone at depths between 6 m and 11 m, are characterized by higher resistivities and P-wave seismic velocities of ~40 to 3,162 ohm.m and ~1,400 to 3,600 m/s, respectively (Fig. 12). These layers, i.e., the overburn, norite, and leuconorite layers, along with the top portion of the norite rock appearing at a depth of 11m and greater are interpreted to constitute the weathered bedrock zone. The layers situated below the weathered bedrock zone, starting with the norite layer at a depth of about 11 m and extending to greater depths, are characterised by much higher resistivities and seismic velocities of ~3,162 to 10,000 ohm.m and ~3,600 to 6,400 m/s, respectively. These high resistivity and seismic velocity zones are interpreted to represent fresh bedrock zones, fresh norite to anorthosite zones, that have been least affected by near-surface weathering processes (Fig 12b-c). The linear features on the GPR GL1 radargram are responses from structural features (joints and faults), which are correlatable with both the resistivity and seismic tomograms (Fig. 12b-d).

The resistivity, seismic inverted models and the GPR radargram for profile 3 (line with RL3, SL3, GL3 and RL3.1) are presented in Figure 13. In both the ERT and SRT depth sections, horizons (i.e., saprolite clay, weathered bedrock and fresh bedrock) are inhomogeneous and present abrupt changes that can be attributed to fracture-related distortions (Fig. 13a-c). The ERT, SRT and GPR sections reveal that the lithology along profile 3 is highly disturbed (Fig. 13a-d).

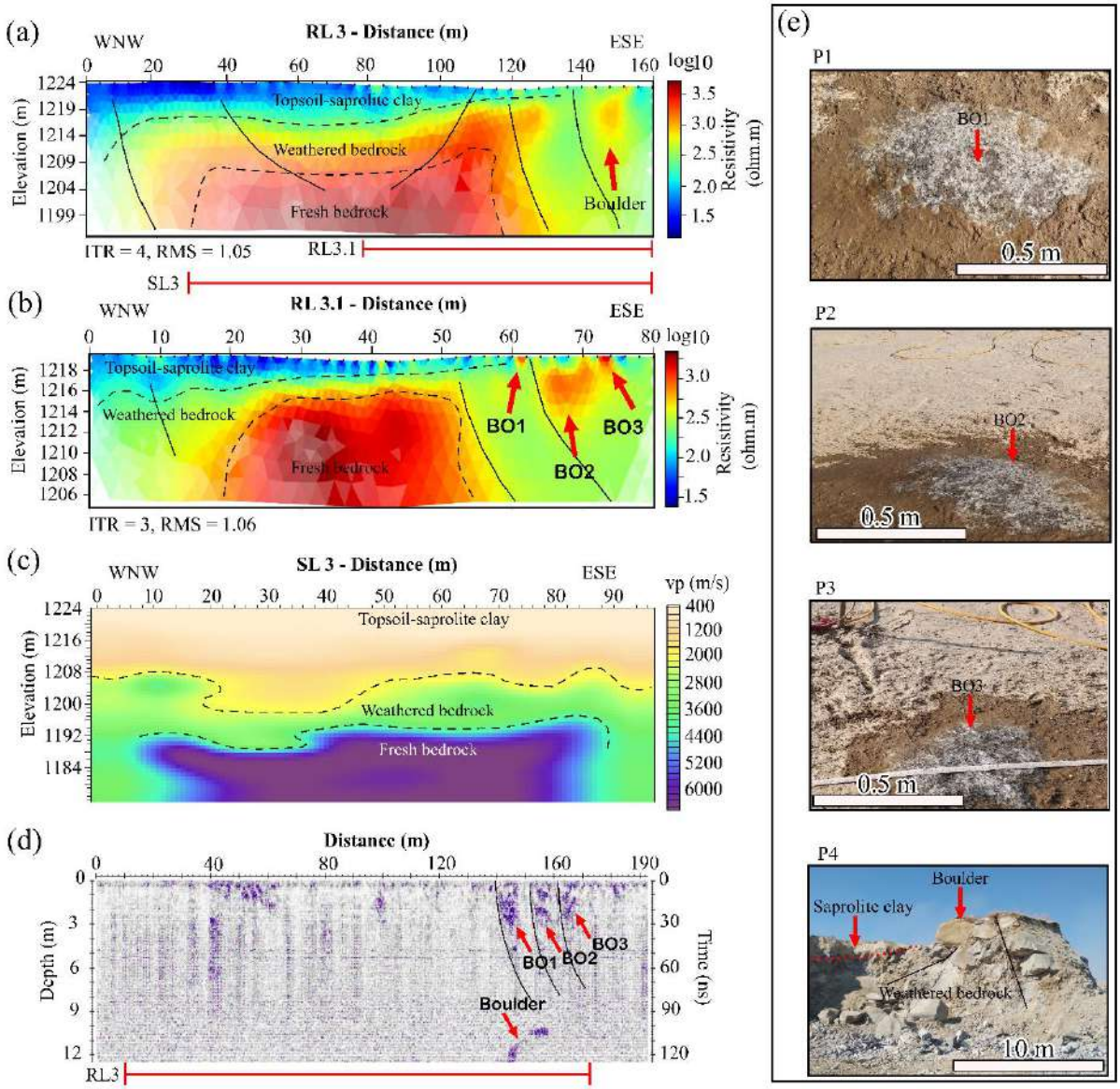


Figure 13: Interpretation and integration of methods for profile 3 (profile where SL3, GL3, RL3 and RL3.1 were acquired). (a) Electrical resistivity tomogram of profile RL3. (b) Electrical resistivity tomogram of profile RL3.1, high-resolution line mapping the outcropped region along RL3. (c) Seismic refraction tomogram for profile SL3. (d) Ground penetrating radar section of profile GL3. (e) Images of the outcropping rocks along profile 3 (pictures P1, P2, P3 and P4). The dotted lines show lithological boundaries between saprolite clay, weathered bedrock and fresh bedrock zones. The solid black lines show joints, fractures, or fault lineaments. BO – boulder outcrops.

At a distance of about 145 m to 160 m, along RL3 and about ~0.5 – 1 m next to the line, exposed rocks (outcrops), likely corresponding to norite boulders, were observed. A high-resolution (1 m) electrical resistivity depth section of the area adjacent to the outcrops along RL3, RL3.1, is presented in Figure 13(b). Notably, the high-resolution resistivity depth section

shows several high resistivity features (boulders) embedded in a zone of low resistivity along the eastern edge of the section. Some of these boulders were outcropping on surface (BO1, BO2 and BO3 in Fig. 13e), which provided confidence in our interpretation. Furthermore, the high-resolution section (RL3.1) details a central high resistivity zone (orange to dark red-colours), interpreted as fresh bedrock, embedded in a low resistivity zone (green to dark blue coloured), which corresponds to weathered/altered rock (Fig. 13b). The central high resistivity zone is suspected to be an underground extension of the norite bedrock, based on outcrops near where profile 3 was conducted. The presence of buried boulders is also seen in the GPR radargram as diffractions. The location and depth of the boulders match relatively well between the resistivity tomograms and GPR radargram (Fig. 13a-d).

The GPR radargram interpretation of grid GPR 3D (Fig. 3) are shown in Figure 14. The maximum depth of penetration of the electromagnetic wave is ~10 m. Figure 14(a-b) show the 3D view interpretation of GPR 3D grid lines along the North – South (X) and East – West (Y) directions, respectively. The steeply dipping linear features observed in the radargram sections likely correspond to reflections emanating from joints and fractures. These structural features have variable dips (~30 – 50°). The formation of these structures could be as a result of gradual mechanical/chemical weathering or recent mining activity (e.g., rock blasting). The linear features could also correspond to boulder interfaces within the saprolite clay horizon (e.g., Fig. 14b). The gentle dipping (~10 – 15^{o}) reflections in GPR 3D data likely correspond to responses emanating from the saprolite clay-boulder and weathered bedrock interface. Several diffractions on GPR data are interpreted as boulders, ranging between 2 – 4 m wide at ~1 – 7 m depth. In future, we plan to process the reflection seismic surveys acquired along these boulders to enhance the detection of these boulders and constrain their 3D geometry through diffraction imaging approaches (Moser and Howard, 2008). The results will be compared to diffraction patterns observed on the GPR data to constrain their interpretation. Several authors (e.g., Khaidukov et al., 2004) have demonstrated the effectiveness of analysing seismic response of similar features through diffraction imaging. Diffraction analysis on the seismic data has the potential to detect even small boulders that are beyond the resolution of other geophysical methods used in this study (Moser and Howard, 2008).

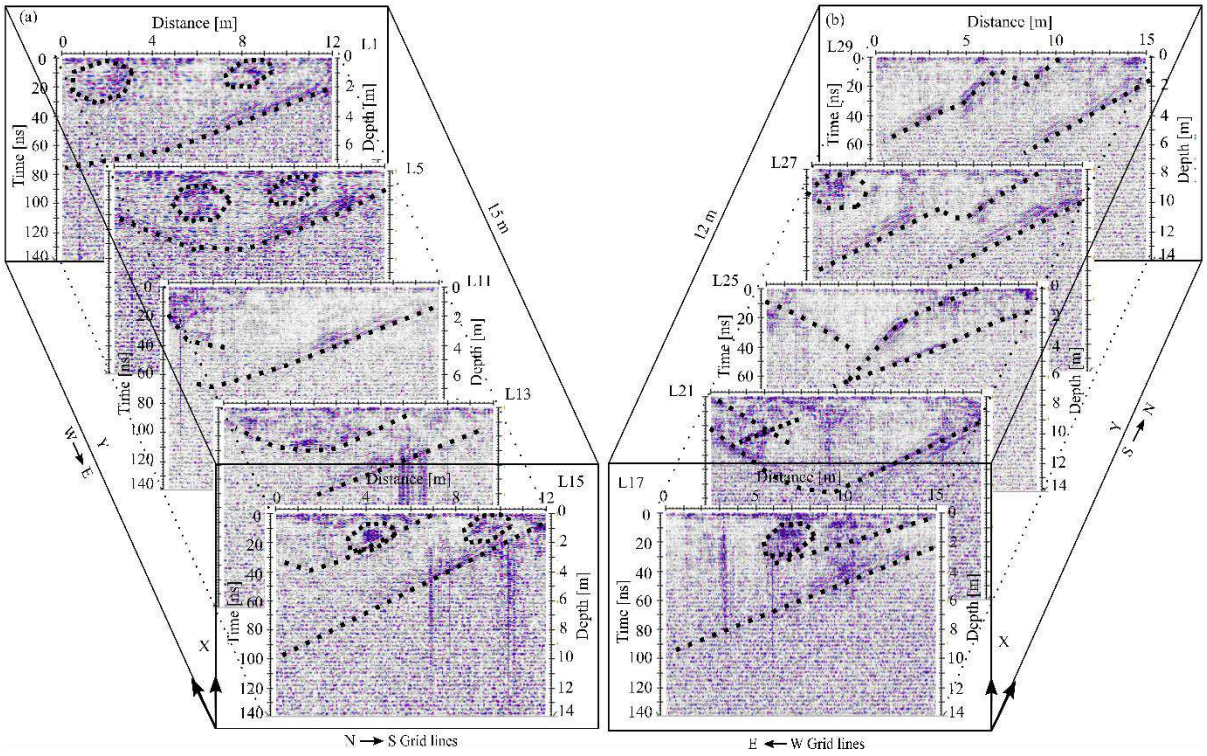


Figure 14: (a) and (b) 3D view interpretation of GPR 3D grid radargram lines along the north – south (X) and east – west (Y) directions, respectively. Note: Y-axes are not drawn to scale and the dotted black lines and circles in all sections correspond to different geological features.

Geological model

By overlaying the electrical resistivity and seismic depth sections on Google Earth maps, we observe that there is strong correlation between the magnetic intensity, P-wave seismic velocity and resistivity variations (Fig. 15). Specifically, the magnetic intensity is higher in regions with a thin low seismic velocity and low resistivity zone.

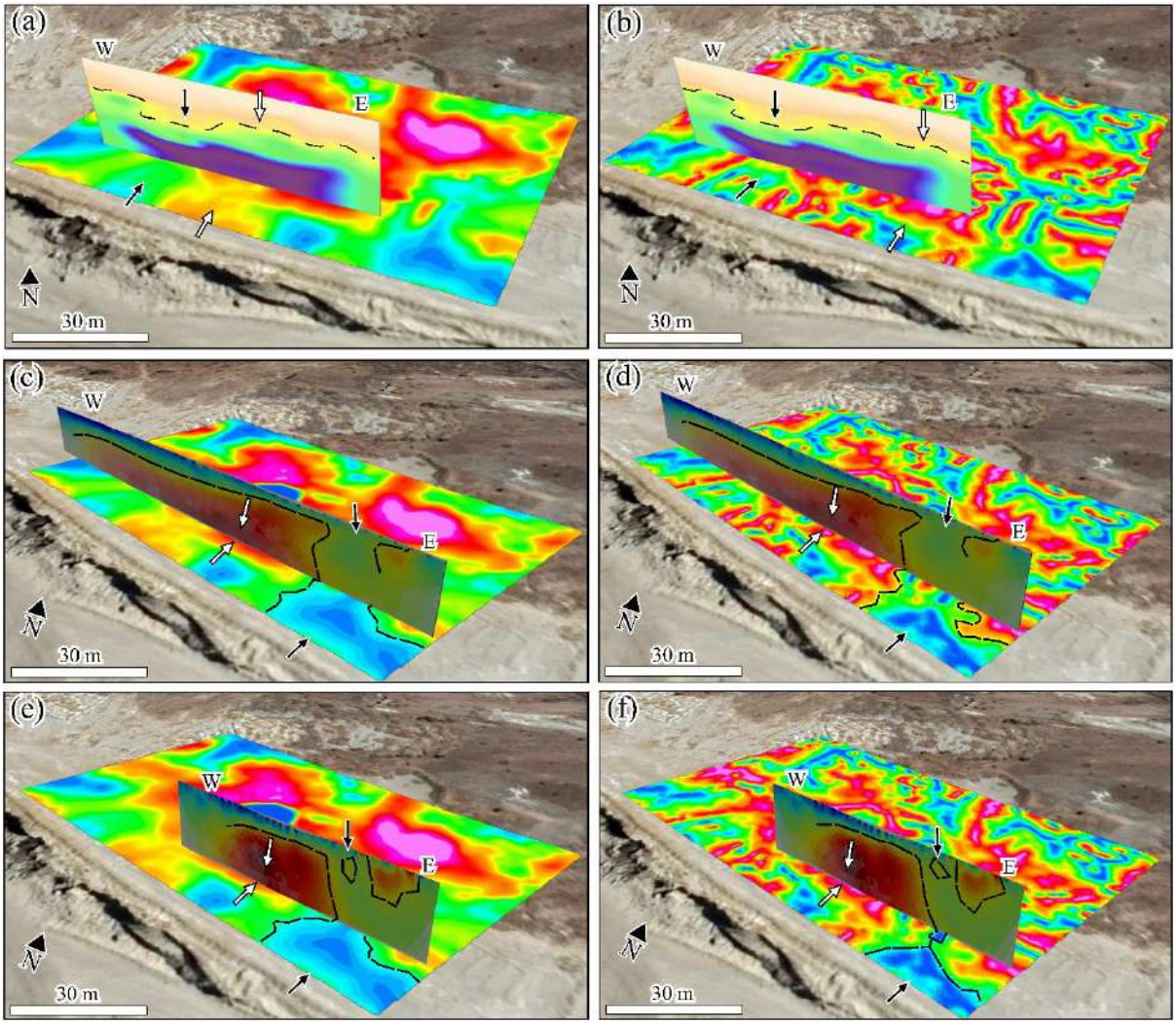


Figure 15: Profile SL3 seismic depth section projected on the TMI (a) and TVDR magnetic (b) maps. Profile RL3 resistivity depth section projected on the TMI (c) and TVDR (d) magnetic maps. Profile RL3.1 resistivity depth section projected on TMI (e) and TVDR (f) magnetic maps. The white and black arrow indicate areas where the is high and low correlation, respectively.

The opposite is also true, whereby magnetic intensity is lower in regions with a thick low seismic velocity or low resistivity zone (Fig. 15a-f). The thicker the low velocity or conductive zone, the less magnetic the area. Thus, there is a strong depth correlation between magnetic intensity, seismic velocity and resistivity (Fig. 15). The correlation is better observed on the TVDR projected images (Fig. 15b, d, f). This may imply that where magnetic highs are prominent, the ground is relatively less weathered, and the depth of the fresh bedrock is closer to the surface. In regions where the magnetic low is prominent, the thickness of the saprolite clay and weathered horizons is larger, and thus the depth to the fresh bedrock is greater (excluding regions where remanently magnetised bodies are present, e.g., above the IRUP). In

areas where boulders were identified (i.e., Figs. 12 and 13a-d), a magnetic high anomaly in a magnetic low zone is observed, which is interpreted to be associated with the less-weathered nature of the boulders as compared to the host rock (Fig. 15c-f). These observations demonstrate that electrical resistivity and magnetic surveys can be successfully used to infer the presence of subterranean boulders in magnetic environments. The integrated geophysical data (Figs. 12, 13 and 14), combined with surface geological observations and borehole lithological data, were used to generate a 3D geological model of the study area (Fig. 16a-b).

The integration of the data is of significant interest for exploration and planning mining activities (e.g., blasting, extraction of ore, slope/ground stability). Interestingly, not all boulders found at Tharisa Mine are subterranean boulders, some are subaerial boulders caused by blasting activity (Fig. 2d). In open-pit mining, subaerial boulders are large rock fragments often formed during excavation and bench blasting, due to inefficient rock breakage. These types of boulders are a recognised by-product of the drill-and-blast techniques (Leng et al., 2020). The drill-and-blasting technique is a cost-effective scheme often used in mines to quickly excavate large areas and break down benches. Oversized boulders are typically formed when the blasting energy is not enough to cause sufficient rock breakage.

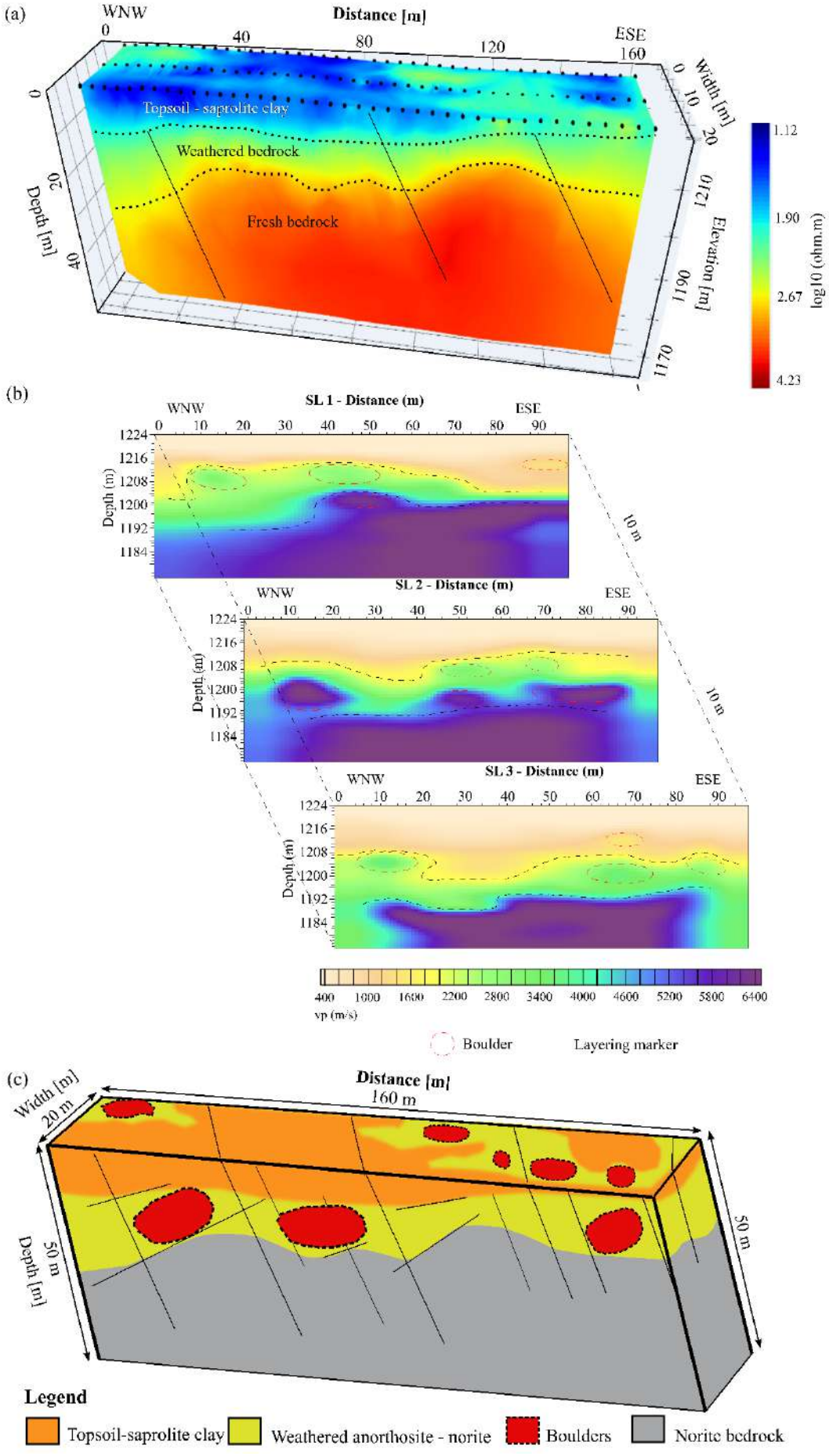

(a)
WNW
Distance [m]
ESE
Topsoil - saprolite clay
Weathered bedrock
Fresh bedrock
Depth [m]
Width [m]
Elevation [m]
log10 (ohm.m)
1.12
1.90
2.67
4.23
(b)
SL 1 - Distance (m)
SL 2 - Distance (m)
SL 3 - Distance (m)
Depth (m)
10 m
vp (m/s)
Boulder
Layering marker
(c)
Width [m]
Distance [m]
160 m
50 m
Depth [m]
Legend
Topsoil-saprolite clay
Weathered anorthosite - norite
Boulders
Norite bedrock

Figure 16: (a) 3D electrical resistivity model of survey lines RL1, RL2 and RL3. (b) 3D view of seismic refraction tomograms of survey line SL1, SL2 and SL3. (c) 3D geological model generated from the combined geophysical methods employed in this study.

The efficiency in rock breakage is affected by several factors, including: 1) uneven distribution of energy, 2) structural features (discontinuities), 3) intact rock properties, and 4) the type of blasting (design) used to break down the rock (Yang et al., 2018; Leng et al., 2020; Park and Kim, 2020). Often, the formation of subaerial boulders is an indication that the drill-and-blast technique used at a mine is not optimized to reduce the formation of boulders or produce sufficient rock breakage. Unoptimized blasting produces large fragments (boulders), which will require extra resources to remediate. Dealing with boulders might necessitate drilling and/or blasting again, which ultimately slows down production.

Additionally, when blasting is not optimised (designed) adequately, excessive throw and fly-rocks occur. Throw and fly-rock are a by-product of blasting that occur when blasting activity is not designed adequately and the blasting energy is misdirected (Monjezi et al., 2011; Raina et al., 2015). Fly-rocks pose a huge safety hazard, as they may cause property damage and injuries at mines. Thus, by using intact rock property and structural discontinuity information obtained from integrated geophysical survey results, one can be able to design optimised drill-and-blasting programs that result in more efficient rock breakage (less boulders), while also reducing throw and fly-rocks (which translates to a safer working environment), thus leading to increased productivity and reduced mining activity costs.

CONCLUSION

This study demonstrates that the integration of magnetic, electrical resistivity, refraction seismic and ground penetrating radar methods can be successfully used to gain a better understanding of the subsurface in order to increase efficient mining and enable sound engineering decisions. We propose the use of integrated geophysical techniques for mining and engineering site characterization to best identify geological features such as boulders, fractures and horizons (i.e., regolith to fresh bedrock). The results presented here demonstrate that by targeting weathering, structural and magnetization effects in subsurface rocks in magnetic environments, geological features that characterize and complicate mining processes can be successfully identified. By mapping the inherent loss of magnetization, presence of remanent magnetization, the degree of weathering, the competence and structural features of subsurface

rocks, we were able to successfully map boulders, fractures, undulating lithological horizons, and remanent igneous features (i.e., iron-rick ultramafic pegmatites). From these findings, it can be concluded that the integration of numerous geophysical methods can be used to improve mine blasting programs, reducing the formation of blasting related boulders, and assisting in making cost-effective decisions.

ACKNOWLEDGEMENTS

We would like to acknowledge Tharisa Mine for funding this project and giving us permission to publish this work. The authors also thank the NRF (National Research Foundation) and DSI-NRF CIMERA (Centre of Excellence for Integrated Mineral and Energy Resource Analysis) for funding this research project. Special thanks go to the post-graduate students from the School of Geosciences at the University of the Witwatersrand who assisted with the data collection and the Tharisa Mine staff, especially Hloniphani Hlongwa and Robey Labuschagne, for assisting us during the data acquisition. Special thanks to Nathi Mntungwa from Tharisa Mine for scientific discussions and support. The authors would also like to acknowledge the constructive comments from two anonymous reviewers which have greatly improved the readability of this manuscript. Chief Editor, Tijmen Jan Moser, and Associate Editor, Alireza Malehmir, are also greatly appreciated for the editorial handling.

DATA AVAILABILITY STATEMENT

The data were acquired by the Wits seismic research centre team and are available on request from the corresponding author, subject to the approval from the mine owners.

CONFLICT OF INTEREST

The authors declare no conflict of interest.

REFERENCES

Barnes, S.J., and Maier, W.D., (2002) Platinum-group element distribution in the Rustenberg Layered Suite of the Bushveld Complex, South Africa. In The Geology, Geochemistry, Mineralogy and Mineral Beneficiation of Platinum-Group Elements. Edited by L.J. Cabri, Canadian Institute of Mining, Metallurgy and Petroleum, Special Volume 54, p. 431-458.

Binley, A., and Kemna, A., (2005) DC resistivity and induced polarization methods. In: Rubin Y., Hubbard S.S. (eds) Hydrogeophysics, Water Science and Technology Library, 50, 129 – 156. Springer, Dordrecht, 50. https://doi.org/10.1007/1-4020-3102-5_5.

Blanchy, G., Saneiyan, S., Boyd, J., McLachlan, P., and Binley, A., (2020) ResIPy, an intuitive open source software for complex geoelectrical inversion/modeling. Computers & Geosciences 137, p.104423.

Campbell, G., (2006) High resolution aeromagnetic mapping of "loss-of-ground" features at platinum and coal mines in South Africa. South African Journal of Geology 109, 439-458.

Cardarelli, E., Cercato, M., Cerreto, A., and Di Filippo, G., (2010) Electrical resistivity and seismic refraction tomography to detect buried cavities. Geophysical Prospecting, 58, 685-696. https://doi.org/10.1111/j.1365-2478.2009.00854.x.

Carollo, A., Capizzi, P., and Martorana, R., (2020) Joint interpretation of seismic refraction tomography by cluster analysis to detect buried cavities. Journal of Applied Geophysics, 178, 1-21. https://doi.org/10.1016/j.jappgeo.2020.104069.

Cawthorn, R.G., (2015) The Bushveld Complex, South Africa. In: Charlier B, Namur O, Latypov R, Tegner C (eds) Layered intrusions. Springer, Berlin, pp 517–587. https://doi.org/10. 1007/978-94-017-9652-1.

Cawthorn, R.G., and Webb, S.J., (2001) Connectivity between the western and eastern limbs of the Bushveld Complex. Tectonophysics 330, 195-209.

Cooper, G.R.J., and Cowan, D.R., (2008) Edge enhancement of potential-field data using normalized statistics. Geophysics, 73, H1-H4. https://doi.org/10.1190/1.2837309.

Dan, M.F.M., Mohamad., E.T., and Komoo, I., (2016) Characteristics of boulders formed in tropical weathered granite: A review. Jurnal Teknologi, 78, 23-30. https://doi.org/10.11113/jt.v78.9635.

Dunlop, D.J., Özdemir, Ö., and Alvarez, V.C., (2010) Magnetic properties of rocks of the Kapuskasing uplift (Ontario, Canada) and origin of long-wavelength magnetic

anomalies. Geophysical Journal International, 183, 645-658. https://doi.org/10.1111/j.1365-246X.2010.04778.x.

Durgin, P.B., (1977) Landslides and the weathering of granitic rocks. Geological Society of America III, 127 – 131.

Eales, H.V., Botha, W.J., Hattingh, P.J., De Klerk, W.J., Maier, W.D., and Odgers, A.T.R., (1993) The mafic rocks of the Bushveld Complex: a review of emplacement and crystallization history, and mineralization, in light of recent data. Journal of African Earth Sciences 16, 121-142.

Eales, H.V., and Cawthorn, R.G., (1996) The Bushveld Complex. Layered Intrusions, p. 181-229.

Ettinger, S., Manville, V., Kruse, S., and Paris, R., (2014) GPR-derived architecture of a lahar-generated fan at Cotopaxi volcano, Ecuador. Geomorphology, 213, 225-239. https://doi.org/10.1016/j.geomorph.2014.01.013.

Felletti, F., and Beretta, G.P., (2009) Expectation of boulder frequency when tunnelling in glacial till: A statistical approach based on transition probability. Engineering Geology, 108, 43-53. https://doi.org/10.1016/j.enggeo.2009.06.006.

Fletcher, R.C., Buss, H.L., and Brantley, S.L., (2006) A spheroidal weathering model coupling porewater chemistry to soil thicknesses during steady-state denudation. Earth and Planetary Science Letters, 244, 44-457. https://doi.org/10.1016/j.epsl.2006.01.055

Gomez, C., Lavigne, F., Hadmoko, D.S., and Wassmer, P., (2018) Insights into lahar deposition processes in the Curah lengkong (Semeru Volcano, Indonesia) using photogrammetry-based geospatial analysis, near-surface geophysics and CFD modelling. Journal of Volcanology and Geothermal Research, 353, 102-113. https://doi.org/10.1016/j.jvolgeores.2018.01.021.

Harding, K.A., Morris, W.A., Balch, S.J., Lapointe, P., and Latham, A.G., (1988) A comparison of magnetic character and alteration in the three granitic drill cores from Eastern Canada. Canadian Journal of Earth Sciences, 25, 1141-1150.

Hunt, E., Latypov, R., and Horvah P., (2018) The Merensky Cyclic Unit, Bushveld Complex, South Africa: Reality or Myth? Minetals, 8, 1-35.

Jee, W.W., and Ha, S., (2007) Feasible boulder treatment methods for soft ground shielded TBM. Underground Space – the 4th Dimension of Metropolises, 217-22.

Khaidukov, V., Landa, E. and Moser, T.J., (2004) Diffraction imaging by focusing-defocusing, an outlook on seismic superresolution. Geophysics, 69(6), 1478–1490.

Kruger, F.J., (2005) Filling the Bushveld Complex magma chamber: lateral expansion, roof and floor interaction, magmatic unconformities, and the formation of giant chromitite, PGE and Ti-V-magnetitite deposits. Mineralium Deposita, 40, 451-472. https://doi.org/10.1007/s00126-005-0016-8.

Lapointe, P., Morris, W.A., and Harding, K.L., (1986) Interpretation of magnetic susceptibility: A new approach to geophysical evaluation of the degree of rock alteration. Canadian Journal of Earth Sciences, 23, 393-401.

Leng, Z., Fan, Y., Gao, Q., and Hu, Y., (2020) Evaluation and optimization of blasting approaches to reducing oversize boulders and toes in open-pit mine. International Journal of Mining Science and Technology 30, 373-380. https://doi.org/10.1016/j.ijmst.2020.03.010.

Lu, S-G., Xue, Q-F, Zhu, L., and Yu, J-Y., (2008) Mineral magnetic properties of a weathering sequence of soils derived from basalt in Eastern China. Catena, 73, 23-33. https://doi.org/10.1016/j.catena.2007.08.004.

Malehmir, A., Durrheim, R., Bellefleur, G., Urosevic, M., Juhlin, C., White, D.J., Milkereit, B. and Campbell, G., (2012) Seismic methods in mineral exploration and mine planning: A general overview of past and present case histories and a look into the future. Geophysics 77, WC173-WC190, https://doi.org/10.1190/geo2012-0028.1.

Monjezi, M. Bahrami, A., and Varjani, A.Y., (2011) Prediction and controlling of flyrock in blasting operation using artificial neural network. Arabian Journal of Geosciences 4, 421-425. https://doi.org/10.1007/s12517-009-0091-8.

Moser, T.J. and Howard, C.B., (2008). Diffraction imaging in depth. Geophysical Prospecting, 56, 627–641.

Musil, M., Maurer, H., Green, A.G., Horstmeyer, H., Nitsche, F.O., Muhll, D.V., and Springman, S., (2002) Shallow seismic surveying of an Alpine rock glacier. Geophysics, 67, 1701-1710. https://doi.org/10.1190/1.1527071.

Onyebueke, E. O., Manzi, M. S. D., and Durrheim, R. J., (2018) High-resolution shallow reflection seismic integrated with other geophysical methods for hydrogeological prospecting in the Nylsvley Nature Reserve, South Africa. Journal of Geophysics and Engineering 15, 2658-2673. https://doi.org/10.1088/1742-2140/aadbe3.

Park, J., and Kim, K., (2020) Use of drilling performance to improve rock-breakage efficiencies: A part of mine-to-mill optimization studies in a hard-rock mine.

International Journal of Mining Science and technology 30, 179-188. https://doi.org/10.1016/j.ijmst.2020.03.010.

Perritt, S., and Roberts, M., (2007) Flexural-slip structures in the Bushveld Complex, South Africa? Journal of Structural Geology 29, 1422-1429. https://doi.org/10.1016/j.jsg.2007.06.008.

Raina, A.K., Murthy, V.M.S.R., and Soni, A.K., (2015) Flyrock in surface mine blasting: understanding the basics to develop a predictive regime. Current Science 108, 660-665.

Reid, D.L., and Basson, I.J., (2002) Iron-rich ultramafic pegmatite replacement bodies within the Upper Critical Zone, Rustenburg Layered Suite, Northam Platinum Mine, South Africa. Mineralogical Magazine 66, 895-914. https://doi.org/10.1180/0026461026660066.

Roberts, M.K.C., and Clark-Mostert, V., (2010) Is there some commonality between the geological structures in the Bushveld Complex and the Great Dyke?. The 4th International Platinum Conference, Platinum in transition 'Boom or Bust', The Southern African Institute of Mining and Metallurgy.

Santana, G.P., Fabris, J.D., Goulart, A.T., and Santana, D.P., (2001) Magnetite and its transformation to hermatite in a soil derived from steatite. Revista Brasileira de Ciêncía do Solo, 25, 33-42.

Schoor, M.V., and Fourie, C.J.S., (2015) A guide for APPLYING GEOPHYSICS to COAL MINING PROBLEMS in South Africa. Struik Nature, South Africa.

Scoates, J.S., Wall, C.J, Friedman R.M., Weis, D., Mathez, E.A., and VanTongeren, J.A., (2021) Dating the Bushveld Complex: timing of crystallization, duration of magmatism, and cooling of the World's largest layered intrusions and related rocks. J Petrol 62:egaa107. https://doi.org/10.1093/petrology/egaa107.

Scoon, R.N., and Mitchell, A.A., (1994) Discordant iron-rich ultramafic pegmatites in the Bushveld Complex and their relationship to iron-rich intercumulus and residual liquids. Journal of Petrology, 35, 881-917.

Shao, J., Zhang, Q., Wu, X., Lei, Y., Wu, X., and Wang, Z., (2020) Investigation on the water flow evolution in filled fracture under seepage-induced erosion. Water 2020, 12, 3188. https://doi.org/10.3390/w12113188.

Sherrod, L., Schlosser, K., Kozlowski, A., Bird, B., Werkema Jr, D.D., and Swiontek, J., (2014) Geophysical Characterization of the Keene Valley Landslide in New York State.

Journal of Environmental and Engineering Geophysics, 19, 139-155. https://doi.org/10.2113/JEEG19.3.139.

Soumya, G.S., Asanulla, R.M., and Radhakrishna, T., (2017). Rockmagnetism in relation to magnetic mineralogy of anorthosites in the southern granulite region of the Indian shield. Geophysical Journal International, 209, 1768-1778. https://doi.org/10.1093/gji/ggx134.

Taylor, C.D., Schulz, K.J., Doebrich, J.L., Orris, G.J., Denning, P.D., and Kirschbaum, M.J. (2009) Geology and nonfuel mineral deposit of Africa and the Middle East. U.S. Geological Survey Open-file Report 2005-1294-E, 1-246.

Twidale, C.R., and Romani, J.R.V., (2005) Landforms and geology of granite terrains. Taylor and Francis Group, London, United Kingdom.

Jinghong, W., Caineng, Z., and Rukai, Z., (2011) Characteristics and controlling factors of fractures in igneous rock reservoirs. Petroleum Exploration and Development 38, 708-715.

Udden, J.A., (1914) Mechanical composition of clastic sediments. Bulletin of the Geological Society of America 55, 655-744.

Wilson, A.H., Jermy, C.A., and Ridgeway, M., (2005) Rock strength and physical properties of Norites of the Merensky and Bastard Units, western Bushveld Complex. Geological Society of South Africa 108, 525-540.

van School, M., (2002) Detection of sinkholes using 2D electrical resistivity imaging. Journal of Applied Geophysics 50, 393-399.

Van School, M., and Fourie, C.J.S., (2015) A guide for APPLYING GEOPHYSICS to COAL MINING PROBLEMS in South Africa. Struik Nature, South Africa.

Vitale, S., and Isaia, R., (2014) Fractures and faults in volcanic rocks (Campi Flegrei, southern Italy): insight into volcano-tectonic processes. International Journal of Earth Science, 103, 801-819. https://doi.org/10.1007/s00531-013-0979-0.

von Dobeneck, T., Müller, M., Bosbach, B., and Klügel, A., (2021) Ground Magnetic Susceptibility and mapping across weathered basalt dikes reveal soil creep and pedoturbation. Frontiers in Earth Science, 8, 1-8. https://doi.org/10.3389/feart.2020.592986.

Yang, X., Zeng, X., Pu, C., and Xiao, D., (2018). Effects of the pre-existing fissures with different fillings in PMMA on blast-induced crack propagation. Advances in Materials Science and Engineering, 17, 1-17. https://doi.org/10.1155/2018/7378282.

Zhihui, W., Xiangmin, C., Jiayong, Y., Jiming, W., Yu, L., and Lei, Z., (2018) Using the integrated geophysical methods detecting active faults: a case study in Beijing, China. Journal of Applied Geophysics, 156, 82-91. https://doi.org/10.1016/j.jappgeo.2017.01.030.

10. Paper IV: Multi-geophysical methods for characterizing fractures in an open pit mine, western Bushveld Complex, South Africa

Moyagabo K. Rapetsoa[1*], Sikelela Gomo[1], Musa S. D. Manzi[1], Ian James[2], Jureya Dildar[1], Mpofana Sihoyiya[1], **Ndamulelo Mutshafa[1]**, Raymond J. Durrheim[1]

[1]School of Geosciences, University of the Witwatersrand, Johannesburg, Private Bag, Wits, 2050, Republic of South Africa

[2]Southern Geoscience Consultants, West Perth, WA, Australia

Acknowledgements

We thank Tharisa mine for providing access to the site to conduct the geophysical surveys and granting permission to publish the work. The authors also thank Wits Seismic Research Center for funding this work. We thank several PhD and MSc students from the University of the Witwatersrand, Johannesburg who took part in the data acquisition stage. We also thank Engineering and Exploration Geophysical Services CC for supporting us with the geophysical equipment, and Schlumberger for the continued support with the licences for Petrel. HiSeis Pty Ltd. and Petrosys are highly appreciated for sponsoring the licenses for Globe Claritas processing software.

Conflict of interest

The authors declare that they have no known competing financial interests or personal relationships that could influence the work reported in this paper.

ABSTRACT

In the Bushveld Complex (BC), South Africa, open pit mines are faced with a challenge of rock slope stability due to geological structures (fractures, faults and dykes) that compartmentalise the rock mass. Geophysical surveys (seismics, magnetics and electrical

methods) were conducted in a 0.2 km^2 area at Tharisa mine, with the goal to delineate fractures that may be potential conduits for water migration into the pit. Special processing techniques were applied to the dataset to obtain good quality seismic, magnetic and resistivity models. The P-wave velocity models show distinct low velocities in the center of the seismic profile, indicating the presence of weak zones associated with faulting or fracturing. Seismic reflection method was used to image the deeper discontinuities and mineralization contacts. Near surface reflections are observed throughout the profiles and are correlated with the contact between the chromitite and host rock. Ground magnetic surveys were conducted to delineate dykes and fractures. De-trending and de-culturing techniques were applied on the magnetic data for correcting regional and temporal variations. The low magnetic regions indicate the presence of fracture systems in the subsurface, while the high magnetic region is correlated with the dolerite dyke that crosscuts the pit. The electrical resistivity tomography exhibits linear low resistivity contrast zones that differentiates between the fractured and undisturbed hard rock at an estimated depth of 4 – 10 m. Resistivity shows discontinuities that suggests the presence of fracturing and dyke-host rock contacts. Correlation between magnetics, P-wave velocity models, resistivity section and seismic data is evident when overlaying the different datasets, implying that the low magnetic regions are highly weathered and prone to fracturing. The integration of geophysical data is encouraging, because it was able to image the depth to the bedrock, fractures within the host rock and dyke in a complex mining environment.

Keywords: Fractures, Water migration, Open-pit mine, Groundwater, Imaging

Data availability statement

The data presented in this study are available upon request from the corresponding authors. The data are not publicly available due to privacy restrictions. Petro-physical data can be found on the website of The Council of Geoscience South Africa

(https://maps.geoscience.org.za/portal/apps/sites/#/council-for-geoscience-interactive-web-map-1).

INTRODUCTION

Tharisa mine is an open pit (Figure 1a) mine located in the North-west province of South Africa, 35 km east of Rustenburg. The mine is located in a hard rock environment within the Bushveld Complex (BC). The BC exhibits joints of tectonic origin, with varying orientation (planar and non-planar) and intensity across the BC. Joints are often coupled with other geological structures such as dykes, veins and faults (Figure 1b). Systematic joints (planar) are a set of parallel joints spaced evenly apart (Perritt and Roberts, 2007; Roberts and Clark-Mostert, 2010). Majority of the joints in the study area are sub-vertical and can be divided into two sets (Figure 1c), parallel sets (cyan, green and blue) and perpendicular sets (pink, yellow, and red) to a fault zones that cross cut the pit and parallel to a dyke (Figure 1b). Non-systematic joints occur randomly in the study area due to mine blast stress regime. The sub-vertical joints intersect the sub-horizontal interlayering planes of the Middle Group chromitites.

Most open pit mines are faced with a challenge of rock slope stability due to geological structures that cause discontinuities of the rock mass. The fractures introduce mining, engineering and hydrogeological challenges. The development of the mine promotes the increase in fractures through blasting and excavation of the bedrock. Fractures may act as conduits for migration of groundwater (e.g. water from rivers, and aquifers) into the pit, which floods the pit and causes delays in production (Titus et al., 2009; Ofterdinger et al., 2019).

Near-surface geophysical methods have grown widely in addressing mining, engineering and environmental problems, e.g., mineral exploration, detection of buried pipes, sinkholes, and fracture mapping. (Dahlin, 1996; Van Schoor, 2002; Amoush and Mashagbeh, 2009; Kerrigan, 2013; Pazzi et al., 2018). The need to delineate the fractures and understand the migration of

water into the mine pit has led to the development of multi-geophysical and hydrological acquisition setups for gathering data in the noisy mine environments. The main objectives of this study are: (1) to use geophysical methods to locate and characterize fractures in an open pit mine, (2) to understand the ground water migration into the pit and associate it with the geological structures around the pit, (3) To delineate the depth of the mineralization and its associated geological structures beyond the mined out areas, (4) to address challenges encountered in geological complex and mine noisy environment when acquiring geophysical data.

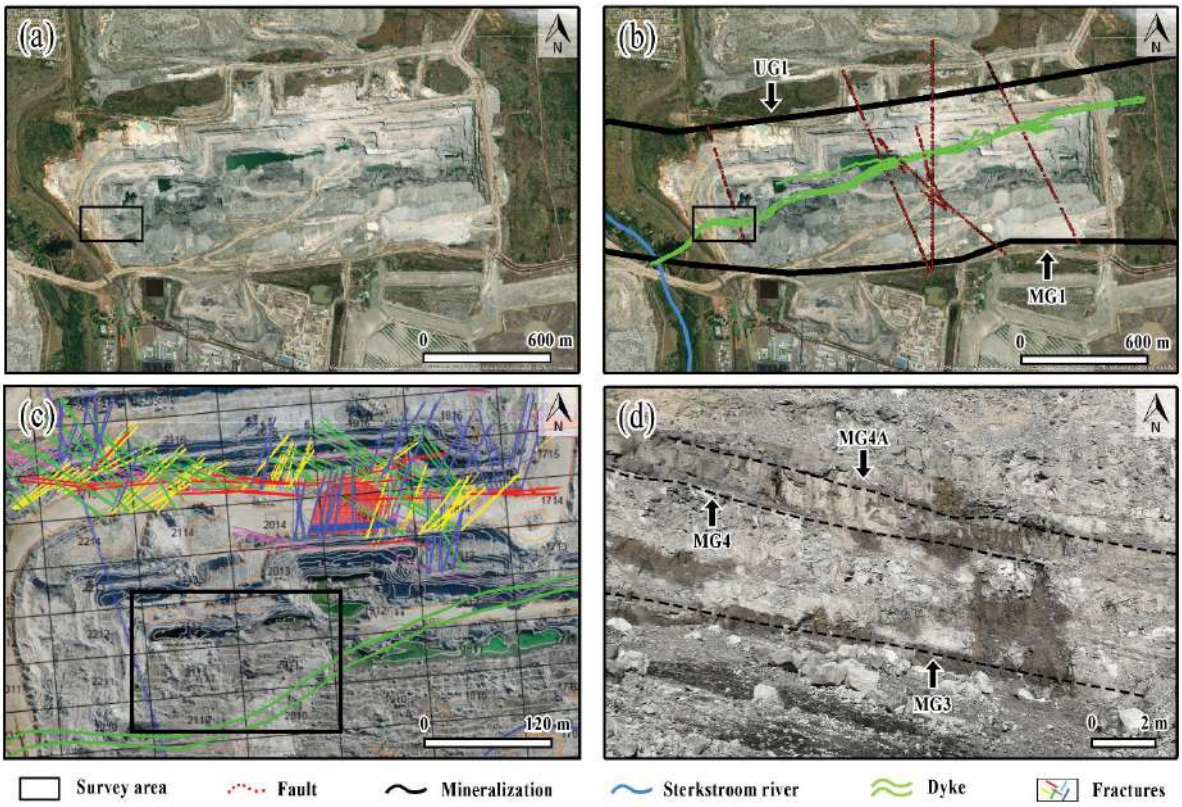


***Figure 1**: (a) Aerial photo of Tharisa mine east pit. (b) Major dyke (green) and faults (red) cross-cutting the west pit at Tharisa mine. Sterkstroom River (blue) divides the mine into a west pit and an east pit. The mineralization (black: UG1 and MG1) runs parallel to the ends of the east pit (c) Mapped fractures (red, blue, green, pink, yellow, and cyan) at the Tharisa*

mine with varying orientations. (d) Sidewall, showing inter-bedding and cross-cutting joints. Dark areas are areas where water is seeping into the pit.

The use of multi-geophysical methods (seismics refraction (SRT) and reflection, magnetics and electrical resistivity tomography (ERT)) to image structures depends on multiple factors such as the survey design (receiver and source positions), physical properties of the host rock, geometry (e.g. size and depth), structural characteristics of the target, and the mine noise levels. In this study we also demonstrate the challenges faced by the geophysical methods (i.e. magnetics, SRT and ERT) to characterize near-surface fractures and mineralization in a mining area with large infrastructure, trucks and electrical powerlines that cause interfering noise during acquisition. This study forms part two of the three part integrated geophysical, hydrogeology and geochemical studies to further unravel and determine the source of water that migrates into the pit. Gomo et al., (2023), presents an integrated geophysical approach to delineate boulders in an active open pit mine as part I. Part III of the study (Dildar et al., 2022) focused on integration of the hydrogeology and geochemical data with near surface geophysical methods.

GEOLOGICAL SETTING AND THARISA MINE

The Bushveld Complex (BC) covers an area of about 65 000 km^2 (Figure 2), typified by a shape of a broad oval, with a long extension of 375 km east-west and 300 km wide to the north-south. The BC is the largest mafic-ultramafic layered igneous intrusion, divided into five limbs that are emplaced on the Transvaal Supergroup at 2058.9 ± 0.8 Ma, with a thickness of 9 km. The geology and stratigraphy of the Bushveld complex (Figure 2a,b) is well documented by several authors (e.g., Eales and Cawthorn, 1996; Kinnaird, 2005; Wilson, 2005; Cawthorn, 2015; Basson, 2019).

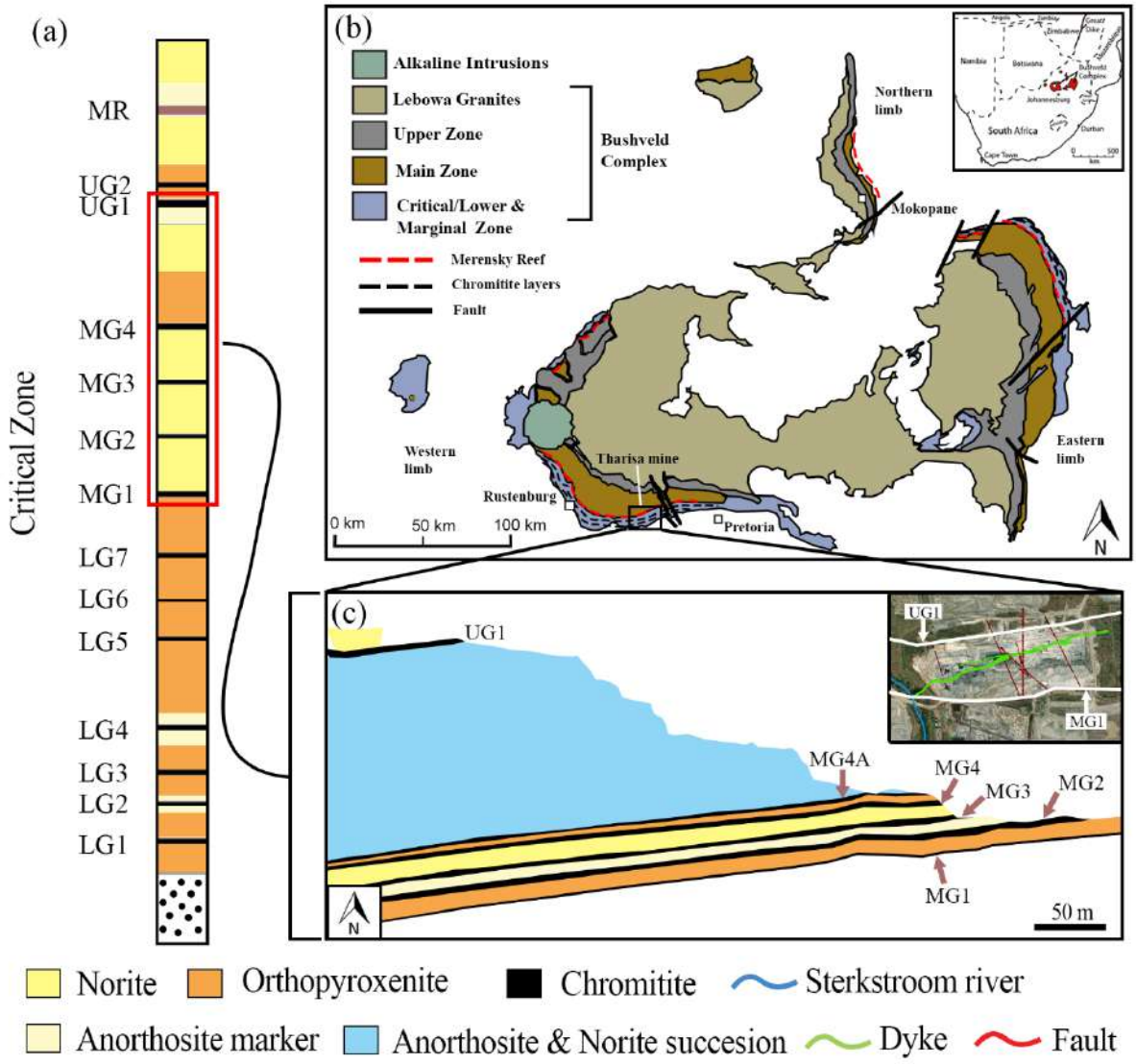


Figure 2: *(a) Stratigraphic column of the critical zone, highlighting the chromitite layers that are exploited at the Tharisa mine. (b) General geological map of the Bushveld complex showing major faults, economical horizons, and the location of the study area. (c) Simplified geology of the Tharisa mine, with an insert showing the location of the far end mineralizations (white: MG1 and UG1) that are being exploited at the mine, together with geological structures and a river that crosscut the east pit.*

The mineralization at Tharisa mine is situated in the critical zone (CZ) of the Bushveld complex. The mine is split into two pits (east pit and west pit) by the Sterkstroom River (Figure

1b) and exploits the Middle Group (MG) chromitites (Figure 2c: MG4, MG3, MG2 and MG1). With the UG1 being 165 to 18 m above the MG. Mining of UG1 happened in the past, with the shallow MG1 being mined underground. The mine plans on having underground operations in the future to exploit the deeper MG2 and MG4 mineralizations. The CZ is made up of pyroxenites, anorthosites, norites and stringers of chromitite. The general dip of the mineralization is between 9° and 15° to the north, with the thickness of the MGs and UG1 ranging from few centimetres to 3 m. The geological structures of the Tharisa mine region have been interpreted using aeromagnetic, drilling data and open pit observations (Lotheringen et al., 2016). An approximately 15 m thick, NE-SW trending and near-vertical dyke that crosscuts the west pit is the most dominant feature mapped by the aeromagnetic data (Figure 1b). Multiple faults are mapped within the pit and crosscut the pit with a predominant strike of NNW-SSE, which coincides with the planes of weaknesses that reactivated during the emplacement of the Bushveld Complex. The fractures in the Bushveld Complex are known to be associated with dykes and faults (Bumby et al., 2012; Hartzenberg and Plessis, 2014). The fracturing is observed on the northern part of the pit and our study focuses on characterizing the fractures on the southern part of the pit.

GEOPHYSICAL DATA

In this section we summarize the physical properties, acquisition and processing of the seismic, magnetics and resistivity data that were collected Tharisa mine.

Data acquisition

Prior to data acquisition, appropriate acquisition parameters need to be assessed, together with the expected response of the target through forward modelling. Forward modelling can also assist in validating the interpretation of the dataset and provide information for mineral

exploration and risk assessment (Malehmir et al., 2013; Manzi et al., 2017; Maries et al., 2020; Rapetsoa et al., 2022).

Physical properties

To complement the geophysical data, rock samples and borehole data were collected from the Tharisa mine. To the best of our knowledge the borehole data only include the geological logging. There is no downhole petro-physical data available for the study site. To complement the borehole data, we have gathered more petro-physical data from the Council of Geosciences database and measurements from Sepato (2015). The data used from the above mentioned database were filtered to boreholes that are closer to Tharisa mine. The laboratory measurements in this study were P-wave velocity, bulk density and magnetic susceptibility measurements, while resistivity measurements where sourced from the literature (Maré, 2022). The samples were norites, anorthosites, chromitite and pyroxenites, and the resistivity measurements for pyroxenite were not found in the literature. The collected samples were prepared for bulk density, P-wave velocity and magnetic susceptibility measurements at room temperature and pressure using ultrasonic frequencies. The ideal conditions to measure the samples is under elevated stress (~ 20-60 MPa) to mimic the in-situ environments, but due to a lack of equipment in our laboratory, the measurements were not done at elevated temperature and stress. A high frequency signal is produced by the transducers and passes through the rock sample. The signal is observed through the oscilloscope and the waveform is recorded by the computer. P-wave velocities are estimated from the measured travel times of the high frequency acoustic pulses through the samples. Bulk densities were collected using the immersion techniques, were sampled were suspended in pure water and the density of the sample was estimated by the use of Archimedes principle.

Seismics

The seismic data for this study were collected in October 2021. Two seismic profiles were collected with a total length of 150 m: one of the seismic profiles (SP1 96 m long) was inside the pit, while SP2 (46 m) was collected at the edge of the pit. As the study area is inside the pit, where certain areas are hard rock, a combination of different geophone setup was used.

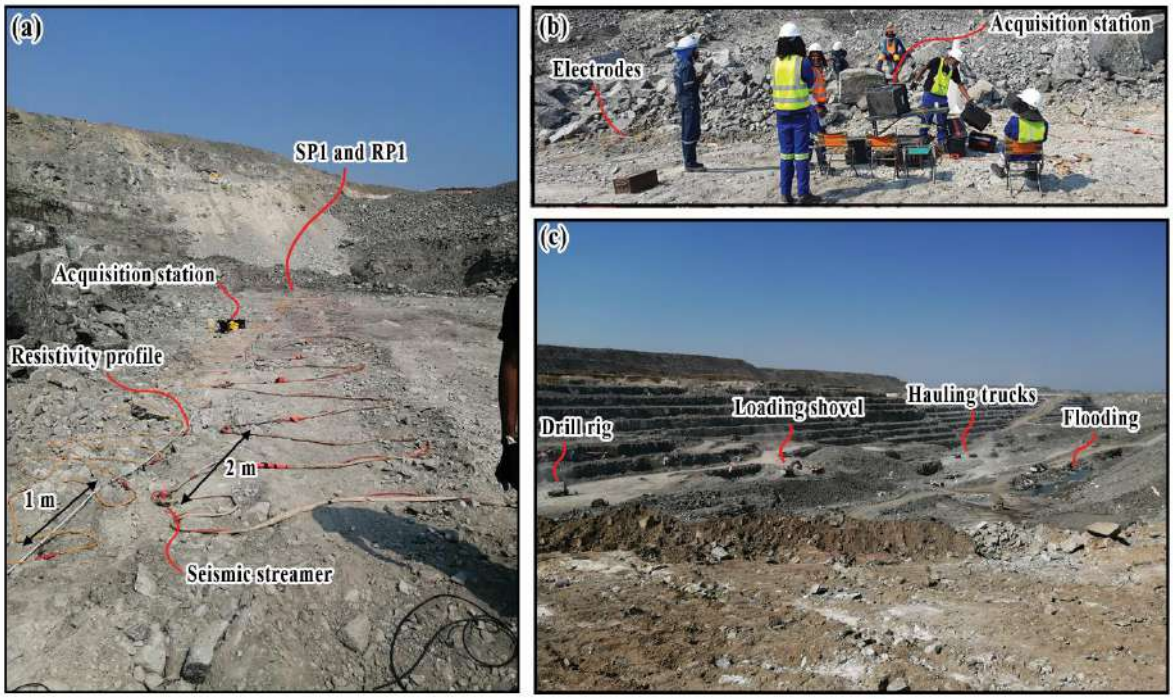


Figure 3: *(a and b) Field photo showing the acquisition setup for seismic and resistivity profiles inside the pit using a seismic land streamer. (c) Field conditions during data acquisition at Tharisa mine, with mining activity near seismic profile.*

A land streamer (4.5 Hz) and spiked geophones (14 Hz) were used along SP1 (Figure 3a and b), with a receiver spacing of 2 m. For SP2, 14 Hz 1C spiked geophones were used, with a receiver spacing of 1 m (Table 1). The seismic profiles (Figure 4a) were setup to be perpendicular to the faults and fractures systems observed on the aeromagnetic data in and around the pit, with the main dyke being parallel to the lines (Figure 4a). For safety reasons, source and receiver positions were limited by the active mine roads, therefore the length of some of the seismic profiles were shorter than desired. Although multiple profiles were

collected (named SP1-SP8), this study focuses on the data obtained from SP1 and SP2 due to their location and essential for studying the fracture system of the east pit.

***Table 1**: Main reflection seismic data acquisition parameters*

Profiles	SP1	SP2
Survey parameters		
Acquisition type	Fixed straight line	Fixed straight line
Acquisition system	Geometric Geode	Geometric Geode
Reciever frequency	4.5 Hz and 14 Hz	14 Hz
Type of base	land streamer and 7 cm spike	7 cm spike
No. of recievers	48	48
Reciever spacing	2	1 m
Source	6.3 kg sledgehammer	6.3 kg sledgehammer
Source spacing	2 m	1 m
Profile length	96 m	50 m
Recording length	1000 ms	500 ms
Sampling interval	1 ms	0.25 ms

Prior to collecting the data, we first performed a test to compare the seismic sources (6.3 kg sledgehammer and a 24 kg accelerated weight drop (AWD)). From the test, it was evident that the sledgehammer was suitable for this study, as it preserved the near-offset traces, while the AWD over drives the near-offset geophones by having powerful source impulse. The sledgehammer was also chosen for its applicability in uneven terrains. Noise conditions were different from profile to profile. When acquiring the data in the open pit, there was drilling, dump trucks and loader (Figure 3c) working near the profile. We did not have permission to acquire seismic data during night time, therefore all our seismic profiles were collected during working hours (08:00 and 17:00) where the mining activity and traffic from the main road were high. The receiver and shot positions (eastings, northings and elevation) were surveyed using

a real time Differential Global Positioning System (DGPS) device. The shots were recorded at every 2 m for SP1 and 1 m for SP2, four shot records were acquired at every shot position using the sledge hammer and vertically stacked to increase the signal-to-noise ratio (SNR). We analysed and tested different sampling rates, with SP2 being recorded first with a sampling rate of 0.25 ms, while SP1 was recorded with a sampling rate of 1 ms. A sampling rate of 1 ms was chosen for the rest of the seismic profiles, as it provided better results with respect to the high frequencies and spurious frequncies. A total of 96 shots and 4608 traces were generated after vertically stacking the repeated shots.

Magnetics

A three phased five-day field survey in 2021 was conducted to collect total magnetic field data at Tharisa mine. The survey started with an assessment of the pit to locate mine benches that have seepage of water and a dyke, which are a guide to the location of fractures (Figure 1d). The magnetic survey covered a total area of 16300 m^2 using two G856 proton precession magnetometers and a G859 cesium vapour magnetometer. The G856 magnetometers were used as base stations and placed at two different locations (with no cultural noise), mounted on a 2.5 m vertical aluminium pole. The magnetometers (G856) were set to record stationary readings at every 30 seconds interval, the data was then inspected and compared for spikes in the diurnal curve. The G895 magnetometer was used as a rover for acquisition of the magnetic profiles. The GPS antenna was vertically mounted ~ 3 m and the magnetic sensor was mounted ~ 2 m. The three grids (Figure 4b) were surveyed in a fast “walking mode”, with the rover magnetometer (G859) carried on a non-magnetic backpack along the profiles. The operator was walking at an approximate speed of 1 m/s on open land, with a sampling rate of 1 s. While certain sections in the pit required a reduction of speed due to deep excavations. The walking mode GPS positioning error is ±1 m. A section of the dyke (Figure 4b: MS1) was surveyed in

great detail with nine parallel N-E ground magnetic lines of 70 m in length, with a line spacing of 10 m. Grid 2 and 3 had magnetic lines of over an area of 20 - 70 m x 10 – 70 m and 40 x 70 m. Regional aeromagnetic data (Figure 4c) were used to identify major structures such as dykes and faults. The dyke crosses the pit (Figure 1b) and covers a full length of 2.91 km and have thickness between 10-15 m.

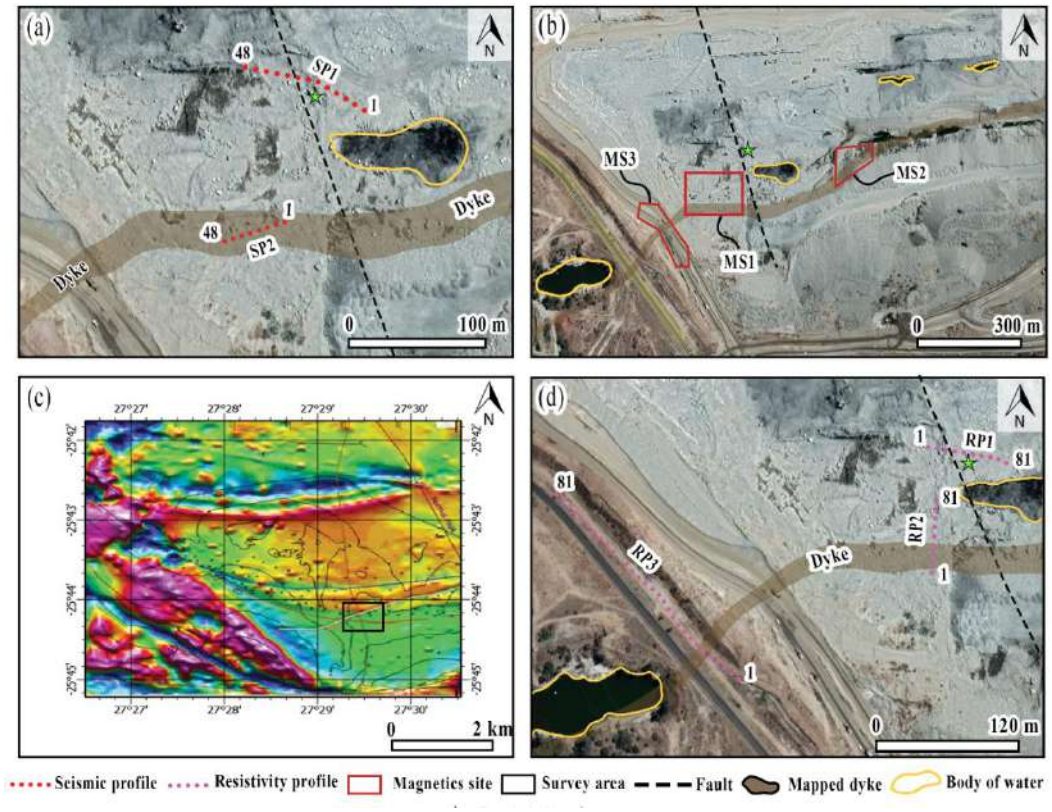


Figure 4: *Aerial photos showing the location of two major geological structures (fault and dyke) and (a) seismic profiles (two seismic profiles inside the pit, with a combination of different sensors), (b) magnetic grids (over the geological structures), (c) Regional aeromagnetic data over the edge of the western Bushveld complex, showing major geological structures and site location and, (d) resistivity profiles. SP: Seismic profile; RP: Resistivity profile, MS: Magnetic site.*

Resistivity

The electrical resistivity surveys were conducted in two phases. The first phase was for testing the method for imaging and characterizing the chromitite orebody prior to drilling. The second phase was the application of resistivity to locate geological structures (faults, fractures and dykes) that may act as conduit for water migration into the pit.

The first phase involved one profile (Figure 4d: RP1) that was located in the pit over known mineralization, with a strike of E-W. The profile was surveyed using the ABEM Terrameter SAS 1200, with 41 fixed electrodes that are spaced 2 m apart in a schlumberger, wenner and dipole-dipole array (Reynolds, 2011). All the electrodes (Figure 3a and b) were hammered at least 20 cm into the ground to ensure good coupling. The input current was set to 10 mA and the contact resistance was of the order 200-3000 Ω. The system automatically reports any anomalous contact resistance (negative resistivity readings) and a solution to this was re-planting the electrode or watering the electrode point. The second phase comprised of two resistivity profiles (Figure 4d) with length of 80 m for RP2 and 240 m for RP3. The first profile (RP2), striking S-N, was conducted at the edge of the pit with the aim of imaging the structures that cause seepage (Figure 1d) into the pit. The survey was conducted over an area with fractured rock and a little topographic variation (<1 m). Forty-one fixed electrodes were used for each of the two profiles, with a spacing of 2 m for RP2 and 6 m for RP3. RP2 was perpendicular to the strike of the mineralization and the length was limited by trenches. RP3, on the other hand, had a strike of SE-NW and was designed to delineate water conduits that might be transporting water from the river to the west of the pit. The profile was acquired over an area covered with loose sandy soil, located parallel to the road in the west of the east pit (Figure 4d).

Data processing

Seismics imaging

The collected seismic profiles were designed to cover the east pit of Tharisa mine, particularly the edge of the pit, where the mapped fractures (Figure 1c) are dominant and there is evidence of water flow on the benches (Figure 1d). The profiles were collected on clear tracks and inside the pit for effective shot positions. This resulted in the introduction of noise due to the proximity of the roads and mine workings. Figure 5 shows raw shot gathers and processed shot gathers. The raw shot gathers (Figure 5a and b) were noisy on the far offsets due to, for example, vibrations generated by drilling (Figure 5a: marked with green arrow) and some shots exhibit events that come in later that are due to secondary sources (e.g., dump trucks and loaders). However majority of the shots have good SNR (e.g., SP2) and show strong shallow P-wave reflections. Processing of the seismic data involved the suppression of the noise to further enhance the P-wave reflections that are caused by lithological boundaries. Reflections are observed in the shallow subsurface between 0 and 100 ms (Figure 5c and d). Data processing flow (Figure 6) started with fixing and adding the geometry for all the seismic profiles, and assigning the common depth points (CDP) spacing of 1 m for SP1 and 0.5 for SP2. Approximately 2358 first breaks were carefully picked (manual) on each profile for refraction statics and to generate a two layered P-wave velocity model. The refraction statics improved the continuity of the first arrivals and enhanced the reflections. A constant replacement velocity of 5000 m/s was chosen together with a matching datum of 1109 m, and 1142 m for SP1, and SP2, respectively. Spectral analysis of the seismic profiles show that the data have frequency range of 0-500 Hz for SP1, while SP2 has a frequency range of 0-2000 Hz due to the sampling rate during acquisition. The source energy frequency of the seismic data was in the range of 35 - 125 Hz, therefore we applied band pass filter of 30-45-180-200 Hz.

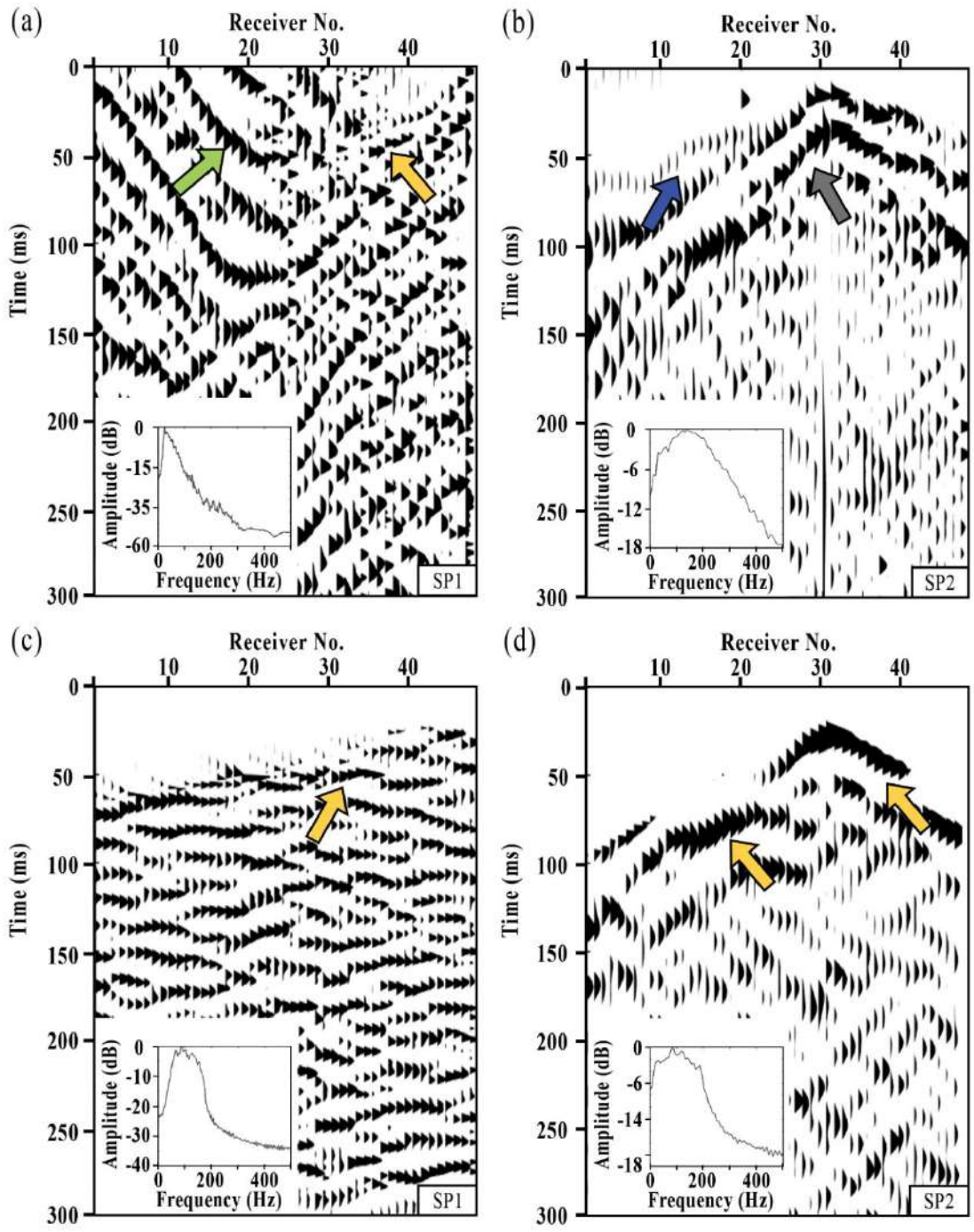


Figure 5: *(a and b) An example of a raw shot gathers from the two seismic profiles (SP1 and SP2), showing the quality of the data inside the open pit, with clear first breaks (blue arrow) on SP2. The green arrow shows noise generated by mine workings. Inserts show amplitude spectra; (c and d) processed shot gathers. The yellow arrows show some reflections recorded in the shot gather, while the grey arrow indicates the surface and guided waves.*

The filter was designed to attenuate the high frequency noise (>300 Hz) introduced during acquisition and also to reduce the low-frequency noise from the ground roll and random noise generated by mine workings. We applied f-k filter on the data to remove the steeply dipping air waves and guided waves. The effect of f-k filter is clearly demonstrated on SP2 by attenuating the steeply dipping secondary source energy (Figure 5b). A gapped deconvolution with a gap length of 6 ms was applied to broaden the frequency spectrum and reduce source signal. The pre-stack processing flow enhanced the subsurface reflections as shown in Figure 5c and d. Prior to normal moveout (NMO) corrections (60% stretch mute), we applied first break mutes to kill the high amplitude first breaks, such that they do not affect the final stack section and enhance near surface reflections. A series of constant velocities were tested ranging from 1500 to 5000 m/s with 250 m/s intervals. Through visual inspection, an estimate NMO velocity of 3000 m/s was used for SP1 and 2500 m/s for SP2 for stacking. Post-stack filtering involved fx-deconvolution, spectral weighting and semblance to enhance the continuity of the reflections and improve the final image. We compared the phase shift and kirchoff migration methods, and the kirchhoff migration with constant velocity of 3000 m/s produced the best image. The seismic data were depth converted using 3000 m/s for final interpretation.

2D Travel time tomography

The target fractures within the subsurface can be imaged using seismic tomography. First break picking was conducted with an average of 2358 picks on each profile. A quality check was conducted and bad quality picks were removed prior to the inversion. Following picking of the data, an initial model was created. A non-linear, first-arrival travel time tomographic inversion with Tikhonov regularisation (Zhang and Toksöz, 1998) was run until convergence was achieved. This processes the ray trace synthetic travel times for each shot such that the difference between the input and synthetic first break picks are minimised. Initial analysis of

the model was conducted, checking the model misfit on a shot-by-shot and receiver-by-receiver basis. Where a significant misfit was present, the first break picks were checked for consistency. Subsequently the data quality was checked, and, provided there was an acceptable convergence, the tomograms were exported and integrated in the interpretation (James et al., 2019).

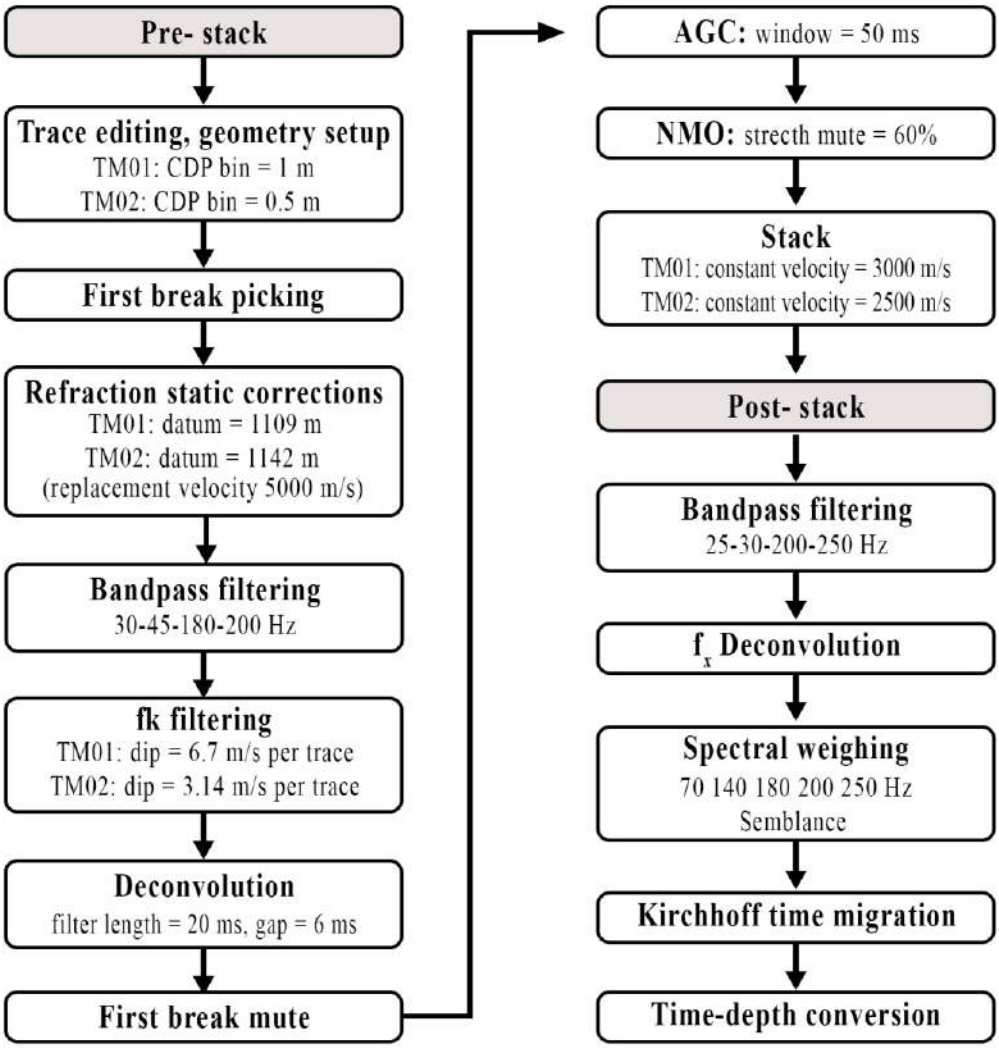


Figure 6: *Processing flow for the reflection seismic datasets of SP1 and SP2, at Tharisa mine.*

The final models for SP1 and SP2 had RMS of about 4 ms and 2 ms after 5 and 10 iterations, respectively. The quality of picks was reasonable considering the noisy environment. The velocities ranging from 500 m/s (loose rocks) to 6500 m/s (bedrock) were considered

reasonable for the final model of the two profiles. Refracted arrivals are noticeable in both SP1 and SP2 when inspecting the first arrival vs offset (Figure 7a and b) used for the tomography. Travel time residuals are shown in Figure 7c and d as a function of offset for both profiles. As a result of the near surface velocity region and maximum offsets between 50 – 100 m, a maximum ray penetration of 16-24 m is observed in the velocity models.

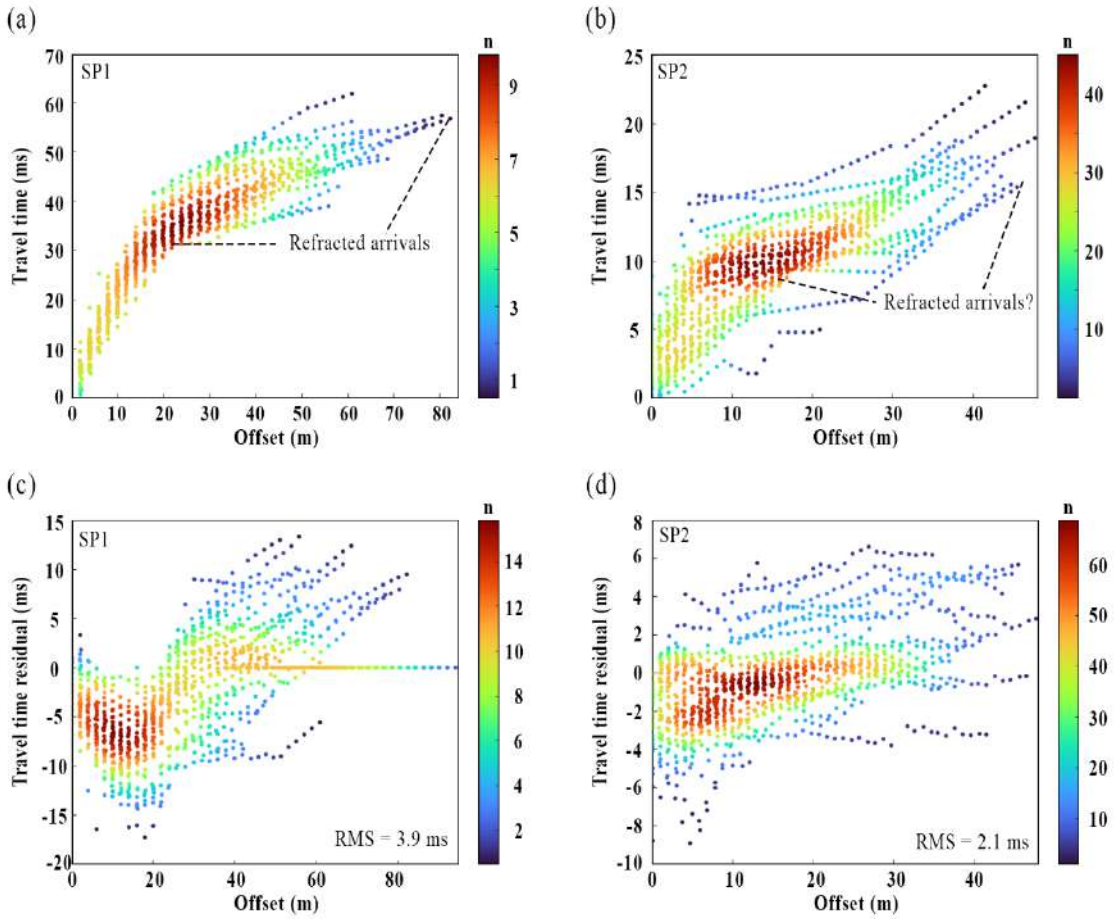


Figure 7: *Quality check of the first breaks and the inverted tomographic models. (a and b) Example of the first break picks for travel time tomogram as a function of offset for SP1 and SP2 respectively. (c and d) Travel time residuals as a function of offset for the same lines after the last iteration of the tomogram, with an RMS value of 3.9 ms and 2.1 ms obtained for the profiles. n: number of points within a range.*

Magnetics

The magnetic data were dumped and corrected for diurnal (temporal) variations. The processing of the data involved the removal of the regional magnetic field (de-trending), manual de-culturing of the original data and interpolating the removed (bad) data points using the minimum curvature technique, which is a favourable gridding technique for gridding potential field data due to its smooth surface approximations (Nabighian et al., 2005; Guo et al., 2012). The Reduction to pole techniques was then applied to reduce the effects of deep magnetization and correct for the positions of the magnetic sources responsible for the observed magnetic signatures. The vertical tilt angle was then applied to enhance the edges of both the shallow and deeper magnetic sources in the data, which in turn enhances the lineaments in the data (Miller and Singh, 1994).

Resistivity

The first step in processing the electrical resistivity data was to edit (eliminate) bad points caused by current deficit at large offsets or bad contact with the ground. The tomographic inversion was carried out using ResiPy with a regularized (weighted least square function) inversion with linear filtering. Prior to the inversion, a triangular finite element mesh was constructed to account for any complex model geometry (Binley and Kemna, 2005; Blanchy et al., 2020). The maximum length, electrodes and data points for the resistivity data was 400 m, 123 and 2110 respectively, therefore the overall calculation time was 114.24 seconds for all the profiles and arrays. The forward modelled apparent resistivity was calculated until the RMS error between the apparent resistivity and modelled resistivity are below 1.5. Table 2 shows the data acquisition and processing parameters. The topographic effect was not taken into account because the elevation difference was less than 1 m along the profiles.

Table 2: *Resistivity acquisition and processing parameters*

Profiles	**RP1**	**RP2**	**RP3**
Acquisition			
Array type	Schlumberger, Dipole-Dipole, Wenner array		
Acquisition system	ABEM Terrameter SAS 1000		
No. of electrodes	41	41	81
Electrode spacing	2 m	2 m	6 m
Strike	E-W		
Profile length	80 m	80 m	240 m
Inversion			
Inversion method	Weighted least square function		
Iterations	Schlumberger: 4 Dipole-Dipole: 7	Schlumberger: 3 Dipole-Dipole: 3	Schlumberger: 2 Dipole-Dipole: 1
RMS	Schlumberger: 0.92 Dipole-Dipole: 1.07	Schlumberger: 0.97 Dipole-Dipole: 1.25	Schlumberger: 1.2 Dipole-Dipole: 1.03

Results

The P-wave velocity, density, resistivity and magnetic susceptibility measurements showed a narrow range of values within the same samples, with a larger variation observed on P-wave velocities compared to density, resistivity and magnetic susceptibility. Physical properties measurements show that anorthosites (5087.5 m/s) have the lowest P-wave velocities and norites (5670 m/s) have intermediate values, while pyroxenites (5950 m/s) and chromitites (6117.5 m/s) have the highest velocities. We paid more attention to the contrast over the actual velocities and density, as the aim of the physical property measurements was to test if we can seismically distinguish the different rock types within the study area. To present the physical property measurements, we used the lithological data and the physical property measurements to recreate downhole-logging results (Figure 8). To better understand the seismic response of the different rock units, we conducted 1D-synthetic seismogram using a MATLAB script (Westgate, 2020) by calculating the reflection coefficient and convolving it with a 130 Hz ricker wavelet. Pyroxenites show the highest magnetic susceptibility (0.014224524 SI) and the lowest density (2744.5 kg/m^3) (Figure 8). They are known to contain > 20% magnesium oxide

as reported by (Sepato, 2015). Although the resistivity measurements of pyroxenites are not available, it is expected to have high resistivity, due to the presence of oxide minerals (Parkhomenko, 1982).

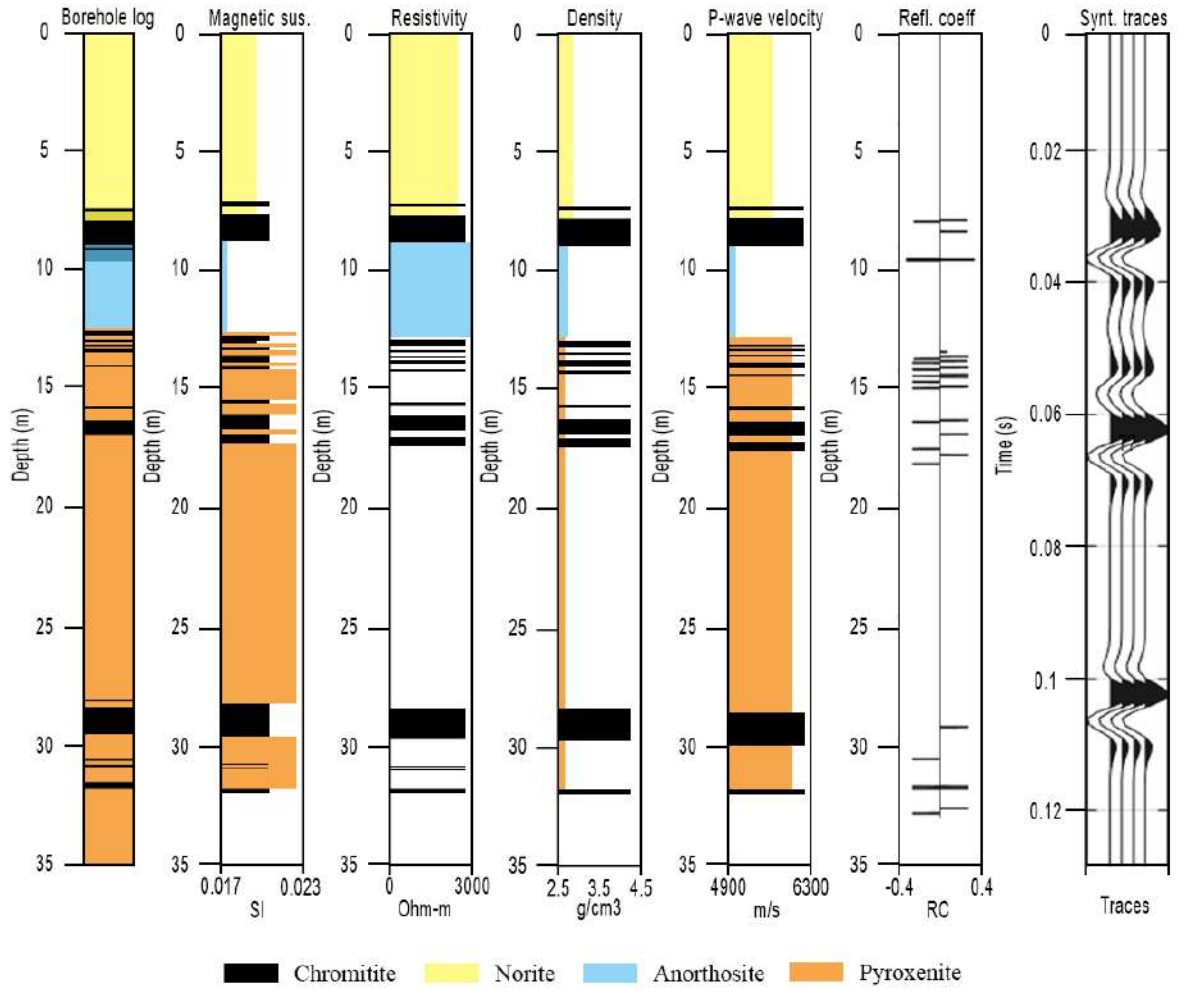


***Figure 8**: Downhole logging and core-logging data that was reconstructed from borehole 1 (BH1) of Tharisa mine. The data shows the contact between the mineralization and the host rock (norites, anorthosites and pyroxenites). Chromitites show a significant density and velocity contrast, making them recognizable from the host rocks. The resistivity log shows less variations in resistivity values across the rocks, with no resistivity data available for pyroxenites. Reflection coefficients were convolved with a 130 Hz ricker wavelet to generate a synthetic seismogram. The colours used for the rock types are consistent throughout the paper.*

Reflection seismic processing focused on cleaning the top 100 ms from ambient and coherent noise in order to enhance target reflections. Although the data were collected in a noisy mine environment, good quality first breaks are observed in all the profiles. Examples of shot gathers from SP1 and SP2 are shown in Figure 5. Note the different noise levels in the profiles. The first profile (SP1) shows evidence of coherent noise (green arrows) on the far offset from drilling. Due to these noise levels in the shot gathers, a significant amount of time was spent on reflection processing with different approaches. The shot gather showed reflections, although it was not convincing. Figure 7 shows the first breaks that were used in the tomography for the profiles in the study area. The plots (Figure 7a and b) show the presence of refracted arrivals on all the seismic profiles, with a root mean square (RMS) between 2 and 4 ms. Given that the seismic data were collected in a noisy area of the mine, the RMS is quite good. Comparing the raw shot gathers and processed shot gathers (Figure 5), the observed noise in the raw gathers has been attenuated and the reflections have been enhanced. A series of reflections are observed in the processed shot gathers at ~55 ms and 100 ms for SP1. Figure 9a, b show 2D velocity models of SP1 and SP2. Note that the seismic tomograms show the presence of three distinct P-wave velocity zones across the two seismic profiles. The near surface P-wave velocities (dark blue zone) exhibit velocities between ~500 and 1300 m/s at varying depths of ~ 0 - 8 m across the profiles. The dark blue zone is underlain by a thin light blue P-wave velocity zone of relatively higher velocities ($\sim 1300 - 2100$ m/s). The thickness of this zone varies across the profiles. The third P-wave velocity zone (light yellow to brown) is characterized by velocities between ~ 2100 and 6500 m/s, with variable depth from surface.

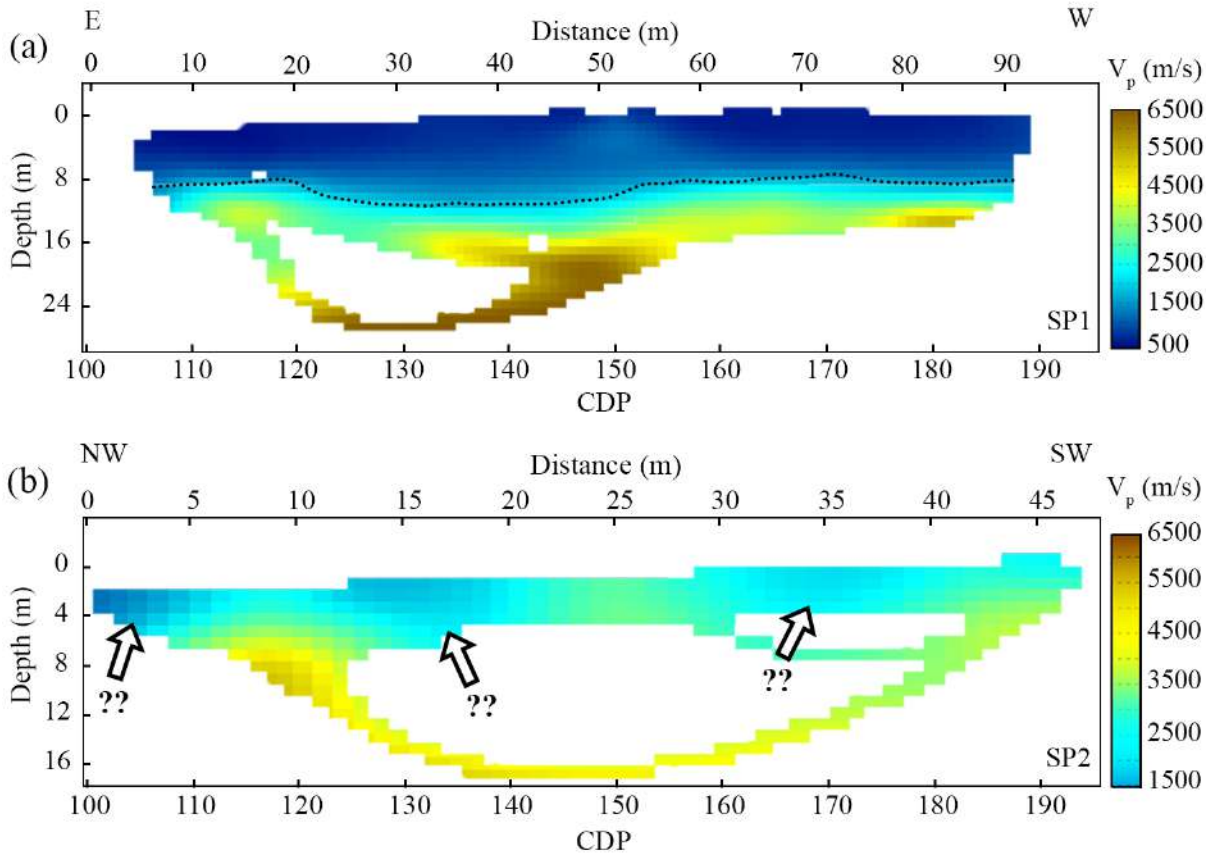


Figure 9: *2D travel time tomography results, with low velocity depressions marked with white arrows. (a) Seismic profile SP1 and (b) profile SP2. Results show ray coverage of approximately 25 m depth.*

The velocity zone consists of abrupt low velocity depression within it, possibly caused by fracturing (Figure 9b: white arrows). However, this is inconclusive as we observe poor ray coverage on SP2. We observe a maximum ray penetration of 20 - 25 m in the velocity models, due to maximum offsets of 98 m. The length of the second profile (SP2) was approximately half the length of the first profile (SP1), thus the depth of penetration for SP2 is lower (~16 m).

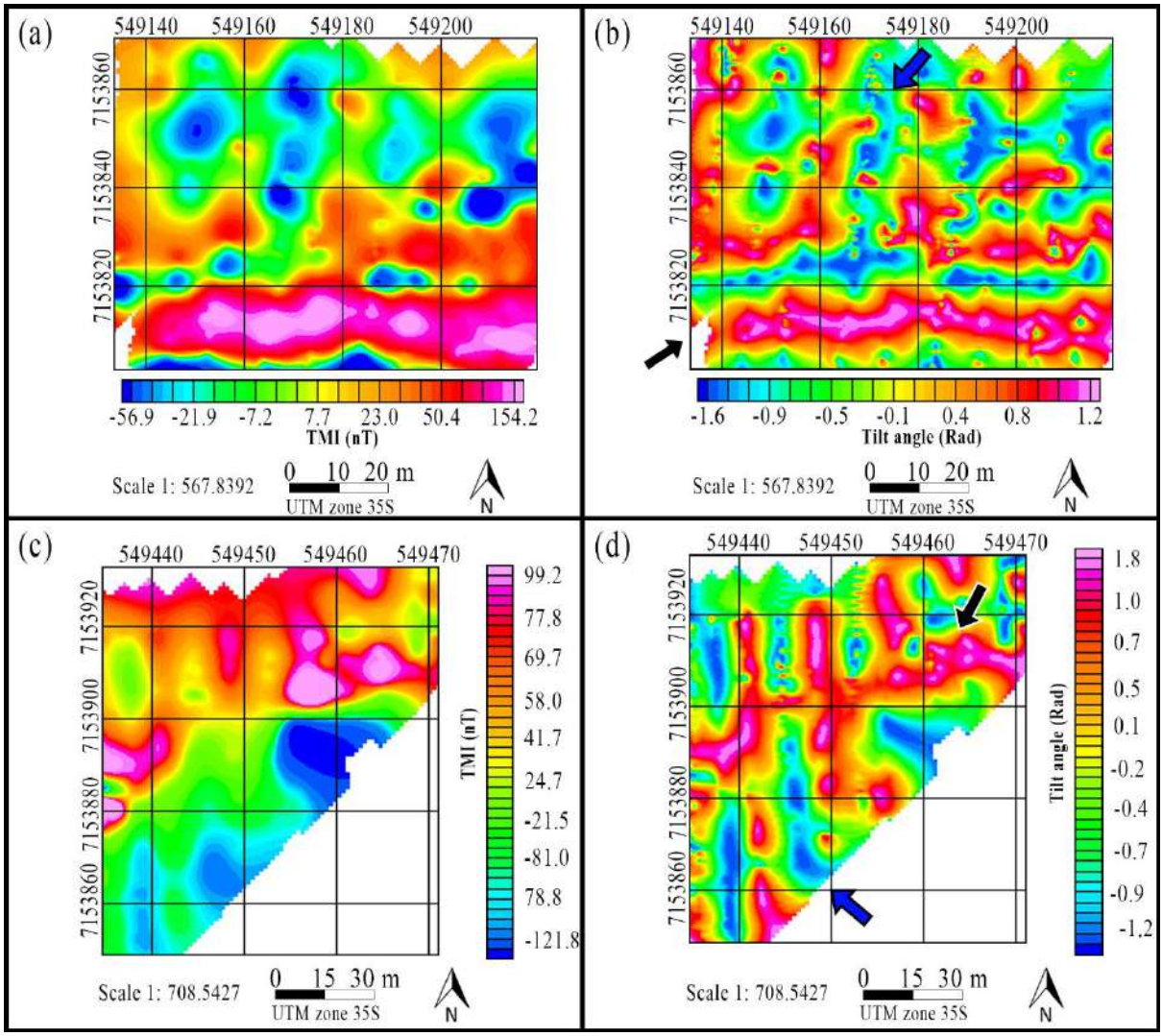


Figure 10: *(a and c) Total magnetic intensity (TMI) map after de-culturing, micro-levelling, and residual de-trending. (b and d) Vertical tilt angle derivative of the TMI maps. The black and blue arrows highlight zones of magnetic highs and lows respectively.*

The total magnetic intensity (TMI) map of the study area is presented in Figures 10a and c. Magnetic data processing focused on enhancing linear features within the open pit. Figures 10b and d are the vertical tilt angles. Features on the TMI are pronounced after the removal of the regional magnetic field and reduction to pole (RTP). The pattern of magnetic anomalies indicates the geological structures of the study area. The positive magnetic anomaly (Figure 10b: black arrow) trending east-west on the southern section of G1. This anomaly is

correlated with the dyke (Figure 4b) that crosses the open pit. The negative magnetic anomalies (Figure 10b: blue arrows) are attributed to fracture zones, where a reduction in magnetic susceptibility of the rocks occurs due to the reduction in magnetite grains and alteration of magnetite into hematite (a mineral with less magnetic susceptibility) by water occurs (Lapointe et al., 1986; Harding et al., 1988). The vertical tilt angle was applied to enhance linear features observed on the TMI. The edges of the strong positive magnetic anomaly, due to the mapped dyke, is enhanced together with the negative magnetic signatures that are linked to fracturing. The same process was applied to G2 and G3, with the negative magnetic signatures (Figure 10d: blue arrows) enhanced and attributed to fracturing. The positive magnetic signature (Figure 11) continues into G3 and follows the trend of the mapped dyke.

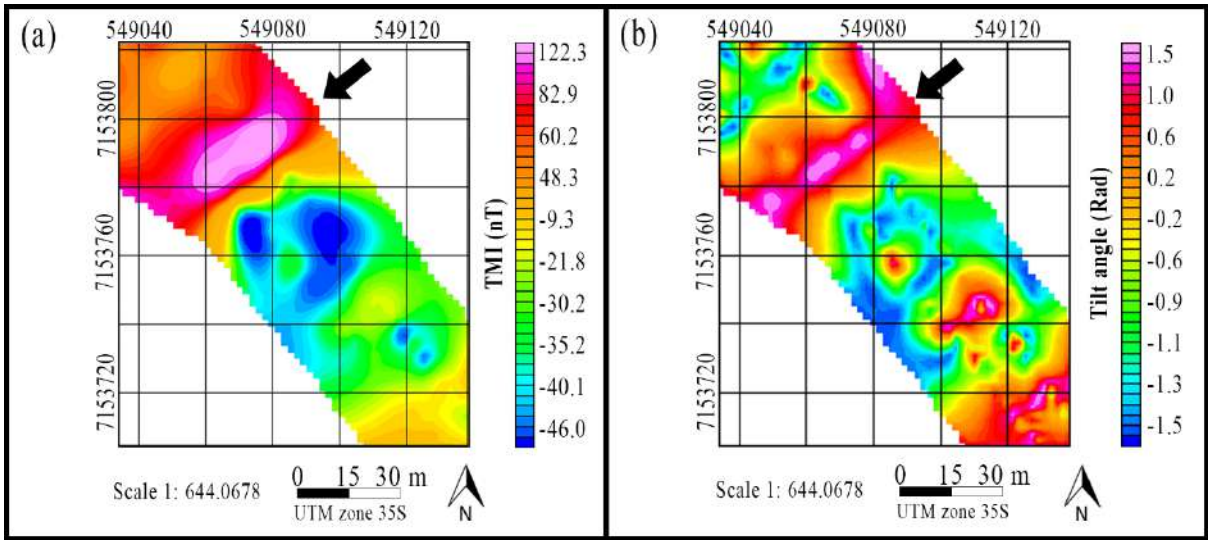


Figure 11: *(a) Total magnetic intensity (TMI) map after de-culturing, micro-levelling, and residual de-trending. (b) Vertical tilt angle derivative of the TMI maps. The black arrows highlight zones of magnetic highs.*

Inversion of the electrical resistivity data provided us with possible resistivity models. Complex lateral and vertical variations of resistivities are observed on the resistivity models. The Schlumberger (Figure 12) and dipole-dipole (Figure 13) models are considered for this

study due to their sensitivity to horizontal (high resistivity zones: white arrows) and vertical (low resistivity: blue arrows) changes in resistivity respectively.

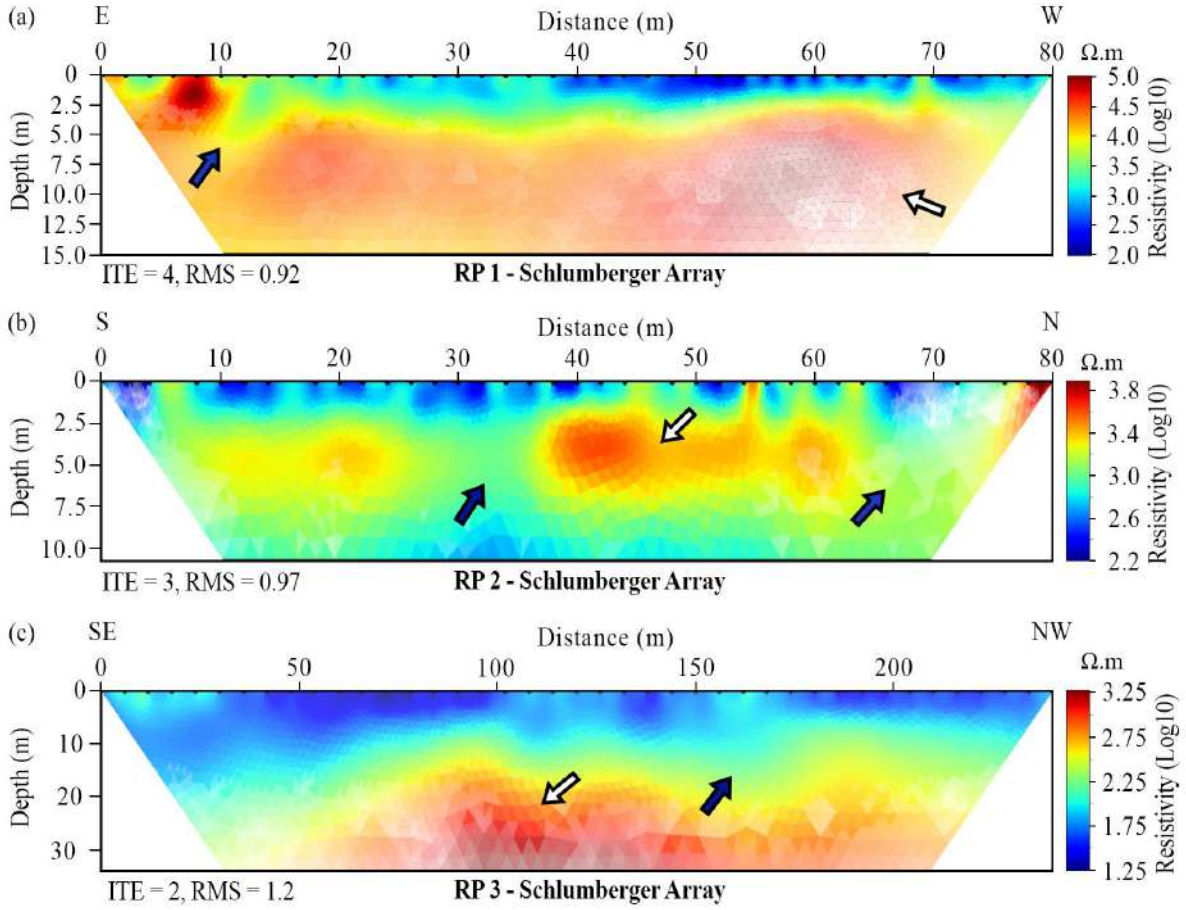


Figure 12: *Schlumberger electrical resistivity inverse sections for profile (a) RP1, (b) RP2, and (c) RP3. The white arrows indicate areas with low resistivity, while the blue indicates high resistivity areas.*

RP1 and RP2 were collected inside the pit, with the top layer of the ground dominated by highly fractured rock (Figure 14a), then followed by fractured bedrock (Figure 14b). This is visible on the resistivity model as a low resistivity zone (blue zone: ~89 – ~213 Ω.m), followed by an intermediate resistivity zone (light green to yellow: ~213 – ~3274 Ω.m). The intermediate resistivity zone is underlain by a zone of much higher resistivities (~3274 – ~20000 Ω.m), coloured as light orange to red zone (Figure 14c: Fresh bedrock). RP3 has the greatest highly

conductive layer that has thicknesses ranging between 8 - 20 m towards south-eastern side of the profile. These are attributed to the loose sandy-clay soil (Figure 14c) that is close to the river. The Schlumberger models show conductive layers (low resistivity, blue coloured zone) thickness between 2.5 – 14 m across the profiles.

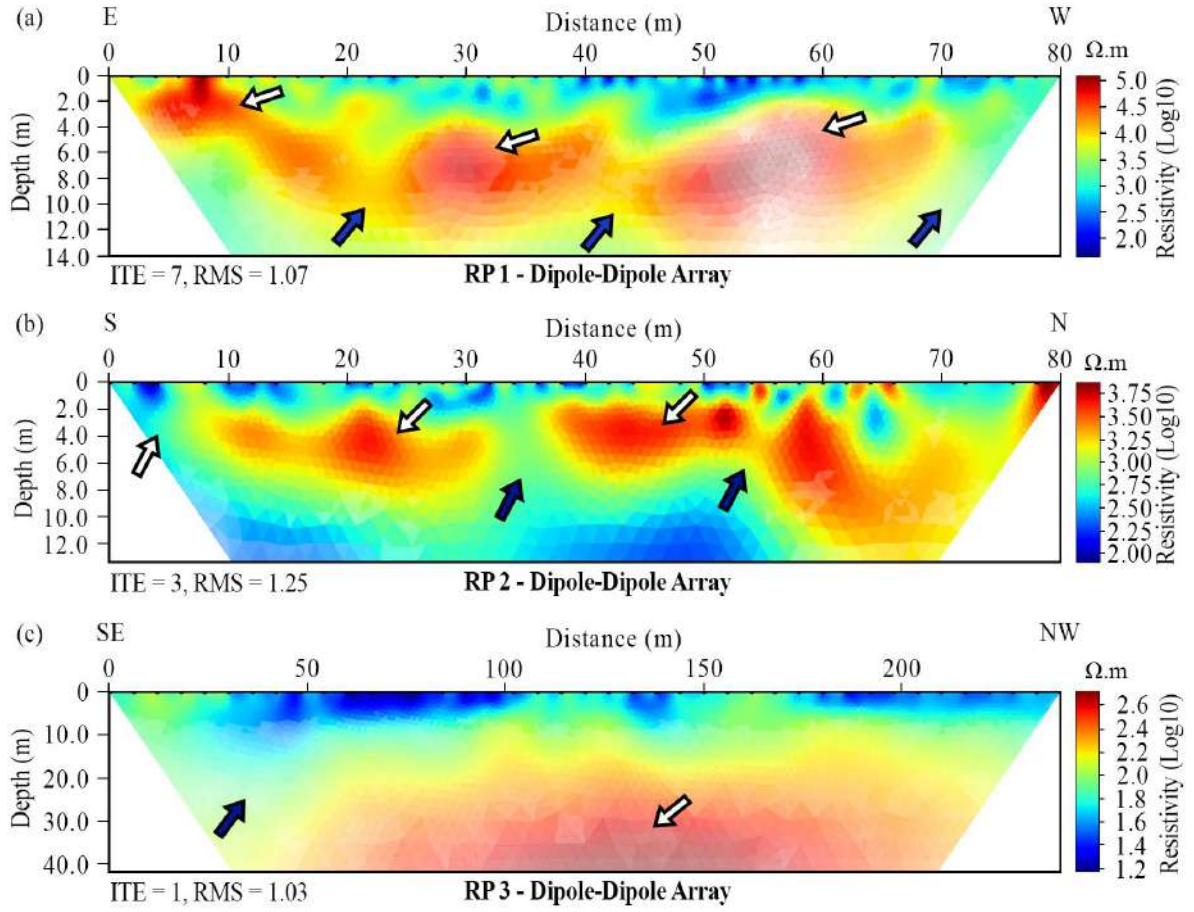


Figure 13: *Dipole-dipole electrical resistivity inverse sections for profile (a) RP1, (b) RP2, and (c) RP3. The white arrows indicate areas with high resistivity, while the blue indicates high resistivity areas.*

Interpretations

Figure 15 compares and correlates the resistivity models, seismic tomograms and seismic reflection data across SP1 and RP1, together with the lithological data from borehole 1 (Figure 4). Both the resistivity model and seismic velocity model results correlate with the borehole (BH1) data.

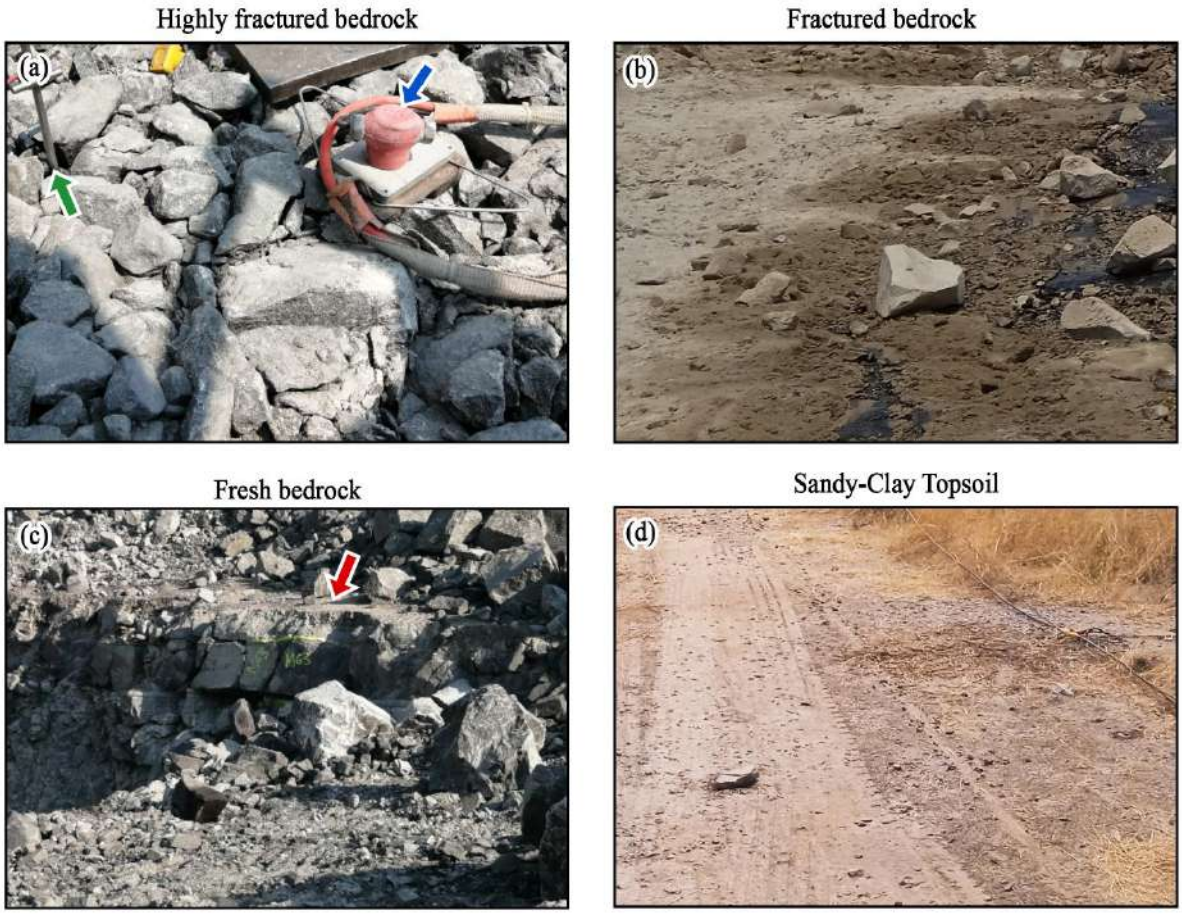


Figure 14*: Field ground conditions. Resistivity and seismic profiles were collected in an active mine. Diagrams show a) highly fracture rock, b) fractured rock and c) fresh bed rock (red arrow) inside an open pit. d) Sandy-clay weathered topsoil outside the pit. Green arrow indicates the resistivity electrodes, while the blue arrows show the land streamer used to collect seismic data*

The top 6 m on the borehole (Figure 15a, b) corresponds with the light blue and dark blue zones, that represent the low resistivity and seismic velocity zones, respectively. The dark blue to light green zones on the resistivity model is characterized by resistivities of $\leq 89 - 213\ \Omega.\mathrm{m}$ and P-wave velocities of $\leq 500 - 1300\ \mathrm{m/s}$. This zone is interpreted to be the top highly fractured norites, due to blasting in the pit. An increase in resistivity and P-wave velocity of the subsurface rocks is observed with increasing depth. The transition between the highly fractured and fresh bedrock at depths of 6 – 8 m is characterized by the higher resistivities and P-wave velocities of $213 - 3274\ \Omega.\mathrm{m}$ and $1300 - 2100\ \mathrm{m/s}$.

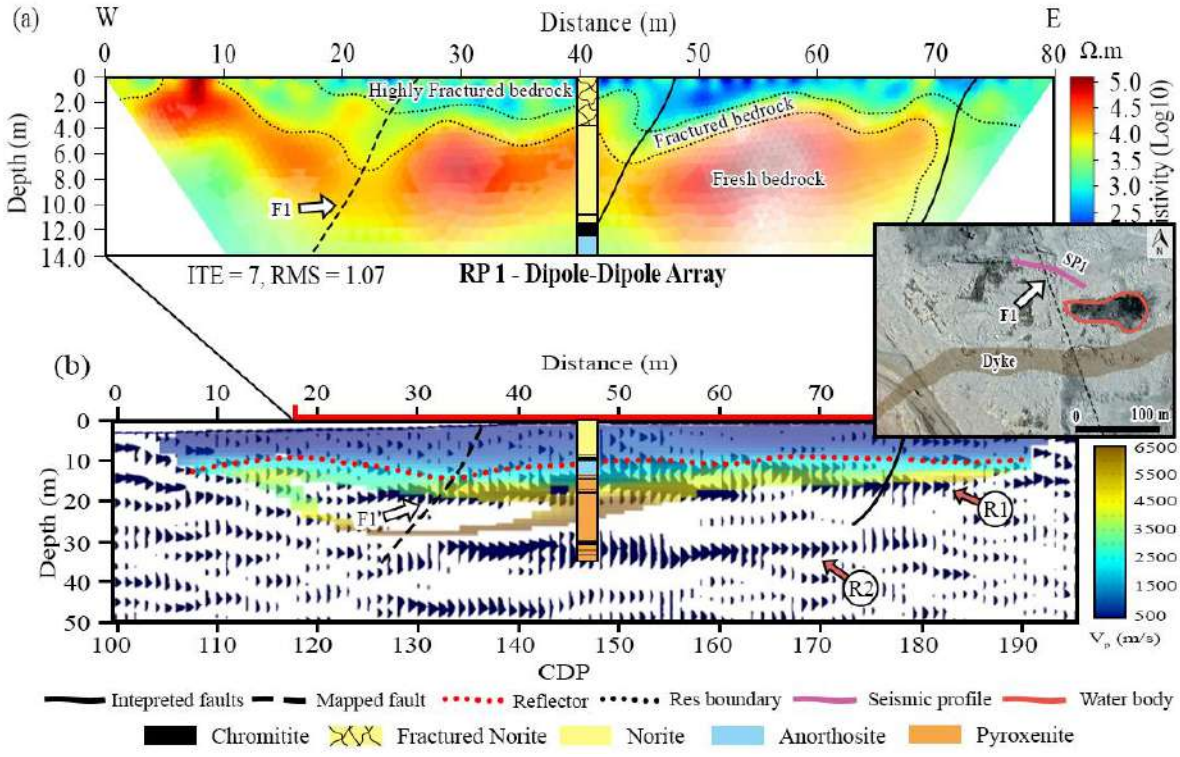


Figure 15: *Integrated and interpreted results of resistivity and seismic refraction and reflection stack. (a) Resistivity tomogram (RP1). (b) Seismic tomogram overlaid on migrated depth stack section for input seismic profile (SP1). The dotted lines show the lithological boundaries between the top weathered rock and fresh bedrock. The solid black lines represent*

the interpreted joints and fractures. Insert shows the location of the resistivity and the seismic profile with the cross-cutting fault pointed with a white arrow.

The layers situated beneath the transition zone, starting with the fresh norite at depths of about 8 m and extending to greater depths, are characterized by higher resistivities of $\sim 3274 - 20000\,\Omega.\mathrm{m}$ and P-wave velocities of $\sim 2100 - 6500\,\mathrm{m/s}$. These layer is interpreted to be the fresh bedrock made up of the norite, anorthosite and chromitite rocks that have not been affected by blasting (Figure 15a, b). The electrical resistivity and seismic velocity models show inhomogeneous horizons, with sudden resistivity changes that are attributed to fractures. However, the P-wave velocity model (Figure 9a) show less lateral velocity changes, therefore no interpretation of lateral P-wave velocity changes can be made. The dipole-dipole resistivity and seismic reflection sections reveal that the lithology within the pit is disturbed. The inversion model (Figure 16a) shows a depression at the center of the profile which can be attributed to the highly fractured bedrock. However, the interpretation of the fracture systems along the bench of the pit is inconclusive as the ray coverage on SP2 is poor. The seismic profiles need to be expanded and improve the ray penetration and coverage before any interpretation can be made. A series of reflections (Figure 16b) observed in SP2 are interpreted to be contacts between highly fractured, fractured bedrock and fresh bedrock. Reflection seismics was mainly used to image the deeper discontinuities and the mineralization contacts. On SP1, a near surface reflection is observed (Figure 15b). The reflection (R1) is generally flat throughout the seismic profile and can be correlated with the subsurface mineral contact between the chromitites and its host rock at depth (Figure 15b). The origin of the reflections are further confirmed by the sidewall mapping (shown in Figure 1d) of the chromitite layers. The continuity of the reflection is disturbed at 30 – 40 m on the migrated stack section, and this correlates with the resistivity discontinuity observed in Figure 15a

(dashed line). This discontinuity is associated with the mapped fault (F1) within the pit (shown on insert of Figure 15).

A similar package of reflections (R2) are observed at 30 m depth, and this can be attributed to the lower mineralization (MG2), however the interpretation of this is inconclusive as there is no borehole information that can constrain the depth of the MG2 mineralization. The two identified reflections are not clear at the edges of the seismic sections and exhibits multiple discontinuities, due to low fold coverage. SP2 was conducted perpendicular to RP2, with the first section of the resistivity profile covering the dyke, while the seismic profile is entirely within the dyke. The dyke is covered by highly fractured rock from the mine workings. This is evident on SP2, as it shows low velocity regions towards the south-western side of the profile at varying depths (Figure 16a).

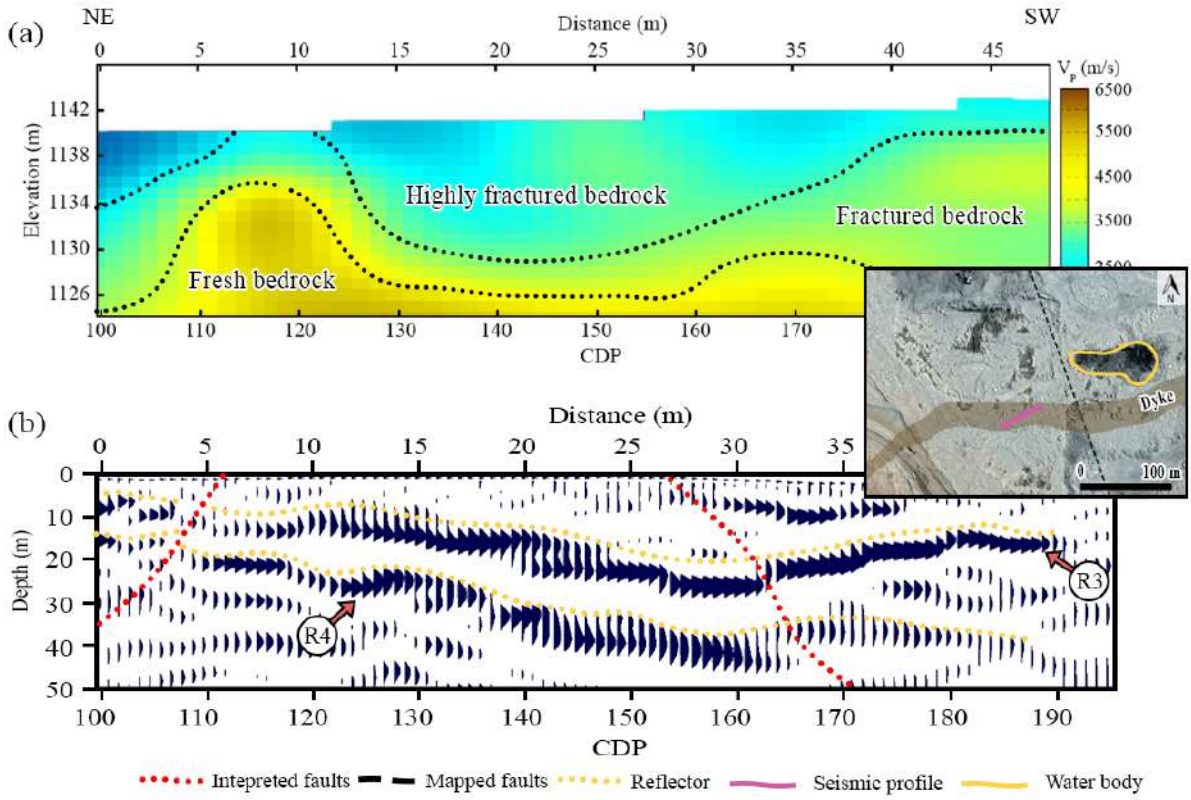


Figure 16: *(a) Tomography results and (b) migrated depth reflection section of SP2 showing reflections dipping to the south west, interpreted as a series of anorthosites and norite succession (grey arrows), that are markers for chromitite mineralization. Low-velocity zones are indicated with red arrows and correspond with interpreted faults on the stack section. Insert shows the location of the seismic profile with the cross-cutting dyke (brown) and fault (black dashed line).*

The migrated depth sections (Figure 16b) shows continuous reflections (R3) that can be followed to the surface towards the north-eastern side of the profile. The top reflection (R3: starting from ~ 8 m in the north east to ~ 25 m in the south west) is associated with the contact between the highly fractured and the weathered dyke, the following reflection (R4: starting from ~ 15 m in the east to ~ 40 m in the west) is associated with the contact between the weathered dyke zone and a fresh rock dyke. The low velocity depression (Figure 16a) at the centre of the profile corresponds to the syncline nature of the reflections in Figure 16b between 10 and 40 m. Resistivity values over the dyke range from 3 000 to $> 10\ 000\ \Omega.\mathrm{m}$. Significant differential weathering of the host rock is observed at the contacts with the host rock. Such areas are potential for hosting ground water, therefor exhibit low resistivity zones (Figure 13b: beginning of the profile and between 30 – 40 m). The tomographic results are presented in a series of 3D views (Figure 17 and 18) to present them in their real location, together with other geophysical data (resistivity and magnetics) and geological data from the mine. Figure 17b shows the low P-wave velocity depression together with the faults (white lines) that were interpreted from regional aeromagnetic data (Figure 4c). The low depressions are thick on the far ends of the profiles and correlate with the projected faults. Further interpretation of the tomography velocity zones resulted in an addition of more fault planes (Figure 17c) that can be associated with fracture systems (Figure 1c) that are mapped in the pit. The interpreted fracture system is evident on the magnetic data (Figure 17d) as low magnetic depressions and

correlates well. A high magnetic signatures (Figure 18a) is observed on the southern part of the magnetic data and the seismic profiles. The signatures is in relation to the dolerite dyke that intruded through the center of the pit (Figure 18b). The low magnetic regions are correlated with weathered host rock at the contacts.

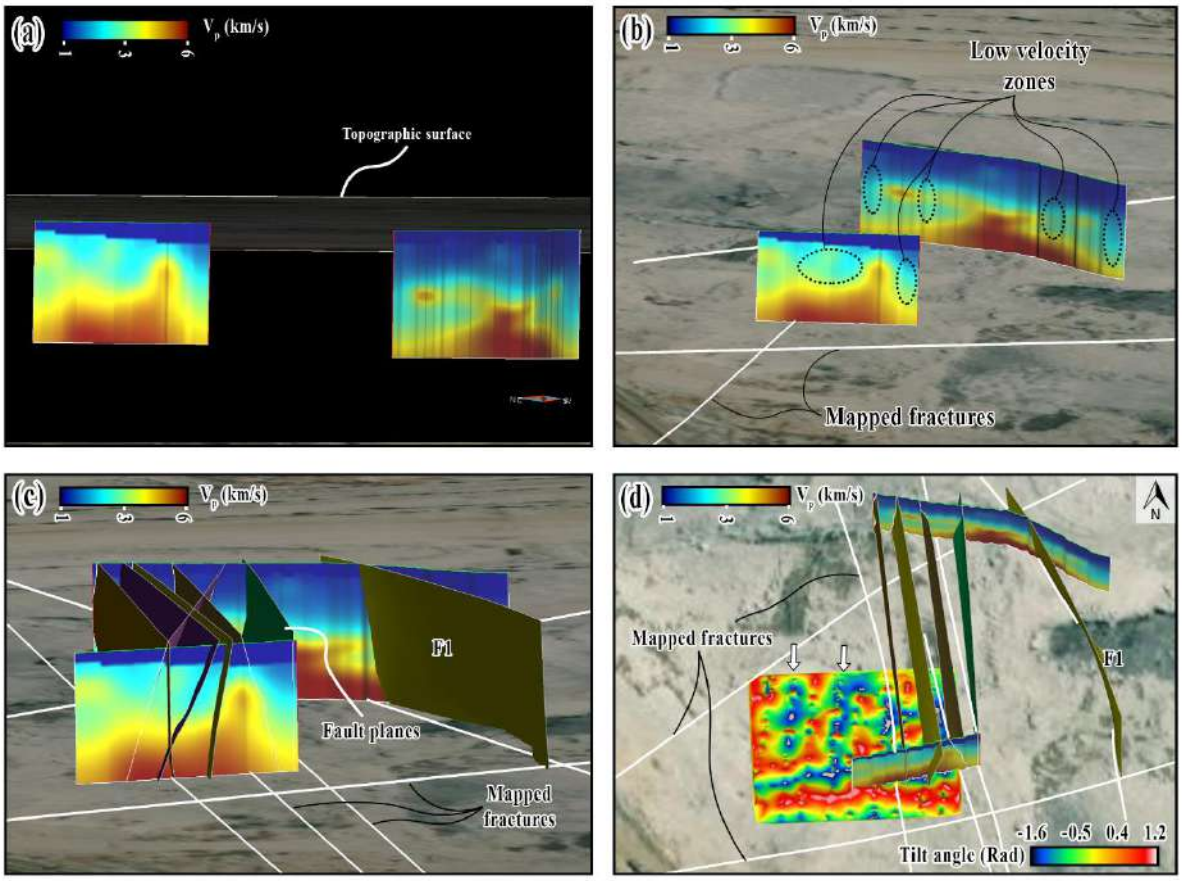


Figure 17: *A series of 3D views showing seismic tomography results with the location of the seismic lines, interpreted major faults from (Figure 3a) aeromagnetic data. (a) Position of seismic profiles, relative to the open pit, (b) tomographic results, with low-velocity zones indicated along SP1 and SP2, (c) shows the relationship between the interpreted low-velocity zones with the fault structures that where mapped within the pit, (d) Top view: relationship between the tilt angle derivative magnetic map and the interpreted fault structures. White arrows indicate areas of low magnetics. White line indicated mapped faults within the pit.*

Discussion

The geophysical data collected at Tharisa mine illustrate that good-quality geophysical dataset can be used to establish regional structural fracture system in an area of interest. This is likely the first multi-geophysical study to be conducted in an open-pit for imaging fractures in the Bushveld Complex. The data were collected without any interruption to mining activity, illustrating the cost and time effectiveness. The most notable reflection, low magnetic and low resistivity zones originate from the fractures within the open pit. This reflection, magnetic and resistivity zone suggests multiple factors that contributed to the fracture system: (1) Geologically induced fractures that were reactivated during the intrusion of dykes; (2) induced fractures due to mine blasting. The fracture systems could act as conduits for water from the water table and the river. A good correlation between magnetics, P-wave velocity models, resistivity section and seismic data is evident when overlaying the different datasets (Figures 16 and 17). For example, the low magnetic regions correlate with low P-wave velocity or low resistivity zones. This implies that the areas with low magnetics are highly weathered and prone to fracturing. This is supported by the identification of the dyke contact with the host rock exhibiting a low magnetic and resistivity values (Figure 18b). The use of multiple geophysical methods was useful in the interpretation and imaging of structures within a few meters, demonstrating the potential for high resolution geophysical methods in mine noisy environment. The quality of the data is attributed to proper survey design, acquisition and processing. This opens up opportunities for the application of multiple geophysical methods in exploration and mine development. Longer and wider seismic and magnetic grids are likely the best approach to this type of geology and challenges. However, this will be challenging as a result of the active mining and infrastructures.

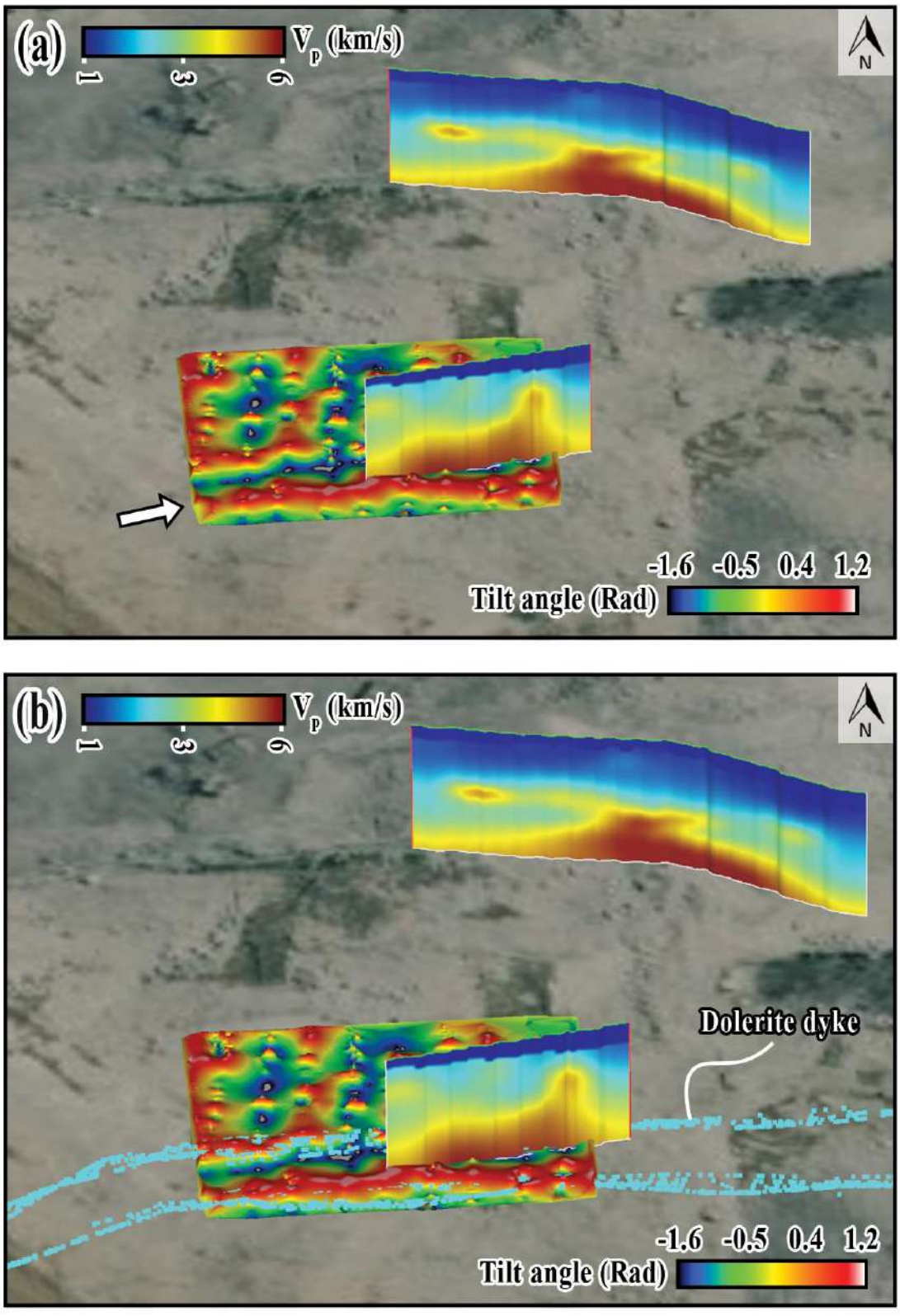


Figure 18: *(a) 3D views showing seismic tomography results with the location of the seismic lines, tilt angle derivative magnetic map. (b) Relationship between the tilt angle derivative magnetic map and the mapped dyke (Figure 1b).*

Conclusion

This study has demonstrated that multi-geophysical methods can be utilized to delineate fractures and faults in an active open-pit mine. The combination of three or more geophysical methods has more advantage in subsurface imaging. The geophysical data were complemented by borehole data and physical property measurements of rock samples. The use of geophysical data in a noisy mining environment proved to be challenging, however seismic data showed good quality first arrivals and refracted arrivals, and this allowed the imaging of the mineralization and host rock along the profiles. Furthermore, the P-wave velocity tomogram provided information about the near surface rock conditions with the highly fractured rock showing as depression zones. Ground magnetic data provided high-resolution delineation of a major dyke that was previously identified through aeromagnetic data and geological mapping. Ground magnetic further showed that the dyke is crosscut by a series of fractures and faults that may be potential conduits for water migration into the pit. Electrical resistivity tomography identified linear low resistivity zones that differentiate the fractured and undisturbed hard rock. These results will be integrated with hydrological and geochemical studies to further unravel and determine the source of water that migrates into the pit.

Reference

Amoush, H. A., and Mashagbeh, A. (2009). Using Geophysical Methods to Image Near-Surface Cylindrical Pipeline: A Case Study on Engineering Applications, Jordan. *Jordan Journal of Civil Engineering*, *3*(2), 13. Retrieved from https://core.ac.uk/download/pdf/234698299.pdf

Basson, I. J. (2019). Cumulative deformation and original geometry of the Bushveld Complex. *Tectonophysics*, *750*, 177–202. https://doi.org/10.1016/j.tecto.2018.11.004

Binley, A., and Kemna, A. (2005). DC Resistivity and Induced Polarization Methods. In Y. Rubin and S. S. Hubbard (Eds.), *Hydrogeophysics* (Vol. 50, pp. 129–156). Dordrecht: Springer Netherlands. https://doi.org/10.1007/1-4020-3102-5_5

Blanchy, G., Saneiyan, S., Boyd, J., McLachlan, P., and Binley, A. (2020). ResIPy, an intuitive open source software for complex geoelectrical inversion/modeling. *Computers and Geosciences*, *137*, 104423. https://doi.org/10.1016/j.cageo.2020.104423

Bumby, A. J., Eriksson, P. G., Catuneanu, O., Nelson, D. R., and Rigby, M. J. (2012). Meso-Archaean and Palaeo-Proterozoic sedimentary sequence stratigraphy of the Kaapvaal Craton. *Marine and Petroleum Geology*, *33*(1), 92–116. https://doi.org/10.1016/j.marpetgeo.2011.09.010

Cawthorn, R. G. (2015). The Bushveld Complex, South Africa. In B. Charlier, O. Namur, R. Latypov, and C. Tegner (Eds.), *Layered Intrusions* (pp. 517–587). Dordrecht: Springer Netherlands. https://doi.org/10.1007/978-94-017-9652-1_12

Dahlin, T. (1996). 2D resistivity surveying for environmental and engineering applications. *First Break*, *14*(7), 275–283. https://doi.org/10.3997/1365-2397.1996014

Dildar, J., Manzi, M., Abiye, T., Gomo, S., Rapetsoa, M. K., and Sihoyiya, M. (2022). An Integrated Approach to Characterise the Subsurface Using Near Surface Geophysical Methods. Presented at the NSG2022 4th Conference on Geophysics for Mineral Exploration and

Mining, European Association of Geoscientists and Engineers. Retrieved from https://www.earthdoc.org/content/papers/10.3997/2214-4609.202220173

Eales, H. V., and Cawthorn, R. G. (1996). The Bushveld Complex. In *Developments in Petrology* (Vol. 15, pp. 181–229). Elsevier. https://doi.org/10.1016/S0167-2894(96)80008-X

Gomo, S., Rapetsoa, M. K., Manzi, M. S. D., Onyebueke, E., Dildar, J., Sihoyiya, M., et al. (2023). Integrated geophysical methods for boulder delineation to improve mining. *Geophysical Prospecting*, 1365-2478.13322. https://doi.org/10.1111/1365-2478.13322

Guo, L., Meng, X., and Shi, L. (2012). Gridding aeromagnetic data using inverse interpolation. *Geophysical Journal International*, *189*(3), 1353–1360. https://doi.org/10.1111/j.1365-246X.2012.05448.x

Harding, K. L., Morris, W. A., Balch, S. J., Lapointe, P., and Latham, A. G. (1988). A comparison of magnetic character and alteration in three granite drill cores from eastern Canada. *Canadian Journal of Earth Sciences*, *25*(8), 1141–1150. https://doi.org/10.1139/e88-112

Hartzenberg, A. G., and Plessis, M. D. (2014). The influence of regional structures associated with the Bushveld Complex on the mechanism driving the behaviour of the UG2 hangingwall beam and in-stope pillars at Lonmin's Marikana Operations, 10. Retrieved from https://repository.up.ac.za/bitstream/handle/2263/71695/Hartzenberg_Structural_2019.pdf?sequence=1

James, I., Hird, G., and Fitzpatrick, A. (2019). Refraction tomography at the Nova Ni-Cu mine. *ASEG Extended Abstracts*, *2019*(1), 1–3. https://doi.org/10.1080/22020586.2019.12073152

Kerrigan, N. P. (2013). *Using shallow geophysical methods to locate a buried stream channel at a stream restoration site in the burd run waterhed, Shippensburg, pa*. SHIPPENSBURG UNIVERSITY, Shippensburg, PA. Retrieved from https://www.ship.edu/globalassets/geo-ess/kerrigan_thesis_131213.pdf

Kinnaird, J. A. (2005). The Bushveld Large Igneous Province. *The Review Paper, The University of the Witwatersrand, South Africa*, 39. Retrieved from http://www.largeigneousprovinces.org/sites/default/files/BushveldLIP.pdf

Lapointe, P., Morris, W. A., and Harding, K. L. (1986). Interpretation of magnetic susceptibility: a new approach to geophysical evaluation of the degree of rock alteration. *Canadian Journal of Earth Sciences*, *23*(3), 393–401. https://doi.org/10.1139/e86-041

Lotheringen, J., James, J., Lomberg, K., and Bornman, H. (2016). *Tharisa Chrome and PGM Mine, South Africa. Competent Persons Report* (Competence report No. JTHA011) (p. 190). Retrieved from https://www.tharisa.com/pdf/investors/annual-reports/2016/cpr-2016.pdf

Malehmir, A., Andersson, M., Lebedev, M., Urosevic, M., and Mikhaltsevitch, V. (2013). Experimental estimation of velocities and anisotropy of a series of Swedish crystalline rocks and ores: *Velocities and anisotropy of a series of crystalline rocks and ores*. *Geophysical Prospecting*, *61*(1), 153–167. https://doi.org/10.1111/j.1365-2478.2012.01063.x

Manzi, M., Durrheim, R., and Webb, S. (2017). 3D seismic attributes for platinum exploration and mine planning in the Bushveld Complex (South Africa). In *International Geophysical Conference, Qingdao, China, 17-20 April 2017* (pp. 665–668). Qingdao, China: Society of Exploration Geophysicists and Chinese Petroleum Society. https://doi.org/10.1190/IGC2017-169

Maré, L. P. (2022). Council for Geoscience Petrophysical Properties Atlas. Council for Geosciences. Retrieved from https://maps.geoscience.org.za/download/petrophysics-map-package.php

Maries, G., Malehmir, A., and Marsden, P. (2020). Cross-profile seismic data acquisition, imaging, and modeling of iron-oxide deposits: A case study from Blötberget, south-central Sweden. *GEOPHYSICS*, *85*(6), B233–B247. https://doi.org/10.1190/geo2020-0173.1

Miller, H. G., and Singh, V. (1994). Potential field tilt—a new concept for location of potential field sources. *Journal of Applied Geophysics*, *32*(2), 213–217. https://doi.org/10.1016/0926-9851(94)90022-1

Nabighian, M. N., Grauch, V. J. S., Hansen, R. O., LaFehr, T. R., Li, Y., Peirce, J. W., et al. (2005). The historical development of the magnetic method in exploration. *Geophysics*, *70*(6), 33ND-61ND. https://doi.org/10.1190/1.2133784

Ofterdinger, U., MacDonald, A. M., Comte, J.-C., and Young, M. E. (2019). Groundwater in fractured bedrock environments: managing catchment and subsurface resources – an introduction. *Geological Society, London, Special Publications*, *479*(1), 1.1-9. https://doi.org/10.1144/SP479-2018-170

Parkhomenko, E. I. (1982). Electrical resistivity of minerals and rocks at high temperature and pressure. *Reviews of Geophysics*, *20*(2), 193. https://doi.org/10.1029/RG020i002p00193

Pazzi, V., Di Filippo, M., Di Nezza, M., Carlà, T., Bardi, F., Marini, F., et al. (2018). Integrated geophysical survey in a sinkhole-prone area: Microgravity, electrical resistivity tomographies, and seismic noise measurements to delimit its extension. *Engineering Geology*, *243*, 282–293. https://doi.org/10.1016/j.enggeo.2018.07.016

Perritt, S., and Roberts, M. (2007). Flexural-slip structures in the Bushveld Complex, South Africa? *Journal of Structural Geology*, *29*(9), 1422–1429. https://doi.org/10.1016/j.jsg.2007.06.008

Rapetsoa, M. K., Manzi, M. S. D., Westgate, M., Sihoyiya, M., James, I., Onyebueke, E., et al. (2022). Cost-effective in-mine seismic experiments to image platinum deposits and associated geological structures at Maseve platinum mine, South Africa. *Near Surface Geophysics*, nsg.12216. https://doi.org/10.1002/nsg.12216

Reynolds, J. M. (2011). *An Introduction to Applied and Environmental Geophysics*. New York: John Wiley and Sons. Retrieved from https://www.wiley.com/en-

sg/An+Introduction+to+Applied+and+Environmental+Geophysics%2C+2nd+Edition-p-9780471485353

Roberts, M. K. C., and Clark-Mostert, V. (2010). Is there some commonality between the geological structures in the Bushveld Complex and the Great Dyke? In *The 4th International Platinum Conference* (pp. 149–153). The Southern African Institute of Mining and Metallurgy. Retrieved from https://www.saimm.co.za/Conferences/Pt2010/149-156_Roberts.pdf

Sepato, O. (2015). *Statistical and wavelet analysis of density and magnetic susceptibility data from the Bushveld complex, South Africa.* University of the Witwaterrand, Johannesburg. Retrieved from http://hdl.handle.net/10539/18528

Titus, R., Witthüser, K., and Walters, B. (2009). Groundwater and Mining in the Bushveld Complex. *International Mine Water Conference*, 7. Retrieved from https://www.imwa.info/docs/imwa_2009/IMWA2009_Titus.pdf

Van Schoor, A. M. (2002). Detection of sinkholes using 2D electrical resistivity imaging. *Journal of Applied Geophysics*, *50*(4), 393–399. Retrieved from http://hdl.handle.net/10204/1474

Westgate, M. C. (2020). *Reappraisal of legacy reflection seismic data using advanced processing techniques and seismic attributes*. University of the Witwatersrand, South Africa. Retrieved from https://hdl.handle.net/10539/31030

Wilson, A. H. (2005). Rock-strength and physical properties of Norites of the Merensky and Bastard Units, western Bushveld Complex. *South African Journal of Geology*, *108*(4), 525–540. https://doi.org/10.2113/108.4.525

Zhang, J., and Toksöz, M. N. (1998). Nonlinear refraction traveltime tomography. *GEOPHYSICS*, *63*(5), 1726–1737. https://doi.org/10.1190/1.1444468

11. Paper V: Integration of ground geophysical methods to characterize near-surface groundwater aquifers within an active mine

Sikelela Gomo[1], **Ndamulelo Mutshafa**[1], Musa S.D. Manzi[1], Julie E. Bourdeau[2], Bojan Brodic[1,3], Ian James[1,4] Gordon R.J. Cooper[1], Raymond J. Durrheim[1]

[1]School of Geosciences, University of the Witwatersrand, Johannesburg, Private Bag, Wits, 2050, Republic of South Africa.
[2]Geological Survey of Canada, 601 Booth Street, Ottawa, Ontario, K1A 0E8, Canada.
[3]Geological Survey of Finland, Espoo, Finland.
[4]Southern Geoscience Consultants, West Pert WA, Perth, Australia.

Abstract

Understanding near-surface groundwater storage, flow patterns, surface and groundwater interactions in mining areas can assist in making more mining more efficient and profitable. This is especially important in opencast mines affected by groundwater inflows that may negatively affect production and increase mining costs. We map and characterise the weathered aquifer system around Tharisa mine located in the southwestern region of the Bushveld Complex of South Africa. The Bushveld Complex contains connected and unconfined alluvial, shallow weathered and crystalline bedrock aquifers, which are often connected by small-scale permeable zones. Seismic refraction tomography (SRT), multichannel analysis of surface waves (MASW), electrical resistivity tomography (ERT) and borehole data are used to map the weathered aquifer system in the region and its relation to water flow into the pit. The P- and S-wave velocity and electrical resistivity results suggest extensive and deep weathering, low overburden protective competency of aquifers, possible high hydraulic conductivity, and surface and groundwater mixing. The geophysical surveys map the overburden, weathered aquifer, and the top of the crystalline rock reasonably well. The results suggest that water flow

into the open pit mine is associated with mining deeper than the weathered and crystalline rock aquifers.

Key words: Bushveld Complex, Aquifer, Water vulnerability, SRT, MASW, ERT

Introduction

The Paleoproterozoic Bushveld Complex in South Africa is renowned for its endowment of Platinum Group Elements (PGE), hosting 90% of the world's reserves (USGS, 2023). The Complex also has extensive reserves of chromium, palladium, nickel, vanadium, copper, tin and cobalt (Zientek et al., 2014). Both underground and opencast mining is used to extract these resources. Locally, mines in the Bushveld suffer from inflows of groundwater, which may delay production and increase the complexity and cost of mining operations. Groundwater inflow rates into deep mines is highly variable and can be due to multiple sources. These range from inflows originating from distinct fracture systems drawing on water from both local and distant sources and water flowing from the shallow weathered aquifer zone (Titus et al., 2009; Gebrekristos and Cheshire, 2012). The structural environment in which mines are located has a considerable impact on the groundwater inflow rates, and this is especially true of mines within the weathered aquifer zone (i.e., opencast mines). In opencast mining, pit flooding occurs when mining levels are below the water table and/or weathered aquifer zone, when rivers and dams overflow, or through constant influx of water into the pits from extensive heavy rainfall. Rather than large faults, which are often found to be analogously dry, groundwater inflows are principally associated with jointing and small-scale faults (Titus et al., 2009).

To understand the near-surface conditions in the top c.a. 50 – 100 m (so called, near-surface) of the crust, different geophysical methods are commonly applied. Among the geophysical methods, seismic refraction tomography (SRT), multichannel analysis of surface

waves (MASW) and electrical resistivity tomography (ERT) are very effective in mapping water-bearing strata, conducting site investigations, studying esker architecture and mapping stratigraphic variations (Shankar, 1994; Brodic et al., 2018; Malehmir et al., 2018; Alcalá et al., 2021; Al-Heety et al., 2021; Ali et al., 2021; Hasan et al., 2021; Salas-Romero et al., 2021; Gomo et al., 2023). These preferred methods are non-invasive and results provide continuous information along profiles (two-dimensional – 2D) and/or areas or volumes (three-dimensional – 3D) (Aizawa, 2014; Kearey et al., 2002). Geophysical methods used for hydrological purposes can delineate groundwater aquifers (e.g., porous and permeable fracture zones, buried valleys and karst and volcanic cave aquifers), map groundwater-controlling features and structures that influence aquifers (e.g., salt domes), assess groundwater potential and overburden protective competency of aquifers, infer groundwater quality, among other uses (Shankar, 1994; Poulsen and Christensen, 1999; Gabriel et al., 2003; Akintoriwa and Olowolafe, 2013; Malehmir et al., 2018).

To demonstrate the potential of near-surface geophysical methods for hydrological purposes, we use a combined approach of SRT, MASW, ERT and borehole data to map the near-surface (weathered) aquifer environment at the Tharisa Mine. Tharisa Mine is an opencast Platinum Group Metals (PGMs) and chrome mine situated in the south-western limb of the Bushveld Complex. Currently, mining at Tharisa Mine is occurring from surface to depths of about 70 m. The mine is seriously affected by mine fissure inflows. This study aims to: (1) image and characterise the near-surface (top ~35 m) weathered aquifer zone; (2) evaluate the nature of the overburden to infer surface and groundwater interaction; and (3) infer how near-surface aquifers in the region may be affected by mining activity. Our results demonstrate that hydrological knowledge gaps can be filled using geophysical methodss, providing valuable insights to mines affected by water fissure inflow and into water-stressed countries like South Africa.

Geological setting of the study area

The Paleoproterozoic (2.06 Ga) Bushveld Complex is situated in the northeastern part of South Africa (Fig. 1; Cawthorn, 2015). The Complex contains the largest continental layered mafic-ultramafic intrusion in the world, called the Rustenburg Layered Suite (RLS), covering an area of approximately 65,000 km^2 and hosts stratiform deposits of platinum group metals (PGMs), chromium (Cr) and vanadium (V) (Eales and Cawthorn, 1996; Hey, 1999; Boorman et al., 2004; Cawthorn, 2015; Scoates et al., 2021). The stratigraphy of the RLS has been subdivided into five zones. From bottom to top: (1) Marginal Zone, consisting of poorly-layered norites and pryroxenites; (2) Lower Zone, consisting primarily of harzburgite, pyroxenite and feldspathic pyroxenite; (3) Critical Zone, which is subdivided into the Upper and Lower Critical Zones (based on where cumulus plagioclase first appears), consisting of layered pyroxenite-norite-anorthosite-chromitite sequences; (4) Main Zone, consisting of poorly-layered norite and gabbronorite; and finally (5) Upper Zone, which consists of ferrogabbro-anorthosite-magnetitite-, and apatite-bearing diorites (Eales and Cawthorn, 1996; Hey, 1999; Boorman et al., 2004; Cawthron, 2015). The study area, Tharisa Mine, is located in the Upper Critical Zone of the south-western limb of the Bushveld Complex (Fig. 1).

RLS rocks are transected by numerous small-scale fractures (faults and joints) related to tectonically controlled geomorphic processes. These discontinuities form complex fracture networks that vary spatially and over time, and act as structural groundwater flow controls (Wilson et al., 2005; Twidale and Romani, 2005; Roberts and Clark-Mostert, 2010). The complex fracture networks, combined with weathered and fresh rocks, enable the formation of near-surface bedrock aquifers (intergranular weathered bedrock aquifers) in the weathering zone as well as deeper (>300 m depth) fractured aquifers (Van Wyk, 2013; Fourie et al. 2017; Govender et al. 2019). The Bushveld Complex is known to host three types of aquifers: (1)

alluvial, (2) shallow weathered bedrock, and (3) a deeper fractured aquifers (Titus et al. 2009; Gebrekristos and Cheshire, 2012). Both the alluvial and shallow bedrock aquifers are within the weathered zone (from surface to about 50 m deep, depending on the locality), while the deeper fractured aquifer is located below the weathered zone and extends to depths where fractures have been closed by increased overburden pressure (Lourens, 2013). The alluvial, shallow, weathered, and deeper fractured aquifers are often connected by structural discontinuities and, in mining areas, the groundwater flow between them is controlled by mine voids and rapid vertical inflow via the interconnected fracture network and weathered zones (Titus et al. 2009; Gebrekristos and Cheshire, 2012). On a regional scale, weathered aquifers may be connected to river systems, alluvial aquifers, and deeper fractured bedrock aquifer systems.

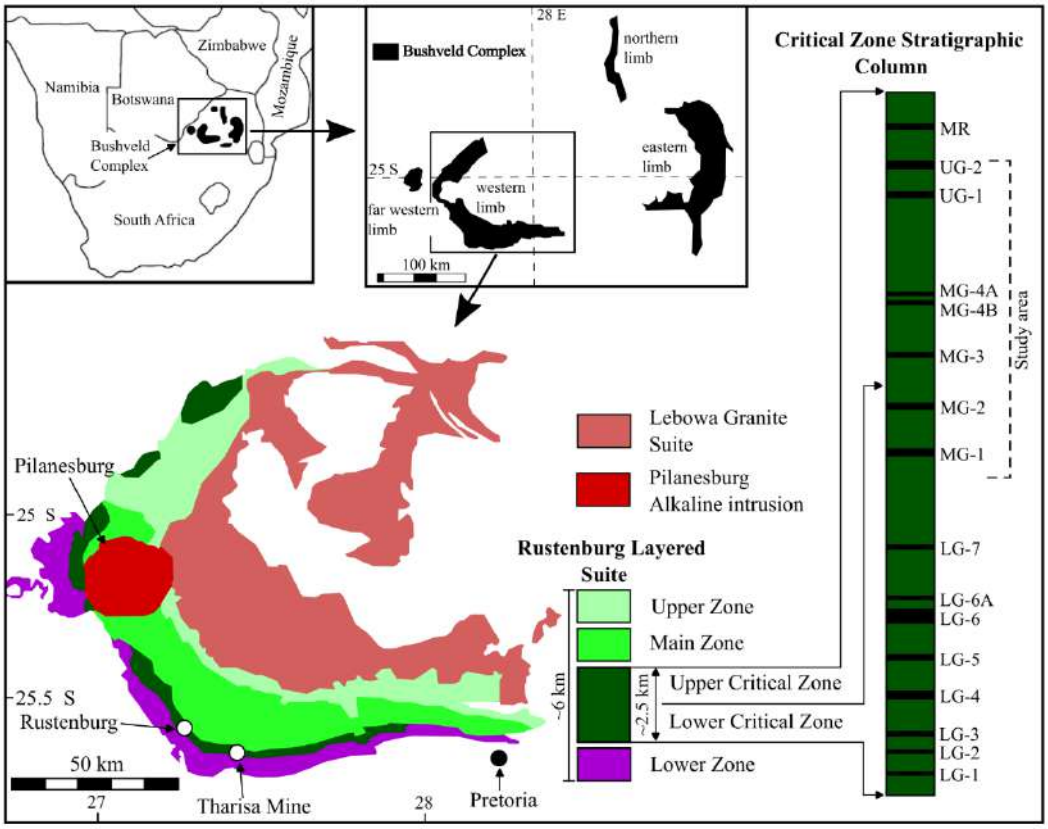


Figure 1: Locations of the Bushveld Complex in South Africa, Bushveld Complex western limb, and Tharisa Mine. The stratigraphy of the Critical Zone, in which Tharisa Mine is situated, is also illustrated (modified after Junge et al. (2016)). The Critical Zone stratigraphy column

shows the chromitite seams of the Lower Group (LG), Middle Group (MG), Upper Group (UG) and the Merensky reef (MR), and their respective locations in the Critical Zone.

Methods and data acquisition

Active-source SRT, MASW and ERT surveys were conducted to map the P- and S-wave velocity and electrical resistivity fields in the top 35 m via 2D profiling (Fig. 2). The data were acquired at three sites located in the vicinity of the mine, next to three different tailings storage facilities (TSFs) (Fig. 2a). All profiles (i.e., P1, P2, and P3) were acquired on relatively flat ground (Fig. 2b, c, d). Borehole data (closest-available borehole data) taken from about 1.5 km west of the study areas is later integrated in the study for interpretation purposes.

Seismic refraction tomography (SRT)

The seismic data used for P-wave first arrival tomography purposes were acquired using a fixed-spread (Site 1) and an end-on acquisition spread (Site 2 and Site 3). For all sites, a 6 kg sledgehammer was used as a seismic source striking a 20 × 20 × 2 cm^3 aluminium plate. Five hits were made at each shot point to improve the signal-to-noise ratio. The data were acquired using a sampling interval of 1 ms and recording length of 1000 ms. At Site 1, the acquisition was carried out using a 48-channel seismograph system with 14 Hz natural frequency vertical component geophones spaced at 4 m intervals. The shots were taken at every receiver location and one offset point, on both sides of the spread. The P-wave tomograms for Site 2 and Site 3 were produced from the same datasets acquired for MASW purposes (end-on spread). The MASW data acquisition is presented in the following section and detailed in Table 1. All shot and receiver locations were accurately surveyed using a differential GPS (DGPS) system with an accuracy of a few centimetres in both the geodetic positioning and elevation.

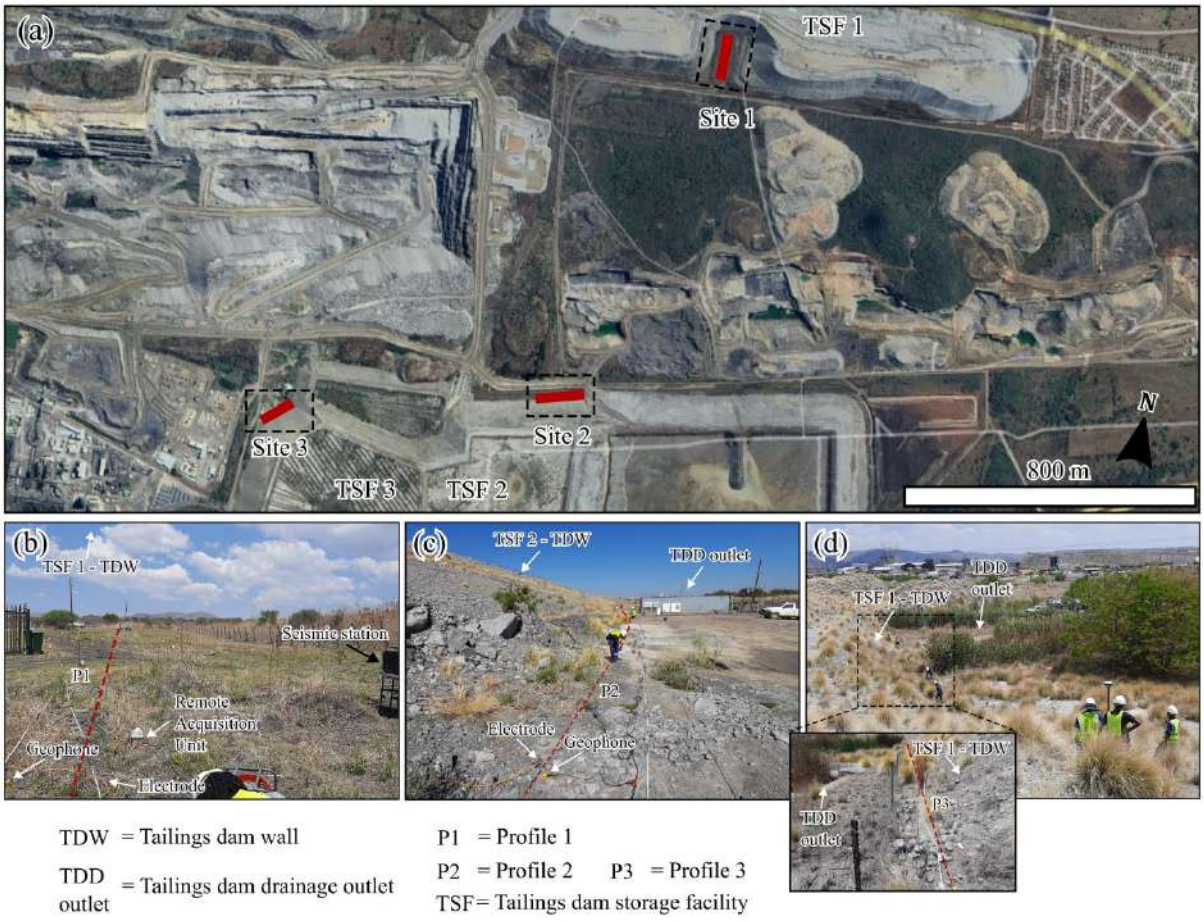


Figure 2: (a) Site 1, Site 2, and Site 3 locations (Google Earth image) at Tharisa Mine. All the sites are located near tailings dam storage facility TSF 1, TSF 2 and TSF 3; (b), (c) and (d) show field photos of Site 1, Site 2 and Site 3, and locations where profile 1, profile 2 and profile 3 were acquired.

At all sites, P-wave first breaks were manually picked after adding corresponding geometry to the SEGY trace headers. The travel-time tomography inversion was done in TomoPlus, a commercial software that uses a non-linear travel-time inversion method, based on inverting travel-time curves rather than travel-times alone, to deduce the velocity models (Zhang and Toksöz, 1998). Cell sizes of 1 m in both inline and depth directions were used to invert the data. Figure 3a, b, c show plots of the travel-time residuals as a function of offset, obtained after 10 iterations, while Figure 3d, e, f shows the distribution of picked P-wave first arrivals as a function of offset. The final P-wave tomograms are shown in Figure 4a, c, e and their corresponding ray-paths in Figure 4b, d, f. Average RMS errors after 10 iterations were

3.52 ms, 1.09 ms and 2.96 ms for profiles P1 (Site 1), P2 (Site 2) and P3 (Site 3) data, respectively.

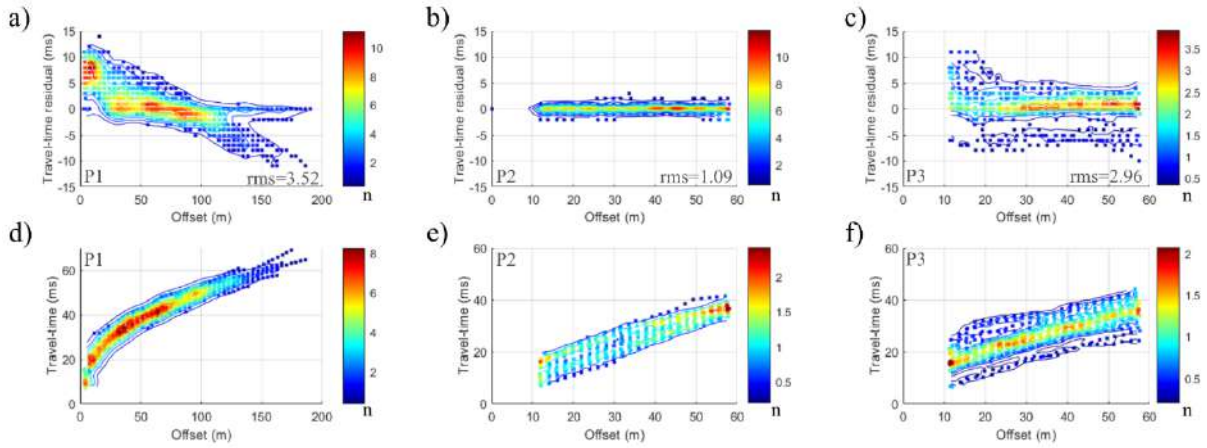


Figure 3: Travel-time residuals (rms misfit) plots obtained after 10 iterations (a, b, c) and picked first break travel-times (d, e, f) for seismic profiles P1 (Site 1), P2 (Site 2) and P3 (Site 3). The data density, where 'n' is the number of points inside a range, is represented by the colour scale used to depict the data. Both first breaks and residuals are plotted using absolute values of the offsets.

Multichannel analysis of surface waves (MASW)

MASW is a non-invasive seismic technique that uses the dispersive nature of surface waves (Rayleigh waves or Love waves) to map the shear wave velocity (V_s) variation with depth (Park et al., 1999; Socco and Strobbia, 2004). In this study, a standard MASW roll-along technique was applied to acquire the data using a 24-channel seismograph system. Single component (vertical) geophones with a natural frequency of 14 Hz and varying geophone interval, source to receiver offset, and roll-along shifts were used to acquire the data, see Table 1.

Table 2: Electrical resistivity tomography (ERT) and multichannel analysis of surface waves (MASW) survey acquisition parameters.

MASW parameters	**Site 1- Parameters**	**Site 2 - Parameters**	**Site 3 - Parameters**
Area	Site 1	Site 2	Site 3
Survey type	Fixed spread roll-along	Fixed spread roll-along	Fixed spread roll-along
Data format	SEG-2	SEG-2	SEG-2
Number of channels	24	24	24
Seismic source	6 kg Sledgehammer	6 kg Sledgehammer	6 kg Sledgehammer
Stack	5 repeated shots per location	5 repeated shots per location	5 repeated shots per location
No. of shot points	17	23	24
Line length	96 m	88 m	46 m
Geophone frequency	14 Hz	14 Hz	14 Hz
Geophone spacing	3 m	2 m	2 m
Roll along spacing	6 m	4 m	2 m
Source offset	21 m	12 m	12 m
Sampling interval	1 ms	1 ms	1 ms
Record length	1000 ms	1000 ms	1000 ms
Geodetic surveying	DGPS	DGPS	DGPS

ERT parameters	**Site 1- Parameters**	**Site 2 - Parameters**	**Site 3 - Parameters**
Equipment	ARES Resistivity Meter	ARES Resistivity Meter	ARES Resistivity Meter
Electrode spacing (m)	2	1	1
Line length (m)	160	80	80
Array types used to acquire data	Schlumberger, Wenner and Dipole-Dipole	Schlumberger, Wenner and Dipole-Dipole	Schlumberger

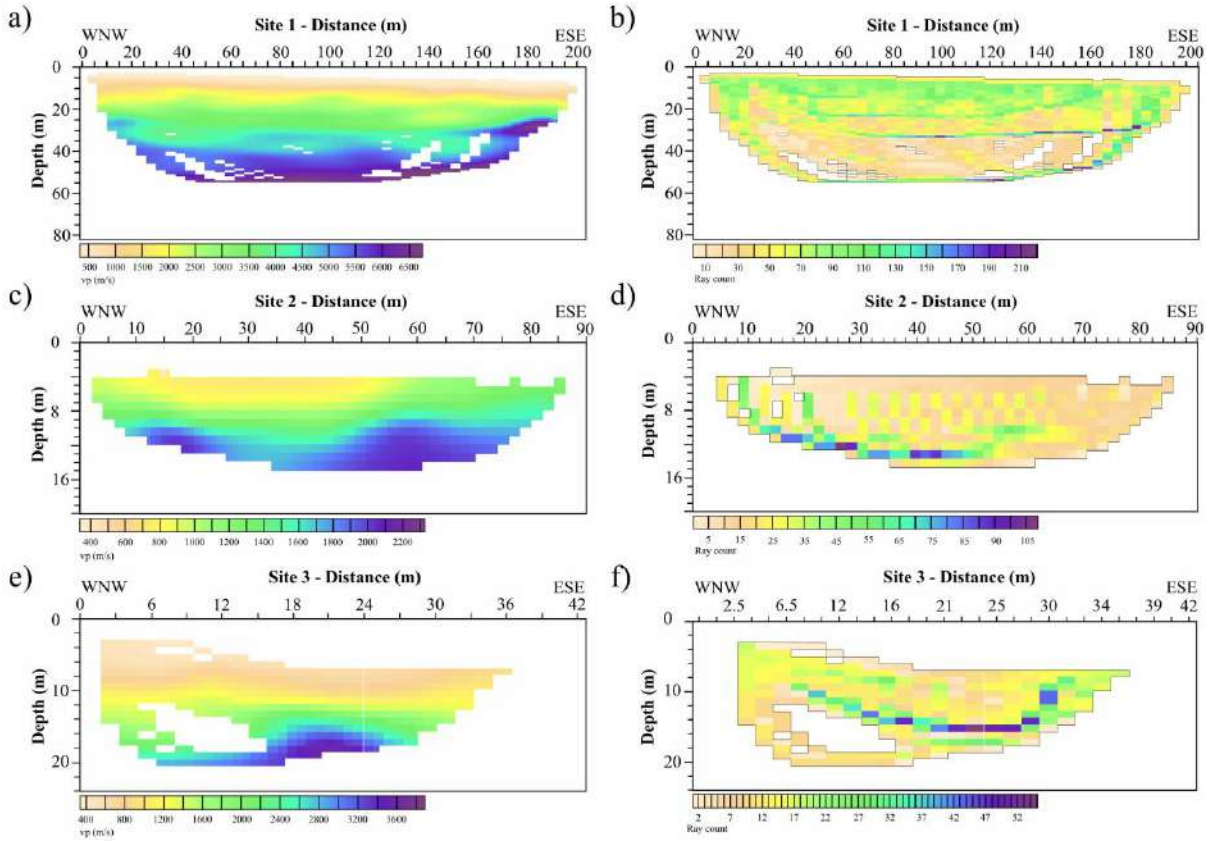


Figure 4: Overview of the P-wave tomography models and their corresponding ray paths at Site 1 (a and b), Site 2 (c and d) and Site 3 (e and f), respectively.

Figure 5 shows a sketch of the field configuration and acquisition approach used to acquire the data.

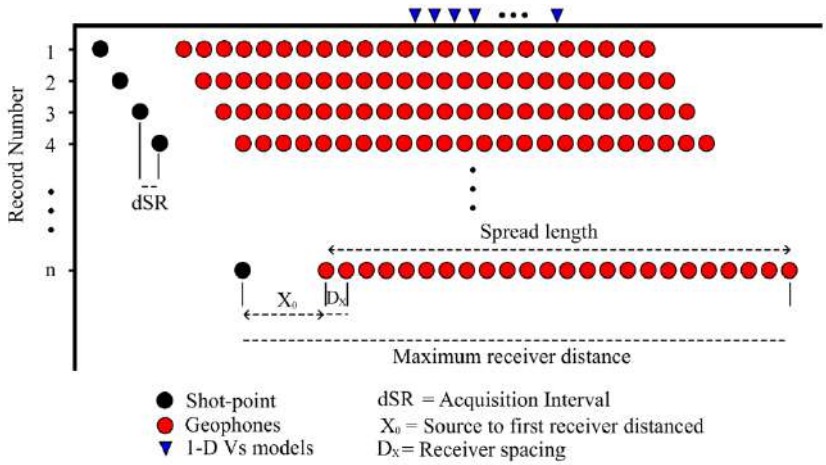


Figure 5: 2D MASW roll-along field configuration and acquisition sketch. Source offset of 12 m was kept consistent throughout entire roll-along acquisition with entire spread moving ahead by 2 m.

Figure 6a and b illustrate the typical data quality obtained, which include the presence of noisy channels, non-continuity of events and guided waves. The shot gathers shown in Figure 6a and b were taken from data at Site 3 and Site 2, respectively.

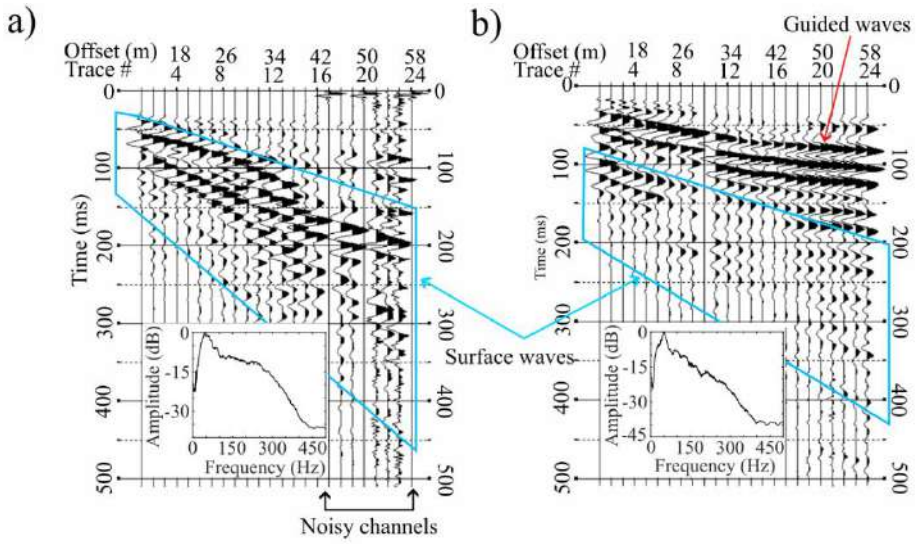


Figure 6: Typical quality shot gathers (with their corresponding amplitude spectra) from data collected at Site 3 (a) and Site 2 (b), respectively. The shot gathers highlight the presence of visible surface wave trends (blue polygons) along with guided waves (red arrow) and high frequency noise (marked using black double headed arrow).

Figure 7a and f show typical quality shot gathers acquired at Site 1 and Site 3, correspondingly. The acquired field data was subjected to pre-processing involving muting of first breaks and guided waves and eliminating bad traces (Fig. 7b, g) to improve the quality and coherency of phase velocity-frequency spectra (Fig. 7c, h). After testing different methods, the phase velocity-frequency spectra (dispersion images) were produced using a phase-shift method (Park et al., 1999). For every shot location, the maximum spectral amplitude deemed to correspond to the fundamental mode was picked to obtain a dispersion curve (Fig. 7d, i).

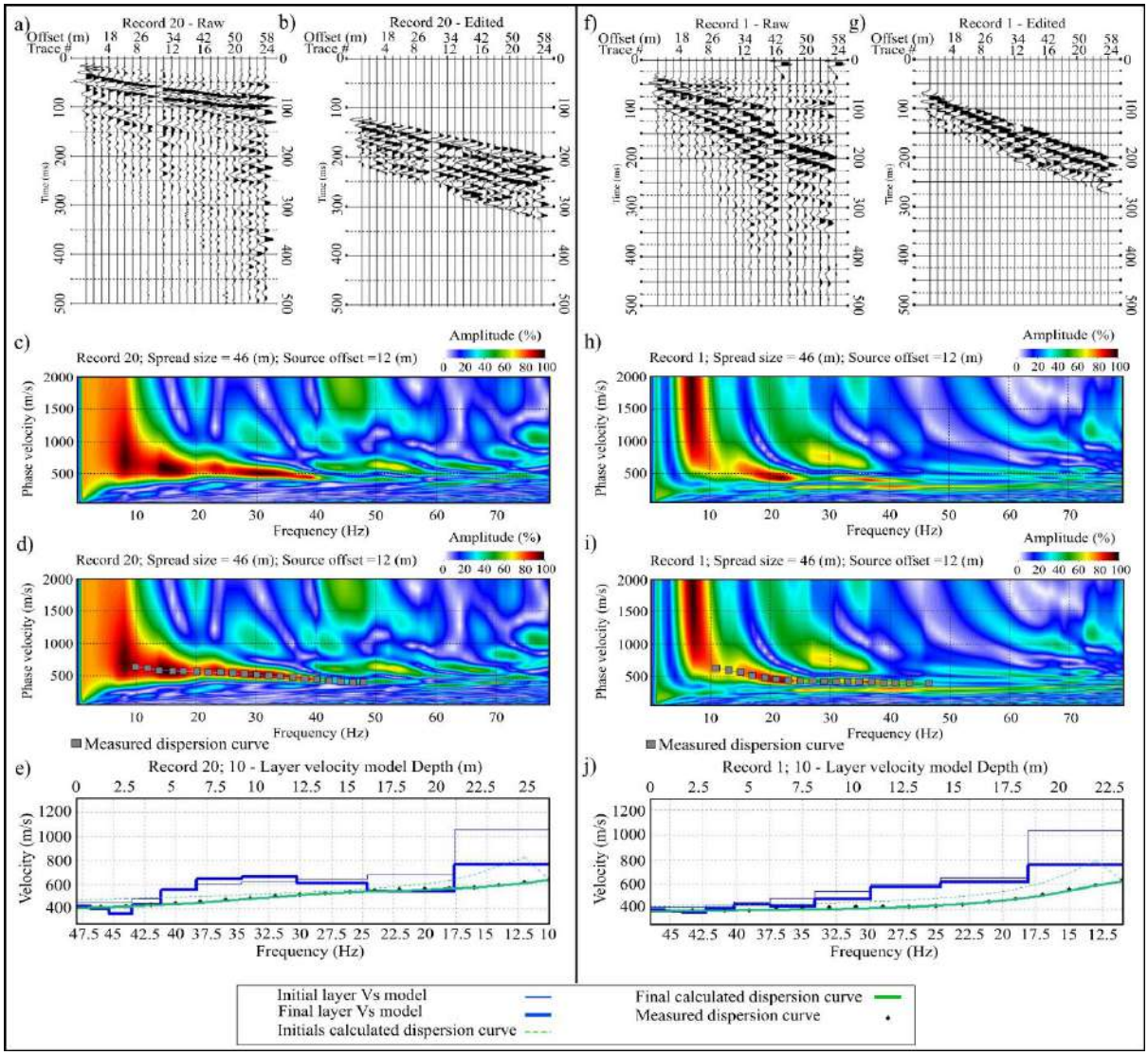


Figure 7: Processing workflow example showing raw shot gathers from Site 1 (a) and Site 3 (f) and their pre-processed (muted) versions (b and g); phase velocity - frequency spectra (dispersion images) obtained via the phase-shift transform method (c) and (h), and with (d) and (i) superimposed picks (dispersion curve) of the fundamental mode of (b) and (g), respectively; (e) and (j) show initial and final 1D shear wave models, along with dispersion curves, for inversion purposes deduced from the dispersion curves in (d) and (i), respectively.

In cases where the fundamental mode was not clearly visible due to high ambient noise levels and/or distortions by higher modes, muting of the effects of these noise sources was carried-

out (Fig. 7b, g). The picked dispersion curves were individually inverted to obtain a 1D shear wave (V_s) velocity profiles (Fig. 7e, j) underneath the middle point of a geophone spread.

The MASW data processing was done in Surfseis 6++, which is a software that adopts a shear wave inversion algorithm from Xia et al. (1999) based on obtaining shear wave velocities (S-waves) by inverting the dispersive phase velocity of Rayleigh or Love waves. To invert the data, a 10-layer model with increasing thickness and density with depth was used. The initial densities used changed in an orderly increasing manner with depth, and ranged from 1.5 to 2 g/cm^3. All the model layers had an initial Poisson's ratio of 0.4. The depth of the half-space used to invert the data was determined from the longest surface wave wavelength measured from the obtained dispersion curves. The inversion algorithm was allowed 10 iterations and an average root-mean-square error of 0.4% was obtained. Using all generated 1D velocity profiles, 2D shear wave velocity pseudo-sections were produced by the bicubic interpolation method.

Electrical resistivity tomography (ERT)

ERT is a non-invasive active source surface geophysical technique that maps subsurface materials based on their ability to transmit electrically-charged particles (i.e. electrical conductivity) (Telford et al. 1990). With the aim of obtaining detailed near-surface electrical property variations in both vertical and horizontal directions along the survey traverse, we acquired the data using a combination of Schlumberger, Wenner and Dipole-Dipole electrode arrays. At Site 1, a spread length of 160 m and an electrode spacing of 2 m was used. At Site 2 and Site 3, high-resolution profiles were acquired using a spread length of 80 m and an electrode spacing of 1 m. The takeout cables were connected to stainless steel electrodes hammered into the ground. The length of the resistivity profiles was restricted by mining activities. As the top layer in the study area was dry and compacted in portions, water mixed

with liquid soap (a conducting solution) was used to decrease the contact resistance and improve the electrode coupling. Table 1 gives the parameters and array types that were used to acquire the resistivity data at all sites. The resistivity data was processed in ResIPy, an open-source software that inverts data based on a regularized objective function combined with weighted least squares (Blanchy et al., 2020). The apparent resistivity data was manually de-spiked and inverted to produce resistivity tomograms and obtain a 2D electrical resistivity distribution model.

Results and Interpretations

The results of SRT, MASW and ERT data (Figs. 8 to 13) were interpreted to better understand the near-surface weathered zone (weathered aquifer), its secondary features (e.g., fractures), and interactions between surface water, near-surface groundwater and possible contaminants. At all sites, SRT, MASW and ERT show a complexly variable subsurface. However, the P- and S-wave velocity and resistivity models are largely consistent.

Site 1

Figure 8 shows P-wave (V_p) first-break and MASW-obtained S-wave (V_s) tomograms from Site 1, along with their corresponding interpreted conceptual models. Both tomograms illustrate a correlating increase in P- and S-waves velocity pattern with depth (Fig. 8a, b, c). Additionally, the tomograms reveal the presence of three main layers, as depicted in the P- and S-wave conceptual models of the site (Fig. 8d, e).

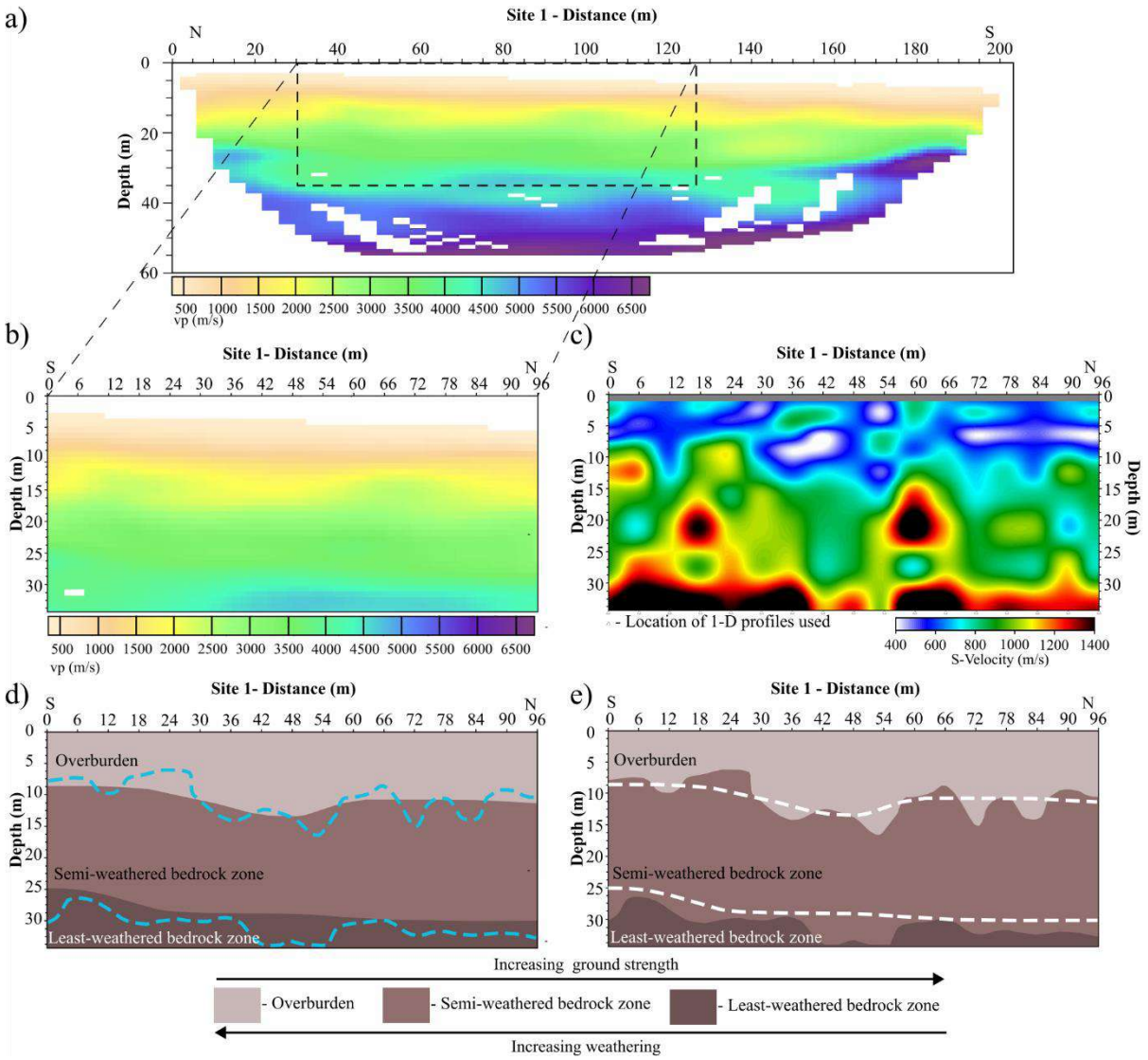


Figure 8: Comparison of P-wave first-break traveltime tomography (a, b) with MASW S-wave (c) velocity tomographs at Site 1. (d) and (e) are interpreted conceptual models for the P-wave and S-wave in (b) and (c), respectively. The conceptual models show the variation in weathering with depth. The dashed blue lines in (d) show the interpreted overburden/semi-weathered and semi-weathered/least-weathered boundaries deduced from the S-wave tomography and projected onto the P-wave tomography, while the dashed white lines in (e) the P-wave tomography projected onto the S-wave tomography.

The three main layers identified correspond to the: (1) overburden, (2) semi-weathered bedrock zone, and (3) least-weathered (fresh to minimally weathered crystalline) bedrock zones. The

zones are characterised by P- and S-wave velocities ranging between: (1) <500 – 1500 m/s and <400 – 700 m/s for the overburden; (2) 1500 – 3500 m/s and 700 – 1400 m/s for the semi-weathered bedrock zone; and (3) >4000 m/s and >1400 m/s for the least-weathered bedrock zones, respectively. The blue and white dashed lines in the conceptual models (Fig. 8d, e) illustrate the depth and lateral variation in the P- and S-wave velocity layers with respect to the three identified zones and each other. Although the P- and S-wave results are similar both in depth and laterally, additional information is gained from the S-wave tomogram (Fig. 8c). This discrepancy is likely due to the inherent smoothness of the P-wave first arrival raytracing tomography, where the velocities obtained are a factor of both the smoothness constraints and an average of different ray paths traversing the individual grid cells (i.e., Tryggvason et al., 2002), while no smoothness is introduced in the MASW inversion process. The MASW obtained S-wave velocities are also able to resolve low velocity zones underlying high velocity zones, unlike the refraction P-wave results, which overall depict an increase in velocity with depth (compare Fig. 8b to c).

Figure 9 shows the ERT (dipole-dipole array) along with a cropped image of the S-wave tomography results at Site 1. The overburden and semi-weathered bedrock zones are apparent in the ERT data (differentiated using a dashed black line), and both zones are characterized by very low resistivities (<100 ohm.m; dark blue to orange colour zones). Considering that this area consists of crystalline rocks (i.e., norites and melanorites), which have negligible intergranular porosity, the low resistivities are most likely due to high conductivity along cracks and fissures, and the presence of charged particles associated with weathering of the crystalline rocks. Unfortunately, the resistivity section appears to rapidly lose sensitivity with depth, rendering the profile rather smooth at depth. The obtained resistivities and S-wave velocities are generally low, ranging between ~<25 to ~125 ohm.m and ~400 to ~1400 m/s, respectively. Considering that fresh rocks often have resistivities of around 2000-

3000 ohm.m, P-wave velocities >3000 m/s, and shear wave velocities greater than >1,500 m/s, this implies the presence of possible water saturation, conductive and less compact sediments (Kirsch, 2006; Gomo et al., 2023).

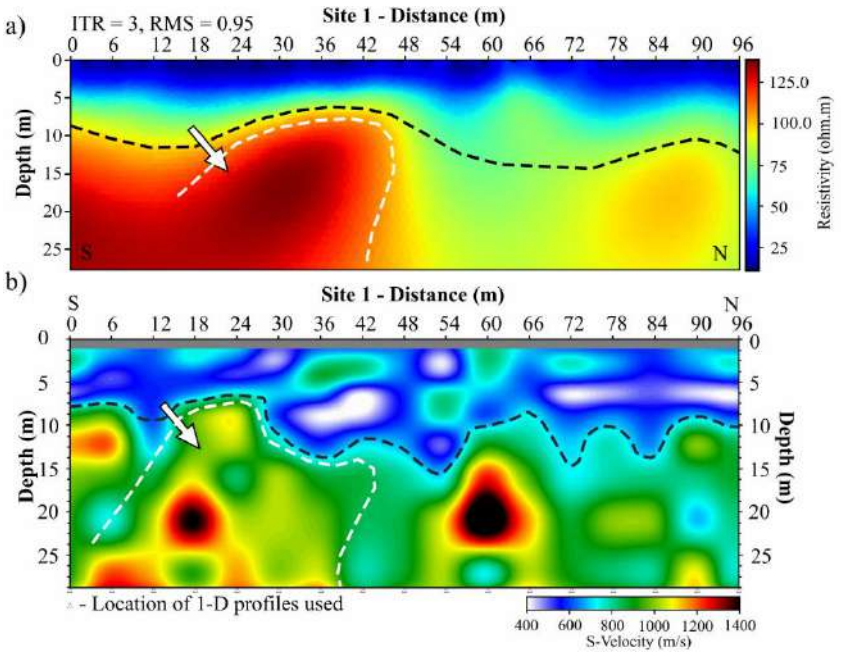


Figure 9: Comparison of electrical resistivity pseudosection and S-wave tomography obtained at Site 1. The black dashed lines mark the interpreted overburden and semi-weathered zone transition zone, the white arrows and white dashed lines mark a direct correlation of higher resistivity and S-wave velocity zones within the semi-weathered zone.

Site 2

Figure 10 shows the P- and S-wave velocity sections obtained at Site 2, along with their corresponding conceptual models. Here, the P-wave and S-wave tomograms vary when compared to one another (compare Fig. 10a to b), which is most likely due to the presence of low S-wave velocity zones (green-blue zones) below high velocity zones (yellow-red-black zones) in the near-surface region (Fig. 10b). The P-wave velocities range between <400 to ~2300 m/s, while the S-wave velocities range between 200 and ~700 m/s. Both P- and S-waves

velocity ranges are quite low, indicating deep weathering, with only the overburden and semi-weathered near-surface zones/layers resolved (Fig. 10c, d).

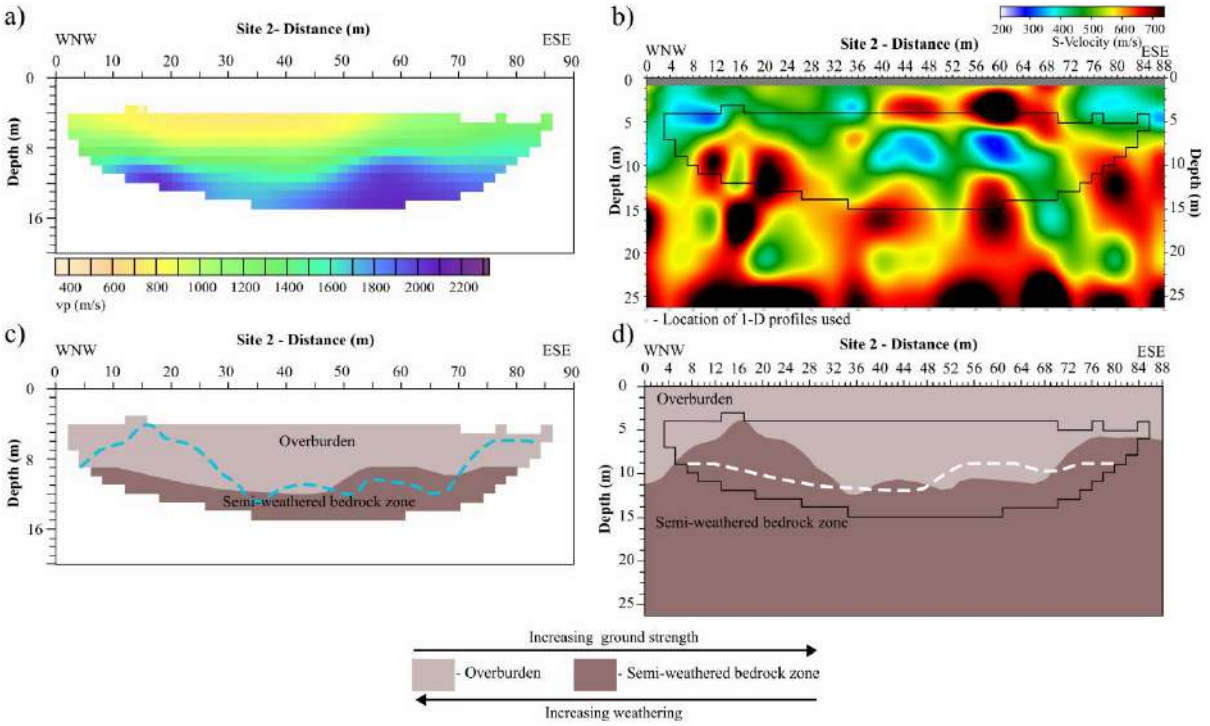


Figure 10: Comparison of P-wave (a) with S-wave (b) velocity tomographs at Site 2. (c) and (d) are conceptual models for the P-wave and S-wave in (a) and (b), respectively. The interpreted conceptual models show the variation in weathering with depth. The dashed blue line in (c) illustrates interpreted overburden/semi-weathered boundary deduced from the S-wave tomography in (b) and projected onto the P-wave tomography conceptual model, while the dashed white lines in (d) the P-wave tomography projected onto the S-wave tomography.

Figure 11 shows the electrical resistivity (Schlumberger array) and S-wave tomography results at Site 2. A direct correlation is observed between the electrical resistivity and S-wave sections as compared to the P- and S-wave velocity sections (Fig. 10). Similar to results obtained at Site 1, the resistivity and S-wave velocities of the shallow-seated rocks at Site 2 are overall low, largely ranging between ~7 to 570 ohm.m, and ~200 to 700 m/s, respectively. Within the mapped near-surface zone (i.e., the top ~12 m) there are three zones of higher

resistivity (observed as light green-, yellow-, red- and black-coloured zones). The first zone, characterized by the highest resistivity (~700 – 4946 ohm.m) is located on the western side of the profile, situated at a lateral distance of 0 to ~16 m and extending from the surface to a depth of ~3 m. This zone is interpreted to correspond to a zone of boulders. The second resistivity high zone (~60 – 600 ohm.m) is situated at a lateral distance of ~10 to ~35 m, and extends from a depth of ~3 to ~12 m. The third resistivity high zone, with similar resistivities to the second high resistivity zone is observed on the western side of the profile, at a lateral distance between 35 to 80 m, and at a depth between ~2 and 12 m. Both second and third resistivity high zones are overlain by and enclose a low resistivity zone (~12 to 70 ohm.m), which extends to depths beyond the ERT survey limits. Both second and third resistivity high zones as well as the resistivity low zone present on the ERT section are closely matched by the S-wave results (compare Fig. 11a to b).

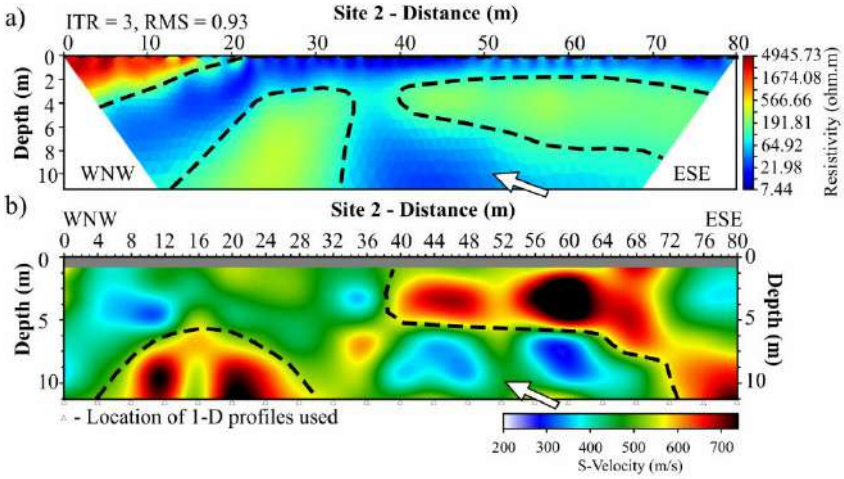


Figure 11: Comparison of electrical resistivity (Dipole-dipole array) pseudosection (a) and S-wave tomography (b) obtained at Site 2. The white arrows indicate the water- and salt- saturate or clay rich unit. The water- and salt- saturate or clay rich unit is also traced out using the black dashed lines in both sections.

The high resistivity and high velocity S-wave zones likely correspond to least-weathered and least water- and salt-saturated zones. The low resistivity and shear-wave velocity zone (dark-light blue to greenish coloured zones) separating the resistivity high zones is interpreted as a highly-weathered zone with a possible high content of conductive minerals and/or water- and salt-saturation, which is altogether a zone that is likely highly hydraulically conductive.

Site 3

Figure 12 shows P- and S-wave tomograms at Site 3, along with their corresponding conceptual models. Similar to the P- and S-wave sections at previous sites, the tomograms at this site reveal the presence of two weathering zone, i.e., the overburden and semi-weathered bedrock. The overburden is characterised by P-wave velocities ranging from ~400 to 1500 m/s and S-waves velocities ranging from 200 to ~650 m/s.

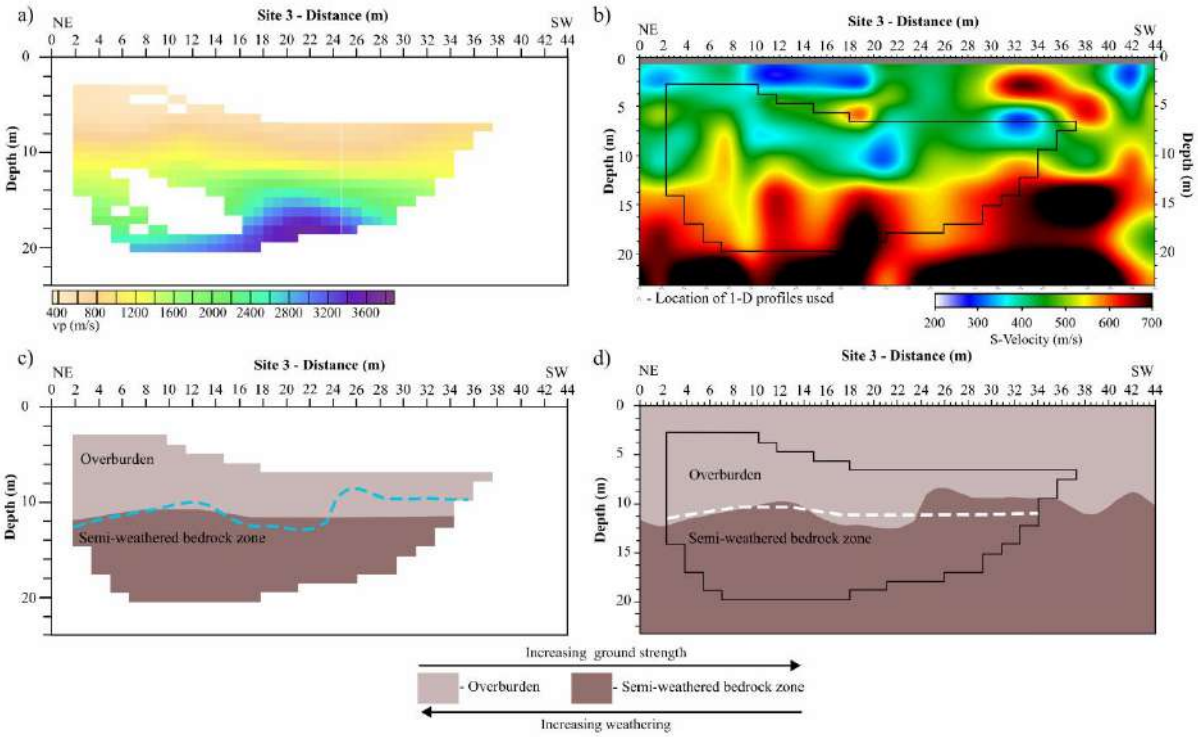


Figure 12: Comparison of P-wave (a) with S-wave (b) velocity tomographs at Site 3. (c) and (d) are interpreted conceptual models for the P-wave and S-wave in (a) and (b), respectively. The conceptual

models show the variation in weathering with depth. The dashed blue line in (c) illustrates the interpreted overburden/semi-weathered boundaries deduced from the S-wave tomography in (b) and projected onto the P-wave tomography conceptual model, white the dashed white lines in (d) the P-wave tomography projected onto the S-wave tomography.

The semi-weathered bedrock layer is characterised by P-wave velocities ranging from ~1500 m/s to 3800 m/s and S-waves ranging between ~650 to 700 m/s. The P- and S-wave results are well correlated between each other (compare Fig. 12a to b) and, similar to the other sites, S-wave results demonstrate the presence of least-weathered zones within the overburden zone and highly-weathered zones within the semi-weathered near-surface zone.

Figure 13 shows the electrical resistivity (Schlumberger arrays) and S-wave velocity (V_s) pseudosection obtained at Site 3, to note is that the first 30 m of the resistivity section corresponds with the last 30m of the S-wave section.

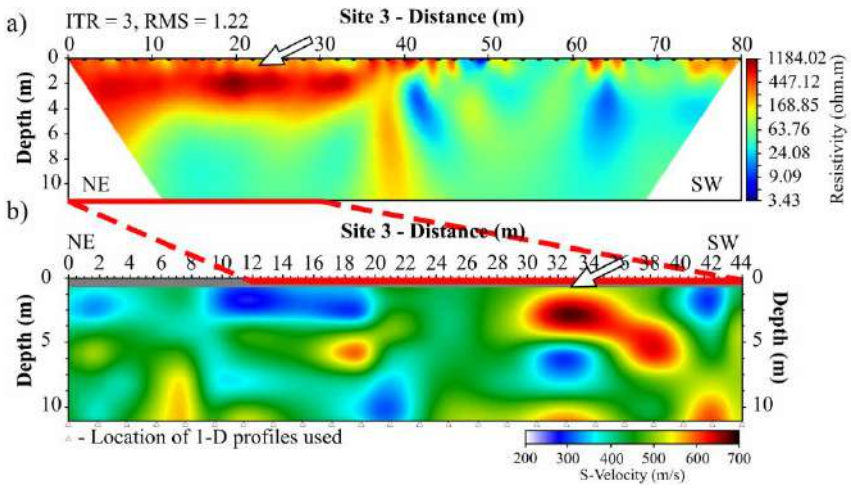


Figure 13: Comparison of electrical resistivity (Schlumberger array) pseudosection (a) and S-wave tomography (b) obtained at Site 3. The red solid and dashed lines illustrate where the two profiles overlap, and the white arrows indicate the directly correlating (high resistivity and S-wave velocity) near-surface boulder zone.

At the depths resolved by the resistivity survey (from 0 to ~11 m below surface), the obtained resistivities and S-wave velocities are generally low, similar to those at the two previous sites investigated, ranging between ~3 to ~1200 ohm.m, and ~200 to ~700 m/s, respectively. Like at other sites, these results also suggest extensive weathering, and the presence of conductive and less compact subsurface sediments. Within the mapped low-resistivity and S-wave velocity zones, on the north-eastern flank, from a depth of ~2 to 7 m and at lateral distances between 0 and ~45 m on the resistivity section (Fig. 13a); and from a lateral distance of 18 to 42 m on the S-wave section (Fig. 13b), notable near-surface high resistivity ((>400 ohm.m, dark red-black coloured) and S-wave velocity (yellow-red coloured) zones (>500 m/s) are observed. These zones are interpreted as least-weathered dense soils, possibly also containing boulders. The high resistivity and S-wave velocity features also exhibit discontinuities, or lower resistivity and S-wave zones (high hydraulic conductivity zones), which are likely caused by rock mass fracturing. At depths around 11 m, the low shear-wave velocity zone is underlain by a zone of higher shear wave velocity (>600 m/s), better observed in Figure 12b, likely corresponding to the semi-weathered bedrock zone.

Discussion

The P-wave, S-wave and electrical resistivity tomograms provide a basis for the interpretation of near-surface characteristics in the study area. In Figure 14 we propose an interpretative geological cross-section of the near-surface aquifer zone at the mine, based on borehole data combined with all geophysical methods applied at the three sites.

Overburden characteristics

The overburden, which constitutes the top ~9 m of the study area is characterized by low resistivities, and low P- and S-wave velocities (Figs. 8 to 13). These results indicate a high electrical conductivity and high weathering within the overburden, in turn suggesting a high

porosity and clay content zone (which can be very conductive in a wet medium), with moderate to high levels of moisture held by soil particles and a possible high availability of nutrients/soluble salts (e.g., sodium, calcium, magnesium, potassium) (Theron and van Niekerk, 1934; Grisso et al., 2005). Results from this study align with the overburden characteristics of the area (Fig. 14a). Specifically, Theron and Niekerk (1934) detail that the region is characterized by black turf soil (heavy clay soil) that is highly fertile (nutrient rich) and capable of retaining moisture.

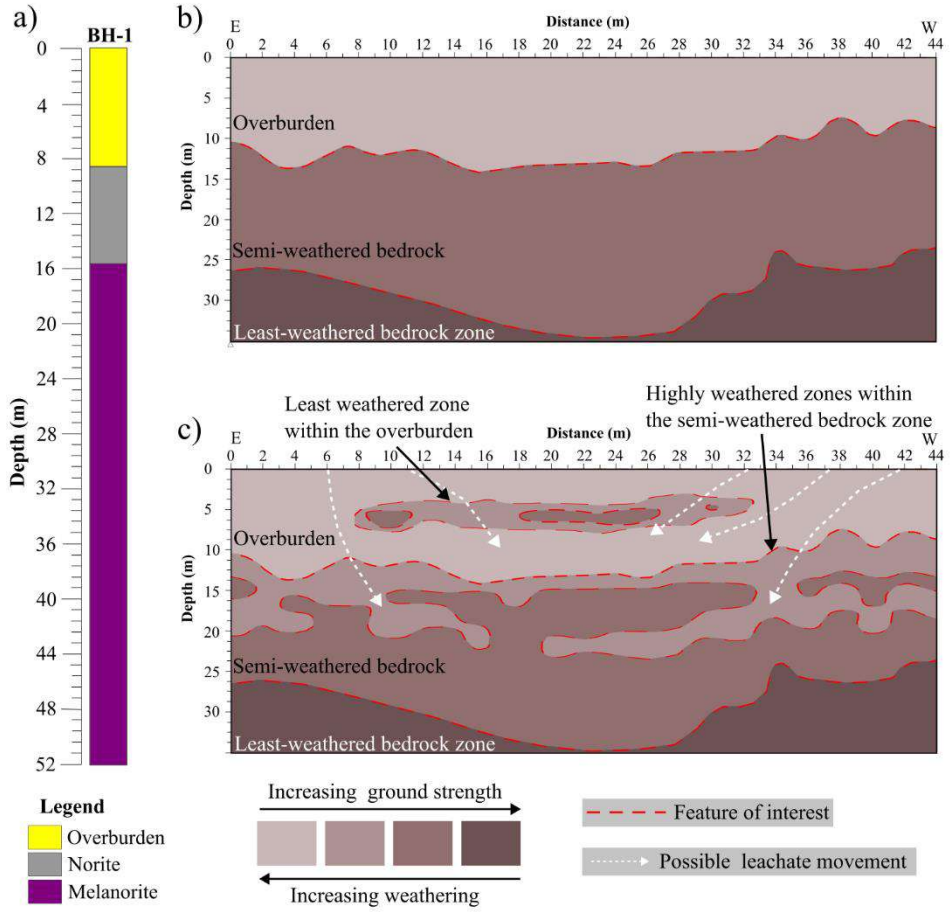


Figure 14: (a) Borehole BH-1, taken from approximately 1.5 km west of the study areas. The borehole illustrates the rock types present in the study area. (b) Conceptual model of the study area, deduced from the knowledge obtained from the acquired data, illustrating variation in layering/ ground strength/ weathering. (c) Complex weathering within the overburden and semi-weathered zones, and possible

leachate migrations pathways within the near-surface. No weathering detail is given for the least-weathered bedrock zone to avoid over interpretation.

The soil formed from the chemical weathering of the underlying RLS rocks (i.e., in the study area: norite and melanorite). Black turf soil is readily pervious to water (permeable) but has a high-water holding capacity that reduces leaching, especially in sub-humid and semi-arid climatic zones. The soil has a highly developed crumb structure and a clay content that varies from 40 to 60%, and a moisture equivalent commonly ranging between 40 to 50% (Theron and van Niekerk, 1934; Oppermann et al., 2017). The turf soil overburden in the western limb of the Bushveld Complex varies between ~1 to 5 m in thickness (De Klerk, 1982; Oppermann et al., 2017). Within the overburden, black turf soils constitute the A-horizon. The A-horizon progresses into the yellow-coloured C-horizon, which varies greatly in depth (from 12 to 50 m) and consists of partially weathered mafic rocks (Titus et al., 2009). The C-horizon is underlain by the R-horizon, which corresponds to unweathered bedrock, characterized by norite and melanorite in the studied area (Fig. 14a). Together, the A – AC – C horizons constitute the soil horizon sequence of the study area. (Theron and van Niekerk, 1934; Oppermann et al., 2017).

Near-surface setting and water inflow implications

The low P- and S-waves velocities, and resistivity zone at the sites of interest (Fig. 2), largely extend from the surface to depths greater than those resolved by the P-wave, S-wave, and electrical resistivity surveys (Figs. 8 to 13). The overburden zone, characterized as a low P-wave, S-wave and electrical resistivity zone, suggests highly to semi-weathered and possibly fractured rocks (Table 2; Fig. 14a to c). According to available borehole data, located approximately 1.5 km west of the study areas, the stratigraphic sequence (up to 54 m) begins with the overburden, characterized as a highly weathered soil to saprolite zone, extending to a

depth of ~9 m. With increasing depth, the overburden is underlain by norite (~9 m) and finally melanorite (>36 m) (Fig. 14a). We observe a good correlation when comparing the thickness of the identified overburden zone from the P-wave, S-wave and resistivity sections with the borehole data (compare Figs. 8 to 13). Unfortunately, due to the dipping nature of the Bushveld Complex rocks and the distance of the borehole from the studied sites, the variation of P-waves, S-waves and electrical resistivity sections at depths greater than the overburden zone could not be determined. Overall, results suggest that in the studied areas, the variation in the weathered zone (i.e., from overburden to semi-weathered bedrock in Fig. 14b to c) is complex and extends to a depth greater than that suggested by the borehole data (compare depths from Fig. 14a to b). This is not surprising, as the western limb of the Bushveld Complex is characterized by deep weathering, extending approximately 25 to 40 m deep (Hey, 1999; Junge et al., 2019).

Table 2: Surface wave seismic velocity and electrical resistivity physical property table of rocks (modified after Kirsch, 2006).

Soil Profiles Type	**Rock/soil description**	**Average S-wave velocity (m/s) top 30 m**		**Rock type**	**Resistivity (ohm.m)**
A	Hard rock	> 1,500		Gravel, sand (dry)	500 – 2,000
B	Rock	760 – 1,500		Gravel, sand (saturated)	40 – 200
C	Very dense soil/soft rock	360 – 760		Fractured rock	60 – 2,000
D	Stiff soil	180 – 360		Solid rock	>2,000
E	Soft soil	<180		Till	30 – 60
F	Special soils requiring site-specific evaluation			Clay	10 – 30

In the inversion models, roughly where norite appears on the borehole data (i.e., about 9 m deep), the P- and S-wave velocities, and electrical resistivities increase, suggesting a boundary and presence of a semi-weathered bedrock zone (norite/melanorite) below the overburden zone. This zone is better observed in both the P- and S-waves sections (Figs. 8 to 13). The semi-weathered bedrock zone appears to be highly fractured and possibly water- and salt-saturated (Table 2; Kirsch, 2006). In the western limb of the Bushveld Complex Gebrekristos and Cheshire (2012) report that the depth of the semi-weathered (weathered aquifer) zone extends to approximately 35 m, similar to the maximum depth of the semi-weathered bedrock zone mapped across Tharisa Mine (Figs. 8 to 14). Gebrekristos and Cheshire (2012), state that the depth and degree of weathering (including in this zone) varies across the Bushveld Complex and is dependent on the underlying lithologies and site-specific physio-chemical conditions. Considering that pre-mining studies conducted within the Tharisa Mine region established that ground water levels were, on average, 10 m below ground level (mbgl) and had a depth range of 2 to 30 mbgl (Cuthbertson, 2022), suggests that the overburden zone forms part of the weathered aquifer zone that is characteristic of the Bushveld Complex.

Below the semi-weathered bedrock aquifer zone is the least-weathered (crystalline) bedrock zone (Fig. 8). The obtained results demonstrate a clear succession from overburden (soil-boulder zone) to semi-weathered bedrock zone (corresponding to the weathered aquifer zone), to the least-weathered (crystalline) bedrock zone with increasing depth, as depicted in the conceptual model of the study area (Fig. 14b, c). It is likely that the least-weathered bedrock zone is fractured and weathered to depths beyond those mapped by the surveys conducted, as indicated by published reports (Hey, 1999; Lourens, 2013; Van Wyk, 2013; Fourie et al., 2017; Govender, 2019; Junge et al., 2019). Generally, in the absence of secondary fractures, the least-weathered bedrock zone forms poor aquifers (in fact, aquitards) due to the insignificant porosity of the rocks. In the presence of regional and/or secondary fractures, high-yielding

aquifers can develop in his crystalline rock zone. The aquifer (i.e., the crystalline aquifer) formed in the least-weathered bedrock zone are often connected with the weathered aquifers and can extend to depths of about 130 – 140 m below ground level (Gebrekristos and Cheshire, 2012). Our results suggest that the water inflow into the pits at Tharisa mine is therefore most probably coming from both the weathered and least-weathered aquifers, as mining is currently happening at depths below the water level of these aquifers (i.e., below 70 mbgl). In addition to the weathered and least-weathered aquifers, there lies a possibility that more sources contribute to the flow of water inside the mine, such as the river (Sterkstroom river) cross cutting the mine lease area and alluvial aquifers associated with the river, making it a possible combined effect of both near-surface groundwater and the surface water flow systems. Dildar et al. (2023) illustrates that some of the water flooding the Tharisa Mine pits is coming from multiple sources, including from the Sterkstroom river, surface water, circulating water coming from deep crystalline sources rising into the pits, water recycling through lineaments around the mine, and tailings dam seepages.

Implications for the management of groundwater systems in the Bushveld Complex

Surface water and groundwater systems are complex and interconnected components that interact in a variety of physiographic and climatic landscapes (Sophocleous, 2002). The contamination of one system can lead to the contamination of the other, depending on several factors, e.g., climate and contaminant concentrations in the systems (Westbrook et al., 2005). The ubiquitous fracturing of the Bushveld Complex rocks, permeable nature of the soils and apparent high hydraulic conductivity (observed from the obtained results), suggest that, if a tailings dam, such as the ones present at the Tharisa Mine, was to leak contaminants or fail, these contaminants are likely to contaminate the shallow bedrock aquifer/s in the region. However, it is difficult to quantify how high the contamination risks are, as such risks depend

on multiple factors, such as: the design of the tailing dam, the type of mine waste contained, age and condition of the dams, underlying lithologies and geological structures (e.g., faults), amongst others. Thus, we cannot decisively ascertain if underground water in the study and its adjacent area is at a high risk of contamination if the tailings dams were to leak contaminants or fail. However, it is such studies that provide knowledge and understanding of the possible effects of tailings dam failures, such as the recent Jagersfontein dam collapse, South Africa (Torres-Crus and O'Donovan, 2023). Fortunately, in the study area, the mine complies with waste legislation, recycles produced hazardous waste (e.g., oil) and builds tailings dams that are lined appropriately to prevent the contamination of underground water, thus mitigating certain risks.

Generally, rocks with connected and closely-spaced fractures favour the circulation of hydrous fluids, while weathering processes enhance the permeability of rocks, including that of igneous rocks (Long et al., 1989; Worthington et al., 2016; Oppermann et al., 2017). Assuming that the near-surface characteristics observed along the survey lines are typical of the near-surface features in the nearby agricultural, municipal and mining areas. The observed presence of weak zones (fracture zones - possible high hydraulic conductivity zones), and deep and extensive weathering (broken-down near-surface rocks) (Fig. 14 b-c) implies that the shallow aquifers in the area are vulnerable to contamination from agricultural, municipal and mining activities. Anthropogenic sources that may contaminate the aquifers include the release of industrial effluents and untreated wastewater, acid mine drainage, urban and agricultural runoff, and infiltration-percolation of water from polluted sites (e.g., landfill) (Verlicchi and Grillini, 2020). These contamination sources often contain hazardous dissolved metals (e.g., heavy/toxic metals), nutrients and pesticides that may pose high contamination risks for: underground water systems, ground water dependent irrigation systems, the food chain, and animal and human health (Lumbroso et al. 2019; Verlicchi and Grillini, 2020). The

contaminants may also penetrate deeper into the subsurface, using known weak zones (e.g., fractures and lithological boundaries) present in the area, contaminating the deeper fractured aquifer/s as well. Figure 14c illustrates possible leachate migration pathways; however, considering that the Bushveld Complex rocks are highly fractured and weathered and that the overburden is permeable, it is likely that there are numerous additional possible leachate migration pathways. In Figure 14c no weathering detail is given for the least-weathered bedrock zone because the acquired data did not have enough depth resolution to revolve detail at those depths, however, it is most likely that the zone is fractured and weathered to depths beyond what was mapped. Fortunately, deep least-weathered bedrock aquifers are generally not at risk of contamination from surface and near-surface activities because of their: 1) deep and confined nature; 2) low primary fracture porosity; and 3) large depths and hydrostatic pressures, which result in small fracture sizes and decreased interconnectivity (Lourens, 2013; Fourie et al., 2017; Govender, 2019).

In a study conducted by Molekoa et al. (2019) in the Mokopane area, located on the central portion of the northern limb of the Bushveld Complex (Fig. 1), the groundwater was noticeably enriched by fluoride and sulfate ions. Molekoa et al. (2019) inferred that the rock-water interaction was responsible for fluoride enrichment; and poor sewage management in the area resulted in the leaching of organic matter, sewage and agricultural runoff, in turn carrying unutilized sulphate ions and introducing secondary salts (i.e., chlorine and sulphate ions) in the groundwater. The findings of Molekoa et al. (2019) partially confirm that the shallow bedrock aquifers in the Bushveld are at risk of contamination from both natural and anthropogenic (i.e., mining, municipal and agricultural) activities. Importantly though, the overall results obtained by Molekoa et al. (2019) showed that, despite the presence of industrialization, municipal and agricultural activities in the area, the groundwater quality in the region was still good. Nonetheless, our study demonstrates that the shallow aquifers in the study area are at risk of

contamination and that gaining knowledge and understanding of the near-surface in the region is perhaps the best way to monitor and protect groundwater systems.

Conclusion

We used an integrated approach involving refraction seismic tomography, multichannel analysis of surface waves and electrical resistivity tomography (ERT) methods to map and characterise the weathered and partially, the least-weathered bedrock aquifer systems at Tharisa mine, located in the western limb, southwestern portion, of the Bushveld Complex. The surveys produced complex but largely correlating and complementary geophysical results. All three methods mapped zones of increasing velocities and resistivities quite well, while the S-wave and ERT methods mapped low velocity and resistivity zones within the near-surface in a satisfactory and complementary manner, demonstrating the advantages of conducting integrated studies. Generally, the results reveal the prevalence of extensive and deep weathering, possible high hydraulic conductivity zones, and the variation in weathering with depth, mainly associated with the overburden zone, semi-weathered bedrock zone (which hosts the semi-weathered aquifer), and the crystalline bedrock zone, where aquifers are associated with joints and fractures. Currently, the pit at Tharisa Mine is about 70 m deep; consequently mining activities occur in both the weathered and crystalline aquifer zones. Water inflows are produced by the flow of water from both the weathered and crystalline aquifers.

By combining the aforementioned methods, we were also able to gain insights into possible environmental risks. The results show that because of the prevalent near-surface conditions, combined with the unconfined and shallow depth of the weathered and crystalline aquifer zone, municipal, agricultural, and mining activities all present contamination risks for the Bushveld Complex shallow bedrock aquifer/s in the study area. Thus, continued research on the aspect is recommended.

Funding

National Research Foundation; DSI-NRF CIMERA (Centre of Excellence for Integrated Mineral and Energy Resource Analysis).

Author contribution

Sikelela Gomo wrote the manuscript under the supervision of Prof. M.S.D. Manzi, Dr. J.E. Bourdeau, Dr. Bojan Brodic, Prof. G.R.J. Cooper and Prof. R.J. Durrheim. Ndamulelo Mutshata assisted in the resistivity processing, reviewed, and editorialized the manuscript, while Ian James assisted with the P-wave seismic data processing.

Conflict of interest

The author declares no conflict of interest.

Acknowledgments

We would like to acknowledge Tharisa Mine for funding this project and giving us permission to publish this work. Special thanks are due to the NRF (National Research Foundation) and DSI-NRF CIMERA (Centre of Excellence for Integrated Mineral and Energy Resource Analysis) for funding this research project. We also wish to extend our gratitude to the postgraduate students from the School of Geosciences at the University of the Witwatersrand who assisted with the data collection and the Tharisa Mine staff, especially Hloniphani Hlongwa and Robey Labuschagne, for assisting us during the data acquisition. Special thanks to Nathi Mntungwa from Tharisa Mine for scientific discussions and support.

References

Aizawa, T. (2014) Application manual of geophysical methods to engineering and environmental problems. Houten, Netherlands: European Association of Geoscientists and Engineers Publication.

Akintoriwa, O.J., and Olowolafe, T.S., (2013) Geoelectric evaluation of groundwater prospect within Zion Estate, Akure, Southwest, Nigeria. International Journal of Water Resources and Environmental Engineering, 5, 12 – 28, https://doi.org/10.5897/IJWREE12.031.

Alcalá, F.J., Martínez-Pagán, P., Navarro, M., Pérez-Cuevas, J., and Domingo, F., (2021) Combining of MASW and GPR imaging and hydrogeological survey for the groundwater resource evaluation in a coastal urban area in southern Spain. Applied Science, 11, 3154, https://doi.org/10.3390/app11073154.

Ali, A., Ullah, M., Barkat, A., Raza, W.A., Qadir, A., and Qamar, Z., (2021) Multi-channel analysis of surface waves (MASW) using dispersion and iterative techniques: implications for cavity detection and geotechnical site investigation. Bulletin of Engineering Geology and the Environment, 80, 9217-9235, https://doi.org/10.1007/s10064-021-02485-y.

Al-Heety, A.J.R., Hassouneh, M.M., and Abdullah, F.M., (2021) Application of MASW and ERT methods for geotechnical site characterization: A case study for roads construction and infractucture assessment in Abu Dhabi, UAE. Journal of Applied Geophysics, 193, 104408, https://doi.org/10.1016/j.jappgeo.2021.104408.

Batte, A.G., Muwanga, A., Sigrist, P.W., and Owor, M., (2008) Vertical electrical sounding as an exploration technique to improve on the certainty of groundwater yield in the

fracture crystalline basement aquifers of eastern Uganda. Hydrogeology Journal, 16, 1683-1693, https://doi.org/10.1007/s10040-008-0348-4.

Blanchy, G., Saneiyan, S., Boyd, J., McLachlan, P., and Binley, A. (2020) ResIPy, an intuitive open-source software for complex geoelectrical inversion/modeling. Computers and Geosciences, 137, 104423.

Boorman, S. Boudreau, A., and Kruger, F.J., (2004) The Lower Zone-Critical Zone transition of the Bushveld Complex: a quantitative textural study. Journal of Petreology, 45, 1209-1235, https://doi.org/10.1093/petrology/egh011.

Brodic, B., Malehmir, A., Pugin, A., and Maries, G., (2018) Three-component seismic land streamer study of an esker architecture through S- and surface wave imaging. Geophysics, 86, B339-B353, https://doi.org/ 10.1190/GEO2017-0747.1.

Cawthorn, R. G. (2015). The Bushveld Complex, South Africa. In: Charlier, B., Namur, O., Latypov, R., Tegner C. (Eds.), *Layered intrusions*, pp. 517-587. Springer. https://doi.org/10.1007/978-94-017-9652-1_12.

Cuthbertson, S., (2022) Environmental management programme amendment application Tharisa Mine, North West Province. https://gcs-sa.biz/wp-content/uploads/2022/06/21-1200-Tharisa-Minerals-EMPr-Amendment-Report-03062022-Public-Review-Annexures.pdf.

Dai, A., (2013) Increasing drought under global warming in observations and models. Nature Climate Change, 3, 52-58, https://doi.org/10.1038/NCLIMATE1633.

De Klerk, W.J., (1982) The geology, geochemistry and silicate mineralogy of the Upper Critical Zone of the north-western Bushveld Complex, at Rustenburg Platinum Mines,

Union section: Unplublished M.S.c thesis, Grahamstown, South Africa, Rhodes University.

Dildar, J., Manzi, M.S.D., Abiye, T., Gomo, S., Rapetsoa, M.K. and Drennan, G., (2023) Groundwater circulation in the shallow crystalline aquifer of Tharisa Mine, South Africa: evidence from environmental isotopes and near-surface geophysics. Water, 15, 2876. https://doi.org/10.3390/w15162876.

Donnenfeld, Z, Crookes, C., and Hedden, S., (2018) A delicate balance: water scarcity in South Africa. Southern Africa Report 13, Institute for Security Studies.

Eales, H.V., and Cawthorn, R.G., (1996) The Bushveld Complex. Layered Intrusions, Elsevier, 181-229.

Fourie, F.D., Allwright, A.J., Makiwane, N., and Govender, N., (2017) Characterisation and protection of deep aquifers in South Africa: Characterisation. 15th Biennial Ground water Conference, Extended abstract.

Gabriel, G., Kirsch, R., Siemon, B., and Wiederhold, H., (2003) Geophysical investigation of buried Pleistocene subglacial valleys in Northern Germany. Journal of Applied Geophysics, 53, 321-180. https://doi.org/10.1016/j.jappgeo.2003.08.005.

Gebrekristos, R., and Cheshire P., (2012) Hydrogeological properties of the UG2 pyroxenite aquifers of the Bushveld Complex. In Proceedings of the 5th Platinum Conference of the Southern African institute of Mining and Metallurgy, Extended Abstracts, 143-152.

Gomo, S., Rapetsoa, M.K., Manzi, M.S., Onyebueke, E., Dildar, J., Sihoyiya, M., Mutshafa, N., Harrison, W., Bourdeau, J.E., Brovko, O. and James, I., (2023) Integrated geophysical methods for boulder delineation to improve mining. Geophysical Prospecting, 1-21. https://doi.org/10.1111/1365-2478.13322.

Govender, N., (2019) CHARACTERISATION OF THE DEEP AQUIFERS OF SOUTH AFRICA - THE BUSHVELD IGNEOUS COMPLEX, CRYSTALLINE BASEMENT ROCKS AND DOLOMITE FORMATIONS (Doctoral dissertation, University of the Free State), pp. 12.

Grisso, R.D., Alley, M.M., Holshouser, D.L., and Thomason, W.E., (2005) Precision farming tools: Soil electrical conductivity. Virginia Cooperative Extension, 442-508.

Hasan, M., Shang, Y., Meng, H., Shao, P., and Yi, X., (2021) Application of electrical resistivity tomography (ERT) for rock mass quality evaluation. Nature, 11:23683, https://doi.org/10.1038/s41598-021-03217-8.

Hey, P.V., (1999) The effects of weathering on the UG2 Chromitite reef of the Bushveld Complex, with special reference to the platinum-group minerals. South African Journal of Geology, 3, 251-260.

Holt, S.M., (2000) Sources of chemical contaminants and coutes into the freshwater environment. Food and Chemical Toxicology, 38, S21-S27.

Roberts, M.K.C., and Clark-Mostert, V., (2010) Is there some commonality between the geological structures in the Bushveld Complex and the Great Dyke?. The 4th international platinum conference, platinum in transition 'Boom or Bust', The Southern African Institute of Mining and Metallurgy.

Junge, M., Oberthür, T., Kraemer, D., Melcher, F., Pina, R., Derrey, I.T., Manyeruke, T., and Strauss, H., (2019) Distribution of platinum-group elements in pristine and near-surface oxidized Platreef ore and the variation along strike, northern Bushveld Complex, South Africa. Mineralium Deposita, 54, 885-912, https://doi.org/10.1007/s00126-018-0848-7.pdf.

Junge, M., Oberth*ü*r, T., Osbahr, I., and Gutter, P., (2016) Platinum-group elements and minerals in the lower and middle group chromitites of the western Bushveld Complex, South Africa. Mineralium Deposita, 51, 841-852, https://doi.org/10.1007/s00126-016-0676-6.

Kearey, P., Brooks, M., and Hill, I., (2002) An Introduction to Geophysical Exploration (3rd ed). Maiden, MA Blackwell Science, pp. 196.

Kirsch, R., (2006) Groundwater Geophysics - A tool for hydrogeology. Springer.

Lourens, P.J.H., (2013) THE RELATION BETWEEN SOUTH AFRICAN GEOLOGY AND GEOHYDROLOGY (Masters dissertation, University of the Free State), pp. 164.

Long, J.C.S., Hestir, K., Karasaki, K., Davey, A., Peterson, J., Kemeny, J. and Landsfeld, M. (1991) Fluid Flow in Fractured Rock: Theory and application. Springer Netherlands, pp. 203-241.

Lumbroso, D., McElroy, C., Goff, C., Collell, M.R., Petkovsek, G., and Wetton, M., (2019) The potential to reduce the risks posed by tailings dams using satellite-based information. International Journal of Disaster Risk Reduction, 38, 101209, https://doi.org/10.1016/j.ijdrr.2019.101209.

Malehmir, A., Bergman, B., Anderson, B., Sturk, R., and Johansson, M., (2018) Seismic imaging of dyke swarms within the Sorgenfrei-Tornquist Zone (Sweden) and implications for thermal energy storage. Solid Earth, 9, 1469-1485, https://doi.org/10.5194/se-9-1469-2018.

Meza, I., Rezaei, E.E., Siebert, S., Ghazaryan, G., Nouri, H., Dubovyk, O., Gerdener, H., Herbert, C., Kusche, J., Popat, E., Rhyner, J., Jordaan, A., Walz, Y., and Hagenlocher, M., (2021) Drought risk for agricultural systems in South Africa: Drivers, spatial

patterns, ad implications for drought risk management. Science of the Total Environment, 799, 149505, https://doi.org/10.1016/j.scitotenv.2021.149505.

Molekoa, M.D., Avtar, R., Kumar, P., Minh, H.V.T., and Kurniawan, T.A., (2019) Hydrogeochemical assessment of groundwater quality of Mokopane Area, Limpopo, South Africa using statistical approach. Water, 11, 1891, https://doi.org/10.3390/w11091891.

Oppermann, L., Junge, M., Schuth, S., Holtz, F., Schwarz-Schampera, U., and Sauheitl, L., (2017) Mobility and distribution of palladium and platinum in soils above Lower and Middle Group chromitites of the western Bushveld Cmplex, South Africa. South African Journal of Geology, 120.4, 511-524, https://doi.org/10.25131/gssajg.120.4.511.

Park, C.B., Miller, R.D., and Xia, J., (1999) Multi-channel analysis of surface waves (MASW). Geophysics, https://doi.org/10.1190/1.1444590.

Poulsen, L.H., and Christensen, N.B., (1999) Hydrogeophysical mapping with the transient electromagnetic sounding method. European Journal of Environmental and Engineering Geophysics, 3, 201-220.

Salas-Romero, S., Malehmir, A., Snowball, I., and Brodic, B., (2021) Geotechnical site characterisation using multichannel analysis of surface waves: A case study of an area prone to quick-clay landslides in southwest Sweden. Near Surface Geophysics, https://doi.org/10.1002/nsg.12173.

Scoates, J.S., Wall, C.J, Friedman R.M., Weis, D., Mathez, E.A., and VanTongeren, J.A., (2021) Dating the Bushveld Complex: timing of crystallization, duration of

magmatism, and cooling of the World's largest layered intrusions and related rocks. Journal of Petrology, 62:egaa107. https://doi.org/10.1093/petrology/egaa107.

Shankar, K.R., (1994) Groundwater exploration. Affordable Water Supply and Sanitation 20th WEDC Conference, 225-228.

Sharma, R.S., and Al-Busaidi, T.S., (2001) Groundwater pollution due to a tailings dam. Engineering Geology, 60, 235-244.

Singhal, B.B.S., and Gupta, R.P., (2010) Applied Hydrogeology of Fractured Rocks. Springer, London, United Kingdom.

Sophocleous, M., (2002) Interactions between groundwater and surface water: the state of the science. Hydrogeology Journal, 10, 52-67, https://doi: 10.1007/s10040-001-0170-8.

Telford, W.M., Geldart, L.P., and Sheriff, R.E. (1990) Applied Geophysics Second Edition. Cambridge University Press. United Kingdom, pp. 283 and 286.

Theron, J.J., and van Niekerk, P. Le R., (1934) The nature and origin of black turf soils. South African Journal of Science, 31, 320346.

Titus, R., Wittüser, K., and Walters, B., (2009) Groundwater and mining in the Bushveld Complex. Abstracts of the International Mine and Water Conference, Extended Abstracts, 178-294.

Torres-Cruz, L.A. and O'Donovan, C., (2023) Public remotely sensed data raise concerns about history of failed Jagersfontein dam. Scientific Reports, 13, p.4953.

Tryggvason, A., Rögnvaldsson, S., ður, T., Flóvenz, Ó.G., (2002) Three-dimensional imaging of the P- and S-wave velocity structure and earthquake locations beneath Southwest

Iceland. Geophys. J. Int. 151, 848–866. http://dx.doi.org/10.1046/j.1365-246X.2002.01812.x.

Twidale, C.R., and Romani, J.R.V., (2005) LANDFORMS AND GEOLOGY OF GRANITES TERRAINS. Taylor and Francis Group, London, United Kingdom.

USGS (2023). Mineral commodity summaries 2023. U.S. Geological Survey, pp. 214. https://doi.org/10.3133/mcs2023.

Van Schoor, M., and Fourie, C.J.S. (2015) A guide for APPLYING GEOPHYSICS to COAL MINING PROBLEMS in South Africa. Struik Nature, South Africa, pp. 43-42, 90-91.

Van Wyk, E., (2013) Southern African pre-Cretaceous deep groundwater flow regimes: Evidence and drivers. In Proceedings of the 13th Biennial Ground Water Division Conference and Exhibition. Extended Abstract.

Verlicchi, P., and Grillini, V., (2020) Surface water and groundwater quality in South Africa and Mozambique – analysis of the most critical pollutants for drinking purposes and challenges in water treatment selection. Water. 12, 305, https://doi.org/10.3390/w12010305.

Westbrook, S.J., Rayner, J.L., Davis G.B., Clement, T.P., Bjerg, P.L., and Fisher, S.J., (2005) Interaction between shallow groundwater, saline surface water and contaminant discharge at a seasonally and tidally forced estuarine boundary. Journal of Hydrology, 302, 255-269, https://doi.org/10.1016/j.jhydrol.2004.07.007.

Wilson, A.H., Jermy, C.A., and Ridgeway, M., (2005) Rock strength and physical properties of norites of the Merensky and Bastard Units, western Bushveld Complex. Geological Society of South Africa 108, 525-540.

Worthington, S.R.H., Davies, G.J., and Alexander Jr, E.C. (2016) Enhancement of bedrock permeability by weathering. Earth-Science Reviews, 160, 188-202, https://doi.org/10.1016/j.earscirev.2016.07.002.

Xia, J., Miller, R.D., and Park, C.B. (1999) Estimation of near-surface shear-wave velocity by inversion of Rayleigh waves. Geophysics, 64, 691-700.

Zhang, J., and Toksöz, M.N. (1998) Nonlinear refraction traveltime tomography. Geophysics, 63, 1726-1737, https://doi.org/10.1190/1.1444468.

Zientek, M.L., Douglas Causey, J., Parks, H.L., and Miller, R.J. (2014) Platinum-Group Elements in Southern Africa-Mineral Inventory and an assessment of Undiscovered Mineral Resources; Scientific Investigations Report 2010–5090–Q, 010, 2010; U.S. Geological Survey: Reston, VA, USA.

12. DISCUSSION

These studies have shown that a reappraisal of legacy reflection seismic data with the present arsenal of new processing and especially interpretational advanced techniques such as attribute mapping yields improved high-resolution imaging of the targeted mineralization or orebody and additional structures not extracted before. Also, the study has demonstrated that the integration of novel multi-geophysical methods can be successful in mapping near-surface groundwater aquifers, boulders, and delineate fractures, and faults in the open pit mining environments. As examples of these advances Papers I and II are submitted as studies from the Witwatersrand Basin for gold exploration and mining and Papers III, IV and V are studies conducted in the Bushveld Complex not only for platinum exploration and mining but also to rase awareness of where fractures and faults could exacerbate possible wall collapse.

Paper I: The surface geology of the two 2D seismic profiles contains areas of dolomitic rocks belonging to the Malmani Subgroup (Transvaal Supergroup) that are well known to cause scattering of seismic energy at the near surface, thus preventing energy propagation into the subsurface. The purpose of the study was to image the BLR below the dolomite and complex geological structures down to 3.5 km depth below the ground surface, intended for mining at the KDC East Mine, using seismic data. Although the gold-bearing horizon's thickness (< 1 m) prevents direct seismic imaging, the BLR mapping is possible due to a strong seismic reflection produced at the contact between the hanging wall (dolomitic rocks) and underlying (basaltic Ventersdorp rocks) stratigraphic units. Comparing PreSDM and PreSTM approaches, PreSDM performs better in imaging complex subsurface geological structures. PreSTM sections for both profiles prove inadequate due to energy dispersion in areas of rapid vertical and lateral velocity changes. The PreSDM approach improves subsurface imaging in regions with changing velocity fields, contributing to better data quality during depth imaging. The raw data possess a relatively good signal-to-noise ratio with clear first breaks across offsets. However, imaging of reflections is hindered by the scattering of seismic energy due to karst weathering of the dolomite outcrops in the Malmani Subgroup. This underscores the complexities and challenges of seismic imaging in this geological setting. The results from this study are encouraging and show the added value of these new approaches in reviving legacy seismic data for mineral exploration in hard-rock environments.

Paper II: The main purpose of the study was to reprocess legacy seismic data to improve the imaging of the Ventersdorp Contact Reef (VCR) gold orebody, situated at depths between 2400 and 4100 m below ground surface in the Fochville mining region, South Africa. The

legacy unmigrated stacked data (processed by the contractor in 1998) was made available, however, there was no information regarding the original processing workflow.

The results of the reprocessed stacked section showed an improvement in the imaging of reflectors and delineation of faults. The Kirchhoff pre-stack time migration (PreSTM) and Phase shift migration (PSMIG) were performed on the seismic data. The comparison between these two techniques illustrates the PSMIG's superiority over the Kirchhoff PreSTM for imaging events with moderately varying lateral velocities, since the PSMIG handles steep dips and curved reflectors better than Kirchhoff PreSTM. Borehole logs and surface geology were used to constrain the interpretation of the profile, and the seismic results and borehole information showed strong correlation. The final interpreted seismic section shows several reflections associated with the orebody dipping towards the SW and suggests their continuation to depths of greater than 4 km. The study illustrates that reprocessing legacy data can help to gain new insights on the structural architecture in the geology that underlies the mining area. The legacy seismic data from this profile showed the importance of today's seismic technologies for mineral exploration through reappraisal.

Paper III: Integrated geophysical data were used to map boulders and geological features that have the potential to impede mining activities in open pit mines. The results show that by targeting weathering, structural and magnetization effects in 'magnetic' subsurface rocks, geological features that characterize and complicate mining activities can be successfully identified. The electrical resistivity and seismic results correlate well with the borehole data, and this is illustrated by core-loss section that corresponds with zones of low resistivity and velocity. Notably, the high-resolution resistivity depth section shows several high resistivity features (boulders) embedded in a zone of low resistivity along the profile in the study area. Some of these boulders were outcropping on surface. The presence of buried boulders is also observed in the GPR radargram as diffractions. In areas where boulders were identified, a magnetic high anomaly embedded in a low magnetic zone is observed, which is interpreted to be associated with the less-weathered nature of the boulders as compared to the host rock. By using a combination of geophysical methods, with surface geological observations and borehole lithological data, the delineation of boulders at Tharisa mine was achieved successfully. This was archived by targeting weathering, structural and magnetization effects in subsurface rocks in magnetic environments. Several boulders have been observed in the Bushveld Complex of South Africa, where they become exposed by mining operations. The

successful identification of such boulders in the direction of mining is very important in identifying threats and gives time for mitigation measures to be planned.

Paper IV: Because of geological characteristics (fractures, faults, and dykes) that compartmentalize the rock mass, most open pit mines face the difficulty of rock slope stability. These challenges encouraged the undertaking of a study using multi-geophysical methods to delineate fractures and faults in an active open pit mine. The methods utilized to address the challenges faced by open pit mines include seismic, magnetic and electrical methods. The reflection seismics was used to image the deeper discontinuities and mineralization contacts, ground magnetic surveying to delineate dykes and fractures, while the resistivity method was employed to map contacts of the mineralization. The results revealed fractures within the open pit mine (Tharisa), suggesting multiple factors that contributed to the fracture system, namely, induced fractures that were reactivated during the intrusion of dykes, or due to mine blasting. The fractures may also act as conduits of water through the rock mass. Multiple geophysical approaches were used to understand and image structures with variable geometry and orientation at different depths. In this study, results from the reflection seismic technique revealed that we can image the deeper discontinuities and the mineralization contacts.

Paper V: The groundwater inflow into a mining excavation is mainly a consequence of the interaction between the groundwater system, hydro-geological characteristics of the rock mass and the mining geometry. The water inflow regime is determined by the incision of one or more aquifers by the mining excavation and the relative hydrogeological characteristics of the various aquifers. Ground geophysical techniques were employed to map groundwater aquifers in an open pit mine (Tharisa). The study area overburden is characterized by low P-wave and S-wave velocities and resistivities, which suggests highly to semi-weathered and possibly fractured rocks. Based on the results generated by seismic refraction tomography (SRT), multichannel analysis of surface waves (MASW) and electrical resistivity tomography (ERT), the interpretative geological cross-sections of the near-surface aquifer zone at the mine were developed. The interpretations were constrained by surface geology and borehole data located approximately 1.5 km northwest of the study area. The results suggest that the water inflow into the pits at Tharisa mine is most probably coming from both the weathered and crystalline aquifers, as the mining is currently happening at the depths below the water levels of these aquifers. It is also possible that the bedrock zone has been fractured and weathered to depths greater than those recorded by the surveys, as suggested by published reports around the Bushveld Complex. The intense fracturing of the Bushveld complex rocks, permeable nature

of the soils and apparent high hydraulic conductivity suggest that if the tailings dam was to leak contaminants or fail, these contaminants are likely to contaminate the shallow bedrock aquifers in the region. However, quantifying the contamination hazards is challenging since such risks are reliant on a number of factors, including the tailing dam's design, the kind of mine waste stored, and the age of the structures.

13. CONCLUSION

This thesis has shown that by using the latest processing algorithms to reprocess and interpret the legacy reflection seismic data, the delineation of mineral deposits and geological structures such as faults, dykes and sills can be improved. This was demonstrated using two case studies of legacy reflection seismic data from the Witwatersrand Basin. The first case study is presented in Paper I and is from Kloof-Driefontein Complex (KDC) East Mine and the second case study is part of Paper II and is from the Fochville mining area. The results from these two case studies are encouraging showing that today's processing tools can much improve the imaging of the gold orebodies (Ventersdorp Contact Reef and Black Reef) at both shallow and deeper depths if the correct processing parameters are applied. The seismic interpretation in the second case study was constrained by the surface geology and borehole logs that were fortunately drilled close to the profile, whereas the seismic interpretation of the first case study was only constrained by surface geology as there were no boreholes logs made available for this study area.

The three case studies from the Bushveld Complex involved the acquisition of multi-geophysical data with the primary aims of delineating boulders, mapping fractures and groundwater aquifers in an open pit mine (Tharisa mine). Different geophysical datasets were acquired, including electrical resistivity tomography, magnetics, seismic, ground penetrating radar and multichannel analysis of surface waves which happened to be in a logistically hard and difficult environment. After the acquisition phase, the datasets were then processed and interpreted with the help from borehole logs and surface geology in the area. The results of these datasets were presented as three separate papers (Papers III, IV and V) in this thesis. The results revealed that integration of geophysical data can be used to accurately delineate boulders, map fractures and groundwater aquifers in an active open pit mine and give a general impression on how fractured and weathered the near surface rock is.

14. APPENDIX

Peer-reviewed extended abstracts

The following extended abstracts were peer-reviewed and presented throughout the course of my Ph.D. and are attached in subsequent pages:

- **Mutshafa, N**., Manzi, M., Westgate, M., James, I., Durrheim, R., and Staley, P. (2021, August). Reprocessing of legacy seismic data for gold exploration: case study from Witwatersrand goldfields, South Africa. In *NSG2021 27th European Meeting of Environmental and Engineering Geophysics* (Vol. 2021, No. 1, pp. 1-5). EAGE Publications BV. https://doi.org/10.3997/2214-4609.202120255

- **Mutshafa, N**., Manzi, M., and Westgate, M. (2022, September). Reappraisal of Legacy Reflection Seismic Data for Gold Exploration: Case Study From Witwatersrand Goldfields, South Africa. In *NSG2022 4th Conference on Geophysics for Mineral Exploration and Mining* (Vol. 2022, No. 1, pp. 1-5). EAGE Publications BV. https://doi.org/10.3997/2214-4609.202220135

- Mabele, N., Manzi, M., Sekiba, M., Rapetsoa, K., Gomo, S., **Mutshafa, N**., and Onyebueka, E. (2022, September). Delineation of the Sinkhole Along R21 Highway in Gauteng (South Africa) Using Integrated Geophysical Methods. In *NSG2022 28th European Meeting of Environmental and Engineering Geophysics* (Vol. 2022, No. 1, pp. 1-5). EAGE Publications BV. https://doi.org/10.3997/2214-4609.202220149

- **Mutshafa, N**., Manzi, M., and Westgate, M. (2022). Reappraisal of Legacy Seismic Data for Gold Exploration in the Witwatersrand Basin (Fochville, South Africa): a case study from the Carletonville Gold Field. 17th SAGA Biennial Conference and Exhibition 2022.

- **Mutshafa, N**., Manzi, M., and Westgate, M. (2021). Reprocessing of legacy seismic data for gold exploration: a case study from Witwatersrand goldfields. 15th AfricaArray Scientific Meeting. 1st – 3rd December 2021.

EAGE

CONFERENCE & EXHIBITION
NEAR SURFACE GEOSCIENCE'21

Reprocessing of legacy seismic data for gold exploration: case study from Witwatersrand goldfields, South Africa

N. Mutshafa[1], M. Manzi[1], M. Westgate[1], I. James[2], R. Durrheim[1], P. Staley[3]

[1] University of the Witwatersrand; [2] HiSeis Pty Ltd; [3] Sibanye Stillwater

Summary

Legacy data are defined as previously acquired data that are no longer in use. Their restoration requires substantial time and money, without the promise of yielding rewarding results. These legacy data sets are often accompanied by poorly preserved documentation, outdated coordinates, and are stored on old tech (e.g., tapes or printed versions/hard copies) that make the data hard to use. The new information acquired from the legacy data may profit future mine planning operations by finding new ore deposits, giving a superior estimation of the resources and information that will assist with sitting and sinking future shafts. In this study we present results from the reprocessed legacy seismic data from Witwatersrand goldfields (South Africa). The purpose of the study is to improve the imaging of the gold orebody known as the Ventersdorp Contact Reef (VCR), which is mined at the Kloof Gold Mine. The VCR occurs at an interface between the Ventersdorp Supergroup and Central Rand Group with contrasting densities and seismic velocities, which makes it a good target for the seismic methods.

Reprocessing of legacy seismic data for gold exploration: case study from Witwatersrand goldfields, South Africa

Introduction

Most geophysicists and mineral explorationists, in general, prefer data from modern instruments than the alleged called 'legacy data' (Malehmir et al., 2019). Legacy data are defined as previously acquired data that are no longer in use. Their restoration requires substantial time and money, without the promise of yielding rewarding results. These legacy data sets are often accompanied by poorly preserved documentation, outdated coordinates, and are stored on old tech (e.g., tapes or printed versions/hard copies) that make the data hard to use. In any case, legacy data have been shown to hold value, particularly if they are from brownfield or close mine investigation sites. These can be restored and improved (Malehmir et al., 2019; Manzi et al., 2019). The new information acquired from the legacy data may profit future mine planning operations by finding new ore deposits, giving a superior estimation of the resources and information that will assist with sitting and sinking future shafts (Manzi et al., 2019; Westgate et al., 2020). Legacy data have advantages such as being less contaminated by noise from mining activities; being acquired in places that presently may be unavailable; being cheaper to reprocess and reinterpret than to collect new data as data acquisition often makes up the bulk of a survey's cost.

Study area and geology

The Witwatersrand Basin is an approximately 7 km thick terrigenous sequence (Coward et al., 1995). The basin is part of the Kaapvaal Craton that formed during the later stages in the development of extensively mineralized segments of the Earth's crust (Robb and Meyer, 1995). Witwatersrand sediments overlie both the Archaean granite-greenstone basement and the volcano-sedimentary Dominion Group. Dominion sediments were deposited over a relatively short time interval, between the minimum ages of 3086±3 and 3074±6 Ma. Witwatersrand deposition can be determined by the age of the Ventersdorp lavas which immediately overlie the sequence over wide areas (Robb and Meyer, 1995). The geological setting of the study area is summarized using Figure 1(a).

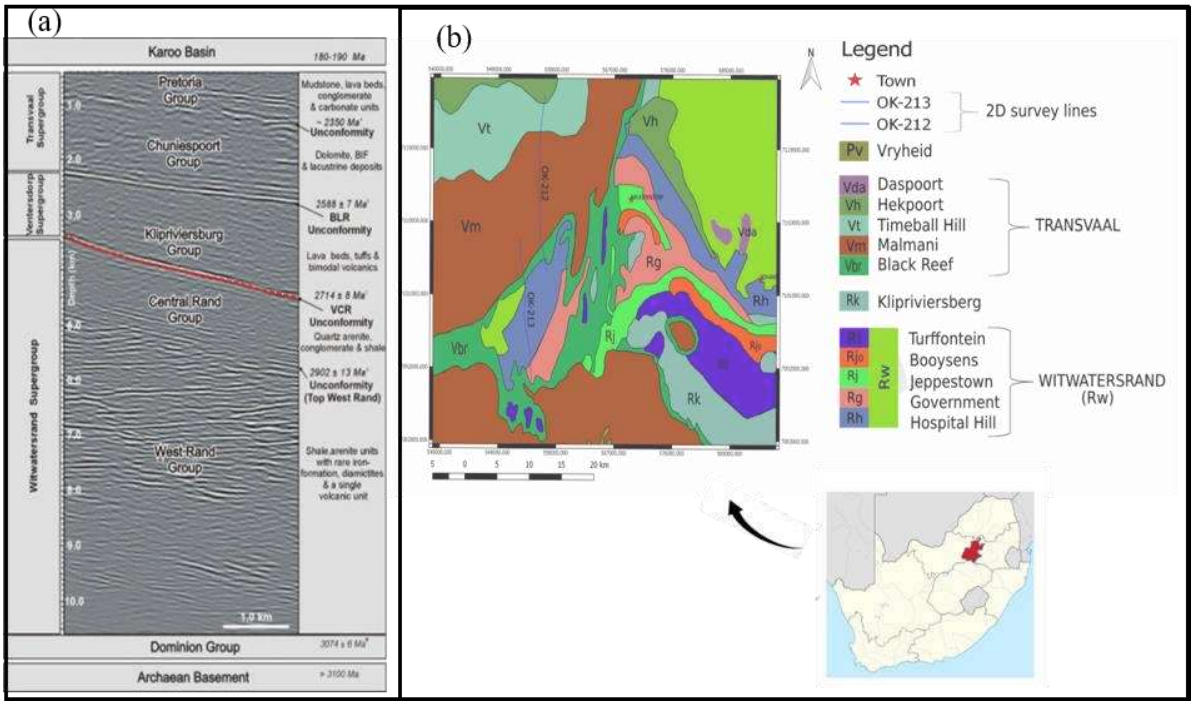


Figure 1 *(a) Generalized seismic stratigraphy of the study area, with dates and ages. After (Manzi et.al., 2014; Kositcin et.al.,2003; Myers et.al., 1990) (b). The geological map of the study area with 2D seismic lines.*

The main purpose of this study is to image the gold orebody known as the Ventersdorp Contact Reef (VCR), which is mined at the Kloof Gold mine of the Witwatersrand goldfields. The VCR occurs at an interface between the Ventersdorp Supergroup and Central Rand Group with contrasting densities and seismic velocities, which makes it a good target for the seismic methods (Figure 1a).

Re-processing of the legacy data

In this study, we have been able to reconstruct coordinates, acquisition geometry, field pegs, and shot records of two legacy 2D seismic lines OK-212 & OK-213 with profile lengths of 16.9 km and 15.7 km, respectively (Figure 1b). The data were acquired using a vibroseis source and 100 m source and 50 m receiver spacing. The record length and sampling interval was 6 s and 4 ms, respectively. Seismic data (Line OK-212 and OK-213) comprised raw shot gathers with strong, visible signals (first break arrivals and reflections), as well as gathers with no visible signals (Figure 2). Both profiles OK-212 and OK-213 exhibit substantial contamination of 50 Hz noise mostly likely due to AC power lines in the region, which were filtered out using a notch filter.

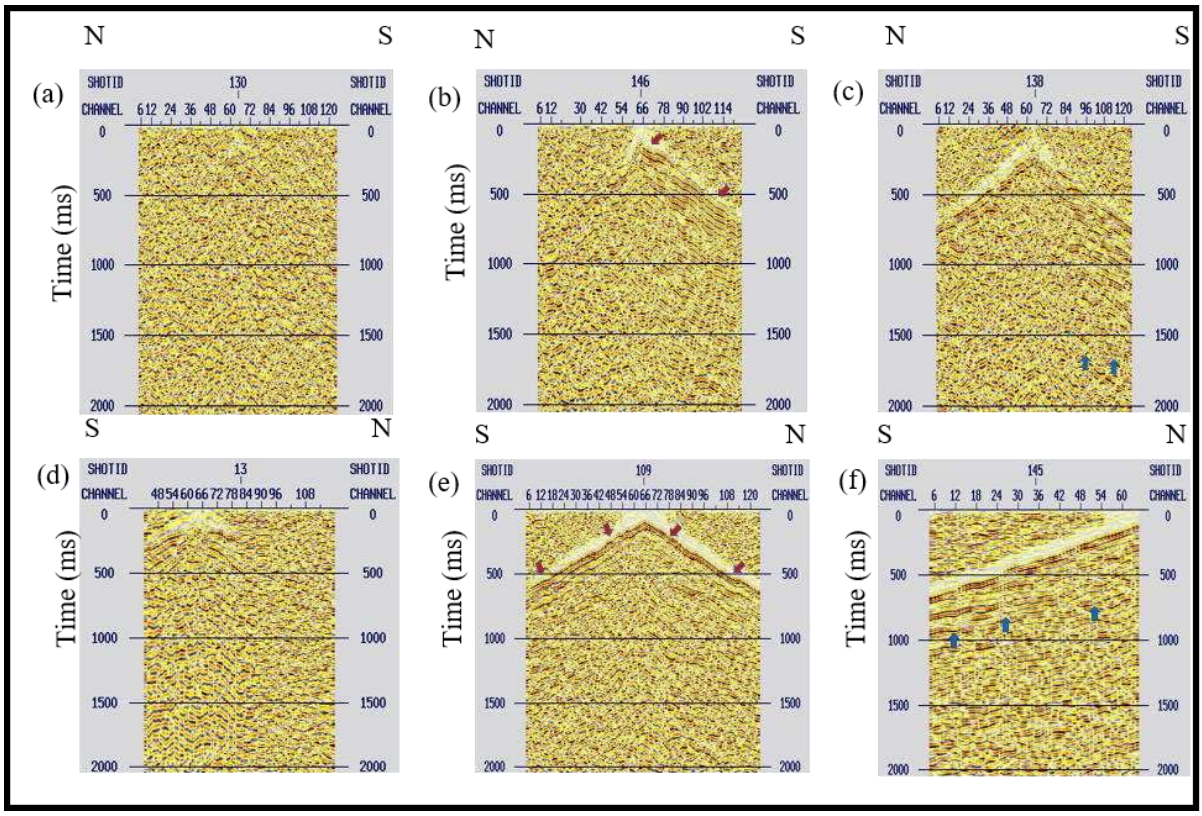


Figure 2 *Example of raw shot gathers of line OK-212 (a-c) and OK-213 (d-f). Shot gathers a & d lack visible first arrivals, shot gathers b & e show partially visible first arrivals indicated by red arrows and shot gathers c & f show possible reflections indicated by blue arrows.*

Figure 3 compares the legacy stacked section processed in 1988 (Figure 3a) with a brute stack section from our preliminary 2021 re-processing work (Figure 3b) for seismic line OK-212. Figure 4 showcases the same for seismic line OK-213. The brute stack sections show a dipping structure (indicated by black arrows) and continuity of a strong seismic reflection located between 1 and 2 s. we interpret the strong seismic reflection to be originating from the VCR orebody. Although the data show potential for imaging the VCR orebody, it should be noted that the central part of the OK-213 survey area remained poorly imaged due to dolomite outcrops (Figure 1b). The poor quality of the data is the result of scattering of the seismic energy due to karst weathering. It is very unlikely that good imaging of the orebody will ever be achieved in this area using surface seismic methods.

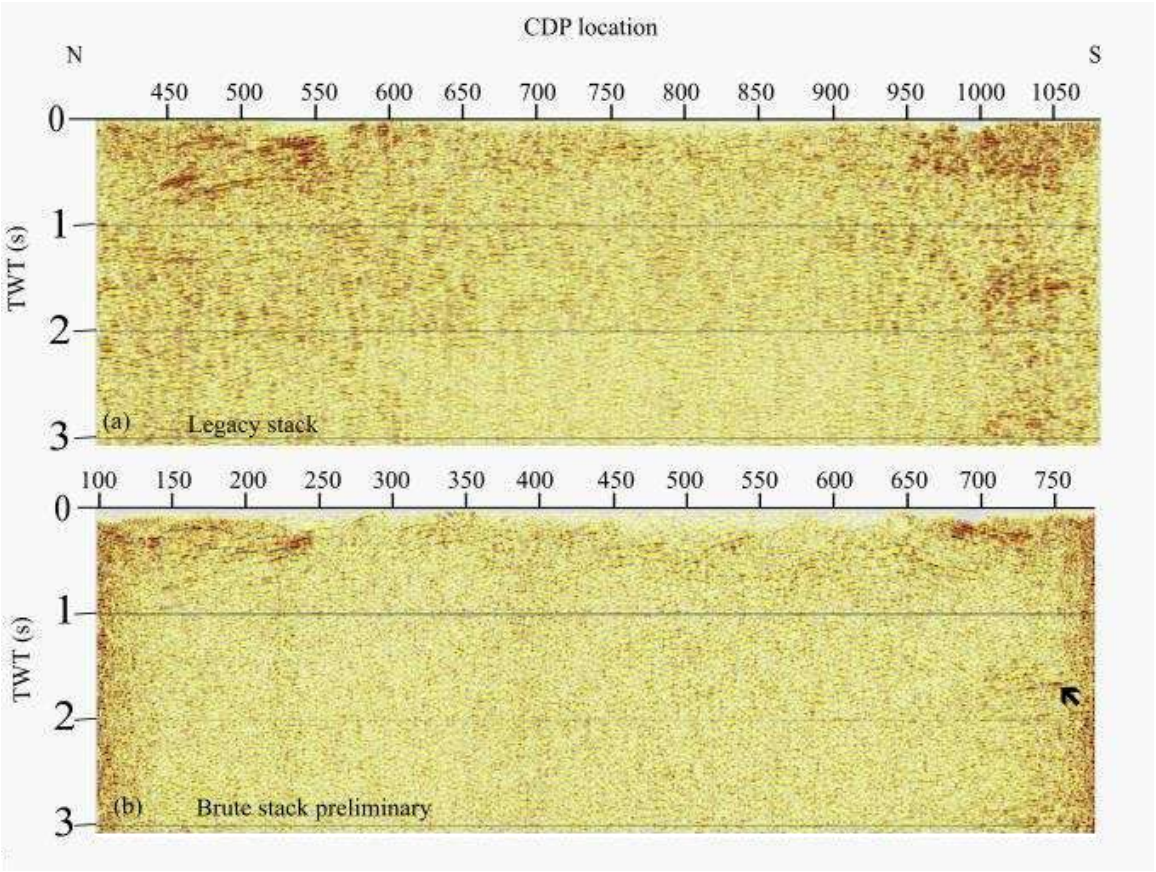


Figure 3 *Comparison between (a) legacy stacked section for profile OK-212, processed in 1988, and (b) preliminary re-processed (brute stack) section from the current study.*

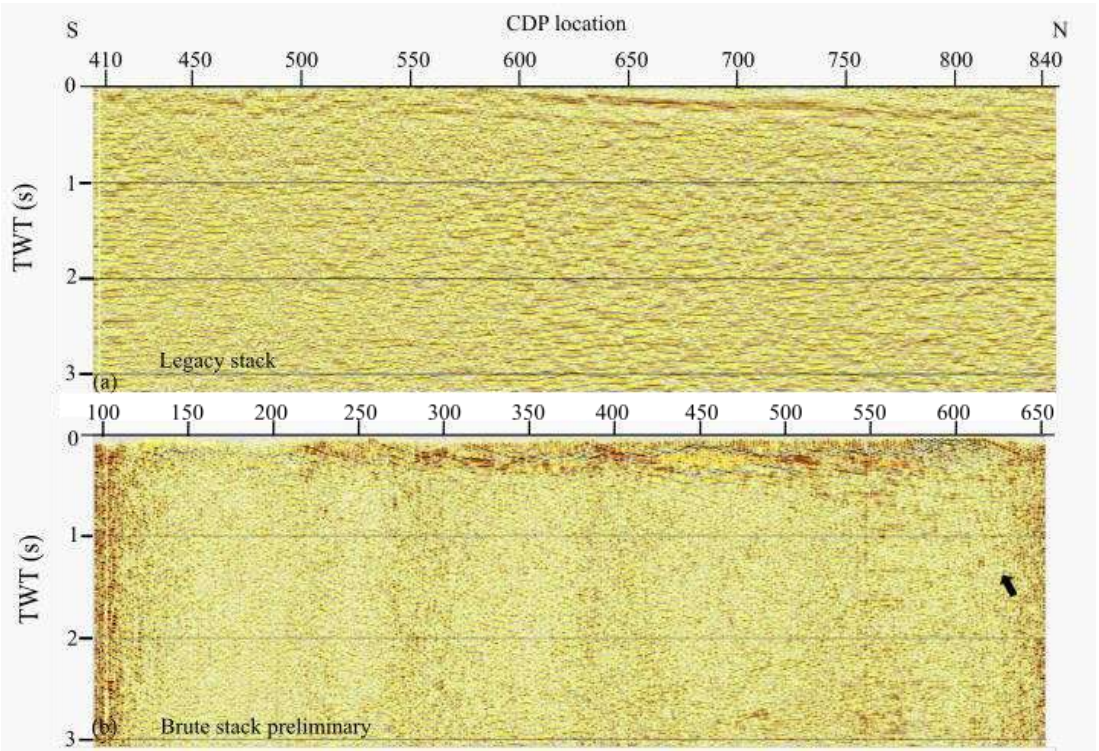


Figure 4 *Comparison between (a) legacy stacked section for profile OK-213, processed in 1988, and (b) preliminary re-processed (brute stack) section from the current study. Note that the re-processed section shows higher resolution, better continuity for the reflections relative to the legacy section.*

Conclusions

There has been notable improvement in the quality of the data after initial re-processing. More in-depth processing work is planned to further improve the image through refined velocity modelling and additional pre-stack time and depth imaging algorithms. This study is further evidence that reprocessing of legacy seismic data acquired in the past can significantly improve the quality of the interpretations.

Acknowledgements

The donation of legacy seismic data by Sibanye Stillwater is acknowledged and greatly appreciated. Council of Geosciences is acknowledged for financial support. We wish to thank HiSeis for funding a license for GLOBE Claritas seismic processing software package.

References

Coward, M., Spencer, R. and Spencer, C. (1995). Development of the Witwatersrand Basin, South Africa. Geological Society, London, Special Publications, 95(1), pp.243-269.

Kositcin, N., McNaughton, N. J., Griffin, B. J., Fletcher, I. R., Groves, D. I., & Rasmussen, B. (2003). Textural and geochemical discrimination between xenotime of different origin in the Archaean Witwatersrand Basin, South Africa. *Geochimica et Cosmochimica Acta*, *67*(4), 709-731.

Malehmir, A., Donoso, G., Markovic, M., Maries, G., Dynesius, L., Brodic, B., ... & Araujo, V. (2019). Smart Exploration: from legacy data to state-of-the-art data acquisition and imaging. *First Break*, *37*(8), 71-74.

Manzi, M. S., Hein, K. A., Durrheim, R. J., & King, N. (2014). The Ventersdorp Contact Reef model in the Kloof Gold Mine as derived from 3D seismics, geological mapping and exploration borehole datasets. *International Journal of Rock Mechanics and Mining Sciences*, *66*, 97-113.

Manzi, M., Malehmir, A., & Durrheim, R. (2019). Giving the legacy seismic data the attention they deserve. *First Break*, *37*(8), 89-96.

Myers, R. E., McCarthy, T. S., & Stanistreet, I. G. (1990). A tectono-sedimentary reconstruction of the development and evolution of the Witwatersrand Basin, with particular emphasis on the Central Rand Group. *South African Journal of Geology*, *93*(1), 180-201.

Robb, L. J., & Meyer, F. M. (1995). The Witwatersrand Basin, South Africa: geological framework and mineralization processes. *Ore Geology Reviews*, *10*(2), 67-94.

Westgate, M., Manzi, M., James, I., Harrison, W. (2020). New insights from legacy seismic data: reprocessing of legacy 2D seismic data for imaging of iron-oxide mineralization near Sishen Mine, South Africa. *Geophysical Prospecting, 68*(7), 2119-2140.

Reappraisal of legacy reflection seismic data for gold exploration: case study from Witwatersrand goldfields, South Africa

Introduction

The seismic reflection method is a powerful geophysical technique that uses the reflection of seismic waves to obtain an image of the Earth's subsurface (Manzi *et.al*., 2012; Yilmaz, 2001). Reflected seismic waves bring very useful information about the rocks and geological structures in the subsurface (Amadi, 2015). Active seismic is widely employed by the seismic exploration industry. The primary aim of seismic exploration is to study geological sources of large lateral extent, such as boundaries of geologic formation, and oil and gas deposits (Keydars et.al., 2018). The seismic reflection method provides the highest resolution subsurface images (compared to other Geophysical methods) of geological structures hosting mineral deposits and can be used for direct detection of minerals deposits at depths greater than 1 km (Malehmir et al., 2012; Manzi et al., 2012). The geological setting of the study area is summarized in Figure 1a.

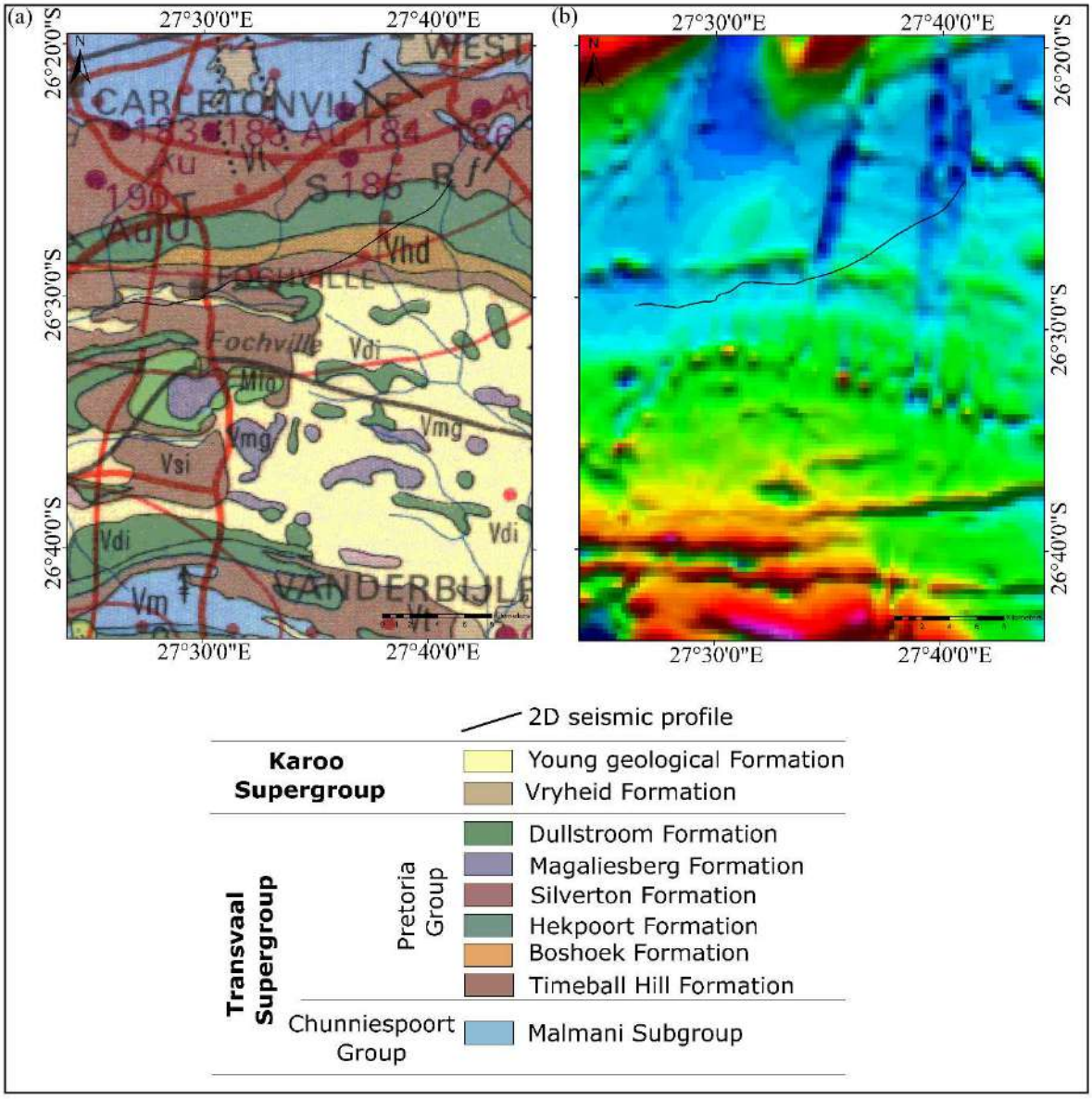


Figure 1 *(a) Geological map of the study area with the distribution of Transvaal (Chuniespoort and Pretoria groups) and Karoo supergroups. (b) magnetic map of the study area with the location of the 2D seismic profile.*

The legacy seismic data has proven capability in mineral exploration and mine planning (Markovic et al., 2020). The reappraisal of legacy reflection seismic data has shown to deliver value, particularly if they are from a brownfield setting, near or even above active mines (Malehmir *et al.* 2014; 2020). Legacy data have advantages such as being less contaminated by noise from mining activities (e.g., blasting, drilling, rock crushing, etc.); being less contaminated by electric/electromagnetic noise; have been acquired in places that presently may be unavailable for new surveys, and ultimately coming at a lower cost compared to new acquisition campaigns (Donoso *et al.* 2020 and references therein).

The main objective of the study is to image the gold orebody known as the Ventersdorp Contact Reef (VCR, ca. 1.5 m thickness) at depths between 2400 and 3900 m below the surface of gold mines in Fochville. More focus will be on imaging the VCR orebody, its continuity, and faults that intersect it. The VCR occurs at an interface between the Ventersdorp Supergroup and Central Rand Group of the Witwatersrand Supergroup.

Seismic Data Acquisition and Processing

The legacy seismic data were acquired in 1983 by the Gold Division of Anglo American as a part of gold exploration (Manzi et al., 2018). The seismic profile was acquired using Vibroseis trucks as a source with a sweep frequency of 10 – 91.25 Hz over a 32 s sweep length at a sampling rate of 4 ms. The data was received as a raw shot gathers that had been correlated in-field and the detailed acquisition information was obtained from field observer's reports as well as from headers. The profile has a receiver and source station spacings of 50 m. The 2D seismic data has a profile length of 25.3 km (Figure 1). The seismic profile has a total of 461 shots with 96 channels/receivers per shot. The receivers had a natural frequency of 10 Hz, and the data were recorded with an 8 Hz low-cut filter. Figure 2 presents an example of two different shot gathers before and after the pre-stack processing sequence with their corresponding amplitude spectra. Few shots of the seismic profile exhibit substantial contamination of 50 Hz noise mostly likely due to AC power lines in the region (Figure 2a).

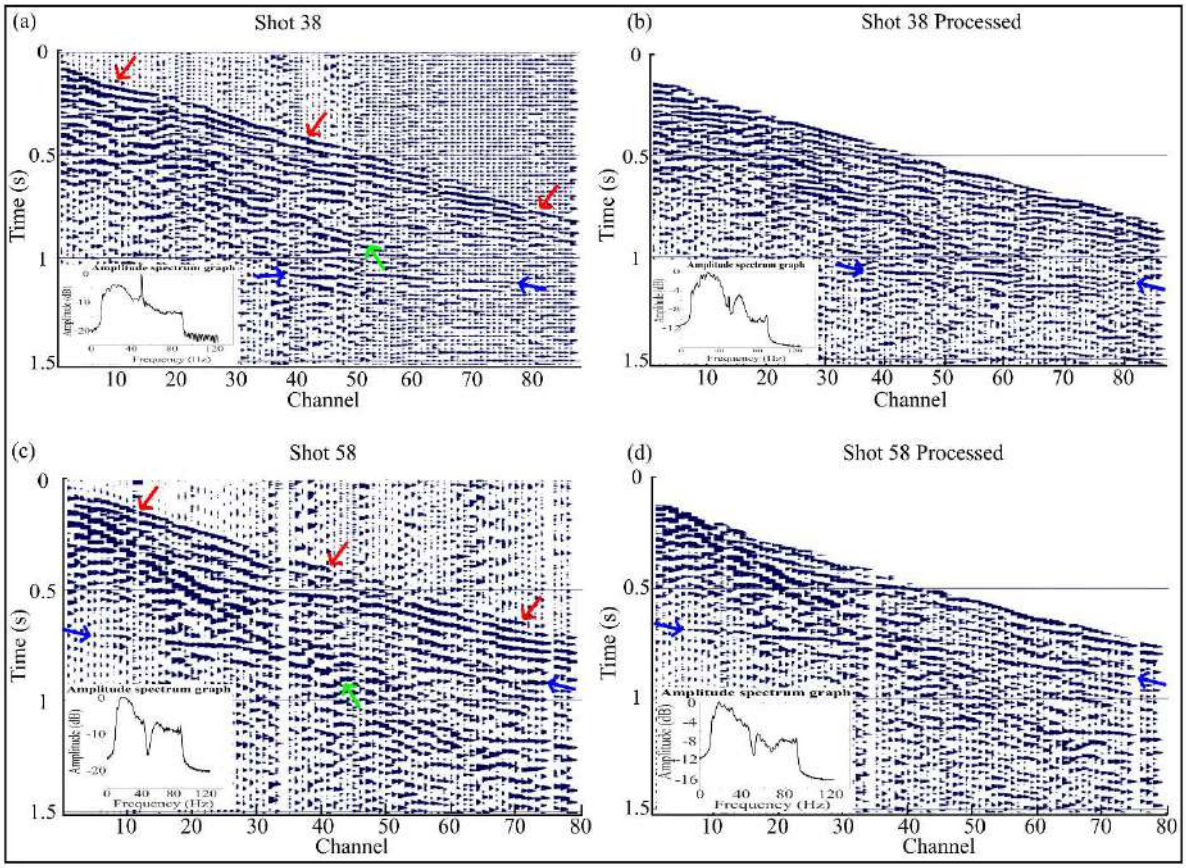


Figure 2 *Two shot gather examples from shots 38 and 58, with their corresponding amplitude spectra. (a, c) Raw shot gathers highlighting clear first breaks marked by red arrows and (b, d) processed shot gathers highlighting clear possible reflections marked by blue arrows. The green arrows indicate ground roll. Note the dominant 50 Hz noise recorded in the shot gathers (notch filtered) (a, b). Some shot gathers already applied notch filter from the field (c, d).*

In this study, we have been able to reconstruct coordinates, acquisition geometry, field pegs, and shot records for the profile. The 2D seismic data came without source and receiver elevations from the headers. We then used Shuttle Radar Topography Mission (or SRTM) data to determine reliable elevations and tied them to the source and receiver locations. After various pre-stack processing steps of legacy data including CDP binning, floating datum, refraction statics corrections, frequency filtering (notch and bandpass), f-k filtering, and predictive deconvolution the shot gathers clearly show possible reflections and first breaks.

A total of 37941 P-wave first breaks were manually picked to compute refraction statics to correct the effect of the variable thickness and lateral velocity variation of weathering. Floating datum statics were applied with a reference datum elevation of 1650 m above mean sea level along with a replacement velocity of 6000 m/s as seen from the refracted P-wave arrivals velocity. An automatic gain control (or AGC) was applied with a window length of 250 ms to recover attenuated amplitudes to all shot gathers. A clear P-wave first breaks are highlighted by red arrows in Figure 2a, c, as well as possible reflections indicated by blue arrows. Ground roll energy was removed by applying an f-k mute filter as indicated by green arrows.

Figure 3 presents the preliminary section (Brute stack) of the 2D seismic legacy profile. Near-surface reflection is imaged, represented by white arrows. All reflections from this section seem to be dipping in the SW direction. Possible reflections are starting to come out just after pre-processing steps (i.e., reflections represented by black, green, blue, and red arrows). According to surface geology (Figure 1a), most of these reflections are due to several groups and formations including Chuniespoort, Pretoria groups, and Witwatersrand Supergroup. Clear interpretation will be done after completing the processing of the 2D legacy seismic data. The preliminary brute stack section shows a dipping structure (indicated by red arrows) and continuity of a strong seismic reflection located between 1 and 2 s. We interpret the strong seismic reflection to be originating from the VCR orebody.

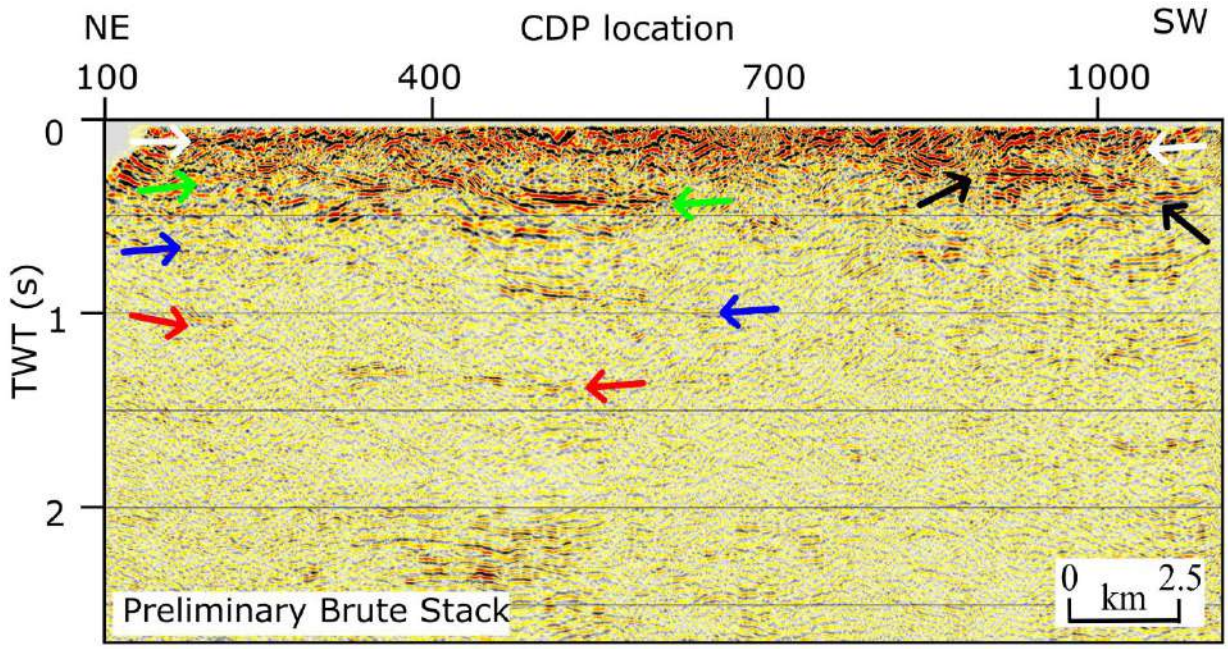


Figure 3 *Preliminary re-processed (brute stack) section from the current study. White, black, green, blue, and red arrows indicate possible reflections coming out after the pre-stack processing steps.*

Conclusions

There has been a notable improvement in the quality of the data after initial re-processing. The data show the potential for imaging the VCR orebody. More in-depth processing work is planned to further improve the image through refined velocity modelling and additional pre-stack time and depth imaging algorithms. This study is further evidence that reprocessing legacy seismic data acquired in the past can significantly improve the quality of the interpretations.

Acknowledgments

The donation of legacy seismic data by Sibanye Stillwater is acknowledged and greatly appreciated. Council of Geosciences, Research Office Carnegie Bursary, and National Research Foundation are acknowledged for financial support. We wish to thank HiSeis for funding a license for the GLOBE Claritas seismic processing software package and the Seismic Research Center at the University of the Witwatersrand for MATLAB licenses.

References

Ahmadi, O. [2015] Application of the Seismic Reflection Method in Mineral Exploration and Crustal Imaging: Contributions to Hardrock Seismic Imaging (Doctoral dissertation, Acta Universitatis Upsaliensis).

Donoso, G.A., Malehmir, A., Pacheco, N., Araujo, V., Penney, M., Carvalho, J., Spicer, B. and Beach, S. [2020] Potential of legacy 2D seismic data for deep targeting and structural imaging at the Neves–Corvo massive sulphide-bearing deposit, Portugal. Geophysical Prospecting, 68(1-Cost-Effective and Innovative Mineral Exploration Solutions), pp.44-61. https://doi:10.1111/1365-2478.12861

Keydar, S., Shtivelman, V. and Arzi, A. [2018] Three-dimensional seismic diffraction imaging for detecting near-surface inhomogeneities. Geophysics

Malehmir A., Durrheim R, Bellefleur M., Urosevic M., Juhlin C, White D., Milkerit B. and Campbell G [2012] Seismic methods in mineral exploration and mine planning: A general overview of past and present case histories and a look into the future. Geophysics 77(5): WC173–WC190.

Malehmir, A., Koivisto, E., Manzi, M., Cheraghi, S., Durrheim, R.J., Bellefleur, G., Wijns, C., Hein, K.A. and King, N. [2014] A review of reflection seismic investigations in three major metallogenic regions: The Kevitsa Ni–Cu–PGE district (Finland), Witwatersrand goldfields (South Africa), and the Bathurst Mining Camp (Canada). Ore Geology Reviews, 56, pp.423-441.

Malehmir, A., Manzi, M., Draganov, D., Weckmann, U. and Auken, E. [2020] Introduction to the special issue on "Cost-effective and innovative mineral exploration solutions". Geophysical prospecting, 68(1), pp.3-6.

Manzi, M. S., Durrheim, R. J., Hein, K. A. and King, N. [2012] 3D edge detection seismic attributes used to map potential conduits for water and methane in deep gold mines in the Witwatersrand basin, South Africa. Geophysics, 77(5), WC133-WC147.

Manzi, M., Malehmir, A. and Durrheim, R. J. [2018] Improved Subsurface Imaging through Re-processing of Legacy 2D Seismic Data-A Case Study from a Deep South African Gold Mine. In 2nd Conference on Geophysics for Mineral Exploration and Mining (Vol. 2018, No. 1, pp. 1-5). European Association of Geoscientists & Engineers. https://doi.org/10.3997/2214-4609.201802705

Markovic, M., Maries, G., Malehmir, A., von Ketelhodt, J., Bäckström, E., Schön, M. and Marsden, P. [2020] Deep reflection seismic imaging of iron-oxide deposits in the Ludvika mining area of central Sweden. Geophysical Prospecting, 68(1-Cost-Effective and Innovative Mineral Exploration Solutions), 7-23.

Yilmaz, Ö. [2001] Seismic data analysis: Processing, inversion, and interpretation of seismic data. Society of Exploration Geophysicists.

Delineation of the sinkhole along R21 highway in Gauteng (South Africa) using integrated geophysical methods

Introduction

The Gauteng province in South Africa is underlain by at least 25% of soil and rock formations that are susceptible to sinkhole and subsidence formation. Sinkholes, in particular, pose huge safety issues to the 4-5 million people residing and working in Gauteng region (Buttrick *et al*., 2001).

The purpose of this study was to use integrated geophysical methods to delineate the lateral and vertical extent of a sinkhole that formed along the R21 highway near Olifantsfontein, in the Gauteng province of South Africa. Electrical resistivity tomography (ERT), refraction seismics, and ground penetrating radar (GPR) were all conducted as part of the study. ERT and GPR are cost effective and non-destructive geophysical methods that are used worldwide to characterise Karst environments and delineate subsidence and sinkholes (Hussain *et al*., 2020). Between February and April 2022, a sinkhole (here termed R21 sinkhole) with a diameter of approximately 8 m (as observed on surface) closed off two northbound lanes of R21 highway, allowing traffic only to flow on the other two lanes. The existence of sinkholes that formed prior the one on the R21 highway indicates that the study area is susceptible to the formation of sinkholes. This is mainly due to the carbonate rocks (i.e., Malmani dolomite sequence) underlying the area as well as hydrogeological influences such as dewatering or water ingress which cause changes in the water table. The underlying dolomite rock is compartmentalized by fractures, joints, faults and dykes that may act as conduits for water migration and, possibly, result in the formation of sinkholes (Montgomery *et al*., 2020). The R21 sinkhole poses a significant risk to the lives of the residences living nearby and may also cause damage to the infrastructure. It is therefore important to assess the effectiveness of the geophysical methods in mapping the position and size of the R21 sinkhole on the subsurface to assist with the remediation process.

Geological Setting

The study area is underlain by carbonate rocks of the Transvaal Supergroup (Clay, 1981; Unpubl. Results). Oaktree, Monte Christo, Lyttelton, Eccles, and Frisco formations are five geological formations that make up the Malmani subgroup (from oldest to youngest). The Lyttelton and Eccles formations form part of the study area. The Lyttelton formation overlies the Eccles formation, displaying a contact where chert concentration increases and dark brown dolomite changes to grey (Obbes, 2000). The Lyttelton formation is made up of chert-poor dolomite that becomes more chert-rich towards the bottom of the stratigraphy. The Eccles formation is made up of alternating layers of dolomite and chert (Obbes, 2000).

Methodology

Sinkholes are usually filled with either air, water or collapse material creating a contrast in physical properties (e.g., density, seismic velocities, electrical conductivity, etc.) with the surrounding competent rocks. It is this contrast that allows for the use of geophysical methods. Seismic reflection and refraction, gravimeter, ground-penetrating radar, electrical resistivity tomography, and multichannel analyses of surface waves are some of the geophysical methods that are widely used for sinkhole exploration (Hussain *et al*., 2020; Montgomery *et al*., 2020). The survey involved the use of ground penetrating radar (GPR), electrical resistivity tomography (ERT) and seismic methods along the R21 highway (Figure 1a). The following survey parameters were used for the survey designs:

- ERT: Profile R1 and R2 were acquired using the dipole-dipole array with the electrode spacing of 2.5 m. Both profiles have a total length of 132.5 m.
- GPR: A GSSI System with 400 MHz antenna was used with dielectric permittivity of 6 f/m (pavement) and 9 f/m (on grass). The parallel profile lengths were 5 lines x 140 m, 25 lines x 9 m, 3 lines x 90 m and 2 lines x 20 m.
- Seismics: A 24 m multi-component land streamer (4.5 Hz geophone, 1C) was used with shot spacing of 1 m-2 m.



Figure 1**:** *Figure 1a, shows the sinkhole formed along the highway, while figure 1b shows its position (green circle). Sinkholes formed prior to the R21 highway sinkhole are shown in red in Figure 1b. Figure 1c,1d, and 1e shows the ground penetrating radar, electrical resistivity tomography and seismic land streamer methods, respectively. Photos in Figure 1a, 1c were taken by Musa Manzi.*

Preliminary Results

GPR results

A total of eight south-north and twenty-seven east-west GPR lines were surveyed as part of the study. This study presents only the results from a few profiles. Figure 2a displays a GPR section that runs south-north of the highway (line G1, shown in blue in Figure 1b), while Figure 2b shows a GPR section of the east-west line along the road (line G2, shown in blue in Figure 1b).

G1 GPR section exhibits a consistent lateral reflection (shown by the white dotted line in Figure 2a), with varying depths from south to north (i.e., ~2 m in the north and ~3 m in the south). This reflection is interpreted to represent the interface between near-surface geological boundaries. A series of diffractions occur between ~5 and 7 m depths (Figure 2a, shown by blue arrows), and may indicate the position of the sinkhole features. Possible metal piece observed on the surface is detected as reflections in the G1 section (Figure 2a, shown by a red arrow). G2 GPR section exhibits a series of reflections that terminate along the section. The zone where reflections terminate (marked by a pink line in Figure 2) suggests that the sinkhole extends by ~2.5 m into the highway and has an estimated depth of ~10 m.

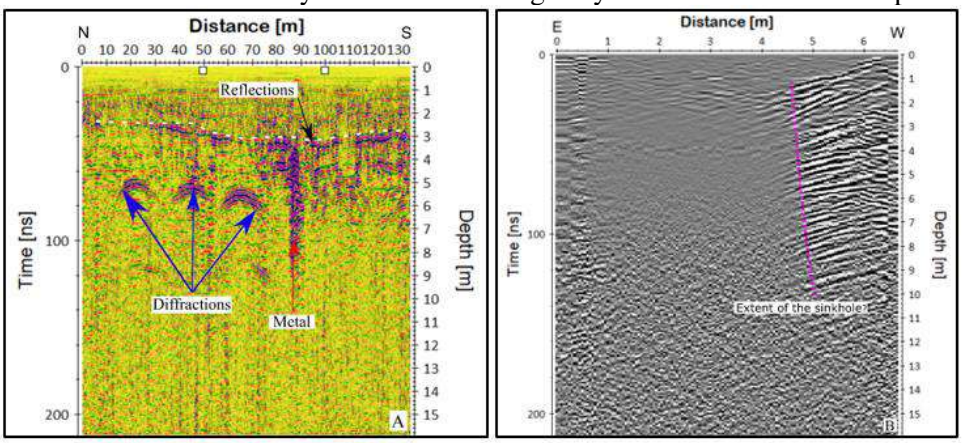


Figure 2: *GPR sections for line G1 (south-north) and line G2 (east-west).*

ERT results

A total of six south-north, 2D ERT lines were acquired (lines R1 and R2, shown in yellow, Figure 1b). According to Montgomery *et al*. (2020) sinkholes filled with loose, unsaturated material or air appear as resistivity highs, while sinkholes filled with water or saturated material appear as resistivity lows, however, the delineation is also dependent on the conductivity of the surrounding material and the depth, shape, and size of the sinkhole.

The ERT section, shown in Figure 3a, exhibits two high resistivity zones that are interpreted as possible sinkholes (marked by green circles at depths between ~5 m and 20 m). In particular, the high resistivity zone with a dotted green circle aligns with the position of the sinkhole observed on the surface, thus it is possible that the detected anomaly is a response of the sinkhole. The high resistivity zone marked by a dotted blue circle indicates another possible sinkhole that has not yet manifested itself on the surface. Below this high resistive area, lies a low resistive zone which is interpreted to be related to the groundwater table, shown by white dotted lines at depths of about ~25 m from surface (Figure 3). Figure 3b shows similar features to Figure 3a, however, the high resistive anomaly in the south is not delineated. This may indicate that this sinkhole does not extend beyond this ERT section. Furthermore, a high resistivity zone towards the north is well aligned with the position of the R21 sinkhole.

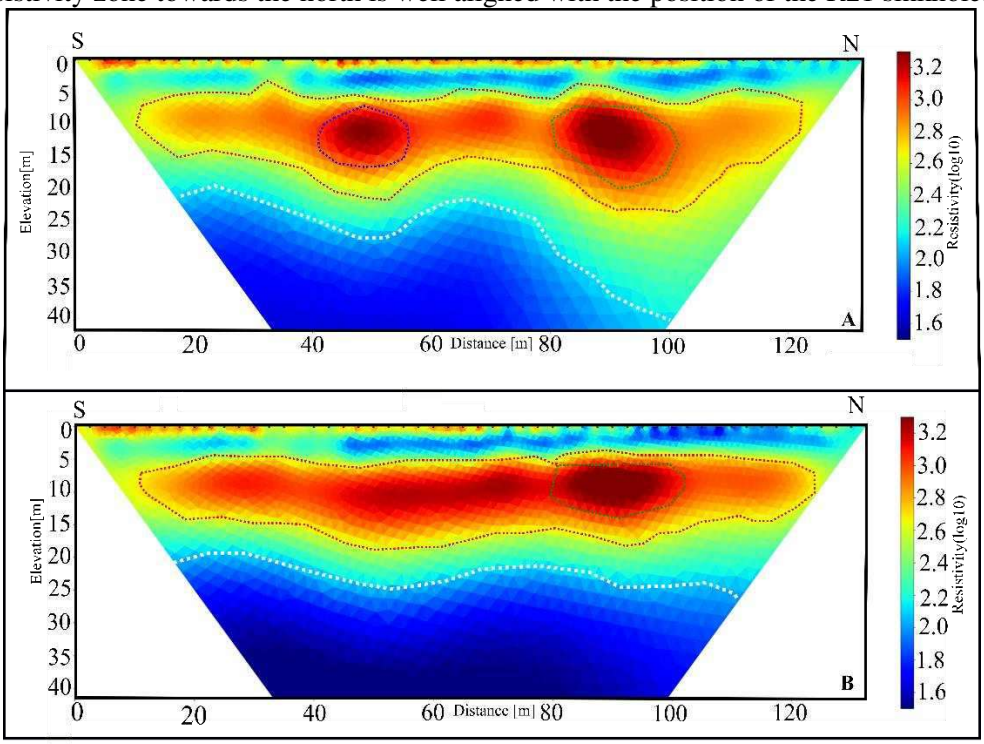


Figure 3: *ERT sections form lines R1 and R2, with the green circular zone showing the sinkhole as observed on the surface.*

Seismic results

Four seismic refraction profiles were conducted along the R21 sinkhole. Only the results from profile S1 (shown in pink, Figure 1b) are shown here. We used a land streamer and a 7 kg sledgehammer as receivers and energy source, respectively.

P-wave refraction tomography in Figure 4 shows two low-velocity zones marked by red and blue dotted lines. The low-velocity zone between distances of 12 m and 28 m, shown by the dotted blue line, may represent the continuation of the R21 sinkhole. The high-velocity zone from the depth of ~9 m indicates possible fresh dolomite bedrock. A possible fault (indicated in a white dotted line), is also mapped. The presence of a fault suggests that it may have acted as a conduit, allowing the flow of water from the surface to the dolomite bedrock. The presence of this structure, together with circulating water eroding the dolomite bedrock, may have accelerated the formation of the sinkhole.

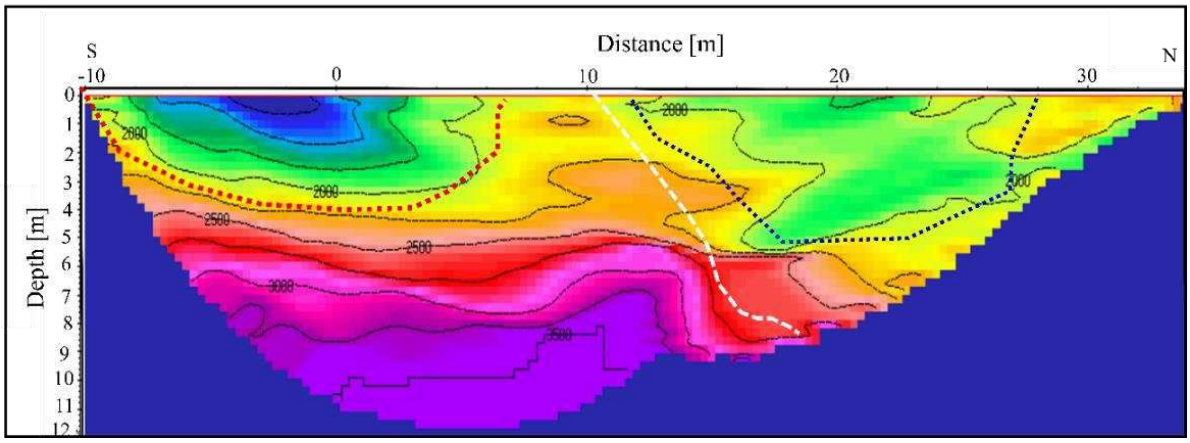


Figure 4: *Interpreted south-north P-wave seismic tomogram for line S1.*

Conclusions

GPR, ERT and seismic surveys were acquired in close proximity to the R21 sinkhole. In addition, at least 6 boreholes have been planned for drilling within the vicinity of the sinkhole. These boreholes will provide substantial data on the overall geology of the study area. On the surface, the sinkhole is observed to be about ~8 m wide, ~8-9 m deep and extends between ~1-2.5 m into the R21 highway. GPR results show that it is between ~8-10 m deep and extends ~2.5 m onto the highway, while seismic results show that the sinkhole is about ~13 m wide and may be related to faulting. The resistivity results suggest that the sinkhole extends to depths of ~10-15 m. Results indicate that sinkholes can be characterised on the subsurface using integrated geophysical methods. The rehabilitation process should also consider the other sinkholes formed on the western part of the highway as these sinkholes have the potential to extend into the highway, if they are not remedied.

Acknowledgements

We thank the Council for Geoscience(CGS) for providing access to the site. We also thank the Wits University geophysics team that assisted with the survey planning, data acquisition and processing.

References

Buttrick, D.B., van Schalkwyk, A., Kleywegt R.J. and Watermeyer, R. [2001] Proposed method for dolomite land hazard and risk assessment in South Africa. *South African Institution of Civil Engineering Journal*, **43**(2), 27– 36.

Carbonel, D., Rodríguez, V., Gutiérrez, F., McCalpin, J.P., Linares, R., Roqué C., Zarroca, M., Guerrero, J. and Sasowsky, I. [2014] Evaluation of trenching, ground penetrating radar (GPR) and electrical resistivity tomography (ERT) for sinkhole characterization. *Earth Surface Processes and Landforms,* **39**, 214–227.

Hussain, Y., Uagoda, R., Borges, W., Nunes, J., Hamza, O., Condori, C., Aslam, K., Dou, J. and Cárdenas-Soto, M. [2020] The Potential Use of Geophysical Methods to Identify Cavities, Sinkholes and Pathways for Water Infiltration. *Water,* **12**(8):2289.

Montgomery, J., Jackson, D., Kiernan, M. and Anderson, B.J.M. [2020] Use of geophysical methods for sinkhole exploration. *The Alabama Department of Transportation*, 930-945.

Obbes, A.M. [2000] The structure, stratigraphy and sedimentology of the Blackreef Malmani Rooihoogte succession of the Transvaal Supergroup southwest of Pretoria. *Council for Geoscience*, **127,** 89 pp.

Reappraisal of Legacy Seismic Data for Gold Exploration in the Witwatersrand Basin (Fochville, South Africa): a case study from the Carletonville Gold Field

N. Mutshafa[1], M. Manzi[1], M. Westgate[1]
1. University of the Witwatersrand, South Africa,
ndamulelo.mutshafa@students.wits.ac.za

Biography

Ndamulelo Mutshafa is a Ph.D. Geophysics candidate at the University of Witwatersrand currently working on reprocessing legacy seismic reflection data. He completed his B.Sc. Honours in Geophysics in 2018 and bachelor's degree majoring in Physics and Mathematics in 2017 at the University of Witwatersrand.
Musa Manzi is an Associate Professor in the School of Geosciences, University of the Witwatersrand, and Director of the Reflection Seismic Research Centre.
Michael Westgate is a post-doctoral fellow in Geophysics at the School of Geosciences, University of the Witwatersrand.

SUMMARY

Reappraisal of legacy reflection seismic data has shown to deliver value, particularly in brownfield settings. The 25.3 km long seismic profile used in this study was acquired in 1983, by the Gold Division of Anglo American, as part of their Witwatersrand goldfields exploration programme. In this work, we demonstrate how the reappraisal of legacy reflection seismic data can be advantageous in the mineral exploration industry by using the latest seismic processing tools to improve the imaging resolution. The purpose of this study is to improve the imaging of the Ventersdorp Contact Reef (VCR) gold orebody, situated at depths between 2400 and 3900 m below the Fochville gold mines surface, South Africa. The preliminary results of the reprocessed legacy seismic section clearly reveal a dipping reflection associated with the VCR mineralization.

Keywords: Legacy, imaging, reappraisal, tomography

INTRODUCTION

The seismic reflection method is a powerful geophysical technique that uses the reflection of seismic waves to obtain an image of the Earth's subsurface (Manzi et al., 2012; Yilmaz, 2001). Reflected seismic waves bring very useful information about the rocks and geological structures in the subsurface (Ahmadi, 2015). Active seismic is widely employed by the seismic exploration industry. The primary aim of seismic exploration is to study geological sources of large lateral extent, such as boundaries of geologic formation and oil and gas deposits (Keydars et al., 2018). The seismic reflection method provides the highest resolution subsurface images (compared to other Geophysical methods) of geological structures hosting mineral deposits and can be used for direct detection of minerals deposits at depths greater than 1 km (Malehmir et al., 2012; Manzi et al., 2012). The geological setting of the study area is summarized in Figure 1a.

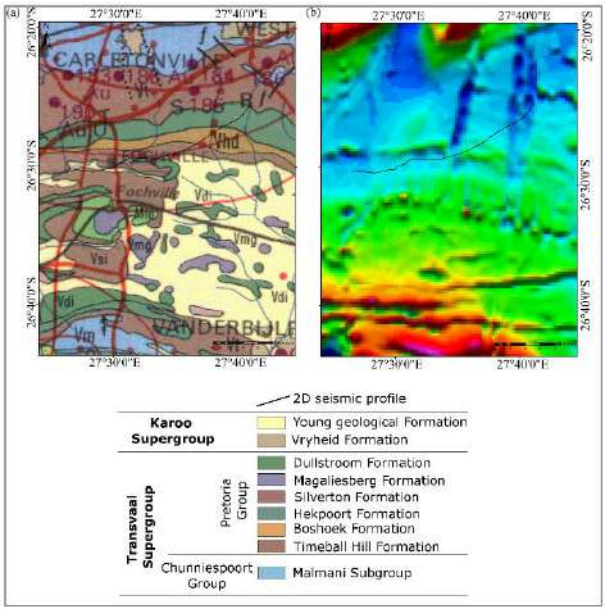


Figure 1. (a) Geological map of the study area with the distribution of Transvaal (Chuniespoort and Pretoria groups) and Karoo supergroups. (b) magnetic map of the study area with the location of the 2D seismic profile.

The legacy seismic data has proven capability in mineral exploration and mine planning (Markovic et al., 2020). The reappraisal of legacy reflection seismic data has shown to deliver value, particularly if they are from a brownfield setting, near or even above active mines (Malehmir et al. 2014; 2020). Legacy data have advantages such as being less contaminated by noise from mining activities (e.g., blasting, drilling, rock crushing, etc.); being less contaminated by electric/electromagnetic noise; have been acquired in places that presently may be unavailable for new surveys, and ultimately coming at a lower cost compared to new acquisition campaigns (Donoso et al. 2020 and references therein).

The aim of the study is to image the gold orebody known as the Ventersdorp Contact Reef (VCR, ca. 1.5 m thickness) at depths between 2400 and 3900 m below the surface from gold mines in Fochville. One of the study objectives is to focus on imaging the orebody, its continuity, and faults that intersect it. The VCR occurs at an interface between the Ventersdorp Supergroup and Central Rand Group of the Witwatersrand Supergroup.

2D SEISMIC DATA

Seismic Data Acquisition

The legacy seismic data were acquired in 1983 by the Gold Division of Anglo American as a part of gold exploration (Manzi et al., 2018). The seismic profile was acquired using Vibroseis trucks as a source with a sweep frequency of 10 – 91.25 Hz over a 32 s sweep length at a sampling rate of 4 ms. The data was received as a raw shot gathers that had been correlated in-field, and the detailed acquisition information was obtained from field observer's reports as well as from headers. The profile has a receiver and source station spacings of 50 m. The 2D seismic data has a profile length of 25.3 km (Figure 1). The seismic profile has a total of 461 shots with 96 channels/receivers per shot. The receivers had a natural frequency of 10 Hz, and the data were recorded with an 8 Hz low-cut filter. Table 1 below summarizes the survey parameters for profile AC-5.

Table 1. List of relevant parameters of the legacy data survey.

Acquisition parameters	
Type of survey	2D Seismic Profile
Year	1983
Profile length	25.3 km
Trend	NE-SW
Field spread	End-on × - 175–4975 m
Recording system	
Recording device	SN338 HR/ ADDIT III/ CMA I
Sampling rate	4 ms
Recording length	6 s
Sweep length	26 s
Sweep frequencies	10 – 91 Hz
Source information	
Source spacing	50 m
Source type	Vibroseis
Receiver information	
Receiver spacing	50 m
Number of channels	96
Geophone type	10 Hz (SM4)

Figure 2 presents an example of two different shot gathers before and after the pre-stack processing sequence with their corresponding amplitude spectra. Few shots of the seismic profile exhibit substantial contamination of 50 Hz noise mostly likely due to AC power lines in the region (Figure 2a).

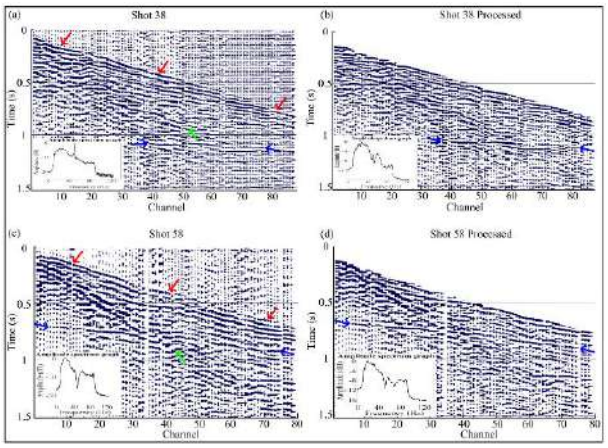


Figure 2. Two shot gather examples from shots 38 and 58, with their corresponding amplitude spectra. (a, c) Raw shot gathers highlighting clear first breaks marked by red arrows, and (b, d) processed shot gathers highlighting clear possible reflections marked by blue arrows. The green arrows indicate ground roll. Note the dominant 50 Hz noise recorded in the shot gathers (notch filtered) (a, b). Some shot gathers already applied notch filter from the field (c, d).

Seismic Data Processing

In this study, we have been able to reconstruct coordinates, acquisition geometry, field pegs, and shot records for the profile. The 2D seismic data came without source and receiver elevations from the headers. We then used Shuttle Radar Topography Mission (or SRTM) data to determine reliable elevations and tied them to the source and receiver locations (Figure 1b). After various pre-stack processing steps of legacy data, including CDP binning, floating datum, refraction statics corrections, frequency filtering (notch and bandpass), f-k filtering, and predictive deconvolution the shot gathers clearly shows possible reflections and first breaks. An automatic gain control (or AGC) was applied with a window length of 250 ms to recover attenuated amplitudes to all shot gathers. A clear P-wave first breaks are highlighted by red arrows in Figure 2a, c, as well as possible reflections indicated by blue arrows. As indicated by green arrows, ground roll energy was removed by applying an f-k mute filter.

A total of 37941 P-wave first breaks were manually picked to compute refraction statics to correct the effect of the variable thickness and lateral velocity variation of weathering. Floating datum statics were applied with a reference datum elevation of 1650 m above mean sea level along with a replacement velocity of 6000 m/s as seen from the refracted P-wave arrivals velocity (Figure 3a). Refraction tomography, which accounted for elevation and was calculated to aid interpretation of the seismic profile up to a depth of 1665 m, and the ray path coverage is displayed in figure 3b.

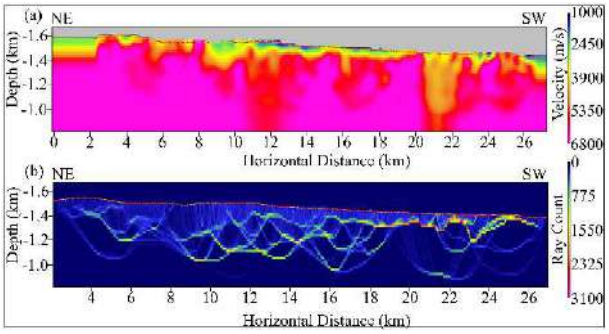


Figure 3. (a) Refraction tomographic velocity model calculated and (b) Ray coverage for the seismic profile.

Figure 4 presents the preliminary section (Brute stack) of the 2D seismic legacy profile. Near-surface reflection is imaged, represented by white arrows. All reflections from this section seem to be dipping in the SW direction. Possible reflections are starting to pop out just after pre-processing steps (i.e., reflections represented by black, green, blue, and red arrows). According to surface geology (Figure 1a), most of these reflections are due to several groups and formations, including Chuniespoort, Pretoria groups, and Witwatersrand Supergroup. Clear interpretation will be made after completing the processing of the 2D legacy seismic data.

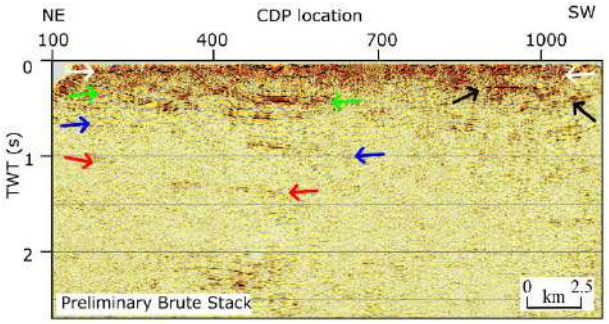


Figure 4. Preliminary reprocessed (brute stack) section from the current study. White, black, green, blue, and red arrows indicate possible reflections coming out after the pre-stack processing steps.

CONCLUSIONS

There has been a notable improvement in the quality of the data after initial reprocessing. More in-depth processing work is planned to further improve the image through refined velocity modelling and additional pre-stack time and depth imaging algorithms. This study is further evidence that reprocessing legacy seismic data acquired in the past can significantly improve the quality of the interpretations.

ACKNOWLEDGMENTS

The donation of legacy seismic data by Sibanye Stillwater is acknowledged and greatly appreciated. Council of Geosciences is acknowledged for financial support. We wish to thank HiSeis for funding a license for the GLOBE Claritas seismic processing software package and the Seismic Research Center at the University of the Witwatersrand for MATLAB licenses.

REFERENCES

Ahmadi, O., 2015, Application of the Seismic Reflection Method in Mineral Exploration and Crustal Imaging: Contributions to Hardrock Seismic Imaging (Doctoral dissertation, Acta Universitatis Upsaliensis).

Donoso, G.A., Malehmir, A., Pacheco, N., Araujo, V., Penney, M., Carvalho, J., Spicer, B., and Beach, S., 2020, Potential of legacy 2D seismic data for deep targeting and structural imaging at the Neves–Corvo massive sulphide-bearing deposit, Portugal. Geophysical Prospecting, 68(1-Cost-Effective and Innovative Mineral Exploration Solutions), pp.44-61. https://doi:10.1111/1365-2478.12861

Keydar, S., Shtivelman, V., and Arzi, A., 2018, Three-dimensional seismic diffraction imaging for detecting near-surface inhomogeneities. Geophysics

Malehmir A., Durrheim R, Bellefleur M., Urosevic M., Juhlin C, White D., Milkerit B., and Campbell G., 2012, Seismic methods in mineral exploration and mine planning: A general overview of past and present case histories and a look into the future. Geophysics 77(5): WC173–WC190.

Malehmir, A., Koivisto, E., Manzi, M., Cheraghi, S., Durrheim, R.J., Bellefleur, G., Wijns, C., Hein, K.A., and King, N., 2014, A review of reflection seismic investigations in three major metallogenic regions: The Kevitsa Ni–Cu–PGE district (Finland), Witwatersrand goldfields (South Africa), and the Bathurst Mining Camp (Canada). Ore Geology Reviews, 56, pp.423-441.

Malehmir, A., Manzi, M., Draganov, D., Weckmann, U., and Auken, E., 2020, Introduction to the special issue on "Cost-effective and innovative mineral exploration solutions". Geophysical prospecting, 68(1), pp.3-6.

Manzi, M. S., Durrheim, R. J., Hein, K. A., and King, N., 2012, 3D edge detection seismic attributes used to map potential conduits for water and methane in deep gold mines in the Witwatersrand basin, South Africa. Geophysics, 77(5), WC133-WC147.

Manzi, M., Malehmir, A., and Durrheim, R. J., 2018, Improved Subsurface Imaging through Re-processing of Legacy 2D Seismic Data-A Case Study from a Deep South African Gold Mine. In 2nd Conference on Geophysics for Mineral Exploration and Mining (Vol. 2018, No. 1, pp. 1-5). European Association of Geoscientists & Engineers. https://doi.org/10.3997/2214-4609.201802705

Markovic, M., Maries, G., Malehmir, A., von Ketelhodt, J., Bäckström, E., Schön, M., and Marsden, P., 2020, Deep reflection seismic imaging of iron-oxide deposits in the Ludvika mining area of central Sweden. Geophysical Prospecting, 68(1-Cost-Effective and Innovative Mineral Exploration Solutions), 7-23.

Yilmaz, Ö., 2001, Seismic data analysis: Processing, inversion, and interpretation of seismic data. Society of Exploration Geophysicists.